CHARACTERISATION AND MODELLING OF NATURALLY FRACTURED RESERVOIRS

重点流程图

天然裂缝性油藏描述及建模

- **NFR**油藏描述和建模基本流程
- **NFR**油藏描述步骤
- **DFN**模型概述
- **DFN**建模一般步骤
- 混合神经网络随机建模流程图
- 最优化模拟一般步骤
- 基于目标的条件全局最优化**NFR**建模步骤

By

Nam Hong Tran

Supervisor: Associate Professor Sheikh S. Rahman



A dissertation submitted to the University of New South Wales in partial fulfilment of the requirements for the Degree of Doctor of Philosophy

In

Petroleum Engineering

School of Petroleum Engineering

The University of New South Wales

Sydney, Australia

July 2004

CERTIFICATE OF ORIGINALITY

I hereby declare that this submission is my own work and that, to the best of my knowledge and belief, it contains no material previously published or written by another person nor material which to a substantial extent has been accepted for the award of any other degree or diploma of a university or other institute of higher learning, except where due acknowledgment is made in the text

(Signed)……..……

Nam Hong Tran

ACKNOWLEDGMENTS

I wish to thank all the people who have so kindly helped me with the preparation of this dissertation, in particular:

Associate Professor Sheik S. Rahman for constant guidance during his supervision of this thesis,

Dr. Mark Berman, Mr. Martin Berry, Dr. Zhixi Chen and Dr. Khalil Rahman for their valuable inputs at various stages of this thesis,

All the staff members and graduate students at the School of Petroleum Engineering, the University of New South Wales for their supports and friendliness.

I also wish to acknowledge Magellan Petroleum Australia Limited, Santos Petroleum Australia Limited and Vietsovpetro Joint Venture for providing valuable data and technical discussions, without which this research could not have been completed.

DEDICATION

To my grandparents, with whom my inspiration is born and shaped,

To my mum and dad and their unconditional love.

Thank you.

ABSTRACT

Naturally fractured reservoirs are generally extremely complex. The aim of characterisation and modelling of such reservoirs is to construct numerical models of rock and fractures, preparing input data for reliable stimulation and fluid flow simulation analyses. This requires the knowledge of different fracture heterogeneities and their correlations at well locations and inter-well regions.

This study addresses the issues of how to integrate different information from various field data sources and construct comprehensive discrete fracture networks for naturally fractured reservoir. The methodology combines several mathematical and artificial intelligent techniques, which include statistics, geostatistics, fuzzy neural network, stochastic simulation and simulated annealing global optimisation.

The study has contributed to knowledge in characterisation and modelling of naturally fractured reservoirs in several ways. It has developed:

- An effective and data-dependant fracture characterisation procedure. It examines all the conventional reservoir data sources and their roles towards characterisation of different fracture properties. The procedure has the advantage of being both comprehensive and flexible. It is able to integrate all multi-scaled and diverse fracture information from the different data sources.
- An improved hybrid stochastic generation algorithm for modelling discrete fracture networks. The stochastic simulation is able to utilise both discrete and continuum fracture information. It could simulate not only complicated distributions for fracture properties (e.g. multimodal circular statistics and non-parametric distributions) but also their correlations. In addition, with the incorporation of artificial fuzzy neural simulation, discrete multifractal geometry of fracture size and fracture density distribution map could be evaluated and modelled. Compared to most of the previous fracture modelling approach, this model is more flexible and comprehensive.

- An improved conditional global optimisation model for modelling discrete fracture networks. The hybrid model takes full advantages of the advanced fracture characterisation using geostatistical and fuzzy neural analyses. Discrete fractures are treated individually and yet continuum information could be modelled. Compared to the stochastic simulation approach, this model produces more representative fracture networks. Compared to the conventional optimisation programs, this model is more versatile and contains superior objective function.

PUBLICATIONS PRODUCED FROM THIS WORK

1. Tran, N.H., Rahman, M.K. and Rahman, S.S. (2002a) Developing a Hot Dry Rock Reservoir in Australia by Hydraulic Stimulation: a Shear-Dilation Model for Design and Evaluation. *Geothermal Resources Council Transactions*, 26.
2. Tran, N.H., Rahman, M.K. and Rahman, S.S. (2002b) A Nested Neuro-Fractal-Stochastic Technique for Modelling Naturally Fractured Reservoirs. *SPE77877, Society of Petroleum Engineers Asia Pacific Oil and Gas Conference and Exhibition, Melbourne, Australia, Oct.8-10.*
3. Tran, N.H., Chen, Z. and Rahman, S.S (2003a) Characterising and Modelling of Naturally Fractured Reservoirs with the Use of Object-based Global Optimisation. *Canada International Petroleum Conference, Calgary, Alberta, Canada, June 10 - 12, PAPER 2003-179.*
4. Tran, N.H., Chen, Z. and Rahman, S.S (2003b) Object-Based Global Optimisation in Modelling Discrete-Fracture Network Map: A Case Study. *SPE Annual Technical Conference and Exhibition, Colorado, U.S.A., Oct.5–8.*
5. Teimoori, A., Tran, N.H., Chen, Z. and Rahman, S.S., (2004) Simulation of Production from Naturally Fractured Reservoirs with the Use of Effective Permeability Tensor. *SPE88620, Society of Petroleum Engineers Asia Pacific Oil and Gas Conference and Exhibition, Perth, Australia, Oct.18-20.*
6. Teimoori, A., Tran, N.H., Chen, Z. and Rahman, S.S., (2004) Simulation of Fluid Flow in Naturally Fractured Reservoirs with the Use of Effective Permeability Tensor. *Annual proceeding of Geothermal Resources Council (GRC) 2004*, Australia.
7. Tran, N.H., Chen, Z. and Rahman, S.S (In review) Integrated Conditional Global Optimisation – an Effective Tool for Characterisation and Prediction of Discrete Fracture Networks. *Journal of Computers & Geosciences.*
8. Tran, N.H., Chen, Z. and Rahman, S.S (In review) A Hybrid Technique for Characterising and Modelling Naturally Fractured Reservoirs. *Journal of Petroleum Science & Engineering.*

TABLE OF CONTENTS

CERTIFICATE OF ORIGINALITY ..... **II**
独创性声明
ACKNOWLEDGMENTS ..... **III**
致谢
DEDICATION ..... **IV**
献词
ABSTRACT ..... **V**
摘要
PUBLICATIONS PRODUCED FROM THIS WORK ..... **VII**

TABLE OF CONTENTS ..... **VIII**
目录
LIST OF TABLES ..... **XIII**
表索引
LIST OF FIGURES ..... **XIV**
图索引
NOMENCLATURE ..... **XXIV**
术语
CHAPTER 1 - INTRODUCTION **1**
引言
1.1 NATURALLY FRACTURED RESERVOIRS 2
天然裂缝性油藏
1.2 NECESSITY FOR COMPREHENSIVE DISCRETE FRACTURE NETWORK MODELS 3
综合离散裂缝网络模型的必要性
1.2.1 Necessity for Modelling Natural Fractures 3
天然裂缝建模的必要性
1.2.2 Necessity for Comprehensive Discrete Fracture Network Models 4
综合离散裂缝网络模型的必要性
1.2.3 Characteristics of Comprehensive Discrete Fracture Models 6
综合离散裂缝模型的特征
1.3 COMPLEXITIES ASSOCIATED WITH THE MODELLING 7
建模的复杂性
1.4 PREVIOUS MODELS 8
已有模型
1.4.1 Equivalent Continuum Models 9
等效连续体模型
1.4.2 Discrete Models 12
离散模型
1.4.3 Integrated Models 15
集成模型
1.4.4 Summary 22
总结
1.5 OBJECTIVES AND SCOPE OF THE THESIS 23
论文的研究目的和范围

1.6 THESIS OUTLINE 24
论文大纲
CHAPTER 2 - FRACTURE CHARACTERISATION 26
裂缝描述
2.1 OVERVIEW 26
回顾
2.2 NATURAL FRACTURE PROPERTIES 27
天然裂缝性质
2.2.1 Fracture Characteristics: Location, Orientation and Size 28
裂缝特征：位置，产状和尺寸
2.2.2 Fracture Aperture 30
裂缝开度
2.2.3 Fracture Density 31
裂缝密度
2.2.4 Fracture Permeability, Connectivity and Porosity 31
裂缝渗透率，连通性和孔隙度
2.3 REVIEW OF FIELD DATA SOURCES 32
现场数据源回顾
2.3.1 Seismology 32
地震
2.3.2 Outcrop Analysis 36
露头分析
2.3.3 Conventional Logging Measurements 37
常规测井方法
2.3.4 Unconventional Logging Measurements 42
非常规测井方法
2.3.5 Core Descriptions 45
岩心描述
2.3.6 Drilling Data 48
钻井数据
2.3.7 Flow and Pressure Tests 48
流动和压力测试
2.3.8 Production Data 49
生产数据
2.3.9 Summary of Fracture Detection Tools 50
裂缝探测工具总结
2.4 CHARACTERISATION OF INTERMEDIATE DATA 52
中间资料特征
2.4.1 Fracture Orientation 52
裂缝产状
2.4.2 Fracture Size 53
裂缝尺寸
2.4.3 Fracture Density 54
裂缝密度
2.4.4 Fracture Porosity and Permeability 57
裂缝孔隙度和渗透率
2.5 DATA SAMPLING ERRORS 58
数据取样误差
2.6 CLOSURE 59
结论
CHAPTER 3 - FRACTURE DATA ANALYSES 60
裂缝数据分析
3.1 OVERVIEW 60
纵览
3.2 STATISTICAL ANALYSES 61
统计分析

3.2.1 Circular Statistics for Fracture Orientation 61
裂缝产装的圆形统计
3.2.2 Multifractal Geometry for Fracture Size 66
裂缝尺寸的多重分维
3.3 SPATIAL ANALYSES USING GEOSTATISTICS 74
利用地质统计学进行空间分析
3.3.1 Fracture Location Distribution 74
裂缝位置分布
3.3.2 Geostatistical Analyses 75
地质统计学分析
3.3.3 Fracture Density Distribution 78
裂缝密度分布
3.4 SPATIAL ANALYSES USING FUZZY NEURAL NETWORK 80
利用模糊神经网络进行空间分析
3.4.1 Artificial Neural Network 81
人工神经网络
3.4.2 Fuzzy Logic 84
模糊逻辑
3.4.3 Fuzzy Reasoning by Neural Network 86
利用神经网络进行模糊推理
3.4.4 Data Characterisation by Fuzzy Neural Network 87
利用模糊神经网络进行数据描述
3.5 CLOSURE 89
结论

CHAPTER 4 - MODELLING OF NATURALLY FRACTURED RESERVOIRS BY HYBRID NEURO STOCHASTIC SIMULATION 90
利用混合神经随机模拟进行NFR建模
4.1 OVERVIEW 90
纵览
4.2 OBJECT-BASED SIMULATION COMPONENT 91
基于对象模拟构成
4.3 STOCHASTIC SIMULATION COMPONENT 92
随机模拟构成
4.3.1 Stochastic Simulation and Fracture Network Modelling 92
随机模拟和裂缝网络建模
4.3.2 Stochastic Simulation of Fracture Orientation 95
裂缝产状的随机模拟
4.3.3 Stochastic Simulation of Fracture Size 99
裂缝尺寸的随机模拟
4.3.4 Estimation of Fracture Aperture 101
裂缝开度估计
4.3.5 Stochastic Simulation of Fracture Centre Points 101
裂缝中心点随机模拟
4.4 CONDITIONAL SIMULATION COMPONENT 103
条件模拟构成
4.5 HIERARCHICAL SIMULATION COMPONENT 104
分级模拟构成
4.6 THE HYBRID STOCHASTIC SIMULATION REALISATION 104
混合随机模拟实现
4.7 APPLICATION 107
应用
4.7.1 Palm Valley Fractured Gas Field 107
Palm Valley裂缝性气田
4.7.2 Available Fracture Data 109
可用裂缝数据

4.7.3 Characterisation of Fracture Properties 110
裂缝性质描述
4.7.4 Application of Fuzzy Neural Network 116
模糊神经网络应用
4.7.5 Results of the Hybrid Stochastic Simulation 127
混合随机模拟结果
4.8 DISCUSSIONS 132
讨论
4.8.1 Fracture Characterisation 132
裂缝描述
4.8.2 Fracture Modelling 134
裂缝建模
4.8.3 Modelling Limitations 135
建模局限性
4.8.4 Modelling Validation 136
建模验证
4.9 FINAL REMARKS 137
结论
CHAPTER 5 - MODELLING OF NATURALLY FRACTURED RESERVOIRS BY CONDITIONAL GLOBAL OPTIMISATION 138
利用条件全局最优化进行NFR建模
5.1 OVERVIEW 138
概述
5.2 THEORETICAL BACKGROUND OF GLOBAL OPTIMISATION 139
全局优化的理论背景
5.2.1 General Optimisation Process 139
一般优化过程
5.2.2 Global Optimisation - Simulated Annealing 141
全局最优化-模拟退火
5.2.3 Global Optimisation and Fracture Network Modelling 143
全局优化和裂缝网络建模
5.3 OBJECT-BASED CONDITIONAL GLOBAL OPTIMISATION 144
基于对象条件全局优化
5.3.1 Problem Representation and Optimisation Procedure 144
问题表征和优化过程
5.3.2 Remarks 150
评论
5.4 APPLICATION 150
应用
5.4.1 Otsego Fault Map 151
Otsego断层图
5.4.2 Reproduction Scenario 152
重构方案
5.4.3 Comparison with Stochastic Simulation 176
同随机模拟的对比
5.4.4 Prediction Scenario 177
预测方案
5.5 DISCUSSIONS 186
讨论
5.5.1 Modelling Advantages 186
建模优点
5.5.2 Modelling Limitations 188
建模局限
5.5.3 Final Remarks 189
结论

CHAPTER 6 - CONCLUSIONS AND RECOMMENDATIONS 190
结论和建议
6.1 CONCLUSIONS 190
结论
6.2 SCOPE FOR FUTURE RESEARCH 193
未来研究方向
BIBLIOGRAPHY 194
参考文献
REFERENCES 194
INTERNET REFERENCES 220
APPENDICES…….. 267
附录

LIST OF TABLES

Table 1.1: Examples of NFR: of different lithology and reservoir types. 3

Table 2.1: Field data sources as tools for fracture detection: scales, response characteristics and usages. 51

Table 2.2: Fracture orientation and corresponding field data sources: scales, response characteristics and usages. 53

Table 2.3: Fracture size and corresponding field data sources: scales, response characteristics and usages. 54

Table 2.4: Fracture density with corresponding field data sources: scales, response characteristics and usages. 55

Table 2.5: Fracture porosity, permeability and connectivity with corresponding field data sources: scales, response characteristics and usages. 57

Table 3.1: Documented works on probability density distributions of fracture size 67

Table 4.1: Summary of statistics for all fracture orientation (dip and azimuth) data observed in six wells (A to F), Palm Valley NFR..... 111

Table 4.2: Summary of correlations and covariances for all fracture dip and azimuth data observed in six wells (A to F), Palm Valley NFR. 113

Table 5.1: Summary of statistics for fracture location x-y coordinates, orientation and radius (Otsego fault map - Reproduction scenario)..... 153

Table 5.2: Correlations and covariances for fracture location x-y coordinates, orientation and radius (Otsego fault map - Reproduction scenario). 153

Table 5.3: Objective function components and their relative optimised ranges for weighting factors (Otsego fault map - Reproduction scenario). 165

Table 5.4: Controlling parameters for the global optimisation algorithm (Otsego fault map - Reproduction scenario). 169

Table 5.5: Comparison of objective function components: total fracture density and simple statistical measurements of fracture radius and orientation. For: Target DFN (0), Initial realisation by hybrid stochastic simulation (1),

and Final realisation by conditional global optimisation (FraCGOM 2) (Otsego fault map - Reproduction scenario). 173

LIST OF FIGURES 图

Fig. 1.1: Integrated NFR Characterisation and Simulation. 5

Fig. 1.2: Idealisation of fracture system in a dual porosity and dual permeability model: Actual reservoir (I), Sugar cube model (II), Layered model (III) and Matchstick model (IV) (with reference to Kazemi and Gilman, 1993). 10

Fig. 1.3: Procedure for a fracture simulation based on Fuzzy logic and ANN (with reference to Zellou and Ouenes, 2001). 18

Fig. 1.4: Overall methodology for NFR characterisation and modelling. 24

Fig. 2.1: Procedure for the NFR characterisation - from raw data to statistics and behaviours of the DFN. 27

Fig. 2.2: Diagram for 2D fracture line: characterised by centre *O(x, y)*, orientation (θ), radius (*Rad*) and thickness (*Aper*) in x-y coordinate system 28

Fig. 2.3: Circular disc model of fracture: characterised by centre *O(x, y, z)*, radius (*Rad*) and orientation of the fracture plane (*Dip* and *Azimuth*) 29

Fig. 2.4: Core fracture interpretation in well A, Palm Valley NFR: showing fracture plane morphology, which is both deformed and mineral filled (with reference to Berry, 1991). 30

Fig. 2.5: An example of a seismic cross-section through well G, Palm Valley NFR: showing different formations and interpreted fractures (with reference to Roe, 1995). 33

Fig. 2.6: An example of seismic interpretation: The upper image shows a seismic time map with horizontal lines being bedding layers in the reservoir

(e.g. lines BT). Some beddings are offset, indicating presence of faults. Faults (F) are pointed out in the lower image. 34

Fig. 2.7: Outcrop of joints in the limb of a non-cylindrical fold in Lavernock Point (Wales, U.K) - A very well connected joint network. The outcrop maps depicts 2D fracture network, which is cross-section of the underground 3D network. Location, orientation and size of all fracture lines can be promptly recognised [http://www.dstu.univ-montp2.fr]. 37

Fig. 2.8: Example of conventional logs on fracture identification in well A, Palm Valley NFR: arrows indicate areas of possible fracturing. 41

Fig. 2.9: FMS fracture interpretation in well E, Palm Valley NFR: showing continuous fractures (red), discontinuous fractures (orange) and beddings (green) as sinusoidal traces at TD: *Dip*/*Azimuth* (with reference to Rayner, 1995). 44

Fig. 2.10: Core samples in well A, Palm Valley NFR: complete core section for different depths, showing different lithological beddings (colour contrast) and fractures (cracks) (with reference to Berry, 1991). 46

Fig. 2.11: Core samples in well A, Palm Valley NFR: open fractures of high dip and large aperture. They are potentially the main conductors for fluid flow. Vertical coloured lines note azimuth direction of oriented core (with reference to Berry, 1991). 47

Fig. 2.12: Core samples in well A, Palm Valley NFR: the left image shows a sub vertical fracture of very low aperture, which is almost healed. The right image reveals a discontinuous crack, which does not fully cut through the core (with reference to Berry, 1991). 47

Fig. 2.13: Penny-shaped fracture propagation prefers the direction perpendicular to minimum in-situ stress. 49

Fig. 2.14: Diagram to calculate fracture density of a fracture intersecting a wellbore. 55

Fig. 3.1: Orientation data available from core analysis for a section of well F, Palm Valley NFR: In (B), dip and azimuth data are co-presented in the

same chart (dip axially and azimuth circumferentially). In (A), rose diagram is displayed for the corresponding strike. 63

Fig. 3.2: Box-counting method for a natural fracture system. 70

Fig. 3.3: Typical logarithmic plots for estimation of fractal dimension (*D*) using box-counting method. 70

Fig. 3.4: Naming convention for separation vector (*h*), whose tail and head are at measuring locations (x_i) and $(x_i + h)$, respectively. 76

Fig. 3.5: Three layer BPNN with *n*-hidden neurons used in this study. 82

Fig. 4.1: DFN model (M) is a composite of total number of fractures (N_F), individual fracture (M_F) and their attributes (L, S, O). Fracture objects can vary in many ways, such that location, size and orientation attributes satisfy their respective boundary conditions (R^1, R^2 and R^3). 92

Fig. 4.2: Procedure for a general stochastic simulation to generate DFN for NFR: from characterisation to random field sampling. 94

Fig. 4.3: Correlation of two normally distributed quantities: before the transformation (A) and after the transformation (B). There is zero correlation after the transformation. 96

Fig. 4.4: Flowchart of the Hybrid Neuro Stochastic simulation: from fracture characterisation by statistical, spatial and artificial neural analyses, to hybrid stochastic realisation of DFN for NFR. 106

Fig. 4.5: Location map of the Palm Valley NFR: showing location of the field, wells and gas pipelines (with reference to Berry et al., 1996). 107

Fig. 4.6: Stratigraphy of the Palm Valley NFR: the gas reservoirs are in Stairway, Horn Valley and Paccota horizons (Ordovician age) (with reference to Oaks et al., 1991). 108

Fig. 4.7: Top P1 unit depth structure map, Palm Valley NFR: as interpreted from seismic data (2D presentation) (with reference to Roe, 1995). 109

Fig. 4.8: Circular statistical analysis: histogram and probability density function plot for fracture dip (Dip_c) (unit degree, range 360°), Palm Valley NFR:

showing one-modal wrapped normal distribution, whose mode is at 180° (equivalent to sub-vertical *Dip* value). 111

Fig. 4.9: Circular statistical analysis: histogram and probability density function plot for fracture azimuth ($Azimuth_c$) (unit degree, range 360°, data shifted to the right by 30°), Palm Valley NFR: showing bimodal wrapped normal distribution. 112

Fig. 4.10: Box-counting method for fractal dimension calculation: for sections of different depth in well A and B, Palm Valley NFR. Fractal dimension values are (negative) slopes of the straight lines. 114

Fig. 4.11: Box-counting method for fractal dimension calculation for sections of different depth in well C and D, Palm Valley NFR. Fractal dimension values are (negative) slopes of the straight lines. 114

Fig. 4.12: Box-counting method for fractal dimension calculation: for sections of different depth in well E, Palm Valley NFR. Fractal dimension values are (negative) slopes of the straight lines. 115

Fig. 4.13: Box-counting method for fractal dimension calculation: for sections of different depth in well F, Palm Valley NFR. Fractal dimension values are (negative) slopes of the straight lines. 115

Fig. 4.14: Fracture density as calculated from FMS and core data in six wells (A to F), Palm Valley NFR (Note: depth sections vary with wells)..... 116

Fig. 4.15: Behaviours of the ANN in training and validation stages for fracture density along wellbores, Palm Valley NFR: showing reduction of error function with iterations and the optimal training time of 1190 epochs..... 117

Fig. 4.16: Prediction result of FNN at validation well E, Palm Valley NFR: showing distributions along the wellbores (continuous lines) for total porosity, fracture density, intensity and multifractal dimension. Sampled data are presented where available for comparison (discrete points). Note: there is no validation data for porosity. 118

Fig. 4.17: Prediction result of FNN at validation well F, Palm Valley NFR: showing distributions along the wellbores (continuous lines) for total

porosity, fracture density, intensity and multifractal dimension. Sampled data are presented where available for comparison (discrete points). Note: there is no validation data for porosity. 119

Fig. 4.18: BPNN validation result at wells E and F, Palm Valley NFR: Target and generated values for total porosity, fracture density and multifractal dimension are similar, with correlation values closed to one. 120

Fig. 4.19: 2D seismic time for the P1 unit, Palm Valley NFR 121

Fig. 4.20: 2D seismic instantaneous frequency for the P1 unit, Palm Valley NFR 121

Fig. 4.21: 2D seismic instantaneous phase for the P1 unit, Palm Valley NFR 122

Fig. 4.22: BPNN training for depth of top structure for unit P1, Palm Valley NFR: showing pattern in which error function reduces with iterations 123

Fig. 4.23: Top P1 unit depth structure map, Palm Valley NFR: a result of artificial neural analysis (2D presentation). 123

Fig. 4.24: Top P1 unit depth structure map, Palm Valley NFR: a result of artificial neural analysis (3D presentation). 124

Fig. 4.25: 3D distribution map for total porosity for the P1 unit, Palm Valley NFR: a result of artificial neural analysis: view of top layer. 124

Fig. 4.26: 3D distribution map for total porosity for the P1 unit, Palm Valley NFR: a result of artificial neural analysis: view of bottom layer and cross-sections (Same value scales as in **Fig. 4.25**). 125

Fig. 4.27: 3D distribution map for fracture density for the P1 unit, Palm Valley NFR: a result of artificial neural analysis: view of top layer. 125

Fig. 4.28: 3D distribution map for fracture density for the P1 unit, Palm Valley NFR a result of artificial neural analysis: view of bottom layer and cross-sections (Same value scales as in **Fig. 4.27**)..... 126

Fig. 4.29: 3D distribution map for multifractal dimension for the P1 unit, Palm Valley NFR: a result of artificial neural analysis: view of top layer. 126

Fig. 4.30: 3D distribution map for multifractal dimension for the P1 unit, Palm Valley NFR: a result of artificial neural analysis: view of bottom layer and cross-sections (Same value scales as in **Fig. 4.29**).....127

Fig. 4.31: Modelling area for hybrid stochastic simulation of Palm Valley NFR, including five sub-regions for nested simulation. The rectangular block covers the geological P1 unit. 128

Fig. 4.32: Final fracture model, Palm Valley NFR: showing all fractures generated from the hybrid stochastic simulation (x 0 to 20000m east to west, y: 0 to 4000m south to north, z: 1000m to 2000m true vertical depth).....128

Fig. 4.33: Major faults in Palm Valley NFR: showing fractures generated from the first run of the hierarchical simulation (to simulate reservoir-scaled fractures in the whole reservoir) (x: 0 to 20000m east to west, y: 0 to 4000m south to north, z: 1000m to 2000m true vertical depth).....129

Fig. 4.34: Medium-scaled fractures in region 1, Palm Valley NFR: showing fractures generated from the second run of the hierarchical simulation on a portion of the reservoir (x: 0 to 4000m east to west, y: 0 to 4000m south to north, z: 1000m to 2000m true vertical depth).....129

Fig. 4.35: Medium-scaled fractures in region 2, Palm Valley NFR: showing fractures generated from the third run of the hierarchical simulation on a portion of the reservoir (x: 4000m to 8,000m east to west, y: 0 to 4000m south to north, z: 1000m to 2000m true vertical depth).....130

Fig. 4.36: Medium-scaled fractures in region 3, Palm Valley NFR: showing fractures generated from the fourth run of the hierarchical simulation on a portion of the reservoir (x: 8,000m to 12000m east to west, y: 0 to 4000m south to north, z: 1000m to 2000m true vertical depth).....130

Fig. 4.37: Medium-scaled fractures in region 4, Palm Valley NFR: showing fractures generated from the fifth run of the hierarchical simulation on a portion of the reservoir (x: 12000m to 16000m east to west, y: 0 to 4000m south to north, z: 1000m to 2000m true vertical depth).....131

Fig. 4.38: Medium-scaled fractures in region 5, Palm Valley NFR: showing fractures generated from the sixth run of the hierarchical simulation on a

portion of the reservoir (x: 16000m to 20000m east to west, y: 0 to 4000m south to north, z: 1000m to 2000m true vertical depth)..... 131

Fig. 4.39: Medium-scaled fractures in the whole model, Palm Valley NFR: showing all fractures generated from the second to sixth runs of the hierarchical stochastic simulation (x: 0 to 20000m east to west, y: 0 to 4000m south to north, z: 1000m to 2000m true vertical depth)..... 132

Fig. 5.1: Procedure for a general optimisation simulation. Different optimisation algorithms possess different schemes for modification and objective function minimisation. 140

Fig. 5.2: Procedure for the object-based conditional global optimisation algorithm for a typical NFR modelling job..... 145

Fig. 5.3: Fault map of Otsego County and the surrounding areas (New York, USA) (digitisation of **Fig. A.1**), with assumptions of some large-scaled fractures..... 151

Fig. 5.4: Histogram and probability density function plot for fracture radius: showing lognormal distribution. One unit of the radius is equivalent to 120m (Otsego fault map - Reproduction scenario)..... 155

Fig. 5.5: Cross plot of Empirical Distribution Function (EDF) against theoretical lognormal distribution, with the approximate 95% and 99% Kolmogorov-Smirnov bounds: confirming lognormal fracture radius (Otsego fault map - Reproduction scenario). 155

Fig. 5.6: Histogram and probability density function plot for fracture orientation (unit degree): showing three modes at approximately 32°, 78° and 136° (Otsego fault map - Reproduction scenario). 157

Fig. 5.7: Scatter plot for fracture centre location – x-y coordinates. One x-y unit is equivalent to 120m (Otsego fault map - Reproduction scenario)..... 158

Fig. 5.8: Target fracture intensity (λ) map, including scatter plot of fracture centres. Intensity distribution is smoothed by kernel method. Lighter colours indicate denser intensity. Contour unit is number of points per

area. One x-y unit is equivalent to 120m (Otsego fault map - Reproduction scenario). 158

Fig. 5.9: Histogram and probability density function plot for fracture centre location – x-y coordinates: showing uniform distributions. One x-y unit is equivalent to 120m (Otsego fault map - Reproduction scenario)..... 159

Fig. 5.10: Empirical density function of point-to-point nearest neighbour distances for fracture centres (G-function plot): showing data evenly spread, no signs of clustering or regularity (Otsego fault map - Reproduction scenario). 160

Fig. 5.11: K-function estimates for fracture centre locations (K-function plot): showing CSR (Otsego fault map - Reproduction scenario). 161

Fig. 5.12: Variance stabilising transformation for fracture centre locations (L-function plot): showing CSR (Otsego fault map - Reproduction scenario). 161

Fig. 5.13: Target grid-based fracture density distribution map (grid-based). Density unit is m/m^2. Lighter colours indicate denser fracture distribution (Otsego fault map - Reproduction scenario)..... 162

Fig. 5.14: Conditional fracture data: observed fractures are maintained throughout the simulation (Otsego fault map - Reproduction scenario). These fractures are also the available inputs for the later prediction scenario. 166

Fig. 5.15: Initial DFN realisation generated from the stochastic simulation module (Otsego fault map - Reproduction scenario). 167

Fig. 5.16: Grid-based density distribution map generated from the hybrid stochastic simulation (initial realisation). Density unit is m/m^2. Lighter colours indicate denser fracture distribution (Otsego fault map - Reproduction scenario). 168

Fig. 5.17: Graph showing how objective function decreases logarithmically with iterations (Otsego fault map - Reproduction scenario). 170

Fig. 5.18: Final DFN image, reproduction result of the object-based conditional global optimisation (Otsego fault map - Reproduction scenario). 171

Fig. 5.19: Final simulated grid-based fracture density distribution map. Density unit is m/m^2. Lighter colours indicate denser fracture distribution (Otsego fault map - Reproduction scenario). 172

Fig. 5.20: Comparison of experiment semi-variogram vectors. For: Target DFN (0), Initial realisation by stochastic simulation (1), and Final realisation by conditional global optimisation (FraCGOM 2) (Otsego fault map - Reproduction scenario). A. fracture size – B. fracture orientation. 174

Fig. 5.21: Comparison of modified multi-histogram mean vectors. For: Target DFN (0), Initial realisation by stochastic simulation (1), and Final realisation by conditional global optimisation (FraCGOM 2) (Otsego fault map - Reproduction scenario). A. fracture size – B. fracture orientation. 174

Fig. 5.22: Comparison of experiment variogram distance vectors. For: Target DFN (0), Initial realisation by stochastic simulation (1), and Final realisation by conditional global optimisation (FraCGOM 2) (Otsego fault map - Reproduction scenario). 175

Fig. 5.23: Comparison of experiment cross-variogram of fracture radius and orientation. For: Target DFN (0), Initial realisation by stochastic simulation (1), and Final realisation by conditional global optimisation (FraCGOM 2) (Otsego fault map - Reproduction scenario). 175

Fig. 5.24: Histogram and probability density function plot for fracture centre location – x-y coordinates: showing uniform distributions. One x-y unit is equivalent to 120m (Otsego fault map - Prediction scenario). 178

Fig. 5.25: Histogram and probability density function plot for fracture radius: showing either lognormal or gamma ray distribution. One unit of the radius is equivalent to 120m (Otsego fault map - Prediction scenario). 179

Fig. 5.26: Histogram and probability density function plot for fracture orientation (unit degree): showing roughly bimodal distribution with modes at 35°, and 78° (Otsego fault map - Prediction scenario). 180

Fig. 5.27: Final predicted DFN image by object-based conditional global optimisation (Otsego fault map - Prediction scenario). 182

Fig. 5.28: Final predicted grid-based fracture density distribution map. Density unit is m/m^2. Lighter colours indicate denser fracture distribution (Otsego fault map - Prediction scenario). 183

Fig. 5.29: Comparison of experiment semi-variogram vectors. For: Target DFN (0), Target data available in Prediction scenario (3) and Final prediction by conditional global optimisation (FraCGOM 4) (Otsego fault map - Prediction scenario). A. fracture size – B. fracture orientation. 184

Fig. 5.30: Comparison of modified multi-histogram mean vectors. For: Target DFN (0), Target data available in Prediction scenario (3) and Final prediction by conditional global optimisation (FraCGOM 4) (Otsego fault map - Prediction scenario). A. fracture size – B. fracture orientation. 184

Fig. 5.31: Comparison of experiment variogram distance vectors. For: Target DFN (0), Target data available in Prediction scenario (3) and Final prediction by conditional global optimisation (FraCGOM 4) (Otsego fault map - Prediction scenario)..... 185

Fig. 5.32: Comparison of experiment cross-variogram of fracture radius and orientation. For: Target DFN (0), Target data available in Prediction scenario (3) and Final prediction by conditional global optimisation (FraCGOM 4) (Otsego fault map - Prediction scenario). 185

Fig. A.1: Fault map of Otsego county and surrounding area (New York, USA) [http://www.nywaterfind.com/fractureotsego.JPG] 221

Fig. A.2: Fault system of North East Mediterranean region (Greece) [http://www.astro.gr/general/earth/icons/fault.jpg] 222

Fig. A.3: Joint system cutting basalt flow in Zambia over which flows the Zambezi River (Victoria Falls): Joints are long, continuous, widely spaced and enlarged by erosion [http://rst.gsfc.nasa.gov/Sect2/Sect2_7.html] 222

Fig. A.4: Fault map of Southern California region (USA). Faults tend the same directions: towards NW and NWW, along the mountain range [http://www.crustal.ucsb.edu/projects/mapcat/images/scal6.jpeg] 223

Fig. A.5: Perspective view of the Transverse Ranges (California, USA) made by combining Landsat imagery with topographic data acquired by JPL's SRTM mission (radar altimetry). Fault lines (in white) have been drawn on the resulting image, which also depicts the Los Angeles Basin (bottom centre) and the Mojave Desert (right) [http://rst.gsfc.nasa.gov/Sect2/Sect2_7.html] 223

Fig. A.6: Example of fault surfaces at very small scales [http://geo.uw.edu.pl/ZASOBY/GEOIMAGE/FAULT/konon02.htm] 224

Fig. A.7: Fault system developed from volcanic activities in Venus [http://www.usd.edu/phys/courses/astronomy/images/Venus/Fault.jpg].... 224

NOMENCLATURE

The following nomenclature is used in this dissertation. All symbols are defined when they first appear in the text. Generally, one definition is assigned to each symbol. In other cases, the correct meaning will be evident from the context in which it is used.

Symbols

a = major radius of the elliptical shape
$Aper$ = fracture aperture or thickness
$Area$ = (cross-sectional) area
$Azimuth$ = fracture azimuth angle
$\tilde{A}$ = fuzzy set
b = minor radius of the elliptical shape
C = 1. proportionality constant
2. sum of cosine
$c(\alpha)$ = continuous co-fractal dimension
$Cor()$ = correlation
$Cov()$ = covariance
$Covc()$ = cross covariance
D = fractal dimension
D_T = topological dimension

D_E = Euclidean dimension

Dip = fracture dip angle

E = energy (error) function, objective function

f = activation function

$f(\alpha)$ = continuous fractal dimension

$\hat{F}()$ = F-function, origin-to-point nearest neighbour statistic

FracDen = fracture density

$\hat{G}()$ = G-function, point-to-point nearest neighbour statistic

h = 1. fracture vertical height
2. separation vector/ distance

$H()$ = multi-histogram mean

i = 1. directional vector or arbitrary number
2. input node of a neural network

j = 1. directional vector or arbitrary number
2. hidden node of a neural network

k = directional vector or arbitrary number

$\overline{K}$ = mean virgin permeability of the fracture medium

$\hat{K}()$ = K-function

l = 1. arbitrary side length
2. number of output nodes of a neural network

L = fracture length

L_o = side length of an arbitrary box

$\hat{L}()$ = L-function, variance stabilising transformation

m = 1. arbitrary number
2. number of input nodes of a neural network

M = object-based model

$M()$ = madogram

$Mc()$ = cross madogram

M_L = location parameter of a lognormal distribution

n = 1. arbitrary number
2. number of hidden nodes of a neural network

N = total number of sample data

$N()$ = normal probability density function

N_{Rad} = number of fractures related to size *Rad*

p = proportional factor

$P()$ = probability, probability density distribution

R = 1. fixed radius
2. resultant length

Rad = fracture radius

$\Re^d$ = space of multiple dimensions (d)

S = sum of sine

S_L = shape parameter of a lognormal distribution

T = control parameter, temperature

Var = variance

$VarDist()$ = variogram distance

w = weighting factor

$WN()$ = wrapped normal probability density function

x = 1. arbitrary fracture location
2. input signal for neural network

y = 1. hidden signal for neural network

z = 1. arbitrary property, fracture property and statistics
2. output signal for neural network

x, y, z = 1. Cartesian direction vectors
2. coordinates of fracture centre

α = 1. coarse Holder exponent
2. arbitrary angle

λ = fracture intensity

$\alpha\alpha$ = arbitrary angle

β = arbitrary angle

$\beta\beta$ = arbitrary angle

$\gamma()$ = variogram

$\gamma c()$ = cross variogram

$\rho()$ = correlogram

$\rho c()$ = cross correlogram

δ= arbitrary angle

Δ = 'change in'

α_1 = learning rate parameter

α_2 = momentum constant

$\mu_{\tilde{A}}()$ = fuzzy membership function

$\mu()$ = mean

θ = fracture orientation

$\sigma()$ = standard deviation

σ_{eff} = the effective normal stress acting normal to the fracture

σ_{nref} = effective normal stress applied to cause 90% reduction in the compliant aperture

Superscripts:

* = training/ target data

Subscripts:

c = circular statistics

F = fracture

L = location

new = newly created value

O = orientation

old = old/ initial value

S = size

Abbreviations:

AI = artificial intelligence

ANN = artificial neural network

AVAZ = amplitude versus angle and azimuth

AVO = amplitude variation with offset

BHTV = borehole televiewer

BPNN = back-propagation neural network

CAL = calliper log

CAST = circumference acoustic scanning tool

CSR = complete spatial randomness

DFN = discrete fracture network

DRHO = density correction log

DT = sonic log

FMI = formation micro image

FMS = formation micro scanner

FNN = fuzzy neural network

GR = gamma ray log

ILD = deep induction log

ILM = medium induction log

LLD = deep resistivity laterolog

LLS = shallow resistivity laterolog

MLP = multiple layer perceptrons

MSFL = micro-spherically focused resistivity log

NFR = naturally fractured reservoir

NPHI = neutron log

PA = photoelectric absorption log

PEF = photoelectric factor log

RHOB = density log

RT = true formation resistivity log

SFL = micro-spherically focused induction log

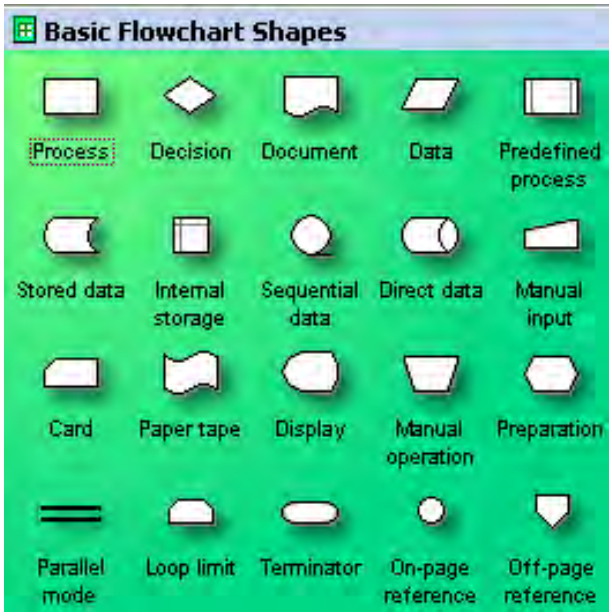
SP = spontaneous potential log

TCF = trillion cubic feet

TD = true depth

VSP = vertical seismic profile

Chart nomenclature:



CHAPTER 1 - INTRODUCTION

Comprehensive modelling of a naturally fractured reservoir (NFR) is important not only in petroleum engineering but also in various earth sciences. However, due to the reservoirs' extreme heterogeneity and lack of efficient techniques to integrate the limited data, such models have not been achieved. This study is carried out to identify and overcome such problems. Based on the theory of geostatistics, fractal geometry, fuzzy neural network, stochastic simulation and global optimisation, a methodology is developed for comprehensive characterisation and modelling of naturally fractured reservoirs.

In this first chapter, the general characteristics of NFR are described. This is followed by the arguments for the necessity of comprehensive DFN models for such reservoirs. Then, based on the criteria and complexities associated with fracture modelling, previously documented modelling approaches are reviewed and discussed. The chapter concludes with a statement of scope and objectives of the thesis.

1.1 NATURALLY FRACTURED RESERVOIRS

Natural fractures are mechanical breaks or discontinuities in rocks, which form in nature in response to high fluid pressures, lithostatic, thermal and tectonic stresses. They refer to all types of generic discontinuities, e.g. cleats, vugs, slickensides, folds, fractures, joints and faults.

Naturally fractured reservoirs (NFR) are oil and gas reservoirs, whose rock matrices contain pores, pore-throats and natural fractures, such that the fractures play significant roles in fluid flow. NFR also include hot dry rock geothermal reservoirs, coal beds, groundwater resources and underground (nuclear waste) storages. Some (very limited) examples are listed in **Table 1.1**. Samples of fracture and fault networks are displayed in **APPENDIX A** (**Fig. A.1** to **Fig. A.7**).

It is estimated that the US domestic natural gas target in NFR could be hundreds to thousands of trillions of cubic feet (TCF). In tight gas reservoirs alone, there is a projected 5000 TCF of in-place gas, in which 200 to 800 TCF is technically recoverable (National Research Council, 1992; Laubach et al., 2000). In addition, hot dry rock represents a significant renewable energy resource, which could contribute to all energy needs of the world for centuries to come (Edwards et al., 1982; Duchane, 1995; Geothermal Resource Council, 1995; Hooper and Duchane, 1996). In Australia, there is about 30 TCF of natural gas contained in NFR in the Cooper Basin alone, together with considerable portion of hot dry rock resource (Narayan et al., 1998). Because of increasing energy needs throughout the world, these reservoirs have recently become commercially significant.

Reservoir	Region	Lithology	Reservoir type
Beaver River	Canada	Dolomite	Oil and gas
Big Sandy	Kentucky, USA	Shale	Oil and gas
Byron	Illinois, USA	Sandstone	Salvage yard
Cooper Basin	Australia	Sandstone/ basement	Oil, gas and geothermal
Dagestan	Russia	Carbonate	Oil and gas
Ekofisk	North Sea	Chalk	Oil and gas
Faud	Oman	Chalky Carbonates	Oil and gas
Fenton Hill	New Mexico, USA	Basement rock	Oil and gas
Geysers	California, USA	Sandstone	Geothermal
Hijiori	Yamagata Prefecture, Japan	Sandstone/ basement	Geothermal
La Paz	Venezuela	Limestone	Oil and gas
Pindale Anticline	Wyoming, USA	Tight sandstone	Gas
Rosemanowes	Cornwall, England	Granite	Oil and gas
San Juan Basin	New Mexico, USA	Sandstone	Gas
White Tiger	Vietnam	Basement granite	Oil and gas

Table 1.1: Examples of NFR: of different lithology and reservoir types.

1.2 NECESSITY FOR COMPREHENSIVE DISCRETE FRACTURE NETWORK MODELS

1.2.1 Necessity for Modelling Natural Fractures

Firstly, natural fractures play significant roles in fluid flow in NFR. For geological reasons, most NFR possess very low matrix permeability so that fractures are the main fluid-conducting medium. Typically, hydrocarbons are accumulated in matrix porosity and transferred to producing wells through permeable pathways of fractures. Fracture systems can also contribute significantly to rock porosity and hydrocarbon storage. For example, in carbonate reservoirs, porosity due to fractures is dominant. In such reservoirs, fractures help the production of hydrocarbons, water and geothermal energy. They also greatly influence drainage and production of methane gas from coal beds.

Secondly, there are many practical engineering problems due to fractures. They pose difficulties in containing waste and toxic substances, in structural stability of mines, tunnels and dams (National Research Council, 1996). For example, lost circulation is an expensive problem associated with drilling through low-pressure fractured zones. Drilling fluid is lost through the intersecting fractures. This increases drilling time and adds costs to the drilling operation (Glowka et al., 1992).

In general, knowledge of underground DFN is critical to development of petroleum fields, economics of heat generation from geothermal reservoirs and exploitation of groundwater resources. It leads to accurate evaluation of reserves and production profiles, maximising recovery. Potential reservoir problems are also limited (Nelson, 1982; National Research Council, 1992).

1.2.2 Necessity for Comprehensive Discrete Fracture Network Models

Extensive modelling of DFN, being an integrated part of NFR characterisation and simulation (**Fig. 1.1**), is critical for various reservoir applications.

First, it is an objective of reservoir planning to identify high and low fracture intensity zones. As a result, drilling wells can be targeted to connect fractures that control fluid flow. Models of fracture density distribution are, therefore, essential.

In addition, details of other fracture properties are also required. This is because fractures with different properties (size, orientation, connectivity) have different effects on reservoir fluid flow. Fractures of bigger size and larger aperture normally conduct fluid more efficiently. Fracture orientation controls reservoir anisotropy and directional permeability. For example, sub-parallel fractures do not connect to form an interconnected network for fluid flow. In such cases, drilling boreholes need to be orientated accordingly to intersect the fractures to raise production efficiency (National Research Council, 1996).

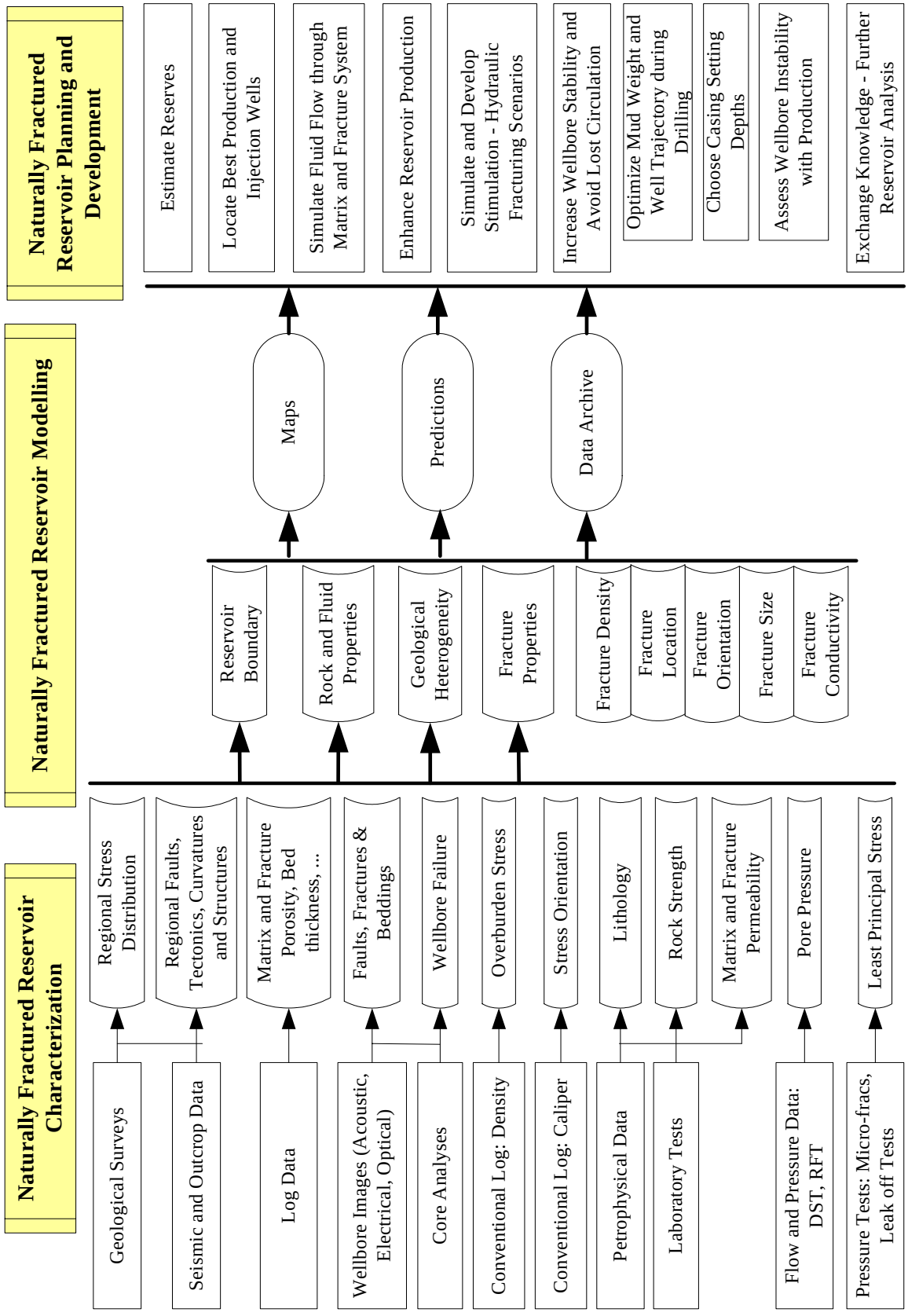


Fig. 1.1: Integrated NFR Characterisation and Simulation.

DFN应用

1、渗透率张量
2、几何统计学
3、其余应用见Bourbiaux、Baker Dershowitz、Sarda

DFN also facilitates numerical simulations for reservoir fluid flow. For example, since fracture geometries (location, orientation and size) are available, they are analytically formulated using boundary element or finite element methods to estimate the equivalent permeability tensor of the DFN (Oda et al., 1987; Lee et al., 1999; Teimoori et al., 2004). Instead of using permeability tensor, Cacas et al. (1990) estimated the large-scaled hydraulic conductivity of fractured rock using fracture geometry statistics. Other applications of DFN models in NFR fluid flow simulation and hydraulic properties estimation are listed in Bourbiaux et al. (1997), Baker et al. (2001), Dershowitz et al. (2002) and Sarda et al. (2002).

Moreover, in NFR (where fractures are not well connected or have low permeability), some permeability enhancement techniques (such as hydraulic fracture stimulation) are essential. However, several investigators (Warpinski, 1991, Rahman et al., 2000; Rodgerson, 2000) have identified that underlying principles of such techniques are complex and further development is hindered due to lack of appropriate geostatistical fracture models. This is especially critical for hot dry rock developments, where behaviours of water injection, fluid flow and heat extraction need to be understood. A NFR model of DFN allows simulation of responses of natural fractures under different stimulation pressure (or pressure for water injection). As a result, the best scenarios for hydraulic fracture treatments and optimum production methods can be developed (Hossain et al., 2000; Rahman et al., 2001; Tran et al., 2002a; Karimi-Fard and Firoozabadi, 2003).

1.2.3 Characteristics of Comprehensive Discrete Fracture Models

Overall modelling of NFR, especially petroleum and hot dry rock reservoirs, involves description of reservoir boundary, rock and fluid properties and geological heterogeneities. It also involves mapping of major faults and medium to small-scaled network of fractures.

Reservoir boundary defines the modelling area, areal and vertical extent of the reservoir, drilled wells and major regional geological features. Rock and fluid properties refer to attributes such as lithology, rock strength, grain size, fluid contents, fluid

density, fluid viscosity, matrix porosity and permeability. Geological heterogeneities include bed thickness, depth, overburden pressure and stresses. These features are typically enclosed in a conventional reservoir characterisation and simulation.

Fault and fracture descriptions consist of geometric as well as fluid flow properties. Reliable DFN models are required to portray both fracture spatial distribution and details of all individual properties such as fracture location, orientation, size, density and conductivity. They should also be conditioned to available reservoir (e.g. geological, geophysical and engineering) data. Such DFN models can then be combined with conventional geological reservoir models as inputs for reservoir simulation and stimulation studies.

1.3 COMPLEXITIES ASSOCIATED WITH THE MODELLING

裂缝产生的复杂性

Natural fractures occur at different scales and are highly heterogeneous. Rock fracturing is a complicated process, which is sensitive to changes in geological conditions. Under lithostatic, fluid pressure, tectonic, thermal and other geological stresses (e.g. volcanoes, uplifting, and salt intrusion), fractures generally initiate and propagate when the stresses become equal or greater to the rock strength. Different geological conditions induce different fracture patterns, thus, different NFR characteristics. Most rocks have simultaneously and sequentially undergone multiple deformational events, which eventually result in very complicated fracture systems (National Research Council, 1996).

裂缝尺寸不一、充填、连通性亦有差别。

In NFR, there are major faults, which can extend from a few hundred metres to lometres (**Fig. A.2**, **Fig. A.3** and **Fig. A.5**). There are also minor cracks, which can be small as a few millimetres (**Fig. A.6**). Other fracture properties such as orientation and aperture also vary tremendously. For example, while larger fractures tend to have bigger aperture, some fractures are fully- or partially-filled by mineral deposition and/or crystallisation. While some fracture networks are well connected (**Fig. A.1**), some are

not (**Fig. A.4**). Nevertheless, all types of fractures contribute to fluid flow, so they need to be fully characterised and modelled.

可获得的数据尺度有差异，没有手段可提供所需要的所有数据。

In addition, since the fracture system is complex, its characterisation is not straightforward. Different field data sources cover different scales (microscopic to regional) and are of different resolutions. Moreover, no single tool can provide all information needed to fully characterise a NFR. For example, seismic and outcrop are regional-scaled data sources, which can only interpret orientation and size of major faults. Well log, core and formation micro scanner (FMS) image have high resolutions but small investigation radii. They reveal orientation, aperture and density of local fractures (Tran et al., 2002b) (More details in **Chapter 2**).

需要一套综合方法可以综合所有的可用数据。

Thus, in order to portray the multifaceted characteristics of natural fractures, an integrated approach is required, where all available field data from wide range of geological, geophysical, petrophysical, drilling and other sources are utilised (Ouenes and Hartley, 2000; Rawnsley and Wei, 2001).

1.4 PREVIOUS MODELS

There have been many different methods to characterise NFR and simulate fluid flow in it in literature. They could be broadly divided into three categories: equivalent continuum, discrete and integrated models.

Classification of the first two categories is based on representation of fractures in the models (National Research Council, 1996). In a continuum model, the simulated area was divided into grid-blocks. Fractures were not individually treated. Their properties were averaged over the large volume of each grid-block. In a discrete model, individual fractures and their properties were essentially simulated. Both methods employed mathematical and geomechanical formulations, with the use of either deterministic or stochastic simulation.

The more advanced integrated models refer to those that could utilise data sources of different scales to simulate heterogeneity of NFR. They combined the mathematically deterministic and stochastic approaches. There were also ones using artificial intelligence tools. Integrated models existed in both continuum and discrete forms.

This section reviews different models of each category, investigating their advantages and disadvantages.

1.4.1 Equivalent Continuum Models

1.4.1.1 Descriptions

Most mathematical and geomechanical models to simulate fracture networks and fluid flow through them were equivalent continuum. They comprised of single porosity (Davison, 1985; Hiseh and Neuman, 1985; Carrera et al., 1990), multiple continuum of dual porosity, dual permeability, interacting and adaptive continuum (Pruess and Narasimhan, 1988; Reeves et al., 1991; Ganzer, 2002).

等价连续体模型
单孔模型

The equivalent continuum models were grid-based, in which individual fractures were not treated explicitly. Heterogeneity of fracture reservoirs was analysed by dividing the reservoir into a limited number of grid-blocks, each of which were represented by a set of constant fracture properties (e.g. porosity, permeability). In single porosity models, fluid flow was considered through open and connected fractures only, regardless of matrix permeability. One uniform porosity value was assigned to each block, which was an average for all the contained fractures.

糖元模型
层状模型
火柴棒模型

Similar presentation was used in dual porosity, dual permeability and stochastic continuum models. Sugar cube, layered and matchstick models were three typical idealisations of the fracture system (**Fig. 1.2**). Each grid-block was represented by uniform geometry and constant block length. In cases of dual porosity and permeability models, matrix and fractures were considered as two overlapping porous media. Equations for fluid flow through porous media were used to evaluate porosity and permeability values.

This figure has been removed due to copyright requirements

Fig. 1.2: Idealisation of fracture system in a dual porosity and dual permeability model: Actual reservoir (I), Sugar cube model (II), Layered model (III) and Matchstick model (IV) (with reference to Kazemi and Gilman, 1993).

基于曲率分析的地质力学方法。

In addition, there were geomechanical approaches using simple curvature analysis, field stress, field strain and fracture growth mechanisms (Lisle, 1994; Chambers et al., 1999; Heffer et al., 1999; Hennings et al., 2000). For example, Heffer et al. (1999) observed empirical relationships between strains and permeability. Thus, matrix and fractures permeability were simulated from 2D or 3D distribution of reservoir rock strains. Similarly, through quantitative tests, Hennings et al. (2000) discovered that fracture intensity was spatially related to strains and total curvature. As a result, 3D predictive model of fractures was built.

1.4.1.2 Discussions

In general, the equivalent continuum methods employed simple mathematical formulations and geomechanical processes to present complexity of fracture systems, which had the benefits of being straightforward to be simulated. 何意？

However, the continuum models are not sufficient, as details of discrete fracture properties (e.g. location, orientation and size) are not considered. As a result, the

未考虑裂缝性质（位置、方位、尺寸）

models' applications in a comprehensive NFR simulation and stimulation study are limited.

确定性方法不适用性。

Furthermore, most models were mathematically deterministic. The deterministic approach typically relied on rules, behaviours and mathematical relationships, which were unrealistic and difficult to be characterised (Shen and Ouenes, 2003). Due to the complex nature of NFR, the deterministic results were simplistic, idealised and subjective (National Research Council, 1996). A common feature of these models was the use of simplistic geometrical description of fracture systems (e.g. homogeneous reservoirs, parallel plate fractures) with primary efforts spent on flow behaviours instead of fracture geometries (Gringarten, 1996). Studies so far have succeeded in modelling only a limited range of fractures or in unrealistic homogeneous reservoirs.

Another major limitation of the equivalent continuum models involved continuum approximations, where effective properties of a grid-block are computed from the contained individual fractures. Since fracture data are limited and often belong to various scales, the continuum approximations might not be justified at the scales of interest (National Research Council, 1996).

多尺度数据问题

Moreover, equivalent continuum methods used limited data sources. In most cases, single data source of either seismic or well log or well test were used. A single data source could only cover a very narrow range of aspects of natural fractures. Thus, simulated fracture networks did not represent characteristic properties of the reservoir. There were models that allowed participation of multiple available data sources (Li et al., 1997). However, the investigators were not able to solve problems due to scales of data sources. In their work, integration was done by conventional averaging, which might not be suitable for the complexity of NFR. In NFR modelling, it is necessary to be able to utilise all available data sources in integrated manners to attain more comprehensive fracture models (Ouenes and Hartley, 2000; Rawnsley and Wei, 2001).

也有随机连续模拟

Lately, there have been several continuum stochastic simulations, which resulted in distribution maps of fracture porosity and permeability (Neuman and Depner, 1988; Doughty and Karasaki, 2000) or fracture intensity index (Pistre et al., 1995; Tamagawa

et al., 2002; Escuder Viruete et al., 2003). First, stochastic continuum methods considered rock heterogeneity as a continuous random field. This could deal effectively with the problem of scaling, in which fracture information obtained might not belong to the scales of interest. Second, the methods could utilise several geostatistical measurements, such as kriging, multiple point geostatistics and indicator variogram. Stochastic simulation encourages uses of geostatistics for better spatial modelling of fracture heterogeneity. Unfortunately, only fracture intensity have been considered, which is inadequate for comprehensive NFR modelling.

1.4.2 Discrete Models

Discrete fracture models simulate individual fracture properties and predict fluid flow behaviour from knowledge of fracture geometry and conductivity. They could be either deterministic or stochastic.

1.4.2.1 Deterministic Discrete Fracture Network Models

Descriptions

Deterministic discrete methods employed mathematical and geomechanical analyses that were similar to the deterministic continuum methods, e.g. equivalent discontinuum approximation (Long et al., 1992), field strain and fracture growth mechanism (Jensen et al., 1989; Bourne et al., 2001; Olson et al., 2001). Initiation and development of NFR were estimated according to fracture growth history.

Discussions

The deterministic methods contain a number of inherent limitations when applying to complex geology of NFR. For example, in Jensen et al. (1989), fracture distribution and directions were evaluated directly from their relationships with stress conditions, structural growth and tectonic history. First, stress field and its relationships with fracture development have not been fully understood and are still under ongoing research. Second, even though fracture directions do relate to field stress, the observation on such relationships would only be indicative. For normal NFR that have

undergone many tectonic changes, fractures directions might not relate directly to current stress distribution anymore. Third, fractures are results of complicated geologic, tectonic and thermal processes over a long period, which make quantification and generation of fractures according to growth history almost impossible. There is also effect of digenesis and mineralisation, which could alter fractures completely after they have been formed.

It is also worth mentioning that exact knowledge of fracture growth history is hard, if not impossible, to be realised. Many investigators pointed out that it was impractical to achieve such deterministic models with our current knowledge of fracture growth mechanisms and computer capacity (Swaby and Rawnley, 1996; Cacas et al., 2001).

1.4.2.2 Discrete Stochastic Simulation

Descriptions

Several DFN models were linked with concepts of probability and stochastic simulation. First, explicit fracture information (e.g. data on fracture orientation, aperture, density) was mostly available at well locations. The data were statistically analysed so that distributions of fracture properties away from the wells could be predicted. Then, fractures were generated by stationary Poisson processes (i.e. random processes), according to the characterised distributions of individual properties. The stochastic generation was carried out until total number of fractures or fracture intensity was satisfied. Detailed procedure of a typical stochastic simulation is presented in **Chapter 4** (**4.3.1**).

Discussions

优点

The discrete stochastic simulations demonstrated many advantages over the deterministically mathematical and geomechanical approaches (both discrete and continuum). One advantage was that continuum approximations could be avoided and the scaled issues were effectively dealt with via the use of probability distributions. Their capabilities also included integrating fracture information from various data

sources and producing fracture system with details of every fracture and respective properties. Besides, despite this being mentioned in only limited number of works (e.g. Cacas et al., 2001), stochastic simulation could be conditioned using known fractures and fluid flux data as constraints. This directly ties the simulated DFN to the reservoir conditions.

However, because fracture distributions away from the well locations were uncertain, accuracy of the simulated models would be only reliable in near-wellbore regions. The unconditioned random filling of the inter-well regions limited applications of such models beyond the near-wellbore scales.

In addition, the stochastic simulation methods relied on assumptions of statistical distributions of fracture properties, which posed two major problems. First, the assumptions could not be validated for all cases. Second, it is difficult to characterise all statistical information.

Regarding the first problem, since the statistical distributions were predefined, they might not be suitable for complex NFR. A typical example concerns fracture orientation, which was usually simulated by uniform or normal distributions (Willis-Richards, 1996; Jensen et al., 1998; Anraku et al., 2000). These unimodal statistics would be too simplistic to characterise NFR, where fracture networks typically contain fractures crossing each other and having at least two predominant mean directions (**Fig. A.1** and **Fig. A.3**). Thus, a multimodal distribution would be more appropriate. Some investigators realised this complexity and divided fractures into sets (Lanyon et al., 1993; Tamagawa et al., 2002) or employed more realistic distributions such as bi-variate Bingham and Von-Mises (Wen and Sinding-Larsen, 1996; Parney et al., 2000). Even then, they did not address relationships between fracture orientation and size. Different fracture size plays different roles towards fluid flow, so orientation measurements of different fracture size should be treated differently. The complexity gets extreme when 3D case is considered, where fracture orientation is typically represented by at least two components (i.e. dip and azimuth). In general, it is essential that the stochastic methods be more flexible and that the statistical distributions be representative and dependant on the actual data.

Regarding the second problem, previous methods have not been able to effectively integrate data of various scales in fracture characterisation. For example, in constructing a distribution for fracture orientation, all samples measured from all available sources (e.g. seismic and borehole images) were linearly combined, disregarding the fact that the data belong to two very dissimilar scales.

Furthermore, fracture spatial distribution and interactions between different fracture properties were not determined. Fracture spatial distribution (i.e. fracture location) was typically simulated deterministically or by simple uniform distribution (Anraku et al., 2000; Parney et al., 2000; Al Qassab et al., 2002). National Research Council (1996) also pointed out that the stochastic simulation models did not distinguish fractures of high and low conductivity. This issue needs to be solved, as partially filled and closed fractures are common.

One final note concerns validation. It remains a major problem to validate a DFN from stochastic simulation, or from any other methods. This subject will be discussed further in **Chapter 4**. However, several field tests in Long et al. (1991), Olsson (1992) and National Research Council (1996) concluded that stochastic models could reproduce behaviours of the observed (target) DFN. Given that the above issues are effectively contended with, discrete stochastic approach can be a competent tool for modelling NFR.

1.4.3 Integrated Models

It could be seen that NFR modelling is a complicated task, which has not been succeeded by either continuum or discrete, deterministic or stochastic approaches above. A combination of the different modelling methods could be beneficial. Several investigators have assimilated deterministic and stochastic simulation for better results. There are also computational intensive models using various artificial intelligence (AI) tools. Integrated models could accommodate multiple data sources and covered various modelling scales.

1.4.3.1 Models Combining Deterministic and Stochastic Approaches

Descriptions

Combination of mathematical, geomechanical and stochastic models provided tools that would be better equipped for modelling NFR heterogeneity. They were able to incorporate various geological information, mechanical prototypes and mathematical relationships (Swaby and Rawnley, 1996; Cacas et al., 2001; Rawnsley and Wei, 2001). The DFN models covered both large and small scales.

Swaby and Rawnley (1996) constructed geological model of 3D fracture network around the wellbores by using geological information of producing fractures and understanding the mechanism that control their conductivity. First, reservoir geological settings and structures were interpreted from 3D seismic data. This step covered large reservoir scales, in which features such as bedding planes and big faults were recognised. At well locations, fracture identification from core and image data was carried out. Next, fractures in the intermediate scales (inter-well regions) were constructed in two ways. Some were manually extrapolated from wells to the 3D surrounding regions. A large number of other small fractures were genetically generated within the near-wellbore region, calibrated to well production and outcrop data. Knowledge of conceptual models of fracture growth, reactivation, dissolution and stress field made the general model more flexible and capable of producing realistic tension fracture patterns (Swaby and Rawnley, 1996; Rawnsley and Wei, 2001).

Cacas et al. (2001) also incorporated different techniques to model a fracture system, including different fracture types at different scales. The multi-scaled issue of fractures was tackled by modelling in a nested manner, covering from large reservoir scales to smaller wellbore scales. First, using mostly seismic data, separate fracture sets were recognised and statistical distributions of various fracture properties were computed at large reservoir scales. This information allowed discrete fractures at sub-seismic scales to be stochastically generated. Some fractures that could be picked up from seismic maps were also deterministically added. The next step was to model a grid-based model, where statistical distributions of fracture properties at each grid-block were obtained from outcrop, well log and core data. Another stochastic simulation was

performed to fill in local discrete fractures within each grid-block. Resulting fracture model was a combination of the discrete models at both scales.

Discussions

It could be seen that the integrated models brought about many advantages in modelling DFN, compared to equivalent continuum and discrete stochastic models. Most notably, the modelling followed nested manner, to account for the multi-scaled complexity of NFR.

However, the stochastic simulation components in both methods were similar to discrete stochastic models, whose disadvantages (as discussed in **Section 1.4.2.2**) have not been improved. These models were largely based on determination of statistical relationships of fracture properties, which did not perform to satisfaction. Geostatistical tools such as variograms could have been used for better spatial characterisation. Moreover, both methods were only reliable for fractures around wellbores, where data were available (e.g. borehole images and cores). At other grid-blocks, fracture statistics were approximated from measurements at well locations. The above models lacked reliable spatial correlation procedures for such approximations.

Furthermore, the interactive model (Swaby and Rawnley, 1996; Rawnsley and Wei, 2001) required very intensive manual interaction, especially for analysing data and understanding fracture behaviours. This limited their applications to typical NFR, which usually contain many fractures of various scales and heterogeneously distributed. In addition, the problems of fracture conductivity and validation have not been addressed.

1.4.3.2 Models using Artificial Neural Network (ANN)

Descriptions

Recently, there were attempts to characterise natural fractures by applying fuzzy logic and neural networks (Zellou et al., 1995; Cebastiant, 1997; Ouenes, 2000; Zellou and Ouenes, 2001; Boerner et al., 2003; Shen and Ouenes, 2003).

The standard procedure of this approach is demonstrated in **Fig. 1.3**. First, data sources and geological features that could have relationships with rock fracturing (geological drivers) are identified, e.g. seismic attributes, porosity, permeability, lithology, bed thickness, state of stress, fault patterns and production data. Then, an ANN (with built in fuzzy logic) was applied to the grided model, where the complex and nonlinear relationships between these geological drivers and a fracture index (fracture intensity) were assessed. This step ranked the geological drivers according to their effects on fracture distribution and calculated the fracture index values for all grid-blocks. For well-developed reservoirs, production history could be used for training and validation. This approach took into account the overall effect of the fracture system upon fluid flow in the reservoir with a primary emphasis on predicting well performance. Barman et al. (2000) extended the above work by incorporating effective permeability using streamline-based inverse modelling. More details on fuzzy logic and ANN (training, validation, capacity and application) are discussed in **Chapter 3** (**3.4**).

This figure has been removed due to copyright requirements

Fig. 1.3: Procedure for a fracture simulation based on Fuzzy logic and ANN (with reference to Zellou and Ouenes, 2001).

Discussions

This approach has emerged as one of the best available tool to evaluate the reservoir's fracture distribution. Compared to the equivalent continuum models, the continuum approximation was replaced by the use of an ANN. ANN efficiently accounts for all the available reservoir data sources. It is capable of computing such complicated relationships that might not even be represented by conventional geomechanical equations. For developed petroleum fields where production data are abundant and history matching is consistent, the result would be considered reliable and could be validated.

However, similar to the equivalent continuum models, these works did not require generation and treatment of discrete fractures. Their outputs were fracture intensity maps, where details of other fracture properties (orientation, size and aperture) were not considered. Moreover, production performance data were assessed for the reservoir at its in-situ condition, at which different hydraulic stimulation and reservoir simulation scenarios could not be assessed. Besides, this approach required many different data sources, including full understanding of geological settings and production history, which would only be available at later stage of reservoir development.

Weighting Method

To upgrade the fracture intensity map to a DFN map (with discrete fracture details), Zellou et al. (1995) used a “weighting method”. The method was described in 2D, where each grid-block was assumed to be associated with a fracture. Each fracture was a line. Orientation of the line was determined by fracture intensities of eight neighbouring blocks. Length of the line was directly related to fracture intensity of the block.

Accuracy of the weighting method was low. First, the generation scheme did not take into account any previously generated fractures, which might cross the centre grid-block and eight neighbouring ones. This would give dramatically wrong information to simulations of fracture orientation and length. Second, for fractures extending outside

the centre and eight neighbouring blocks, their orientations should also be determined based on fracture intensities of further blocks.

In addition, the basic assumption of one fracture per grid-block was debatable. For example, to model networks of closely spaced fractures, block size should be very small. This resulted in a large number of grid-blocks, each with smaller intensity value. Hence, small grid-blocks tended to result in overestimation of small fractures, or rather underestimation of big-sized ones.

What's more, the weighting method was based fully on fracture density distribution. To account for complex nature of NFR, many other fracture properties such as orientation and size should also be considered. The evidence suggests that the weighting method would produce different results when different grid size was applied. In addition, this generation was not conditioned to field data such as known fractures to attach the realisations to more reality. Thus, it could be argued that the resulting fracture map would not be representative for the reservoir fractures.

Summary

In general, models using ANN represent one of the most advanced continuum methods. The use of ANN integrates simultaneously data sources of different scales and qualifies complicated relationships between data and fracture properties. Even though they have not illustrated themselves as comprehensive and conclusive DFN models, they could be considered an effective tool for complex data mining applications, e.g. for NFR data analysis.

1.4.3.3 Models using Global Optimisation

Descriptions

Optimisation (or global optimisation) approaches represent another computational AI tool. The methods are based on combination of geostatistics and different optimisation techniques (either sequential indicator simulation with Markov chain or simulated annealing). Optimisation purposes are to generate fracture network

realisations that match different statistics and geostatistics of target fractures. Characteristics of a general optimisation approach are demonstrated in **Chapter 5** (**5.2**).

Similar to the AI methods using ANN, most of the optimisation models attempted to evaluate spatial distribution of fracture intensity or some other indexes defining fracture presence (i.e. continuum models) (Mauldon et al., 1993; Sahimi, 1995; Day-Lewis et al., 2000; Guerreiro et al., 2000; Nakao et al., 2000; Gauthier et al., 2002). Long et al. (1991) targeted tomography of only large fractures, which dominated the hydraulic conducting behaviour.

In the continuum models, simulated area was divided into small grid-blocks, each of which was represented with a fracture index value. The overall distribution of fracture index values was measured using several statistical and geostatistical measurements, e.g. variance, histogram and variogram. These measurements were combined to form an "objective function", representing difference in fracture index distribution between realisations and the target. The simulated fracture network model was continually modified, by swapping those grid-blocks between one another. While doing so, the objective function was minimised. In the end, the final realisation matched the predefined statistics and intensity distribution of the target fractures.

There were also works by Farmer (1992) and Soares et al. (1996), which modelled DFN using simulated annealing. The investigators incorporated a number of different measurements in the objective functions, such as multi-histogram and covariance of fracture orientation and length. They also used fractal dimension, number of intersections and total density of the fracture network.

Discussions

Simulated annealing, as an optimisation tool, could always find the optimum solution (i.e. converging to the global minimum) (Sen and Stoffa, 1995). "Finding an optimum ordering is equivalent to generating a numerical model" (Deutsch and Journel, 1994). It is an integrated tool as data from different sources and of different nature could be used as different components of the objective function. Furthermore, this method

could also be made conditional to experimental information (data). For example, at well locations, the simulated density is set to be equal to measured values. With appropriate choice of objective functions and modification scheme, this method has great potential in geoscience modelling.

As the aim of an optimisation model is to generate realisations that match target fractures, it is utmost important to choose the measurements that are representative for the whole system. However, the statistics used in the previous models were not adequate. First, even though histogram and variogram were proved to be effective, many other statistical and geostatistical measurements could be added for better characterisation. Second, it is just impossible to count the number of fracture intersections in a real reservoir. More importantly, the models did not consider interactions between different fracture properties. Fracture orientation, size and density were treated separately by using respective statistics. For most optimisation models were grid-based, their outputs were fracture intensity images, with no reference to fracture orientation and size.

It is noted that simulated annealing is computationally intensive and requires trials and errors to fine-tune. Components of the objective functions need to be chosen carefully so that they not only represent the fracture network, but also facilitate the program to converge. The previous works did not tackle this important aspect.

It is also observed that the previous programs did not address the multi-scaled issue in a complex NFR. Simulation was carried out in limited scales, where data were abundant for statistical representation. The models did not relate themselves to reservoir geological contexts. Despite great potential of global optimisation, previous works presented themselves to be at early stage towards the comprehensive NFR modelling.

1.4.4 Summary

In general, there exist many different approaches for NFR modelling. Some of them offer great advantages over others. However, none have been able to satisfactorily

characterise and model DFN of a NFR. In order to fulfil this task, it is essential to develop a model that allows efficient integration of field fracture data. The integrated reservoir modelling should consist of computational tools and methods that utilise simultaneously, or sequentially, various data sources, representing different reservoir characteristics at different scales. This can reduce uncertainties, reproducing all observed reservoir fracture characteristics.

1.5 OBJECTIVES AND SCOPE OF THE THESIS

目标
1、研究复杂性
2、综合数据的方法
3、建模方法

This research aims to contribute to an improved understanding of the fracture network distribution in NFR, especially in petroleum and hot dry rock reservoirs. The primary objectives of this thesis are to:

1. Investigate the complexities of fracture data characterisation from conventional Petroleum Engineering data sources.
2. Develop a methodology to integrate multi-scaled and diverse information from all available sources.
3. Develop a methodology to model DFN in NFR.

The novel integrated methodology incorporates features of geological, statistical and AI techniques to characterise and then simulate the DFN observed in the field. It consists of two modules: Hybrid neuro stochastic simulation and Object-based conditional global optimisation. Both modules start with fracture data characterisation, statistical and spatial analyses. The fracture data are then amalgamated in different ways to produce discrete networks of fractures. **Fig. 1.4** illustrates process of the overall methodology.

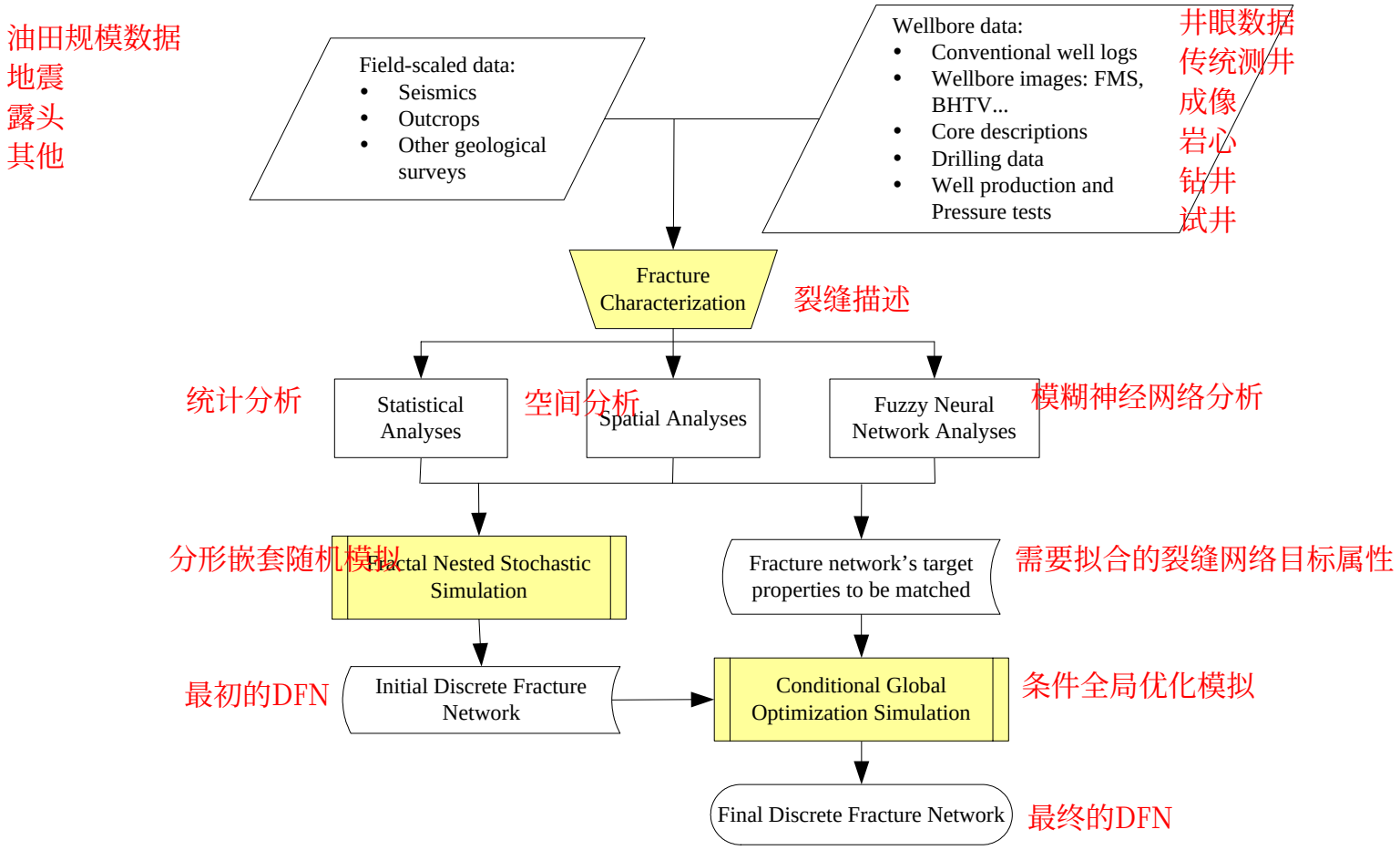


Fig. 1.4: Overall methodology for NFR characterisation and modelling. 回到首页

1.6 THESIS OUTLINE

The thesis is presented according to the procedure of the modelling method. It is divided into two major parts: NFR characterisation (**Chapters 2** and **3**) and NFR modelling (**Chapters 4** and **5**).

In order to put this work in the correct perspective, important fracture properties are first introduced. This is followed by review of the importance and significance of all conventional petroleum engineering data sources upon fracture characterisation. Determination of discrete fracture properties from different data is also outlined (**Chapter 2**).

Chapter 3 presents various methods that utilise and integrate results of **Chapter 2** to delineate the fracture behaviours. First, circular statistics for fracture orientation and multifractal geometry for fracture size are depicted. Then, variograms and other geostatistical measurements of fracture distribution are illustrated. Finally, fundamentals of fuzzy neural networks and their applications in characterising fracture spatial distribution are demonstrated.

Chapters 4 and **5** present the theoretical setup and field examples of the two modules for NFR modelling. In **Chapter 4**, the hybrid neuro stochastic simulation module is introduced through evaluations of stochastic, conditional and hierarchical simulation components. The case study on the Palm Valley NFR (Australia) summarises all the characterisation and modelling procedure, from statistical and fuzzy neural data analyses to stochastic realisation of the actual fractured gas field.

In **Chapter 5**, the object-based conditional global optimisation module is presented. It includes problem formulation and modelling procedure, which starts from stochastic simulation initialisation, through modification, to final realisation of the optimised behaviours. This is followed by a case study on the actual Otsego fault map (USA). A comparison between the optimisation and stochastic simulation methods is also drawn.

Finally, **Chapter 6** summarises the major findings of this work and recommendations that could be useful for future works.

CHAPTER 2 - FRACTURE CHARACTERISATION

2.1 OVERVIEW

总述

Characterisation is the first step of a reservoir study, preparing data for modelling and simulation stages. The aim of NFR characterisation is to determine reservoir and fracture properties, at well locations as well as correlation and interpolation throughout the inter-well regions (Haldorsen and Damsleth, 1993). In doing so, it is essential that all available field data be effectively combined and utilised.

In this work (**Chapters 2** and **3**), a systematic approach to NFR characterisation is presented in two major steps:

1. Processing of data sources to give information on fracture properties (from raw data to intermediate data)
2. Analysis and integration of intermediate information to establish characteristics, interrelationships and spatial distributions of all fracture properties for the whole reservoir. Analyses are performed in both large and small scales.

The procedure is summarised in **Fig. 2.1**.

This chapter begins with an overview of fracture characteristics, which are to be assessed and modelled. This is followed by a summary of all typical data sources, ranging from seismic and outcrop surveys to different logging tools, wellbore images, core, drilling data and well tests. The focus is on the data sources' scales of investigation and capability upon acquiring intermediate fracture information. Important data sources, hence, are recognised for later fracture data integration and characterisation (e.g. fuzzy neural analysis in **Chapter 3**). Through out the chapter, several illustrations are taken from the actual Palm Valley NFR (Queensland, Australia). This chapter ends with a short note on data sampling errors.

油田规模的数据

井眼规模数据

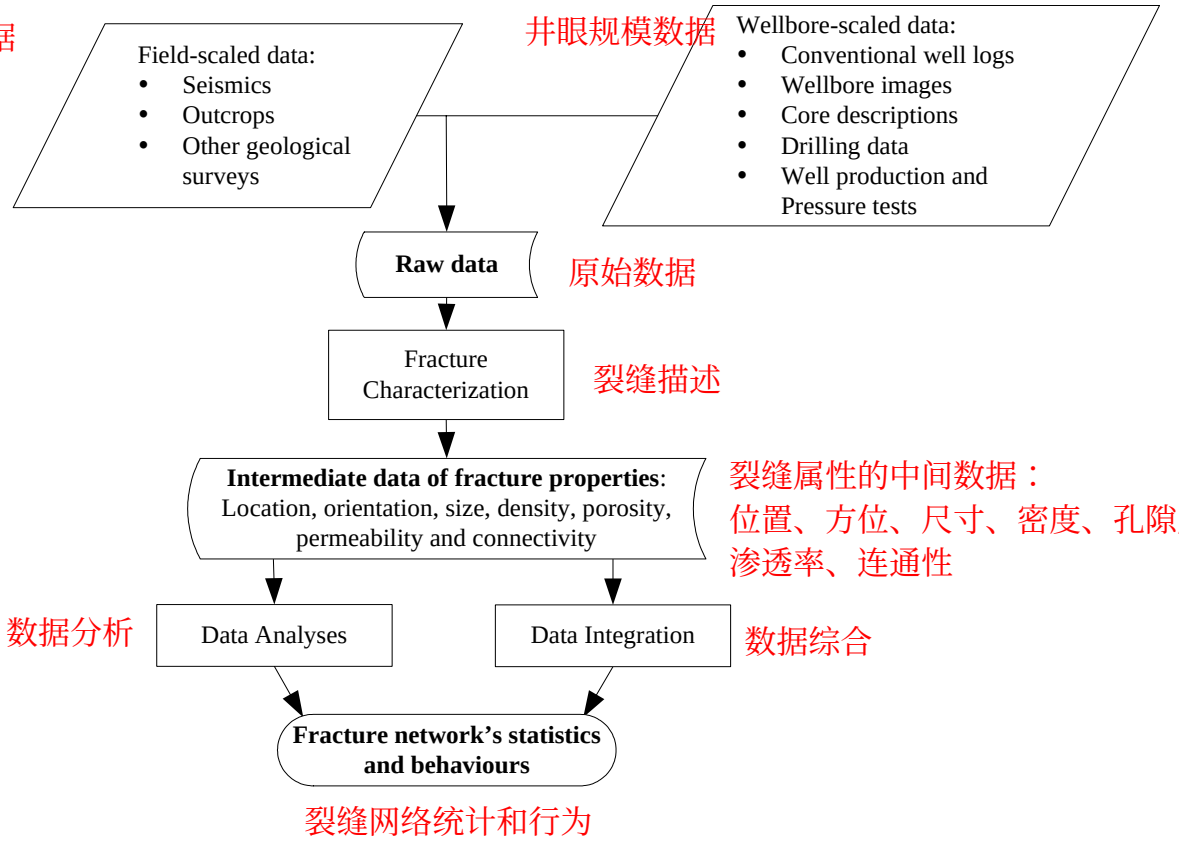


Fig. 2.1: Procedure for the NFR characterisation - from raw data to statistics and behaviours of the DFN.

回到首页

2.2 NATURAL FRACTURE PROPERTIES

天然裂缝性质

Natural fractures can be classified in many different ways. For example, Twiss and Moores (1992) categorised them into joints and faults (normal, thrust, reverse). Nelson (2001) used four groups: tectonic, regional, contractional and surface related fractures. In this work, all fractures are defined in the same way, referring to any mechanical breaks in rocks. One fracture is distinguished from another by a set of properties of location, orientation, size, density, porosity, connectivity and permeability. The properties define fluid flow characteristics of the fracture network, hence, are controlling factors for oil and gas recovery in NFR. They are reviewed in the following subsections.

裂缝分类

2.2.1 Fracture Characteristics: Location, Orientation and Size

裂缝描述：位置、方位、尺寸

传统的平行板模型过于简单，本文采用圆盘模型。

Fractures are commonly presented as lines or arcs in 2D and lines, rectangular planes or circular (penny-shaped) surfaces in 3D. Traditional models considered fractures as parallel plates for solving ground water flow problems (Gringarten et al., 1975; Bazant and Ohtusubo, 1978; Shibuya et al., 1985; Bodvarsson, 1988; Brown, 1987). However, these models were too simplistic and failed to address many of the fundamental problems encountered in NFR simulation (Watanabe and Takahashi, 1995). In this work, fractures are portrayed as a line or channel in 2D and as a penny-shaped object (circular-shaped) in 3D, as used in Dershowitz and Einstein (1988), Willis-Richard (1996) Hossain (2001) and Tamagawa et al. (2002).

2D裂缝模型。

In 2D, a fracture line is defined by coordinates of centre (x, y), orientation (θ), length (L) or radius (*Rad*) and thickness (*Aper*) (**Fig. 2.2**). Fracture orientation is measured from the y-axis (north direction), positively clockwise. The orientation value is equivalent to azimuth angle in 3D case. The line thickness is equal to effective fracture aperture. If a fracture is filled by depositions and fluid flow is restricted, value of effective aperture would be much closed to zero.

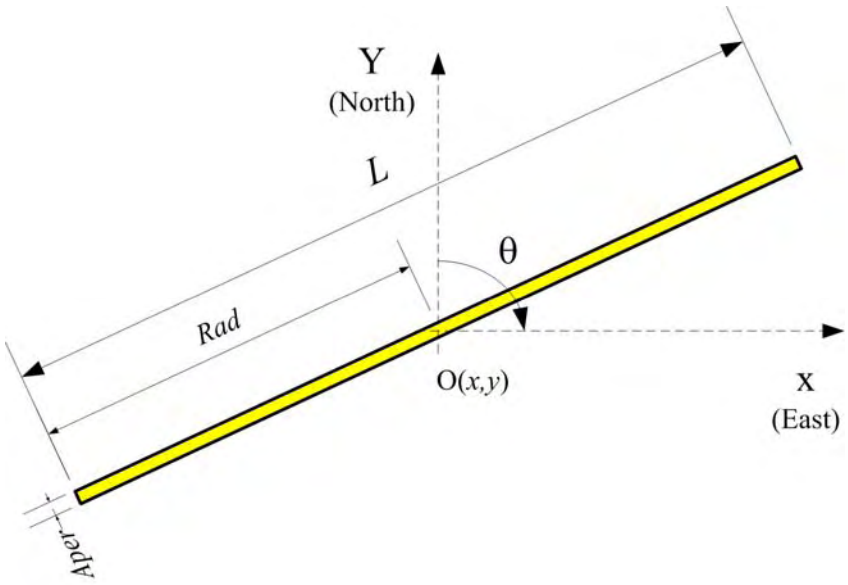


Fig. 2.2: Diagram for 2D fracture line: characterised by centre $O(x, y)$, orientation (θ), radius (*Rad*) and thickness (*Aper*) in x-y coordinate system

In a typical 2D fracture surface, fracture properties can vary tremendously. Fracture length can be as small as wellbore scales (less than a metre) or as big as reservoir scales (more than a few kilometres). As fractures are presented as lines without directions, their orientation can vary between zero and 180°. Behaviour of fracture aperture is also complex.

3D圆盘模型介绍

In 3D, a penny-shaped fracture object is composed of a circular surface with a thickness (*Aper*). The circular surface is defined by coordinates of centre (*x*, *y*, *z*), two orientation values (*Dip* and *Azimuth*) and radius (*Rad*) (**Fig. 2.3**). *Dip* is the inclination of fracture plane from horizontal. It is measured perpendicular to the intersection of the two planes (i.e. fracture strike). *Azimuth* is the angle between the above intersection line and true north or magnetic north direction, measured in the horizontal plane clockwise from north.

Similar to 2D case, fracture radius can vary between near zero to the size of the reservoir model. Aperture can also be as small as zero (for fully filled fractures). Dip angle is between zero and 90° while azimuth angle runs half the circle (zero to 180°).

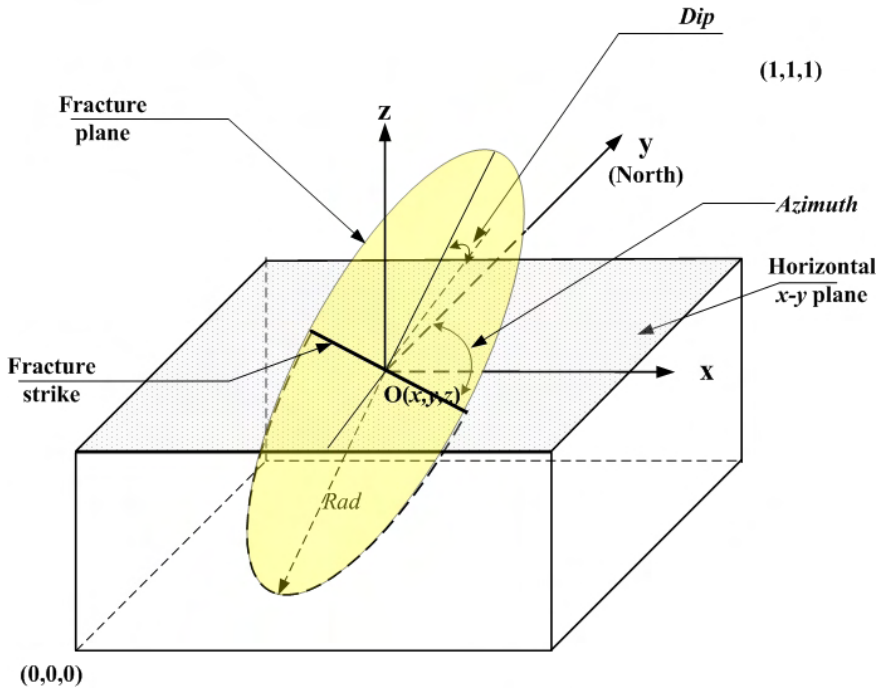


Fig. 2.3: Circular disc model of fracture: characterised by centre *O(x, y, z)*, radius (*Rad*) and orientation of the fracture plane (*Dip* and *Azimuth*)

2.2.2 Fracture Aperture

裂缝开度

Fracture aperture refers to morphology of the fracture planes and is a significant element of fracture porosity and permeability. There are four basic types of natural fracture plane morphology (Nelson, 2001):

1. Open fractures
2. Deformed fractures: gouge filled fractures or slickensides (e.g. **Fig. 2.4**)
3. Mineral filled fractures (e.g. **Fig. 2.4**)
4. Vuggy fractures.

Openness or width of fractures is controlled by the aperture property, which is defined as distance between the two fracture surfaces.

This figure has been removed due to copyright requirements

Fig. 2.4: Core fracture interpretation in well A, Palm Valley NFR: showing fracture plane morphology, which is both deformed and mineral filled (with reference to Berry, 1991).

2.2.3 *Fracture Density*

裂缝密度

Fracture density and fracture intensity are among the most important characteristics of a fracture network. In qualitative term, many fractures exist and form clusters in high-density zones. As fractures greatly facilitate fluid flow, these zones are preferred for most reservoir applications, except in controlling wastes and leakages.

传统定义裂缝密度单位面积或体积内裂缝数量。由于裂缝尺寸不同，作用不同，故此定义未尽完善。

Most of previous documents assigned fracture density as number of fracture counts per unit area or unit volume (Deutsch and Journel, 1994; Soares et al., 1996; Zellou and Ouenes, 2001). Although this convention shows qualitatively high and low fracture intensity zones, it could not do so quantitatively. As large and small fractures play different roles in fluid flow, they need to be distinguished.

在此定义：
裂缝强度如上密度定义。
裂缝密度定义为：
单位面积裂缝总长度或
单位体积裂缝总面积。

In this work, the above definition refers to fracture intensity. Fracture density (*FracDen*) is formulated as total fracture length per unit area (in 2D) or total fracture area per unit volume (in 3D). This definition reflects total number of fracture counts and their relative sizes. It has been found the most useful density measurement for discrete fracture characterisation (Dershowitz and Herda, 1991). High value of fracture density does indicate a particular part of the reservoir being highly populated by fractures.

$$2D: FracDen = \frac{2 \cdot \sum_i Rad_i}{Model \quad Area} \tag{2.1}$$

$$3D: FracDen = \frac{\pi . \sum_i (Rad_i)^2}{Model \quad Volume} \tag{2.2}$$

2.2.4 *Fracture Permeability, Connectivity and Porosity*

裂缝渗透率、连通性和孔隙度

Fracture permeability and conductivity measures the ability to transmit fluids. Fracture permeability is typically high as they connect isolated pores and provide a pathway for fluid flow. In a fractured system, permeability refers to the combinatorial effect due to rock matrix and fractures.

裂缝渗透率

Fracture connectivity is formally defined as number of counts of fractures within a unit area or volume that intersect one another. It is important to identify whether

裂缝连通性
1、难以确定

fractures within the reservoir are well connected or not, as this directly affects overall fluid flow. In reality, fracture connectivity is extremely hard to determine quantitatively.

裂缝孔隙度
1、主要指次生孔隙。
2、裂缝本身空隙体积不大，但同原生孔隙连通时，孔渗都大有改变。
3、裂缝孔隙体积有尺寸开度确定。

Fracture porosity is a type of secondary porosity produced by rock fracturing. Fractures themselves typically do not have much 'empty volume', but when joining with pre-existing pores, both porosity and permeability improve dramatically. The fracture pore volume could be directly computed from other properties such as size and effective aperture.

有些油藏，次生孔隙是很大的。

In some reservoirs, where fracture porosity is high, fractures are not only the fluid conduits but also storage. Secondary porosity is most notable in carbonate reservoirs. Another example is that non-reservoir rocks such as granite can become hydrocarbon storage if sufficient fracturing occurs. Granite basement reservoirs are common in South and East China Sea.

2.3 REVIEW OF FIELD DATA SOURCES

矿场数据回顾

总述不同尺度、分辨率的矿场数据。

There are various data sources for fracture characterisation in NFR. Different tools cover different scales and have different resolutions. Reservoir-scaled sources include seismic and outcrop data. Wellbore-scaled sources are made up by a range of logs, borehole images, cores, drilling data, production and pressure tests. Each of them describes different aspects of the fracture network. In this section, all conventional field data surveys are reviewed, identifying relevant data sources that play significant roles in fracture characterisation, their capacity and limitations.

2.3.1 Seismology

地震

2.3.1.1 General Overview

Seismology is one of the most important data sources that could provide reliable fracture information for the entire NFR, especially for inter-well regions. When conducting seismic surveys, acoustic energy sources and receivers are positioned on the

ground. The acoustic waves transmit into the ground at a velocity dependent on density and elastic properties of the rock material through which they travel. When the waves reach an interface where the layer velocities change dramatically, a portion of the energy is transmitted into the lower layer, and the rest is reflected back to the surface receivers. Seismic maps (2D or 3D) are collections of the sinusoidal signals, as results of processing travel time of energy signals recorded in the receivers (e.g. **Fig. 2.5** and **Fig. 2.6**).

This figure has been removed due to copyright requirements

Fig. 2.5: An example of a seismic cross-section through well G, Palm Valley NFR: showing different formations and interpreted fractures (with reference to Roe, 1995).

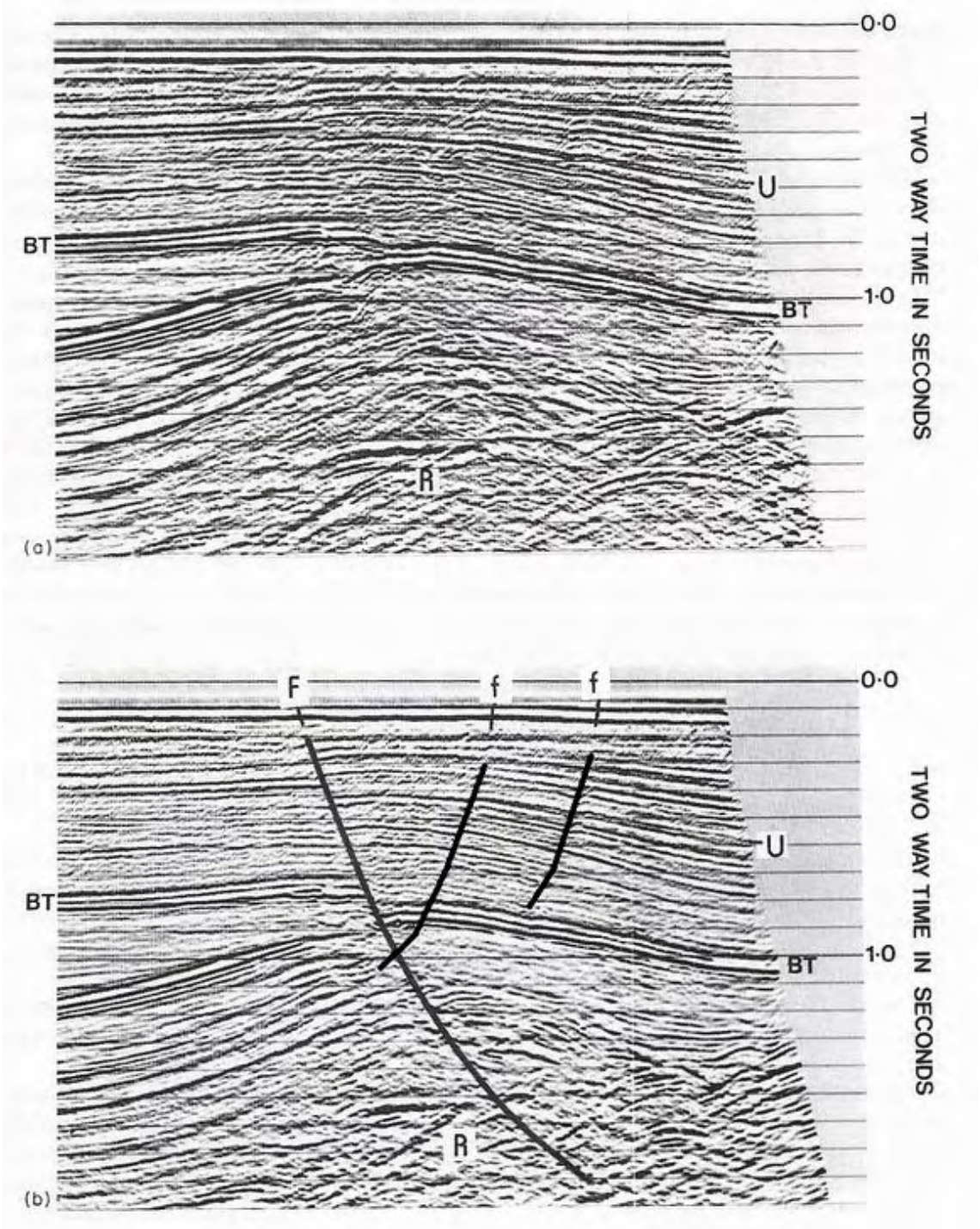


Fig. 2.6: An example of seismic interpretation: The upper image shows a seismic time map with horizontal lines being bedding layers in the reservoir (e.g. lines BT). Some beddings are offset, indicating presence of faults. Faults (F) are pointed out in the lower image.

通过地震能识别的属性

In general, 2D and 3D seismic profiles are regional-scaled data, with resolution varying from tens to hundreds of feet depending on amplitude and wavelength of signal waves. The seismic data describe reservoir structure, thickness, lithology and curvature of various formations. From seismic maps, big faults and fractures can be interpreted (e.g. **Fig. 2.6**). The tool can also characterise strength and hydraulic properties of fractured rock mass since seismic responses are indicative of permeable and low rock strength zones. 3D seismic reveals principal and Gaussian structural curvatures, preferred fracture orientation and density (Kuwahara et al., 1991; Padgett and Nester, 1991; Ass'ad et al., 1992; Lee et al., 1994; Pyrak-Nolte, 1996; Boadu, 1997a; Boadu, 1997b; Aarland and Skjerven, 1998; Boadu, 1998; Bates et al., 1999; Belfield, 2000; Bates et al., 2001; Bunge, 2001; Shen and Ouenes, 2003).

垂直地震剖面技术
VSP

There are also wellbore seismics, where the receivers are placed along the borehole. The wireline measurements produce vertical seismic profiles (VSP), which include vertical seismic profiling offset, compressional reflection wave (P-wave) and some shear wave (S-wave) splitting. VSP technique, with the advantage of enhanced resolution, has great use in identifying the presence of reflections (e.g. beddings, fractures) near the well. These reflections can be verified with surface seismic profile maps to correlate petrophysical properties measured in the borehole. VSP can have very large radius of investigation (up to thousands of feet), by increasing the distance of seismic sources away from the well.

纵波（P-Wave）显示裂缝密度、方位。穿越裂缝，尤其是垂直、高角度缝时，P-Wave变弱。

P-wave shows fracture density and fracture azimuth. It attenuates as velocity anisotropy gets slow when perpendicular to fractures. It is even more attenuated by vertical and high angle fractures. Compared to other seismic attributes, P-wave is less expensive and more easily processed (Lee et al., 1994; Lefeuvre et al., 1993; Cicerone and Toksoz, 1995; Kuwahara et al., 1995; Lynn et al., 1995; Beckham, 1996; Ohminato et al., 1996; Nakagome et al., 1998; Gray et al, 2002).

S波的作用

When propagating through stress-aligned fluid-filled fractures, S-wave is polarised into fast and slow directions because of fractured anisotropy. Mapping of the polarisation can yield principal fracture orientation. Finding the time delay between polarised waves can determine fracture density. In addition, S-wave attenuation is

directly proportional to permeability and inversely proportional to bulk density. S-wave amplitude seems to be more attenuated by horizontal and low angle fractures. Compared to other seismic attributes, S-wave is more analytic and useful (Crampin et al., 1989; Iverson, 1992; Meadows and Winterstein, 1994; Kuwahara et al., 1995; Lynn et al., 1996; Li, 1997; Song et al., 1998; Quintero et al., 2001).

2.3.1.2 Seismic Attributes

地震属性

A seismic signal has several attributes, most of which are affected by reservoir heterogeneities such as fractures. The attributes are based on amplitude, phase and velocity of the seismic signals. Examples include amplitude variation with offset (AVO), amplitude versus angle and azimuth (AVAZ), instantaneous phase and instantaneous velocity. Each attribute can delineate different aspects of the fracture network.

AVO
1、裂缝方位
2、各向异性、间隔密度

Amplitude variation with offset (AVO) has been used to recognise anomalies in the seismic wave reflection due to fracture orientation. 3D AVO can also interpret fracture anisotropy, spacing and density (Lynn et al., 1995; Ruger and Tsvankin, 1997; Sayers and Ebrom, 1997; Sayers and Rickett, 1997; Gray and Head, 2000; Renfang et al., 2002; Shen et al., 2002; Aguilera, 2003; Neves et al., 2003).

AVAZ
1、裂缝填充

Amplitude versus angle and azimuth (AVAZ) analysis can identify open, fluid filled or gas filled fractures. Fracture orientation and density are interpreted from variations of the amplitudes of the long shot receiver offsets of P-wave seismic (Lynn et al., 1996; Gray and Head, 2000; Smith and McGarrity, 2001; Aguilera, 2003).

2.3.2 Outcrop Analysis

露头
通过表面推知地下

Similar to seismic, outcrop image is at regional scales and is an important fracture data source. It establishes underground fractures as the surface measurements being extrapolated into subsurface. It reveals many fracture characteristics, e.g. length, aperture, spacing, orientation and density (**Fig. 2.7**). Other obtainable information includes stress sensitivity, spatial distribution (clustering) and interconnectivity of the

fracture network (Ericsson and Ronge, 1989; Padgett and Nester, 1991; Harstad et al., 1995; Lynn et al., 1995; Olson et al., 1996; Baker and Kuppe, 2000; Baker et al., 2001).

由于风化、应力等原因，由露头推知地下并不简单。

Nevertheless, the conversion of surface 2D outcrop image to underground 3D fracture network is not straightforward. There is difference between surface and burial states of stress (Quintero et al., 2001; Aguilera, 2003). Fracture properties reading from outcrops depend on stress relief and weathering. For example, there are typically more fractures on the outcrop than in the subsurface (Wealthall et al., 2001).

This figure has been removed due to copyright requirements

Fig. 2.7: Outcrop of joints in the limb of a non-cylindrical fold in Lavernock Point (Wales, U.K) - A very well connected joint network. The outcrop maps depicts 2D fracture network, which is cross-section of the underground 3D network. Location, orientation and size of all fracture lines can be promptly recognised [http://www.dstu.univ-montp2.fr].

2.3.3 Conventional Logging Measurements

For over half a century, well logging has developed as one of the most effective engineering tools for subsurface characterisation. Well logs are of high resolution, relatively cheap and widely available at most boreholes. A complete theory behind

conventional well logs can be found in Serra (1986), Hurst et al. (1992) and Schlumberger (1996).

传统测井反映的是组合效应。即其同裂缝有关系，但关系还没弄清。

Detailed fracture characterisation, however, is not possible from conventional well logs alone. This is because the logs respond to combinatorial effects from different rock, fluid and fracture properties, which are difficult to distinguish. In other words, there are relationships between well log responses and fractures, but they have not been fully understood (McCoy et al., 1980; Suau and Gartner, 1980; Aguilera, 2003). Moreover, pre-existing fractures at well sites are damaged during drilling process, e.g. washouts, vugs, lithology, mud invasion, wellbore pressure, fracture instability and fracture reactivation (Atkinson and Theircelin, 1995). Thus, conventional well logs have only been used for fracture detection purposes; realising zones of high and low fracture density along the wellbores (Song et al., 1998; Ouenes and Hartley, 2000; Rogers, 2000).

2.3.3.1 Calliper Log 井径测井

Calliper log (CAL) shows an increase in the borehole diameter due to crumbling of fracture zones and/or borehole breakout. It gives broad information on general trend for fracture orientation, as fractures are normally found both parallel and perpendicular to borehole breakouts. As similar calliper responses are observed for vugs and shale, the observations are only indicative. In addition, if lost circulation material is used and built up in the fractures, calliper might read smaller values than normal (Grove and Whittaker, 1985; Iverson, 1992).

2.3.3.2 Gamma Ray and Photoelectric Absorption Logs

High readings in gamma ray (GR) (0.3m investigation radius) could indicate precipitation of uranium in fractures. Nevertheless, the high GR readings are also due to potassium-based mud and carbonate precipitation in permeable zones (Hirsch et al., 1981; Grove and Whittaker, 1985; Castrejon-Vacio and Porres-Luna, 1994; Bunge, 2001).

High values of photoelectric absorption (PA) (0.1m investigation radius) could also infer presence of fractures due to barite invasion, but this is only applicable when heavy barite mud is used. As photoelectric cross-section of barite is 267, compared to 1.9 for sandstone and 4.9 for limestone, a mud filled fracture should easily be detectable. Responses are also affected by drilling damage (Grove and Whittaker, 1985; Schlumberger, 1996).

2.3.3.3 Neutron, Density and Sonic Logs

Neutron density log (NPHI) (0.1m investigation radius) identifies secondary porosity and lithology independent of porosity, which effectively indicates fractures. Density log (RHOB) and density correction curve can spot porosity anomalies due to edges of fractures being chipped away during drilling. They can also detect high fracture permeability zones having movable fluids (Grove and Whittaker, 1985; Iverson, 1992; Castrejon-Vacio and Porres-Luna, 1994; Elkewidy and Tiab, 1998; Fitzgerald et al., 1999; Adams, 2000).

Sonic log (DT) (0.1m investigation radius) can identify fracture zones in several ways (Grove and Whittaker, 1985; Iverson, 1992; Yearsley and Crowder, 1992; Castrejon-Vacio and Porres-Luna, 1994; Lefeuvre et al., 1993; Fitzgerald et al., 1999; Saito and Hayashi, 1999; Jin and Zhang, 2002). First, cycle skipping of sonic transit time happens mostly near fractures perpendicular to the tool axis. Second, high attenuation of sonic waveform logs (a more complicated version of sonic transit time) is also indicative of fractured zones. Third, sonic tool array emits a given amount of energy, which is expected at the receiver. High-received signal strength indicates a competent rock with low probability of fractures while very low signal strength indicates high probability of fractures. Similarly, rock with high value of Poisson's ratio, which can be estimated from sonic velocities and transit times, is more likely to contain fractures. Some information on fracture orientation could be suggested from further investigation on sonic shear wave, whose energy is reduced due to reflection, conversion and refraction at the fracture interface. In addition, sonic and neutron logs can be combined into a pseudo-acoustic curve and compared with seismic velocity (Song et al., 1998). The difference indicates fracture presence.

Thus, it can be seen that neutron, density and sonic logs are very useful for the purpose of fracture identification. Unfortunately, similar responses are also due to closed fractures, thin layers of different lithology or changes in the well diameter. The signals are also confused by vugs, gas bearing zones and drilling mud invasion. No conclusion on fracture orientation can be drawn, except for vertical ones where there is high differential attenuation of the P-wave and only slight attenuation of the S-wave.

2.3.3.4 Resistivity and Induction Logs

Resistivity and induction logs look deeper into the formation (up to 5m radius). There is an evident resistivity reduction and positive separation between three resistivity logs of micro-spherically focused (MSFL), shallow (LLS) and deep laterolog (LLD) in fractured zones. There is also a positive separation between three induction logs of micro-spherically focused (SFL), medium (ILM) and deep (ILD). However, both resistivity and induction logs are not applicable for oil-based mud. Moreover, induction logs are insensitive to fractures parallel to the wellbore axis and in oil-bearing zones (Grove and Whittaker, 1985; Castrejon-Vacio and Porres-Luna, 1994; Elkewidy and Tiab, 1998; Song et al., 1998; Fitzgerald et al., 1999; Jin and Zhang, 2002).

2.3.3.5 Example of Fracture Detection from Well Logs

An example of fracture identification from resistivity logs is presented in **Fig. 2.8** (Palm Valley fractured gas field, Australia). The analysis is carried out at the well section where core data are also available (as presented in **Fig. 2.10**). The three resistivity-curves separate noticeably in two instances, one at around 5886ft and the other at around 5900ft. Furthermore, the three resistivity-curves show small separations from 5876ft to 5889ft, which are further supported by higher borehole radius (washout at fractured zone). It is expected that there could be fractured zones at the depths.

However, the fracture characterisation by resistivity logs above is not conclusive and possibly misleading. At 5886ft and 5900ft, the spontaneous potential curve (SP) goes low, indicating a sand layer. It is likely that the large resistivity separations are due to the lithological changes. In the other instance, where there are indications from

resistivity logs and calliper, result might be more reliable, except at the bottom section where similar lithological change is observed. In addition, core images show many fractures at other depths that are not at all indicated on the logs. In other words, the various logging tools fail to positively identify fracture zones.

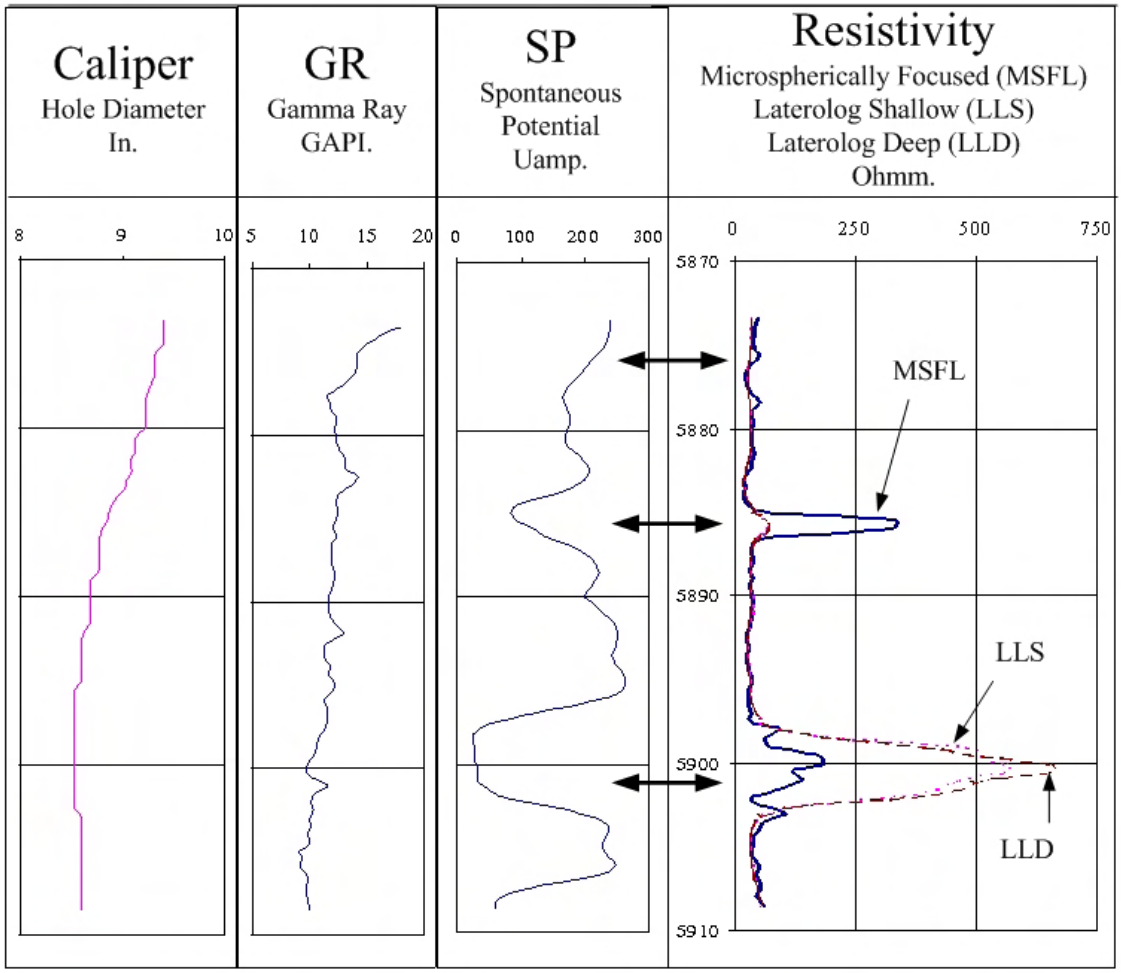


Fig. 2.8: Example of conventional logs on fracture identification in well A, Palm Valley NFR: arrows indicate areas of possible fracturing.

The example has explained that conventional logs do provide some information concerning fractures but they are not effective data sources for detailed delineating applications. There is no single conclusive tool. Even though most conventional well logs have positively small resolution, their investigations are limited to around the wellbores, where drilling induced fractures could interfere with readings. In addition, the results are usually biased and incorrect, especially for fracture detection. Well logs

respond to many different rock properties and results are affected by many factors such as drilling damages, mud, vugs and wellbore pressure. As will be shown later in **Chapter 3**, a possible application of conventional well logs in quantitative analysis is to correlate fracture properties with core and wellbore image data.

2.3.4 Unconventional Logging Measurements

Compared to conventional logs, unconventional tools, such as dip-meter, formation micro-scanner, borehole televiewer and circumference acoustic scanning tool, represent better data sources for fracture characterisation. They belong to a group of only a few tools that allow direct measurements of fracture properties. There are also video (optical) imaging and borehole camera that can provide visual images of the wellbores, depicting intersecting fractures with orientation, aperture and density (Overbey Jr. et al., 1988; Palmer and Sparks, 1991; Haller and Porturas, 1998; Trice, 1999; Rogers, 2000; Ozkaya and Mattner, 2003).

2.3.4.1 Dipmeter and Formation Micro Scanner Logs

Among the most popular unconventional logs, oriented micro resistivity logs, including dip-meter and formation micro scanner (FMS), are able to identify opened and fluid filled fractures. Fracture orientation can be estimated from large separation between readings on adjacent pads of the dipmeter tool**.** This is because mud filtrate, when invading a fracture system, causes a lower dipmeter reading from the pad positioned opposite the fracture. Dip-meter tool contains four pads of 90° apart. Fracture orientation is determined by knowing orientation of the pads, which are in contact with fractures (Babcock, 1978; Grove and Whittaker, 1985; Emmendorfer, 1989; Bell et al., 1992; Iverson, 1992; Gurpinar et al., 1999).

The tool FMS uses microelectrodes to measure micro resistivity variations of the formation and transform them into high-resolution images of the borehole. Thus, it reveals not only fracture orientation but also many other important aspects, e.g. fracture aperture, density and distribution pattern. Due to small resolution of the tools of 0.01m, they can portray almost all fractures crossing the wellbore. FMS can detect between

open and closed fractures (Laubach et al., 1988; Iverson, 1992; Kubik and Lowry, 1993; Schlumberger, 1996; Sanchez et al., 1999; Baker and Kuppe, 2000).

However, similar to resistivity logs, dipmeter and FMS logs are not applicable in oil-based mud and are affected by drilling mud invasion. Other drawbacks include shallow depth of investigation and high cost.

2.3.4.2 Borehole Televiewer and Circumference Acoustic Scanning Tool

Borehole televiewer (BHTV) uses ultrasonic signals, whose amplitude is reduced due to dispersion of energy at fractures, to provide the borehole images. Vertical fractures show as straight lines, while oriented fractures appear as sinusoidal traces. Despite high cost and slow logging speed of less than 300 feet/hour, BHTV (together with FMS) has been used widely in reservoir studies, especially in those containing fractures (Zemanek et al., 1969; Kuwahara et al., 1991; Paillet and Goldberg, 1991; Lefeuvre et al., 1993; Schlumberger, 1996; Fitzgerald et al., 1999; Bunge, 2001).

Circumference acoustic scanning tool (CAST) images the borehole and intersecting fractures by using reflected high frequency acoustic/ sonic pulses. The pulses are generated and received by rotating acoustic transducers. Amplitude and two way travel time of reflected pulse are recorded. The measurements are then converted into borehole images in both amplitude and travel time format (Chilingarian and Fertl, 1987; Noblett and Fertl, 1987; Iverson, 1992; Kubik and Lowry, 1993). There is also the circumferential microsonic tool for fracture identification, which consists of a modified four-arm dipmeter sonde with acoustic transducers replacing the electrodes on the arms. Acoustic energy amplitude drops when crossing a fracture (Hirsch et al., 1981).

2.3.4.3 Example of Fracture Characterisation from FMS

An example of how fractures and their properties are identified from wellbore images is illustrated in **Fig. 2.9** (Palm Valley fractured gas field, Australia). A FMS image from four receiver pads is plotted versus depth. The contrasted micro resistivity variations indicate geological features such as beddings and fractures. These features are

interpreted on the right hand image sequence. They are located by notations *TD*, with the corresponding dip and azimuth values. Fracture height can be directly measured. Fracture aperture is calculated by comparing FMS conductivity response in an open fracture and conductivity of the fluid filling in that fracture. For this particular depth section from 2326m to 2333m, there are three bedding layers, two continuous and seven discontinuous fractures. Most fractures are near sub-vertical (i.e. $Dip \approx 90°$), while beddings are near horizontal (i.e. $Dip \approx 0°$). Azimuth values vary. Discontinuous fractures are identified due to minor energy loss or they only show up in two or three receiver pads. In addition, minimum fracture aperture computed suggests these features are poorly connected deeper into the formation.

This figure has been removed due to copyright requirements

Fig. 2.9: FMS fracture interpretation in well E, Palm Valley NFR: showing continuous fractures (red), discontinuous fractures (orange) and beddings (green) as sinusoidal traces at TD: *Dip*/*Azimuth* (with reference to Rayner, 1995).

Apart from orientation, aperture and density, Ozkaya and Mattner (2003) demonstrated a method to estimate fracture connectivity (i.e. number of intersections per fractures) and fracture length from wellbore images. Even though fracture size could not be interpreted directly, it was shown to be related to relative frequency of fracture traces on image logs. LaPointe et al. (1993) presented a similar method to estimate fracture size from the percentage of fractures intersecting all four FMS pads.

2.3.5 Core Descriptions

Core analysis has also been used widely for subsurface study. There have been a great number of applications and limitations of cores on NFR characterisation in literature (Locke et al., 1989; Padgett and Nester, 1991; Kubik and Lowry, 1993; Lorenz and Hill, 1994; McDonald et al., 1997; Aarland and Skjerven, 1998; Tamanya et al., 1998; Gray et al., 1999; Gurpinar et al., 1999; Sanchez et al., 1999; Baker and Kuppe, 2000; Gray and Head, 2000; Baker et al., 2001; Bunge, 2001; Hirst et al., 2001; Baraka-Lokmane, 2002; Jin and Zhang, 2002; Aguilera, 2003).

Cores, especially oriented cores, provide direct observations and measurements of lithology, bed thickness, rock contents, grain size, porosity and permeability. They also describe subsurface fracture features, e.g. height, aperture, spacing, orientation, density, permeability and degree of mineralisation. Generally, bed thickness is inversely related to fracture density. Lithology also gives certain hints about fracture presence. For example, there is highest probability for fracturing in quartzite, then in dolomite, quartzite, calcite cemented sandstone and limestone. Degree of fracturing is also greater in rocks with fine grain and in rocks with high Poisson’s ratio. Furthermore, fracture size tends to be larger for rocks with high Young's modulus. The magnitude of the variation is more pronounced in high stress formations (Sterns and Friedman, 1972; Schlumberger, 1996; Rahim and Al-Qahtani, 2001a).

This figure has been removed due to copyright requirements

Fig. 2.10: Core samples in well A, Palm Valley NFR: complete core section for different depths, showing different lithological beddings (colour contrast) and fractures (cracks) (with reference to Berry, 1991).

This figure has been removed due to copyright requirements

Fig. 2.11: Core samples in well A, Palm Valley NFR: open fractures of high dip and large aperture. They are potentially the main conductors for fluid flow. Vertical coloured lines note azimuth direction of oriented core (with reference to Berry, 1991).

This figure has been removed due to copyright requirements

Fig. 2.12: Core samples in well A, Palm Valley NFR: the left image shows a sub vertical fracture of very low aperture, which is almost healed. The right image reveals a discontinuous crack, which does not fully cut through the core (with reference to Berry, 1991).

A series of examples where fractures can be directly observed from orientated cores are illustrated in **Fig. 2.10**, **Fig. 2.11** and **Fig. 2.12** (Palm Valley fractured gas field, Australia). **Fig. 2.10** demonstrates core samples metre per metre. Fractures, depositional and lithological changes are visually recognised. For example, at 5891m, there are two fractures, both are around 70^{o} dip and have relatively high apertures. The upper one is continuous and the lower one is not. **Fig. 2.11** and **Fig. 2.12** provide a closer look at different core sections. It is necessary to note that due to restricted scales of core investigations, actual fracture size could not be directly accessed.

2.3.6 Drilling Data

Observations made while drilling can also bring forward indications of possible fractured zones. They include excessive loss of mud (i.e. lost circulation), larger pieces of cuttings with characteristic shapes, oil content in cuttings and abnormally high rates of penetration (Holbrook, 1989; Dyke et al., 1995; Brown et al., 1999; Hews, 2000; Bunge, 2001). By nature, there are many uncertainties associated with drilling data. Similar effects are noted due to hole-collapses and drilling induced fractures. Abnormally high rates of penetration could also be a result of soft formation or under compaction. Even though this data source is purely qualitative, it provides the first clear indications of fractures in the area.

2.3.7 Flow and Pressure Tests

Several works have pointed out that flow and pressure well tests can disclose fracture information, especially fluid flow conductivity of fracture and matrix system. For example, flow meter, tilt meter and tracer test could be used to determine total effective permeability, fracture permeability, skin and connectivity (Locke et al., 1989; Baker et al., 2000; Jin and Zhang, 2002; Rahim and Al-Qahtani, 2001b). Build up or interference test could expose fracture length and connectivity.

Other pressure tests such as leak off and MWD can identify stress field (Holbrook, 1989). The field stress distribution is directly related to creation and development of fracture system. In general, fractures form and propagate when stresses

equal or greater than the rock strength. Fracture planes tend to be forced apart in the direction that contains the least obstacles, which is minimum in-situ stress. As a result, fractures propagate in the direction perpendicular to the minimum stress (**Fig. 2.13**). Theory of fracture propagation is presented in Tran et al. (2002a). With higher stress value, propagation is limited and fractures become increasingly contained.

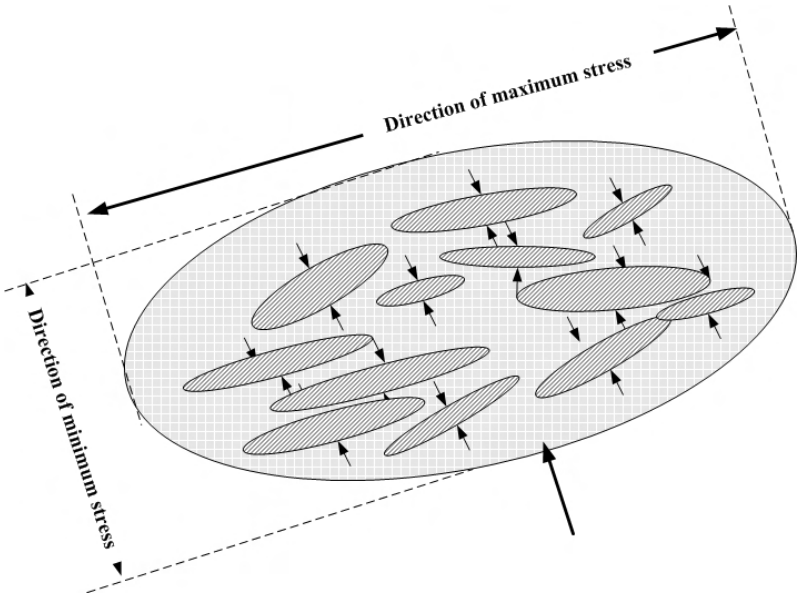


Fig. 2.13: Penny-shaped fracture propagation prefers the direction perpendicular to minimum in-situ stress.

In general, well tests represent the only data type that provides information on fluid flow capacity (e.g. connectivity and permeability) of an overall fracture system, in the in-situ condition. However, direct measurements of the properties are unreliable due to lack of understandings on the fracture and matrix system. Thus, results from well tests would better be used qualitatively, or be integrated with other data sources.

2.3.8 Production Data

Production measurements at individual wells for the whole field life constitute an indirect yet important data source. Even though direct quantitative relationships between production and fracture properties are not assessable, high production at a well would indicate that particular well intersect fracture sweet spot (high density) (Baker et

al., 2001; Quintero et al., 2001; Zellou and Ouenes, 2001). Moreover, in both conventional and fractured reservoirs, simulation of production data is an essential step for overall reservoir study. Production history matching can be used in such simulations to validate the reservoir matrix and fracture models. This could also applicable in NFR modelling to authenticate not only geological fracture model but also fluid flow calculation through the fracture and matrix system.

2.3.9 Summary of Fracture Detection Tools

A summary of all field data sources and their capacities for fracture detection is demonstrated in **Table 2.1**. The table also exemplifies responses of each tool in fracture zones. Most of them cover very small scales (except regional seismic and outcrop surveys). Only a limited number of sources such as seismic, outcrop, wellbore images and core can portray individual fractures (or part of). Others can only indicate possibility of fracture presence. Relationships between these measurements and fracture properties have not been mathematically formulated.

Fracture parameters	Data sources	Scale/ Coverage of Investigation	Characteristics	Notes
Fracture detection - Location of fractured zones	Seismic	Regional	2D or 3D maps of field scaled structures - Gives details of large fractures	Large scaled only
	Outcrop	Local and Regional	Surface mapping reveal large to medium scaled fracture network	No vertical resolution
	Conventional logs			
	Calliper	Wellbore	General trend for orientation from borehole break out	Qualitative only
	Gamma ray (GR)	Wellbore	Detect precipitation of uranium in fractures	
	Photoelectric absorption (PE)	Wellbore	Detect fractures when barite mud used	
	Density correction	Wellbore	High activity opposite possible fractures	
	Sonic log	Wellbore	Identification based on sonic transit time and energy loss, attenuation of sonic waveform…	
	Resistivity logs - MSF, LLS, LLD	Wellbore	Resistivity reduction and positive separation between three logs	
	Induction logs - SFL, ILM, ILD	Wellbore	Separation between three logs	
	Unconventional logs			
	Dip meter	Wellbore	Large separation between readings on adjacent pads.	Show exact depths and locations
	BHTV, FMS, FMI, video imaging, borehole camera, image logs	Wellbore	Visual image of individual fractures crossing boreholes. Exact fracture density measured	
	Core	Local	Direct measurement	Quantitative
	Geological sources	Wellsite and regional	Bed thickness, lithology, curvature of various formations relates to the degree of fracture intensity	Qualitative only
	Drilling data	Wellbore	Inexplicable losses of mud, gain/Los volume, shape of cuttings, oil content in cuttings, hydrocarbon presence in the drilling mud, and abnormally high rates of penetration	Qualitative only
	Well production testing	Inter-wells scale	Flow and pressure tests reveal fractures	Qualitative only

Table 2.1: Field data sources as tools for fracture detection: scales, response characteristics and usages.

2.4 CHARACTERISATION OF INTERMEDIATE DATA

Having discussed capacities and limitations of the conventional field data sources, measurements of individual fracture properties (intermediate data) are possible. **Table 2.2** to **Table 2.5** summarise the most important tools that can be used to obtain the intermediate information. Scales, resolutions and characteristic responses of the tools are also discussed. The intermediate fracture data will be further analysed in **Chapter 3** to achieve characteristics of fractures.

2.4.1 Fracture Orientation

Large- and regional-scaled faults can be interpreted from seismic and outcrop maps. Their orientation values are readily measured. For example, **Fig. 2.5** and **Fig. 2.6** show 2D vertical cross-sections of seismic profiles, revealing fractures with dip angles and lengths. 3D seismic maps can disclose values of both dip and azimuth. On the other hand, outcrop maps, which are normally 2D horizontal cross-section, can portray azimuth.

At well locations, dip and azimuth of fracture intersections with boreholes are directly observed from orientated core and wellbore images (**Fig. 2.9** and **Fig. 2.10**). Dip-meter logs also reveal dip angles of other geological features, e.g. beddings. Moreover, conventional logs such as calliper, sonic and resistivity logs are affected by fracture orientation. However, direct characterisation is ambiguous and not reliable. It is important to note that the orientation values obtained at wellbores could belong to fractures of all sizes, as actual size measurements can not be made from wellbore data.

Fracture parameters	Data sources	Scale/ Coverage of Investigation	Characteristics	Notes
Orientation (Dip and Azimuth)	Seismic	Regional	Major faults are mapped	Major faults only
	Outcrop	Local and Regional	Surface measurements reveal fracture network	Only for Azimuth
	Conventional logs			
	Calliper	Wellbore	General trend for orientation from borehole break out	Best with 4 arm calliper
	Sonic log	Wellbore	Sonic transit time can identify orientation	
	Resistivity logs	Wellbore	Affected by fracture orientation	Qualitative only
	Unconventional logs			
	Dip meter	Wellbore	Large separation between readings on adjacent pads.	Only for fractures intersecting wellbores. Very shallow depth of investigation
	BHTV, FMS, FMI, video imaging, borehole camera, image logs	Wellbore	Visual image of individual fractures crossing boreholes	
	Core	Wellbore	Oriented cores give orientation	

Table 2.2: Fracture orientation and corresponding field data sources: scales, response characteristics and usages.

2.4.2 Fracture Size

Fracture size denotes the extent of a fracture, which includes properties such as length, area, width and aperture. Width or aperture can be observed and measured from directly outcrop maps and core samples (**Fig. 2.7**, **Fig. 2.11** and **Fig. 2.12**). Wellbore images also provide good information, however, readings are affected by drilling damages.

It is generally harder to determine fracture length and area. Only large fractures and very small cleats can be noted. On the one hand, seismic and outcrop maps are the only sources from which large- to medium-scaled fractures can be interpreted (**Fig. 2.5**, **Fig. 2.6** and **Fig. 2.7**). On the other hand, some micro fractures and cleats (maximum lengths are in ranges of millimetres) could be observed from core and wellbore images. Moreover, conventional resistivity logs and well tests are affected by fracture size. Again, the relationships are not straightforward and too complicated to be mathematically formulated.

Fracture parameters	Data sources	Scale/ Coverage of Investigation	Characteristics	Notes
Size (Width, length, radius, area) - Aperture and spacing	Seismic	Regional	Indicative of major faults and smaller fracture patterns	Larger scaled features only - No aperture
	Outcrop	Local and Regional	Surface measurements provide the spatial distribution and length	Most useful for aperture, spacing
	Conventional logs			
	Resistivity logs	Wellbore	Affected by fracture width and length	Qualitative only
	Unconventional logs			
	BHTV, FMS, FMI, video imaging, borehole camera, image logs	Wellbore	Visual image of individual fractures crossing boreholes. Showing aperture, spacing and size distribution within wellbore scale	Can not show actual fracture size, unless for very small ones
	Core	Local	Show fracture aperture, spacing, height, size of small cleats, general fracture size distribution	
	Well production testing	Wellbore	Pressure tests indicates fracture length, connectivity	Qualitative only

Table 2.3: Fracture size and corresponding field data sources: scales, response characteristics and usages.

2.4.3 Fracture Density

Fracture density can be calculated from results of fracture length (in 2D) and area (in 3D), according to **Eq. 2.1**. However, these maps interpret only medium- to big-scaled features, which do not represent all fractures in the regions. As a result, the computed density is not correct. Even though wellbore images and core are not able to yield fracture size, they represent the best sources for density determination (**Table 2.4**).

Fracture parameters	Data sources	Scale/ Coverage of Investigation	Characteristics	Notes
Fracture density	Seismic	Regional	Direct measurement of mapped fractures	Able to map only major fractures
	Outcrop	Local and Regional	Surface mapping reveal large to medium scaled fracture network	Not able to map all fractures
	Unconventional logs			
	BHTV, FMS, FMI, video imaging, borehole camera, image logs	Wellbore	Visual image of individual fractures crossing boreholes. Exact fracture density measured	Main data sources
	Core	Local	Direct measurement	
	Geological sources	Wellsite and regional	Bed thickness, lithology, curvature of various formations relates to the degree of fracture intensity	Qualitative only
	Well production testing	Wellbore	Flow tests relate fracture density	Qualitative only

Table 2.4: Fracture density with corresponding field data sources: scales, response characteristics and usages.

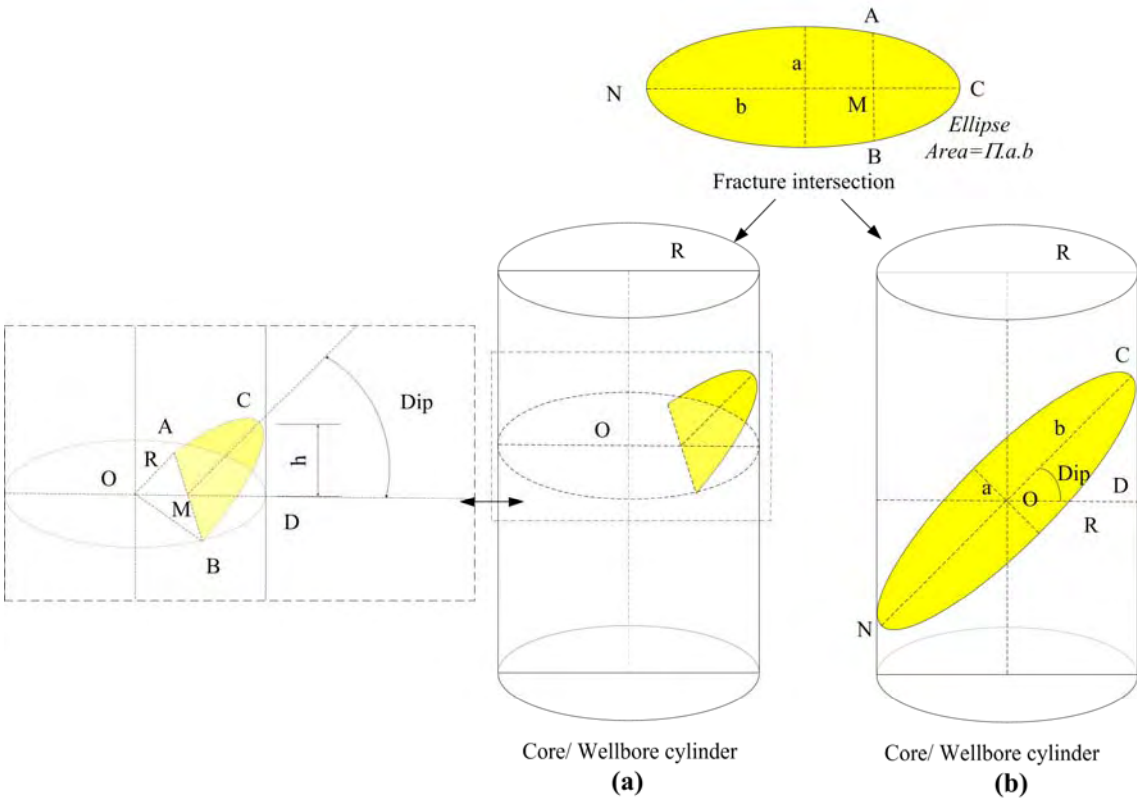


Fig. 2.14: Diagram to calculate fracture density of a fracture intersecting a wellbore.

Two cases of fracture intersections with a wellbore are illustrated in **Fig. 2.14**. Case (a) occurs when a discontinuous fracture fails to cut through the wellbore (i.e. partial intersection) and case (b) illustrates a full intersection. The data obtainable from wellbore images and core analyses are dip angle of the fracture plane ($Dip = \angle CMD$) and fracture height ($h = CD$). Radius of the investigating cylinder (R) is also available. In order to compute density, the intersecting area (shaded area) needs to be calculated.

As shown in **Fig. 2.14 (b)**, when a surface crosses a cylinder, the intersection is an ellipse. In that case, the fracture length satisfies **Eq. 2.3**:

$$h = 2 \cdot \frac{R}{\cos(\,Dip\,)} \tag{2.3}$$

For an ellipse with two radii a and b, its area is calculated as:

$$Area\ = \pi \cdot a \cdot b \tag{2.4}$$

$$Area = \pi \cdot R \cdot \frac{R}{\cos(Dip)} \tag{2.5}$$

For case (a) where only part of the ellipse is concerned, the measured fracture length is smaller than value in **Eq. 2.3**. Let angle $\beta = \angle CMD$ as in **Eq. 2.6**:

$$\beta = 2 \cdot \arccos\left[\frac{R - \dfrac{h}{\tan(\,Dip\,)}}{R}\right] \tag{2.6}$$

Area of the shaded ACB is determined as:

$$Area\,(ACB\,) = \frac{Area\,(ABD\,)}{\cos(\,Dip\,)} \tag{2.7}$$

$$Area(ACB) = \frac{Area(OABD) - Area(OAB)}{\cos(Dip)} \tag{2.8}$$

$$Area(ACB) = \frac{1}{\cos(Dip)}\left\{\frac{\pi \cdot R^2 \cdot \beta}{2 \cdot \pi} - \frac{1}{2} \cdot \left[R - \frac{h}{\tan(Dip)}\right] \cdot \left[2 \cdot R \cdot \sin(\frac{\beta}{2})\right]\right\} \tag{2.9}$$

$$Area(ACB) = \frac{R^2 \cdot \beta}{2 \cdot \cos(Dip)} - \frac{R^2 \cdot \sin(\frac{\beta}{2})}{\cos(Dip)} + \frac{h \cdot R \cdot \sin(\frac{\beta}{2})}{\sin(Dip)} \tag{2.10}$$

Fracture density value (*FracDen*) is the sum of all intersection areas per unit volume (cylinder volume of radius *R* and length of 1m).

$$FracDen = \frac{\sum Area}{\pi \cdot R^2 \cdot 1} \tag{2.11}$$

Local fracture density is an important property and will be extrapolated along the wellbores as well as for the whole reservoir (**Chapter 3: 3.4.4**).

2.4.4 Fracture Porosity and Permeability

Measurements of fracture porosity and permeability are only possible from wellbore-scaled sources, which can be evaluated in the same ways as matrix porosity and permeability. Conventional neutron density logs detect fracture secondary porosity and high permeability zone having movable fluids. Core samples give direct observations and measurements of the properties. In addition, well pressure and flow tests such as flow meters also reveal total (matrix and fracture) effective permeability.

Fracture parameters	Data sources	Scale/ Coverage of Investigation	Characteristics	Notes
Fracture porosity	Conventional logs			
	Neutron density log	Wellbore	Detect fracture secondary porosity	
	Sonic log	Wellbore	Detect fracture secondary porosity	
	Direct calculation from fracture dimensions			
Fracture permeability and connectivity	Seismic and Outcrop	Regional	Spatial distribution and interconnectivity of fractures	Qualitative only
	Conventional logs			
	Neutron density log	Wellbore	Detect high fracture permeability zone having movable fluids	No connectivity indication
	Core	Local	Direct measurement of permeability and degree of mineralization	No connectivity indication
	Well production testing: Flow and pressure tests	Inter-wells scale	Reveal fracture permeability, skin, connectivity and density	Large scale, overall effect

Table 2.5: Fracture porosity, permeability and connectivity with corresponding field data sources: scales, response characteristics and usages.

2.5 DATA SAMPLING ERRORS

Data sampling typically contains errors and biases. The problem becomes more serious when combining with complexity and high degree of heterogeneity of NFR. Even though reducing data sampling errors is out of the scope of this work, it is necessary to understand their causes.

All physical measurements contain uncertainty factors, which originate from equipments and human judgement. For example, orientation is misread from cores that are twisted on extraction; extents of interpreted fractures are wrongly defined from seismic maps that possess lots of noise. Apart from limits and uncertainties of the survey tools, there are two major uncertainties associated with data sampling process, namely observational bias and censoring.

Sampling observational biases occur in measurements of various fracture properties. For example, it is hard to measure orientation of fractures parallel to the sampling line or plane. The orientation bias is not easily corrected, as it is not possible to identify if the absence of those fractures is real or due to sampling bias (Terzaghi, 1965). In addition, due to truncation effect, a fault length tends to be underestimated. This observational bias happens more to smaller fractures (Clark et al., 1999).

Censoring or geometrical bias happens when the model boundary is confined and fractures continue beyond the study area. For example, fractures are censored due to observational scales, so that fracture size determination from outcrop and wellbore data is difficult and inaccurate. The bias tends to get more dramatic to longer fractures, which are usually more important fluid conduits. Discussions on ways to reduce biases in data collection and data analysis could be found in Long and Billaux (1987) and Clark et al. (1999).

2.6 CLOSURE

In this chapter, the first part of NFR characterisation has been reviewed. Responses of most popular reservoir data sources to natural fractures are studied and assessed. Evaluations of intermediate information on fracture orientation, size, density, porosity, permeability and connectivity from the reservoir data sources are then described. Discussions on some data sampling errors are also included, so that they could be taken into considerations in the modelling process.

There are many data sources for NFR characterisation. However, due to complex nature of the fracture systems, the fracture characterisation is extremely complicated. While one data source can describe different aspects of the fracture network, a fracture property can be detected by several sources. In addition, the data sources cover different scales, have different resolutions and different volumes of investigation. There are also uncertainties due to model, boundary conditions, geological representation, engineering performance predictions, statistics and spatial distribution (Einstein et al., 1980). Therefore, it is essential that a comprehensive NFR model is able to effectively combine data from as many tools as possible.

The next chapter will present different methods to analyse and integrate the intermediate fracture information. Determinations of statistics and behaviours of each fracture properties as well as their correlations will be discussed.

CHAPTER 3 - FRACTURE DATA ANALYSES

3.1 OVERVIEW

As a continuation of **Chapter 2**, this chapter discusses the second part of NFR characterisation. The intermediate fracture information is categorically analysed and integrated by statistical, geostatistical and spatial neural methods. The purposes are to determine representative statistics and behaviours of each fracture properties (e.g. location, orientation, size and density) as well as their correlations and spatial distributions. The results will be used as inputs in the modelling procedures of hybrid stochastic simulation (**Chapter 4**) and object-based conditional global optimisation (**Chapter 5**).

中间数据
即：位置、尺寸等

This chapter starts with statistical analysis of fracture orientation and size. Their probabilistic distributions could be in either parametric or non-parametric forms. Parametric considerations include circular multimodal dip and azimuth, and discrete multifractal radius. Next, fracture locations are examined, both statistically and by measurements of spatial randomness. In addition, correlations between orientation, size and the marked point spatial distribution are also studied. Spatial characterisation and integration are performed by geostatistical variograms and fuzzy neural analysis, whose descriptions constitute the last part of the chapter.

方位、尺寸的统计学分析
裂缝位置

3.2 STATISTICAL ANALYSES

Simple statistical analyses are first carried out, identifying statistical behaviours of the fracture location, orientation and size. Representative probability density functions are proposed, which are essential for various simulation programs, especially stochastic simulation.

A wide range of methods could be used for density estimations, e.g. histograms, kernel estimator, nearest neighbour method, maximum likelihood estimator and weight function estimator (Silverman, 1998). These methods are included in most statistical software packages (their detailed descriptions are out of the scope of this thesis). It is important to note that that the density estimation be a data-driven process (i.e. be determined by the actual data available, not be presumed).

In this section, the most common probability density functions for individual fracture geometric properties of orientation and size are described. Basic statistical measurements for each function and their determination from the intermediate data are also explained.

3.2.1 Circular Statistics for Fracture Orientation

As discussed in **Chapter 2**, fracture orientation data could be obtained from many sources, especially from wellbore images and core. Compared to other fracture properties, intermediate orientation data are usually abundant. Thus, reliable distributions can be targeted.

Fracture orientation is represented as a single value in 2D and as two components in 3D. In previous works, fracture orientation components of dip and azimuth were treated individually. In most cases, symmetrically unimodal distributions were used, e.g. uniform, normal or Von-Mises functions (Wen and Sinding-Larsen, 1996; Willis-Richards, 1996; Jensen et al., 1998; Anraku et al., 2000). In a limited number of other cases, investigators recognised fracture orientation having more than one mode (Lanyon

et al., 1993; Cacas et al., 1995; Parney et al., 2000; Tamagawa et al., 2002). However, such representations were simplistic, correlations between dip and azimuth components were not considered. Multimodal circular statistics are used in this work for better portrayal of fracture orientation.

3.2.1.1 Circular Data Presentation

In circular statistics, data are "wrapped" around a circle, resulting in different statistical distributions and measurements. Circular data range from zero to 360° (Fisher, 1993). Azimuth angle (*Azimuth*) runs half the circle (between zero and 180°). Dip angle (*Dip*) ranges between zero and 90° (**Chapter 2: 2.2.1**). They can be converted to circular azimuth ($Azimuth_c$) and circular dip (Dip_c) by simple linear transformations:

$$Azimuth_c = Azimuth * 2 \tag{3.1}$$

$$Dip_c = Dip * 4 \tag{3.2}$$

The use of circular data is important for accurate characterisation by avoiding observational bias. For example, two direction angles of 1° and 359° have mean value of zero (i.e. pointing north), not 180° (i.e. pointing south) as would be calculated in linear statistics. The statistical analysis is performed in two steps. First, probability density function of single orientation component is assessed. Next, correlations between dip and azimuth angles are evaluated.

首先确定倾角、方位角各自的概率密度函数；
然后，估计其相关性。

For circular data, there are two typical forms of histograms: linear and angular. Linear histogram is constructed as if the data were linear, not angular. Angular histogram is achieved by wrapping the linear histogram around a circle. Rose diagram is one typical kind of angular histogram. **Fig. 3.1** displays an example of rose diagram presentation of all orientation data measured in a well of the Palm Valley NFR.

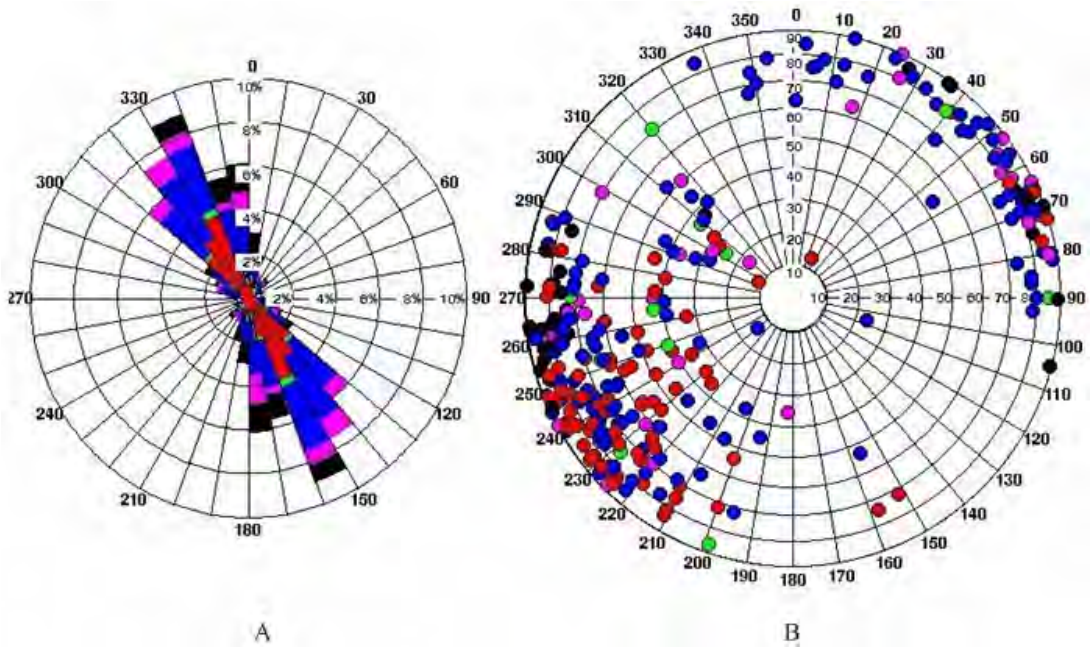


Fig. 3.1: Orientation data available from core analysis for a section of well F, Palm Valley NFR: In (B), dip and azimuth data are co-presented in the same chart (dip axially and azimuth circumferentially). In (A), rose diagram is displayed for the corresponding strike.

Once histograms have been constructed, probability density distributions are fitted. Orientation of fractures in a NFR could be fitted by different probability density functions, e.g. standard normal, uniform, lognormal, gamma distributions or functions in nonparametric forms.

3.2.1.2 Simple Circular Statistics

Linear mean and variance

Simple statistics include mean, variance and standard deviation of the dataset. If a unimodal distribution is assumed, they can be promptly obtained from the intermediate data. Parameters for many probability density functions can be estimated from the simple quantities [http://mathworld.wolfram.com].

Mean (μ), as first order moment, represents mathematical expectation of the N orientation values (θ_i). Variance (*Var*) is second order moment about the expectation mean.

$$\mu = \frac{1}{N} \cdot \sum_{i=1}^{N} \theta_i \tag{3.3}$$

$$Var = \frac{1}{N} \cdot \sum_{i=1}^{N} [\theta_i - \mu)]^2 \tag{3.4}$$

Circular trigonometric moments

To calculate circular statistics, the orientation is considered as N vectors (θ_i) (unit radian). The vectors are combined in the forms of secondary parameters (C_c, S_c and R_c). C_c and S_c equal to sum of cosine and sine of orientation values, respectively. R_c is length of the resultant vector:

$$C_c = \sum_{i=1}^{N} \cos(\theta_i) \tag{3.5}$$

$$S_c = \sum_{i=1}^{N} \sin(\theta_i) \tag{3.6}$$

$$R_c = \left(C^2 + S^2\right)^{0.5} \tag{3.7}$$

The secondary parameters are used to determine circular mean direction (μ_c), circular variance (Var_c) and circular standard deviation (σ_c)*:*

$$\mu_c = \begin{cases} \tan^{-1}(S_c / C_c) & S_c > 0, C_c > 0 \\ \tan^{-1}(S_c / C_c) + \pi & C_c < 0 \\ \tan^{-1}(S_c / C_c) + 2\pi & S_c < 0, C_c > 0 \end{cases} \tag{3.8}$$

$$Var_c = 1 - \frac{R_c}{N} \tag{3.9}$$

$$\sigma_c = \{-2 \cdot \log(1 - Var_c)\}^{0.5} = \{-2 \cdot \log R_c\}^{0.5} \tag{3.10}$$

3.2.1.3 Multimodal Wrapped Distribution

Generally, natural fractures tend to be distributed in more than one dominant direction, which correspond to field maximum and minimum stresses and tectonics history. Fracture orientation measurements are consequently expected to belong to multimodal distributions (e.g. **Fig. 4.11** and **Fig. 5.7**).

Multimodal distribution is a linear combination of unimodal ones. For example, if fracture orientation follows bimodal wrapped normal distribution, the data set is divided into two parts, with proportional factors p_c and (1-p_c). Two sets of means, resultant lengths and standard deviations of $(\mu_{c1}, R_{c1}, \sigma_{c1})$ and $(\mu_{c2}, R_{c2}, \sigma_{c2})$ can be subsequently calculated from **Eqs. 3.8**, **3.9** and **3.10**. The resultant distribution WN(θ) is linear combination of two wrapped normal distributions WN(μ_{c1},σ_{c1}) and WN(μ_{c2},σ_{c2}):

$$\mathrm{WN}(\theta) = p_c \cdot \mathrm{WN}(\mu_{c1}, \sigma_{c1}) + (1 - p_c) \cdot \mathrm{WN}(\mu_{c2}, \sigma_{c2}) \tag{3.11}$$

$$\mathrm{WN}(\mu_{ck}, \sigma_{ck}) = \frac{1}{2\pi}\left(1 + 2 \cdot \sum_{i=1}^{\infty} {R_{ck}}^{i^2} \cos\left[i\left(\theta_i - \mu_{ck}\right)\right]\right) \quad 0 \le \theta_i < 2\pi, 0 \le R_c \le 1, k = 1...2 \tag{3.12}$$

搞不懂啊！！！

The wrapped normal distribution WN(μ_c,σ_c) is obtained by wrapping the normal distribution N(μ_c,σ_c).around a circle of unit radius.

3.2.1.4 3D Circular Correlation

In 3D, orientation is spherical data. As displayed in Mardia (1986), there are different presentations of spherical data, which include use of polar coordinates, azimuthal projections or geological systems. In NFR, fractures tend to follow certain patterns, which are results of geological deformations. For example, many reservoirs contain systems of sub-vertical fractures, whose dip angles are around 90°. Thus, the geological system is applied, which defines spherical data as two circular quantities of dip and azimuth.

Assume that distributions of fracture dip and azimuth follow **Eq. 3.11**, where p_c, μ_{ci} and σ_{ci} correspond to proportional factor, circular mean and standard deviation, respectively.

$$Dip_c = p_{cD} \cdot \mathrm{WN}(\mu_{c1}, \sigma_{c1}) + (1 - p_{cD}) \cdot \mathrm{WN}(\mu_{c2}, \sigma_{c2}) \tag{3.13}$$

$$Azimuth_c = p_{cA} \cdot \mathrm{WN}(\mu_{c3}, \sigma_{c3}) + (1 - p_{cA}) \cdot \mathrm{WN}(\mu_{c4}, \sigma_{c4}) \tag{3.14}$$

Define correlation (Cor_{ij}) between two data sets (θ_i, θ_j) from covariance ($Cov_c(\theta_i, \theta_j)$) and standard deviations ($\sigma_c(\theta_i)$, $\sigma_c(\theta_j)$) of the two sets:

$$Cor_{ij} = \frac{Cov_c(\theta_i, \theta_j)}{\sigma_c(\theta_i) \cdot \sigma_c(\theta_j)} \tag{3.15}$$

$$Cov_c(\theta_i, \theta_j) = 0.5 \cdot \left[Var_c(\theta_i) + Var_c(\theta_j) - Var_c(\theta_i + \theta_j) \right] \tag{3.16}$$

Each variable is then controlled by a set of parameters:

$$Dip_c = (\mu_{c1}, \sigma_{c1}, \mu_{c2}, \sigma_{c2}, p_{cD}, Cor_{12}, Cor_{13}, Cor_{14}, Cor_{23}, Cor_{24}) \tag{3.17}$$

$$Azimuth_c = (\mu_{c3}, \sigma_{c3}, \mu_{c4}, \sigma_{c4}, p_{cA}, Cor_{34}, Cor_{13}, Cor_{14}, Cor_{23}, Cor_{24}) \tag{3.18}$$

3.2.2 Multifractal Geometry for Fracture Size

As mentioned in **Chapter 2**, there are not many data sources for fracture size (i.e. length, area and aperture). The lack of reliable field measurements makes it difficult to be analysed statistically. When data are sufficiently available, appropriate probability density functions can be fit. As can be seen in **Table 3.1**, fracture length and area could belong to any of such distributions as negative exponential, exponential, lognormal, fractal or power law. However, even in such cases, the properties have not demonstrated a consistent trend for similar results being interpreted in other general cases. Similar observations could be made for fracture spacing and aperture. When there is limited data, delineation of exact distribution as well as corresponding parameters is not practical. Then, fractal mathematics provides what could be the most effective tool for fracture size assessment. Heterogeneity of fracture size is further respected by considering multifractal.

Property	Distribution	Reference
Length or Area	Negative Exponential	Panek, 1985; Miller, 1993; Bloomfield, 1996
	Exponential	Rouleau and Gale, 1985
	Lognormal	Baecher et al., 1978; Rouleau and Gale, 1985; Jensen et al., 1989; Gale et al., 1991; Miller, 1993; Deng et al., 1995; Sahimi, 1995; Bloomfield, 1996; Gurpinar et al., 1999
	Fractal or Power Law	Gudmundsson, 1987; Heffer and Bevan, 1990; Herrmann, 1995; Willis-Richards, 1996; Jamison, 1997; Odling, 1997; Koike and Kaneko, 1999; Sahimi, 2000; Al Qassab et al., 2002; Tamagawa et al., 2002
Fracture Spacing	Negative Exponential	Rives et al., 1992; Gross and Engelder, 1995
	Exponential	Baecher et al., 1978
	Lognormal	Rouleau and Gale, 1985; Gale et al., 1991; Rives et al., 1992; Miller, 1993; Gross and Engelder, 1995; Bloomfield, 1996
	Fractal or Power Law	Barton and Zoback, 1992; Gross and Engelder, 1995
Fracture Aperture	Lognormal	Snow, 1970
	Power Law	Barton and Zoback, 1992; Gross and Engelder, 1995; Marrett and Peacock, 1997
	Estimated from Length	Willis-Richards, 1996; Mazureck et al., 1998; Hossain, 2001; Tamagawa et al., 2002

Table 3.1: Documented works on probability density distributions of fracture size

3.2.2.1 Fractal Geometry and Box-counting Method

Fractal geometry and fracture characterisation

Fractal is a fundamental concept in the field of theoretical geometry. It describes features that appear self-similar under varying degrees of magnification. The invariant self-similarity can be portrayed by a single quantity of fractal dimension (D) (Mandelbrot, 1983). According to fractal geometry concept, number of features (N_{Rad}) is

related to size (*Rad*) by fractal dimension (*D*) and a proportionality constant (*C*), as in **Eq. 3.19**. The relationship is also understood as power law or Pareto distribution.

$$N_{Rad} = \frac{C}{Rad^{D}} \tag{3.19}$$

Fractal geometry realises proper mathematical framework for characterising and simulating geometry of many complex non-Euclidean shapes found in nature. A wide range of examples includes clouds, mountains, coastlines, trees, distribution of mineral deposits, percolacous fingers and geological faults (Hewett, 1994).

In addition to quantifying objects that appear similar at different scales, fractal is especially suitable for discontinuous ones. Both aspects make it appealing in studying fractures. There have been numerous investigations on fractal characteristics of different fracture geometry, including trace length (Clark et al., 1999), aperture, spacing (Cox and Wang, 1993; Boadu and Long, 1994), clustering (Babadagli, 2001), surface roughness (Charkaluk et al., 1998), branching and propagation (Lei and Chen, 1995) and those listed in **Table 3.1**. Fractal assessments have also been verified over a wide range of scales from microfractures (Main et al., 1990) to multi-scaled fault systems in Japan (Hirata, 1989; Nanjo et al., 1998), Turkey (Babadagli, 2001) and the San Andreas Fault in USA (Scholz and Aviles, 1986). In general, length frequency distributions of the subsurface fracture networks have shown to have a power law trends across many orders of magnitude. Fractal-like concepts have also been applied to modelling of fluid flow through fractures (Barker, 1988; Hewett, 1994).

To depict fracture patterns of underground rock, fractal dimension as in **Eq. 3.19** is used. N_{Rad} is number of fractures, whose radii greater than a radius value (*Rad*). The fractal dimension is a function of strength, tectonic history and lithology of the fractured rock mass (Boadu and Long, 1994). It is usually non-integer and greater than topological dimension (D_T) and less than Euclidean dimension (D_E):

$$D_T = 1.0 < D < 2.0 = D_E \leftarrow 2D \tag{3.20}$$

$$D_T = 2.0 < D < 3.0 = D_E \leftarrow 3D \tag{3.21}$$

Box-counting method

There are many methods that can be used for fractal dimension determination, e.g. area perimeter, box-counting, divider relation, Kocak's law, power spectrum and variogram (Klinkenberg, 1994). Among them, box-counting is the most popular method for fracture traces on a map. It can be applied on fracture traces from cores, wellbore images, outcrops and seismic maps.

Procedure for the box-counting method is examined for 2D fracture traces. 3D analysis can be performed in an entirely analogous manner. A fracture system is enclosed by a square region with a side length (L_o) (**Fig. 3.2**). The region is then divided into L_0^2 / l^2 boxes of side length l. Let $N(l)$ be the number of boxes that intersect or contain fractures. From **Eq. 3.19**, $N(l)$ can be expressed as:

$$N(l) = \frac{C}{l^D} \tag{3.22}$$

Where D corresponds to the fractal dimension and C is proportionality constant. By plotting on logarithmic scales $N(l)$ against $1/l$ for the sample data, fractal dimension (D) can be estimated as slope of the resulting line (**Fig. 3.3**).

In general, fractal dimension is a single quantity to represent self-similarity. As shown through many research works, it is vastly suitable for natural complexity such as fractures. Value of fractal dimension can be easily evaluated by the graphical box-counting analysis on core, wellbore images, outcrop and seismic data.

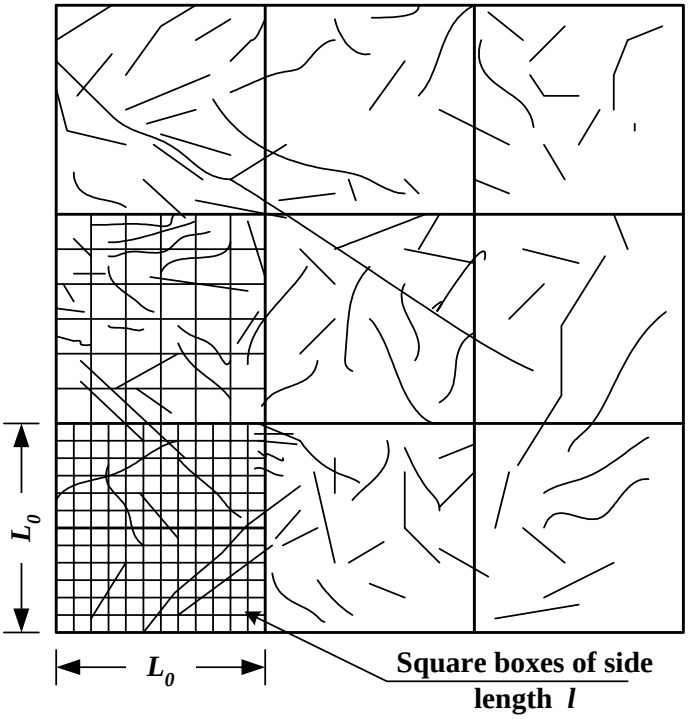


Fig. 3.2: Box-counting method for a natural fracture system.

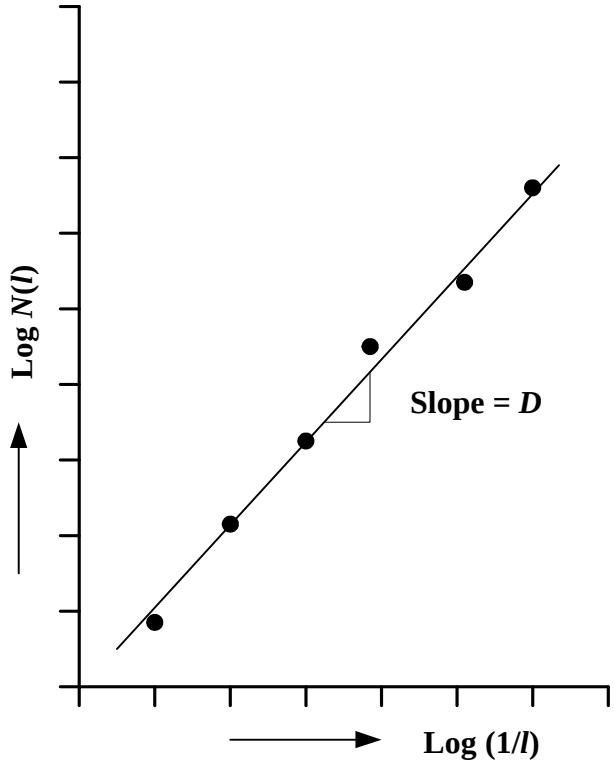


Fig. 3.3: Typical logarithmic plots for estimation of fractal dimension (D) using box-counting method.

3.2.2.2 Multi-scaled Multifractal

分数维随着盒子的尺寸变化。单一分数维是不合适的。采用多级分形。

Although a large number of investigations validated fractal characteristics of a DFN, many others disagreed (Walsh and Watterson, 1993; Berkowitz and Hadad, 1997; Stach et al., 2001; Wilson, 2001). Several investigators used the box-counting method to realise that fractal property of a DFN is scale-variant (Castaing et al., 1997; Belfield, 1998; Xie et al., 1999). Fractal dimension was calculated to vary with box size. The plotted line was not straight, contradicting power law relationship. Thus, single fractal dimension is not always sufficient to explain natural fractures over a significant range of scales. The fracture data have been argued to actually possess multifractal characteristics.

既有微尺度，又有油藏尺度，存在几个自相似范围。

A fractal object has a lower and upper length limits (Takayasu, 1990). Self-similarity, scale-invariance and therefore fractal dimension can only be observed within the limited scales. For complicated network of micro-scaled and regional-scaled fractures, there exist several self-similarity ranges. Due to the irregularities, multifractal analysis is essential.

一系列不同的分数维解决自相似不同范围。

In broad terms, objects with more than one fractal dimensions are multifractal. In other words, multifractal objects contain a union of subsets, with separate scaling exponents. There are two approaches for extension from single fractal to multifractal. One is to introduce new parameters to account for spatial intertwines of fractal dimensions. Fractal dimension is generalised by continuous fractal spectrum. Most of existing multifractal models employ this approach. The other approach uses discrete multifractal, where a set of different fractal dimensions (i.e. discrete fractal spectrum) account for all ranges of self-similarity (Cheng, 1997).

Continuous multifractal spectrum

Application of multifractal analysis is examined on a DFN, similar to one in **Fig. 3.2**. The network is divided into boxes with linear size (l) and $N(l)$ is the number of boxes that intersect or contain fractures. Values of fractal dimensions, as derived from **Eq. 3.22**:

$$\alpha = D(l) = -\frac{\log N(l)}{\log l} \tag{3.23}$$

where α is called the coarse Holder exponent (Evertsz and Mandelbrot, 1992). Define $N(l,\alpha)$ as the number of boxes of size (l) having coarse Holder exponent (α). The probability of a cell corresponding to value α is:

$$P(l,\alpha) = C \cdot N(l,\alpha) \cdot l^2 \tag{3.24}$$

where C is a constant. By considering the limit $l \rightarrow 0$, the continuous fractal dimension ($f(\alpha)$) (Evertsz and Mandelbrot, 1992) and co-dimension ($c(\alpha)$) spectra (Cheng and Agterberg, 1996) are defined as:

$$f(\alpha) = \lim_{l \to 0}\left[-\frac{\log N(l,\alpha)}{\log l}\right] \tag{3.25}$$

$$c(\alpha) = \lim_{l \to 0}\left[\frac{\log P(l,\alpha)}{\log l}\right] \tag{3.26}$$

Multifractal can be represented by either of the two. In case of mono fractal, the limit $f(\alpha)$ converges to the single fractal dimension value. The continuous multifractal can be evaluated using the box-counting procedure and **Eqs. 3.25** and **3.26**.

Discrete multifractal

Alternatively, the discrete multifractal model is used. Discrete values of the coarse Holder exponent (α_k) ($k = 1,\ldots, m$) corresponds to m discrete values of $f(\alpha_k)$:

$$f(\alpha_k) = \lim_{l \to 0}\left[-\frac{\log N(l,\alpha_k)}{\log l}\right], \quad k = 1,...,m \tag{3.27}$$

Discrete multifractal values can be calculated based on the moment method as in Cheng (1997). According to the author, discrete multifractal exists and can be used in many fields of science.

3.2.2.3 Discrete Multifractal Application in Fracture Characterisation

It could be observed that multifractal analysis is desired for DFN characterisation. When there are sufficient representative data, both continuous multifractal dimension function and discrete multifractal values can be accurately determined, based on methods described above. However, it is usually not the case. Limited data include a few major faults from seismic maps, local 2D network map from outcrops and small-scaled fractures from cores and wellbore images. Thus, even though it is likely that multifractal exists, its characterisation is difficult.

数据量很少。
虽然存在多级分形
但确定是很困难的。

In this work, discrete multifractals are used to study fracture spatial distribution, and especially to characterise fracture size. Their determination is made possible from combination of the usual box-counting method and fuzzy neural network (FNN). First, discrete fractal dimensions are calculated at different ranges of available data. Graphical box-counting method is routinely applied. Then, a FNN integrates other data sources to predict values of fractal dimensions at all scales and locations. This procedure is not analogous to conventional interpolation and extrapolation method as kriging. When predicting dimension value for a point (region) in the field, the result depends on not only geographical locations but also geological, lithological, seismic and/or well log responses. Due to the lack of representative data, a great deal of predictive modelling is involved. As a result, despite popularity of continuous multifractal, discrete multifractal is believed to be more suitable for fracture characterisation and modelling. Application of the procedure on actual field data will be illustrated in the next **Chapter 4**.

首先，利用已知数据计算不同范围的分数维；
然后，利用神经网络结合其他数据源预测所有尺度、所有位置上的分数维。

Use of discrete multifractal and integration of FNN in characterising NFR denote a number of important advantages. First, multifractal is a powerful tool that has been used in various fields of science for self-similarity characterisation. It can distinguish patterns in the spatial distribution of geological features (Cheng, 1997). Second, as argued for fractal geometry, multifractal is also especially suitable for natural fractures.

By using multifractal to represent the fracture length distribution, inconsistent and inaccurate probability density functions can be avoided. Thus, it is a great deal more suitable, representative, informative and flexible for fracture size characterisation. Besides, together with fracture density, multifractal signifies relationships between the number of fractures, their size and spatial distribution. Third, FNN allows consistent computation of discrete multifractal dimensions over the whole reservoir. Finally, as will be mentioned in **Chapter 4** (**4.3.3.2**), the mapped discrete multifractal can be easily applied in the modelling procedure.

3.3 SPATIAL ANALYSES USING GEOSTATISTICS

In the previous section, statistical behaviours of fracture orientation and size have been investigated. Even though correlations between orientation angles of dip and azimuth have been considered, orientation and size were examined individually. This section studies the patterns at which fractures are spatially distributed. It also analyses associations between fracture orientation and size and how they vary in space. The geostatistical and spatial analyses are based on the observations and assumptions that regionalised variables vary according to a particular structure. Autocorrelation exists between two values at two locations (Deutsch and Journel, 1992).

3.3.1 Fracture Location Distribution

原来裂缝位置分布是均匀分布。但只有数据点符合完全空间随机分布时，均匀分布才适用。

In previous works, fracture (location) distribution was simulated deterministically or by using simple uniform distribution (Willis-Richards, 1996; Anraku et al., 2000; Parney et al., 2000; Al Qassab et al., 2002). However, as mentioned earlier, the use of any statistical distributions should be data-driven. 何意？ Uniform distribution would only be justified if the data points satisfy complete spatial randomness.

In this work, spatial points are first observed for any systematic patterns: clustering, regularity or complete randomness. As defined by Diggle (1983), complete

spatial randomness (CSR) refers to events that follow homogeneous Poisson process. It obeys the following criteria:

- Intensity of the point pattern does not vary over the bounded region,
- There are no interactions (e.g. inhibition or encouragement) among the points.

需要对裂缝空间分布模式进行检测。分析可参见附录B。具体操作可见第五章。

A mixture of measurements is required for testing spatial patterns, including simple statistics of coordinates of fracture location, intensity map, nearest neighbour methods and K-function tests. Together, they take care of variations in intensity, spatial interactions and phenomena exhibiting first and second order effects. The analyses are described in **Appendix B**, with reference to Cressie (1991) and Bailey and Gatrell (1995). Applications on actual fracture systems are illustrated in **Chapter 5** (**5.4.2.1**).

3.3.2 Geostatistical Analyses

本文采用了一些地质统计学工具进行描述，如变差函数、协方差、等。
地质统计学测量不仅可以描述裂缝位置的空间点分布模式，而且可以描述方位、尺寸的空间分布。
地质统计学分析的结果将会被用于DFN模型的生成。

其中最重要的问题是这些统计结果如何应用于模型的生成。

In addition to quantitative measurements of CSR, this work employs several geostatistical tools such as variogram, covariance, correlogram and madogram. As discussed earlier, NFR are extremely heterogeneous. Individual fractures of different properties play different roles in geometry of the whole system. The geostatistical measurements can portray not only spatial point patterns of fracture locations, but also distributions in space of fracture properties such as orientation and size. In addition, interactions between different properties can be assessed. Results of the geostatistical analysis will be combined with other fracture characteristics to generate a representative DFN model (**Chapter 5: 5.4.2.1**).

3.3.2.1 Variograms 变差函数

Variogram, an intrinsic stationary process, is used for visualising, modelling and exploiting spatial continuity and spatial variability of regionalised variables (Cressie, 1991). Variogram is also a generalised variable characterised by both generalisation and randomness. It is used widely in geostatistical modelling, especially in spatial distribution modelling (Deutsch and Cockerham, 1994). An experimental semi-variogram ($\gamma(h)$) describes how a property (z) (either orientation or size) varies in space as a function of lag distance between two measuring locations (x_i) and $(x_i + h)$, as:

$$\gamma(h) = \frac{1}{2N(h)} \cdot \sum_{i=1}^{N(h)} \left[z(x_i + h) - z(x_i) \right]^2 \tag{3.28}$$

where *N(h)* is total number of data pairs separated by separation vector (*h*). The separation vector is conventionally defined to connect the two locations *(x_i)* (tail) and *(x_i + h)* (head) (**Fig. 3.4**). Thus, experimental variogram vector *γ(h)* provides quantitative measurements for spatial variability. It takes into consideration absolute values of fracture property (*z*) and separation vector (*h*), measuring the difference on average as separation distance increases along a given direction. In general, separation vector is specified with some direction and lag distance tolerance.

A cross-variogram ($\gamma c_{12}(h)$) represents variogram between two different variables ($z_1(x_i)$) and ($z_2(x_i)$), as in **Eq. 3.29**. It measures cross variability between fracture orientation and size through $z_1(x_i)$ and $z_2(x_i)$.

$$\gamma c_{12}(h) = \frac{1}{2N(h)} \cdot \sum_{i=1}^{N(h)} \left[z_1(x_i + h) - z_1(x_i) \right] \cdot \left[z_2(x_i + h) - z_2(x_i) \right] \tag{3.29}$$

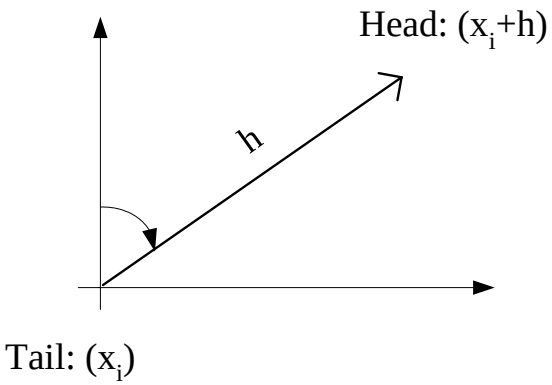


Fig. 3.4: Naming convention for separation vector (*h*), whose tail and head are at measuring locations *(x_i)* and *(x_i + h)*, respectively.

Depending on direction of the separation vector (*h*), there are directional and omni-directional variograms. The former is calculated when data are correlated along a preferential direction. When there is no dramatic anisotropy, the later is considered.

Omni-directional variograms are the average of all directional variograms. In practice, they are set by a large angle tolerance of 90°.

In many conventional geostatistical applications such as kriging and stochastic modelling, experimental variograms were not directly utilised. They needed to be fitted to theoretical variogram models. Details of the process and its applications are discussed in Cressie (1991), which are out of scope of this work. However, the fitting process is usually erroneous and biased. Besides, not all systems can be fitted. It depends on distribution of the experimental variograms and geological knowledge. Therefore, in this work, experimental variograms are desired while variogram models are avoided.

采用实验变差函数而未采用变差函数模型。

问题是：
如何将变差函数应用进来？？

3.3.2.2 Other Geostatistical Measurements

Covariance is a commonly used statistical measurement. Experimental covariance (*Cov(h)*) and cross covariance (*Covc*$_{12}$*(h)*) are calculated as:

$$Cov(h) = \frac{1}{N(h)} \cdot \sum_{i=1}^{N(h)} z(x_i) \cdot z(x_i + h) - \mu(z)_{-h} \cdot \mu(z)_{+h} \tag{3.30}$$

$$Covc_{12}(h) = \frac{1}{N(h)} \cdot \sum_{i=1}^{N(h)} z_1(x_i) \cdot z_2(x_i + h) - \mu(z_1)_{-h} \cdot \mu(z_2)_{+h} \tag{3.31}$$

where $\mu(z)_{-h}$ and $\mu(z)_{+h}$ stand for means of the tail and head values, respectively:

$$\mu(z)_{-h} = \frac{1}{N(h)} \cdot \sum_{i=1}^{N(h)} z(x_i) \tag{3.32}$$

$$\mu(z)_{+h} = \frac{1}{N(h)} \cdot \sum_{i=1}^{N(h)} z(x_i + h) \tag{3.33}$$

Correlogram ($\rho(h)$) is obtained by standardised covariance over tail and head standard deviations ($\sigma(z)_{-h}$) and ($\sigma(z)_{+h}$). With zero separation vector (h), cross-correlogram ($\rho c_{12}(h)$) is reduced to correlation coefficient between the two properties:

$$\rho(h) = \frac{C(h)}{\sigma(z)_{-h} \cdot \sigma(z)_{+h}} \tag{3.34}$$

$$\rho c_{12}(h) = \frac{Cc(h)}{\sigma(z_1)_{-h} \cdot \sigma(z_2)_{+h}} \tag{3.35}$$

$$\sigma(z)_{-h} = \frac{1}{N(h)} \cdot \sum_{i=1}^{N(h)} z^2(x_i) - \mu(z)_{-h}^2 \tag{3.36}$$

$$\sigma(z)_{+h} = \frac{1}{N(h)} \cdot \sum_{i=1}^{N(h)} z^2(x_i + h) - \mu(z)_{+h}^2 \tag{3.37}$$

Madogram takes similar form as the traditional variogram (**Eqs. 3.28** and **3.29**), with absolute difference between the data pairs ($z(x_i)$) and ($z(x_i+h)$) instead of squared difference. Madogram ($M(h)$) and cross-madogram ($Mc_{12}(h)$) are valuable measurements for large-scaled structures.

$$M(h) = \frac{1}{2N(h)} \cdot \sum_{i=1}^{N(h)} \left| z(x_i) - z(x_i + h) \right| \tag{3.38}$$

$$Mc_{12}(h) = \frac{1}{2N(h)} \cdot \sum_{i=1}^{N(h)} \sqrt{\left| z_1(x_i) - z_1(x_i + h) \right|} \cdot \sqrt{\left| z_2(x_i) - z_2(x_i + h) \right|} \tag{3.39}$$

In this work, a modified multi-histogram is also employed. It originates from histogram and variogram measurements. Instead of counting the frequency of a variable (z) within an equally divided interval, the concept of separation vector (h) as in variogram is used. Multi-histogram mean vector ($Hm(h)$) is defined as mean values of data pairs that are separated by h, as in **Eq. 3.40**. Multi-histogram mean is a first order spatial statistic.

$$Hm(h) = \frac{1}{N(h)} \cdot \sum_{i=1}^{N(h)} \left[z(x_i) \right] \tag{3.40}$$

The total distance of the same data pairs are averaged to form the variogram distance vector ($VarDist(h)$), as:

$$VarDist\ (h) = \frac{1}{N(h)} \cdot \sum_{i=1}^{N(h)} h \tag{3.41}$$

3.3.3 Fracture Density Distribution

Density is defined as mean fracture area per unit volume (in 3D) or fracture length per unit area (in 2D) (**Section 2.2.3**). It is one of the most important fracture characteristics, being directly proportional to the total number of fractures, their relative

size and distribution. It is an improved version of intensity, which refers to mean number of fractures per unit volume. Density takes into account the different roles that big and small fractures have. Fracture density map quantifies degree of fracture clustering and represents true measurement on spatial point pattern (random, regular, clustered or mixed).

Due to its importance, both characterisation and simulation of fracture density are desired in NFR modelling. Nevertheless, previous works did not present these steps satisfactorily. Firstly, most works involved only fracture intensity, whose map can reveals just certain patterns of centre points (Tamagawa et al., 2002; Escuder Viruete et al., 2003). Secondly, the characterisations employed simple methods such as least squared errors, kernel and kriging. The predictions of density or intensity values from well data over the field were made by pure mathematical estimations (Long et al., 1992; Pistre et al., 1995). They could be greatly improved by incorporating variations in physical conditions such as rock strength and lithological contents. Finally, despite the need to develop fracture density and intensity maps into DFN, grid-based models stopped at output fracture intensity maps (Ouenes, 2000; Boerner et al., 2003). On the other hand, due to mathematical intricacy, most of discrete models neglected density or intensity distribution data.

二、对于裂缝密度/强度的预测方法过于简单只是采用克里金等常规方法，应该结合岩性变化。

In this work, fracture density values are first calculated directly from fracture data at wellbores. Two of the most consistent data sources are wellbore images and core (**Chapter 2**). Density map of the field is then developed by applying a FNN. Neural network is one of the most complicated and accurate data regression tools, whose theory and advantages are described below. The resulting fracture density map is expected to be more reliable compared to results of previous methods. Moreover, simulation of fracture density plays a significant part in developing DFN. As will be shown in **Chapters 4** and **5**, density map is one of several important fracture characteristics that are utilised in both stochastic simulation and global optimisation schemes.

本文首先计算井点的裂缝密度，然后利用神经网络，预测井间。利用神经网络预测比前面的方法要好。
此外，裂缝密度的模拟也很重要。裂缝密度图无论在全局优化还是随机模拟中，都十分重要。参见4、5章。

一个很重要的问题是：如何在建模和全局优化中使用裂缝密度/强度？

3.4 SPATIAL ANALYSES USING FUZZY NEURAL NETWORK

It has been presented in **Chapter 2** that a variety of fracture information could only be measured for limited sections at well locations. However, for a thorough network model, it is necessary to generalise statistics and behaviours of fractures for the whole reservoirs. Examples of such properties include fracture density (for fracture spatial distribution) and fractal dimension (for discrete multifractal).

In most of previous works (e.g. Long et al., 1992; Pistre et al., 1995; Li et al., 1997; Doughty and Karasaki, 2000), the task has been performed by regression using simple least squared errors, kriging and geostatistical variogram. Nevertheless, the tools are simplistic and linear. They can usually handle at most one secondary data and require assumptions of intrinsic stationarity. In addition, the approximation is done pure mathematically, where geological and physical knowledge is not taken into consideration. This is only suitable for homogeneous system. For heterogeneous NFR, where interrelationships of data sources and their relevancies on fracture characterisation are very complicated, a more sophisticated scheme is desired.

首先，在井点处，利用岩心分析或者成像测井计算裂缝密度和分数维。对于没有取心的井段，利用模糊神经网络，结合测井曲线，计算其裂缝密度和分数维。然后，井间仍然利用模糊神经网络，结合井间地震数据，预测井间的裂缝密度和分数维。

To overcome the problems, a fuzzy neural network (FNN) is incorporated to integrate the multi-scaled data and to characterise complex relationships that might exist between them and the fracture properties. First, wellbore data such as core samples and images are used to calculate density and fractal dimension values at well locations. However, the data are scarcely available and irregularly distributed. FNN is required to combine these secondary measurements with well logs, predicting values in un-sampled intervals (2D along wellbores where core and images are not available). Then, a second FNN simulation generalises and approximates fracture density and fractal dimension for the 3D reservoir. At this stage, instead of well logs, the FNN takes advantages of seismic and other geological surveys that denote physical environment of the inter-well region. This section outlines theoretical background and practical application of the artificial intelligence tool in NFR characterisation.

3.4.1 Artificial Neural Network

Artificial neural networks (ANN) are computational systems that attempt to mimic the biological neural networks of the mammalian brain. They use a set of processing elements (or nodes) that are similar to brain neurons. These nodes are interconnected in a network that can then identify complex behaviours in the input data (Kosko, 1992; Smith, 1993; Gallant, 1994; Kacewicz, 1994). A major application of ANN is function approximation. For a given set of data samples, ANN can be used to study complicated and nonlinear mathematical patterns. The resulting relationships can be used for prediction, regression and classification. ANN have previously been used in a wide range of geological applications, e.g. well test analysis (Al-Kaabi and Lee, 1990), seismic processing (Boadu, 1997b), log interpretation (Wong and Shibli, 1998; Wong, 1999), lithofacies modelling (Tamhane et al., 2002), porosity and permeability modelling (Wong et al., 1998; Wang et al., 1999).

3.4.1.1 Back-Propagation Neural Network with Multiple-Layered Perceptrons

Back-propagation neural network (BPNN) is a supervised learning technique, which can learn almost any function regardless of data noise or complexity of their relationships. For supervised training, a large set of known input-output data patterns (i.e. training patterns) is required. After successful training, from a set of input data alone, the BPNN can compute a set of output values that approximate the desired result.

The BPNN also contains multiple layer perceptrons (MLP): one input layer, one output layer and at least one hidden layer (**Fig. 3.5**). In this work, the nodes in input layer represent field data types (e.g. different log responses, different seismic attributes) and two nodes in output layer correspond to fracture density and fractal dimension values. The input data are combined with a set of weighting factors. Each input node is attached with all hidden nodes by simple weighted links. Then, each output node receives similar weighted signals from all hidden nodes. This design is very efficient for highly nonlinear problems.

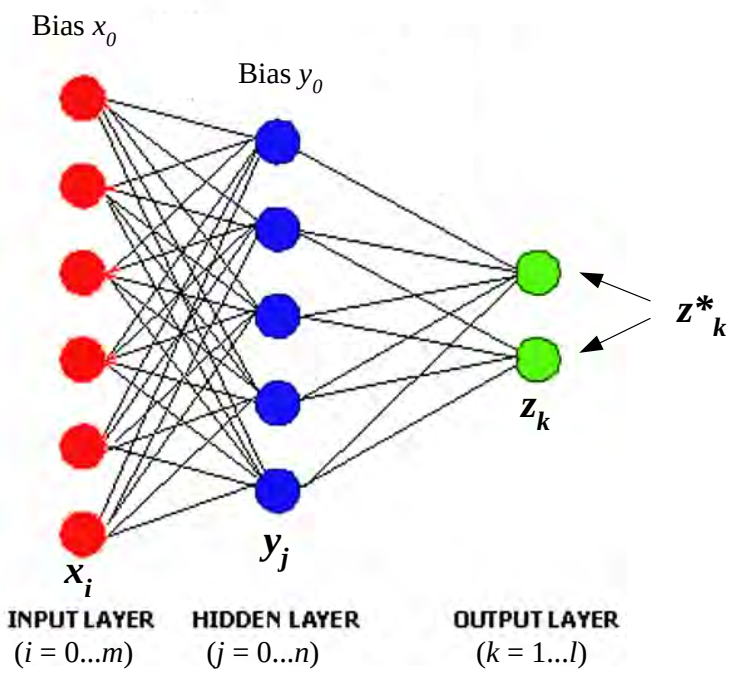


Fig. 3.5: Three layer BPNN with *n*-hidden neurons used in this study.

3.4.1.2 Learning Algorithm

The BPNN learns through an iterative procedure. The aim of the training process is to continually adjust the weighting factors so that errors in the outputs are minimised (i.e. better fit the model). Assume a set of normalised input data (x_i), which are converted at the hidden layer by the weighting factors (w_{ij}) (i.e. from input (i) to hidden node (j)), as

$$y_j = \sum_{i=1}^{m} w_{ij} \cdot x_i + w_{0j} \qquad j = 1..n \tag{3.42}$$

where m is total input nodes and n is the total hidden nodes. w_{0j} indicates all possible biases for hidden node (j), which can be omitted from the equation by introducing an extra input variable (x_0, $x_0 = 1$):

$$y_j = \sum_{i=0}^{m} w_{ij} \cdot x_i \qquad j = 1..n \tag{3.43}$$

Similarly, the output signals (z_k) are mathematically represented as:

$$z_k = \sum_{j=0}^{n} w_{jk} \cdot y_j = \sum_{j=0}^{n} w_{jk} \cdot f(\sum_{i=0}^{m} w_{ij} \cdot x_i) \quad k = 1..l \tag{3.44}$$

where l is total output nodes and w_{jk} are weighting factors from hidden node (j) to output (k). f is an activation function that is obtained by transforming the linear sum in **Eq. 3.43**.

The output signals (z) are then compared with the training data (z*) to formulate the quadratic energy (error) function (E):

$$E = \frac{1}{2N} \sum_{p=1}^{N} \sum_{ki=0}^{l} (z_{pk}^{*} - z_{pk})^2 \tag{3.45}$$

where N is the total training data available. The energy function (E) are used to update weighting factors from w to w':

$$w' = w - \alpha_1 \cdot \left.\frac{\partial E}{\partial w}\right|_{w} - \alpha_2 \cdot \left.\frac{\partial E}{\partial w}\right|_{w'} \tag{3.46}$$

where α_1 is a small positive learning rate parameter that determines step size in gradient descent. α_2 is a momentum constant that decreases sudden gradient changes, stabilising the learning procedure. The two parameters are bounded by [0, 1].

Iterations are repeated until the energy function or error is less than a tolerance value. There are also limits for the minimum magnitude of gradient and maximum number of allowable epochs (i.e. iterations). Then, the BPNN has been trained; the final weights from the learning process are used for prediction purposes.

3.4.1.3 Practical Considerations

In essence, a BPNN is a combination of neural architecture and an optimisation algorithm. Like many other optimisation programs (as will be discussed in **Chapter 5**),

it requires trials and errors to optimise the network configuration (e.g. number of hidden nodes, learning speed and momentum constant). This is done by dividing the data set into two parts with similar characteristics: training set and validation set, for example, using data from some wells for training and the rest for validation (Wong and Shibli, 1998). The validation set is used to limit over-fitting of the training data (i.e. overtraining). Overtraining happens after too many epochs, the training patterns are memorised, rather than generalised.

ANN is a powerful tool and yet simple to implement for function approximation. It studies and generalises a variety of relationships embedded in the training data set, which could be highly sophisticated. Their strength is that rather than starting from some theoretical or empirical relationship, they are data-driven. This limits biases by preconceived concepts or assumptions. Instead, on being presented with data, ANN begins to recognise patterns and develops its own generalisation.

It is important to note that ANN simulation only works if there exist relationships between the input and output parameters. For example, when applying ANN along the wellbores, logs (inputs) need to have some certain relations to the fracture properties (outputs) to be used. In other words, geological and physical knowledge is necessary for the initial screening. Fuzzy logic is one competent tool to recognise and ranked the importance of input parameters. As a result, approximations that are more reliable can be obtained.

3.4.2 Fuzzy Logic

There are many uncertainties and ambiguities in reservoir characterisation and in numerical optimisation processes. Probability is one way of handling the uncertainties. Fuzzy logic or fuzzy reasoning is a more modern tool, integrating linguistic or descriptive rules (Cressie, 1991). It is very suitable for estimating reservoir properties from indirect data sets such as well logs and seismic (Wong, 1999; Tamhane et al., 2002).

Fuzzy logic was first introduced by Zadeh (1965). As the name suggested, it deals with the concept of partiality. Fuzziness or vagueness refers to not only crisp definition of conventional Boolean logic (e.g. true or false) but also continuous form of anything in between (i.e. partially true and partially false). The partial membership behaviour can be characterised deterministically and mathematically by fuzzy sets (or fuzzy membership functions) and a set of fuzzy "if-then" rules (or fuzzy rules). In other words, descriptive uncertainties can be quantified. Complete theoretical descriptions of fuzzy logic (fuzzy sets, memberships and rules) can be found in Kosko (1992). A brief background is summarised herein:

Fuzzy membership ($\mu_{\tilde{A}}(x)$) (or partial or non membership) of an element (x) ranges continuously from zero to one. The fuzzy set ($\tilde{A}$) is defined based on the membership function ($\mu_{\tilde{A}}(x)$), as:

$$\tilde{A} \equiv \left\{\left(x, \mu_{\tilde{A}}(x)\right) : x \in \Re^d\right\} \tag{3.47}$$

$$0 \le \mu_{\tilde{A}}(x) \le 1 \tag{3.48}$$

where $\Re^d$ denotes a space of multiple dimensions (d).

Fuzzy sets are analogous with the usual crisp sets, except that membership is either zero or one in the latter. Fuzzy sets also have similar properties, such as union, intersection and complement (Cressie, 1991), as:

$$\tilde{A}_1 \cup \tilde{A}_2 \equiv \left\{\left(x, \max(\mu_1(x), \mu_2(x))\right) : x \in \Re^d\right\} \tag{3.49}$$

$$\tilde{A}_1 \cap \tilde{A}_2 \equiv \left\{\left(x, \min(\mu_1(x), \mu_2(x))\right) : x \in \Re^d\right\} \tag{3.50}$$

$$\tilde{A}_1^c \equiv \left\{\left(x, 1 - \mu_1(x)\right) : x \in \Re^d\right\} \tag{3.51}$$

Fuzzy reasoning is an inference procedure that combines fuzzy “if-then” rules and known facts to derive some conclusions. Antecedent of the “if-then” rules (e.g. "if x is $\tilde{A}$") can be expressed quantitatively by a fuzzy set ($\tilde{A}$) of quantitatively scaling attributes or linguistic terms (e.g. "low, medium, high" or "1, 2, 3, … 10"). It is important for an application of fuzzy logic to acquire the proper fuzzy rules (Ouenes, 2000). ANN models are among the various methods available in literature (Kosko, 1992; Jang et al.,

1997; Huang et al., 1999; Ouenes, 2000; Nikov and Stoeva, 2001). It is especially suitable for applications in petroleum reservoirs (NFR in particular), where large amounts of vastly different data samples are present.

3.4.3 Fuzzy Reasoning by Neural Network

In this thesis, fuzzy logic is incorporated with ANN for the purposes of data classification and input ranking. First, many petroleum reservoir data (e.g. lithology, lithofacies, sedimentary facies and fracture connectivity) are descriptive. For example, lithology is described as sandstone and/or shale. These properties can be quantified by fuzzy sets and rules. Second, while all the learning data of quantitative inputs (e.g. seismic and quantified lithology index) and outputs (fracture density and fractal dimension) are set and the neural analysis is performed, fuzzy logic determines which of the input data have actual impacts on the outputs. This process concentrates the ANN on inputs that are more important to improve the overall performance.

3.4.3.1 Data Classification

In the first step, descriptive data such as lithology and other linguistic indicators are quantified into indexes. The fuzzy logic allows each data value (e.g. lithology) to belong to more than one class (e.g. sandstone, shale) with different degrees of membership (ranging from zero to one). That mean a sample is not restricted to be either sandstone or shale. It can be partially sandstone, partially shale and partially others. Linguistic observations and descriptions of lithology are converted into quantitative lithological index, which can now be input as components (inputs or outputs) for the neural learning.

For m descriptive data types, each having n fuzzy scaling terms or classes, the fuzzy set ($\tilde{A}_n$) of membership functions ($\mu_m(x)$) is defined as:

$$\tilde{A}_n \equiv \{(x_i, \mu_{\mathrm{m}}(x_i))\}, \quad i = 1...N, \quad 0 \le \mu_{\mathrm{m}}(x_i) \le 1 \tag{3.52}$$

where N is the total training data. For example, when there are three types of lithology recognised as sandstone, shale and carbonate, the value of n is three. The

fuzzy membership rules for each data types are added as outputs of the BPNN model. Then, number of output nodes is increased from 2 to (n+2).

In the next step, the BPNN is carried out on the training data, delineating relationships between input data and the fuzzy membership rules. With these rules, descriptive or linguistic properties can be quantified.

3.4.3.2 Inputs Ranking

Similar application of fuzzy logic can be applied for ranking the input data. After neural training, it is possible to determine which inputs that have real impacts on the outputs. For the same ANN as in **Fig. 3.5**, l recorded outputs (z_k) are represented by membership functions ($\mu_{ik}(x)$) of m inputs (x_i), as:

$$z_k \equiv \left\{\left(x_i, \mu_{\mathrm{ik}}(x_i)\right)\right\}, \quad i = 1...m, \quad k = 1...l \quad 0 \le \mu_{\mathrm{ik}}(x_i) \le 1 \tag{3.53}$$

In an analogous manner as data classification step, the ANN can evaluate the membership functions of each input types. The membership functions are then averaged to single values, each of which is indicative of the relevance of corresponding input on the outputs. Hence, unimportant input parameters are identified and ignored in future neural modelling to reduce computational cost and improve accuracy.

3.4.4 Data Characterisation by Fuzzy Neural Network

After the fuzzy data classification and inputs ranking steps, the FNN scheme is applied to determine distribution maps of fracture density and discrete multifractal dimensions. At this stage, the training and validation concentrate on relationships between reservoir data inputs and fracture properties outputs. FNN is applied twice, along the wellbores and over the field.

As mentioned above, values of fracture density and fractal dimension can be calculated for limited and irregular sections of the wells (e.g. from limited cores and images). In addition, in many boreholes, only a simple suite of logs is run. As discussed in **Chapter 2**, the relationships between wireline log responses and fracture information

recorded in drill core are markedly nonlinear. Fracture frequency prediction is a less-than-straightforward output from conventional analyses such as statistical regression and kriging. Thus, FNN is applied to solve for such relationships. The training and validating data include all computed fracture density, fractal dimension and different log responses (e.g. sonic, neutron, resistivity and conduction). Once the network has been trained, prediction can be made along all wellbores in the reservoir (i.e. regression based on well logs).

In the second run, fracture density and fractal dimension are simulated spatially over the whole reservoir. This time, field-scaled seismic, outcrop and other geological surveys are used. This group of data has resolution ranging from a few inches to several feet. They reveal reservoir structure, thickness, lithology and curvature of various formations. These factors are directly related to several fracture characteristics, such as fracture length, spacing, orientation and density. Among these tools, the most abundant and informative sources are the seismic attributes such as velocity, amplitude, phase. Training data also include values of fracture density and fractal dimension at the multiple wellbores, which have just been analysed in the first FNN run (along wellbores). Predicted outputs are in the forms of grid-based distribution maps, according to the format of available data (i.e. regression based on seismic and outcrop).

Application of FNN in NFR characterisation is illustrated in the case study in **Chapter 4**.

3.5 CLOSURE

In this chapter, the second part of NFR characterisation, where various analyses are performed on the measured intermediate data, is reviewed. Purpose of the exercise is to define characteristic behaviours of the fracture system.

Data sources for NFR are not only scarce, but also of different scales and relevancies. First, statistical and spatial analyses are applied to the fracture location, orientation and size. Their results include multimodal circular statistical distribution for orientation, probability density functions for size, measurements of CSR and variograms. In addition, continuum secondary parameters such as fracture density and discrete multifractal are established for better characterisation of the fracture system.

An ANN is then incorporated to establish relationships among the secondary properties, wellbore-scaled data (e.g. wireline logs) and reservoir-scaled data (e.g. seismic, outcrop and other geological surveys). Application of fuzzy logic allows assessment of qualitatively descriptive data. It also classifies the importance of each data source. The FNN reveals how fracture density and multifractal dimension distribute spatially, producing fracture distribution maps over the reservoir.

The fracture characteristics obtained represent the target fracture system to be simulated. They will be considered in the modelling stage, as parameters for the hybrid stochastic simulation, or as components of objective function in conditional global optimisation, or as conditional data in both models (**Chapters 4** and **5**).

CHAPTER 4 - MODELLING OF NATURALLY FRACTURED RESERVOIRS BY HYBRID NEURO STOCHASTIC SIMULATION

4.1 OVERVIEW

In **Chapters 2** and **3**, a systematic procedure for NFR characterisation has been presented. The results include statistical distributions and correlations of fracture location, orientation and size. They also contain pixel-based maps of reservoir fracture density and discrete multifractal. The purpose of a comprehensive NFR modelling methodology is to build a reliable fracture model through integration of the reservoir's geological knowledge and all the characterised discrete and continuum information. NFR modelling will be discussed in the second part of the thesis (**Chapters 4** and **5**).

In this **Chapter 4**, a hybrid neuro stochastic methodology is introduced, which combines features of discrete stochastic, conditional and hierarchical simulations. The chapter begins with overviews of each individual modelling components. First, the object-based fracture model is discussed. This is followed by explanation of selective random sampling (stochastic) schemes in which fracture properties are generated. Several advanced features of the hybrid stochastic simulation are then described, including modelling of correlations and non-parametric distributions of fracture properties, integration of continuum measurements of spatial complexity into the discrete model and hierarchical ordering simulation. After the fracture modelling methodology has been formulated, a case study is illustrated for the naturally fractured Palm Valley gas field. The chapter concludes with discussions on advantages and drawbacks of the hybrid stochastic methodology.

混合随机建模的优点。

4.2 OBJECT-BASED SIMULATION COMPONENT

Most of previous fractured network models were grid-based, yielding only fracture intensity maps (National Research Council, 1996; Hennings et al., 2000). These maps could only indicate presence of fractures. In such models, details of fracture properties such as orientation, size and aperture were not available (**Section 1.4.1**). An extensive understanding of a NFR, however, requires knowledge of not only fracture density distribution, but also details of every fracture. Only then, comprehensive simulations of different stimulation scenarios and fluid flow become possible. In addition, results of object-based modelling (or marked point process) are more accurate and reliable, by allowing analyses on individual fracture attributes and their interrelationships (**Chapter 3**).

基于对象的建模，示性点过程。

他们的相互作用如何应用到建模？？

In this work, individual fracture is treated as an object, characterised by its location, orientation and size. Each object possesses a variety of rules for behaviours in space such as shift, rotate, grow, shrink, multiply or disappear. The DFN model (*M*) is defined as a composite of total number of fractures (N_F), individual fracture (M_F) and their attributes (Kumar et al., 1999). In other words, the network model encloses geometrical model, behaviour model and boundary conditions of fracture attributes. Single fracture object, being the base attribute, serves as base model for fracture location (M_L), orientation (M_O) and size (M_S) attributes, as in **Eq. 4.1** and **Fig. 3.4** herein:

$$M = M_F \otimes N_F \{M_L(M_F) \otimes M_O(M_F) \otimes M_S(M_F)\} \qquad (4.1)$$

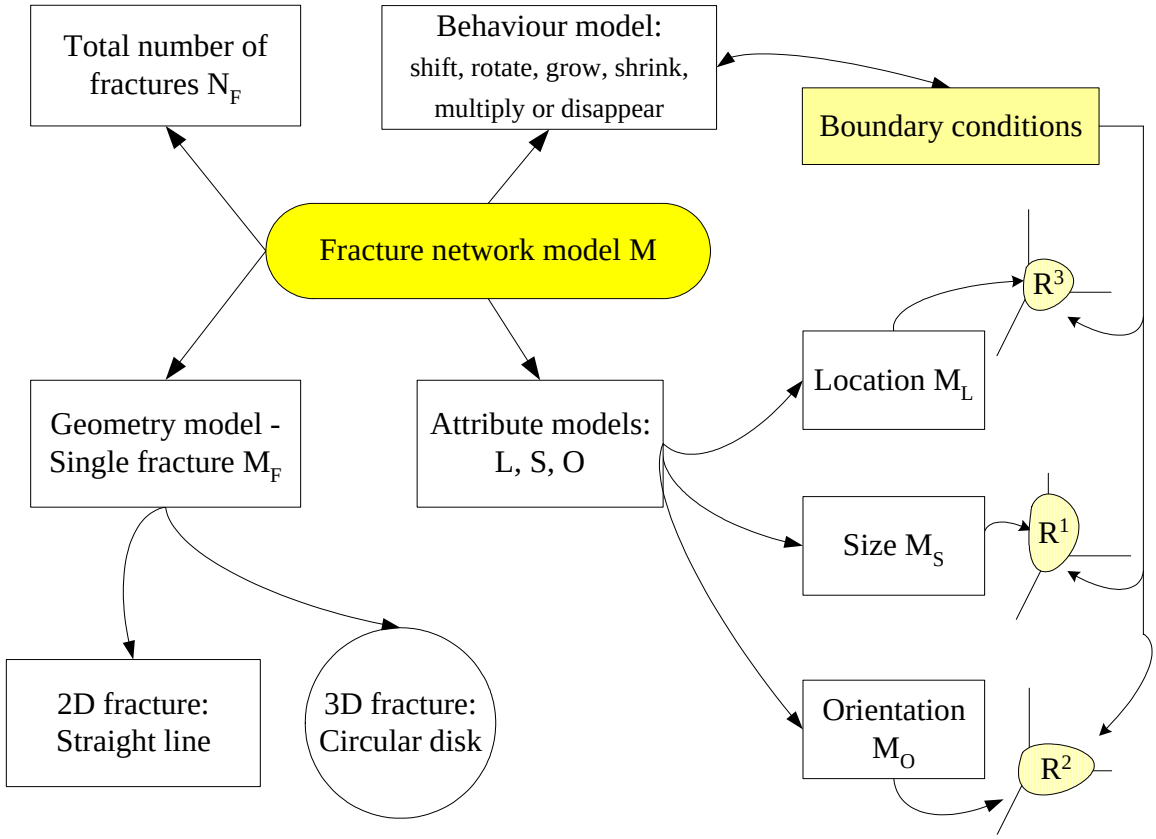


Fig. 4.1: DFN model (M) is a composite of total number of fractures (N_F), individual fracture (M_F) and their attributes (L, S, O). Fracture objects can vary in many ways, such that location, size and orientation attributes satisfy their respective boundary conditions (R^1, R^2 and R^3).

返回首页

4.3 STOCHASTIC SIMULATION COMPONENT

4.3.1 Stochastic Simulation and Fracture Network Modelling

In deterministic simulation, values of fracture properties at un-sampled locations are interpolated or predicted based on the sampled data (at different locations) and a set of criteria, e.g. unbias and minimum error variance. However, the estimations are often overly simplistic and local details of spatial variation are smoothed out. Many statistics and geostatistics such as variograms and density distribution map could not be utilised.

密度分布图在确定性建模中是无法利用的。

As opposed to deterministic simulation, stochastic simulation produces fast and precise estimations to posterior probabilities in probabilistic networks. Unknown

后验概率是怎么一回事？？

information is treated probabilistically, from which a model realisation is selectively and randomly sampled. Stochastic simulation is able to construct many equi-probable realisations, all honouring the model statistics. Sequential Gaussian simulation and sequential indicator simulation are two basic stochastic simulation techniques. More advanced algorithms include truncated Gaussian, PluriGaussian models and Boolean algorithms.

序贯高斯模拟
和
序贯指示模拟

For a general object-based fracture model using sequential Gaussian stochastic simulation (**Section 1.4.2.2**, with reference to Sahimi (1995), Jensen et al. (1998) Parney et al. (2000) and Tamagawa et al. (2002)), a procedure as in **Fig. 4.2** can be applied. Fractures are marked points, which are represented by geometrical properties, e.g. location, orientation and size. First, a fracture is generated by random realisations for each property, based on their probability density distributions. Each realisation of fracture is then checked to be within the model boundary. If not, another generation is performed. The reservoir model is filled with one fracture after another, until limits such as total fracture density of total number of fractures are met. The output DFN satisfies probabilistic conditions for all individual fracture properties.

首先，根据裂缝概率密度分布随机生成一条裂缝。然后检查该裂缝是否在模型的边界内，如果不在，进行另一次生成。依次类推，直到满足总的裂缝密度或者裂缝数目。

The hybrid neuro stochastic simulation is introduced as an improvement upon the general sequential Gaussian simulation. First, the selective random samplings of fracture geometrical properties are dictated by statistical behaviours that are more complicated (using multimodal circular statistics for fracture dip and azimuth; discrete multifractal for fracture size). Second, continuum distribution maps of fracture density and fractal dimension are also incorporated in the discrete model. In the following sections, theoretical settings for stochastic generation of individual fracture properties are outlined.

混合神经随机模拟在普通序贯高斯模拟的基础上进行了改进。
首先，采用了更为复杂的统计学特征，如多峰圆周分布，离散分数维等。
第二，连续裂缝密度分布图和分数维分布图同离散模型相结合。

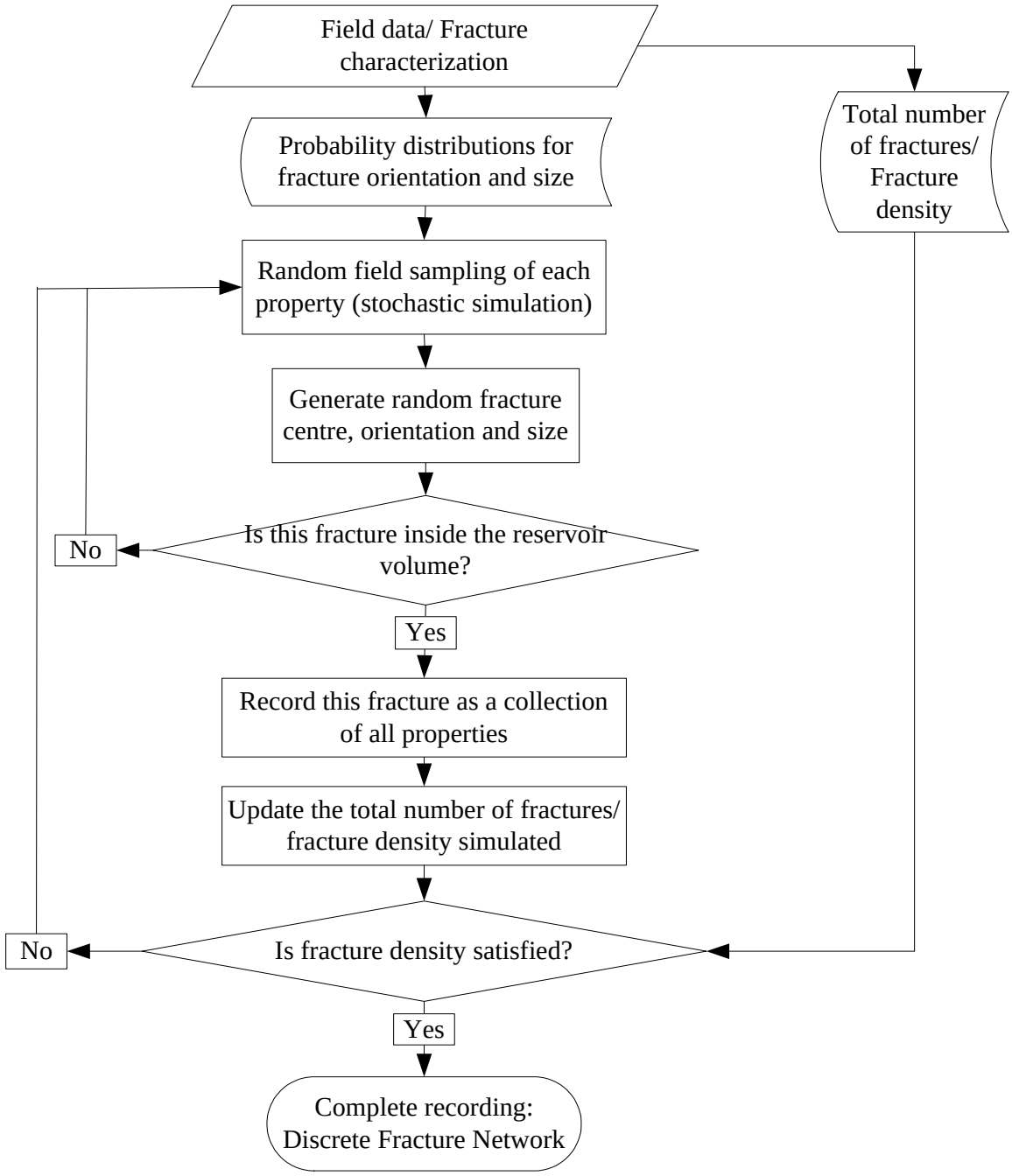


Fig. 4.2: Procedure for a general stochastic simulation to generate DFN for NFR: from characterisation to random field sampling.

普通序贯高斯模拟

返回首页

4.3.2 Stochastic Simulation of Fracture Orientation 裂缝方位的随机模拟

原来的文献中，随机模拟是基于单峰分布或均匀分布。倾角和方位角的关系亦未考虑。
本文中，裂缝方位的生成是根据多峰圆周密度函数。
同时考虑了方位角和倾角之间的关系。

In most of previous works, the stochastic generation is based on either uniform or unimodal distributions. Correlation between dip and azimuth has not been assessed (Willis-Richards, 1996; Jensen et al., 1998; Anraku et al., 2000). In this work, fracture orientation is generated according to its multimodal circular density function, as characterised in **Chapter 3** (**3.2.1**). Correlations between different modes of the multimodal dip and azimuth are also simulated. For correct perspective, stochastic simulation of orientation following unimodal distributions are first examined. Then, an analogous procedure can be applied for the case of multimodal circular.

4.3.2.1 Orientation Angles of Unimodal Distributions 单峰分布的方位角

Let α_0 and β_0 be two arbitrary circular orientation quantities, which could be, but not restricted to, dip and azimuth. The two circular angles follow one-modal distributions, which could be of any forms, ranging from uniform, normal, gamma to non-parametric. For a common case, they are assumed one-modal wrapped normal with mean (μ) and resultant length (R):

$$\alpha_0 = \mathrm{WN}(\mu_1, R_1) \tag{4.2}$$

$$\beta_0 = \mathrm{WN}(\mu_2, R_2) \tag{4.3}$$

They can be simulated from α and β, whose distributions are one-modal normal with the same mean (μ) and standard deviation (σ) as in **Eq. 4.4**. α and β have correlation parameter Cor_{12}:

$$\sigma = \{-2 \cdot \log R\}^{0.5} \tag{4.4}$$

$$\alpha = \mathrm{N}(\mu_1, \sigma_1) \tag{4.5}$$

$$\beta = \mathrm{N}(\mu_2, \sigma_2) \tag{4.6}$$

If there is no correlation between the two orientation properties (Cor_{12} = 0), stochastic angles could be individually generated as in **Eqs. 4.5** and **4.6**. However, such generations do not apply to nonzero correlation.

Thus, when correlation exists, α and β are first transformed to $\alpha\alpha$ and $\beta\beta$ such that their correlation becomes zero. Being independent, $\alpha\alpha$ and $\beta\beta$ can be individually generated. Then, the random realisations are reversely transformed back to α and β. After that, they are wrapped around a circle to obtain final realisations that satisfy the original distributions (**Eqs. 4.2** and **4.3**). The forward transformation and backward generation are carried out in the following subsections.

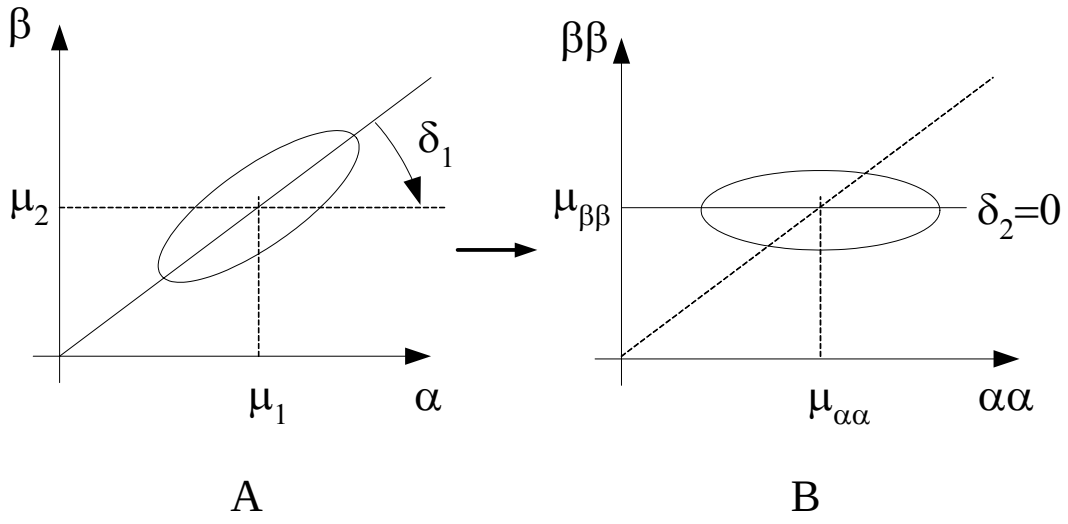


Fig. 4.3. Correlation of two normally distributed quantities: before the transformation (A) and after the transformation (B). There is zero correlation after the transformation.

Forward transformation

As α and β are normally distributed, they can be presented as in **Fig. 4.3 (A)**. The angle δ relates to correlation of the two sets. When δ becomes zero or 90^{O}, α and β have zero correlation. The transformation is done by rotating the two data sets by an amount δ clockwise:

$$\alpha\alpha = \alpha \cdot \cos\delta + \beta \cdot \sin\delta \tag{4.7}$$

$$\beta\beta = -\alpha \cdot \sin\delta + \beta \cdot \cos\delta \tag{4.8}$$

At this stage, the task is to compute transformation angle (δ). Since correlation between $\alpha\alpha$ and $\beta\beta$ is zero, their covariance ($Cov(\alpha\alpha,\beta\beta)$) is zero.

$$Cor(\alpha\alpha, \beta\beta) = \frac{Cov(\alpha\alpha, \beta\beta)}{\sigma(\alpha\alpha) \cdot \sigma(\beta\beta)} = 0 \tag{4.9}$$

From **Eqs. 4.7** and **4.8**, variances and covariance of $\alpha\alpha$ and $\beta\beta$ are evaluated based on other statistics of α and β, as:

$$Var(\alpha\alpha) = \sigma_1^2 \cdot \cos^2\delta + \sigma_2^2 \cdot \sin^2\delta + 2Cor_{12} \cdot \sin\delta \cdot \cos\delta \tag{4.10}$$

$$Var(\beta\beta) = \sigma_1^2 \cdot \sin^2\delta + \sigma_2^2 \cdot \cos^2\delta - 2Cor_{12} \cdot \sin\delta \cdot \cos\delta \tag{4.11}$$

$$Cov(\alpha\alpha, \beta\beta) = Cor_{12} \cdot \left(\cos^2\delta - \sin^2\delta\right) + \left(\sigma_2^2 - \sigma_1^2\right) \cdot \sin\delta \cdot \cos\delta \tag{4.12}$$

$$Cov(\alpha\alpha, \beta\beta) = Cor_{12} \cdot \cos 2\delta + \frac{1}{2}\left(\sigma_2^2 - \sigma_1^2\right) \cdot \sin 2\delta \tag{4.13}$$

By combining **Eqs. 4.9** and **4.13**, it is possible to obtain δ:

$$\delta = \frac{1}{2} \cdot \left[\tan^{-1}\left(\frac{2Cor_{12}}{\sigma_2^2 - \sigma_1^2} \right) + \pi \right] \tag{4.14}$$

Means and standard deviations of $\alpha\alpha$ and $\beta\beta$ can also be calculated as:

$$\mu_{\alpha\alpha} = \mu_1 \cdot \cos\delta + \mu_2 \cdot \sin\delta \tag{4.15}$$

$$\mu_{\beta\beta} = \mu_2 \cdot \cos\delta - \mu_1 \cdot \sin\delta \tag{4.16}$$

$$\sigma_{\alpha\alpha} = \left[Var(\alpha\alpha)\right]^{0.5} \tag{4.17}$$

$$\sigma_{\beta\beta} = \left[Var(\beta\beta)\right]^{0.5} \tag{4.18}$$

Backward generation

To stochastically generate original orientation quantities α_0 and β_0, the procedure as herein is followed. If distributions of α_0 and β_0 are not wrapped normal, this procedure can be modified accordingly.

- Generate random, normally distributed, non-correlated $\alpha\alpha$ and $\beta\beta$ individually, with $\alpha\alpha = N(\mu_{\alpha\alpha}, \sigma_{\alpha\alpha})$ and $\beta\beta = N(\mu_{\beta\beta}, \sigma_{\beta\beta})$ (**Eqs. 4.15** to **4.18**).

$$Z = z \quad \in N(0,1) \tag{4.19}$$

$$\alpha\alpha = \sigma_{\alpha\alpha} \cdot Z + \mu_{\alpha\alpha} \quad \in N(\mu_{\alpha\alpha}, \sigma_{\alpha\alpha}) \tag{4.20}$$

$$\beta\beta = \sigma_{\beta\beta} \cdot Z + \mu_{\beta\beta} \quad \in WN(\mu_{\beta\beta}, R_{\beta\beta}) \tag{4.21}$$

- Perform linear transformation from $\alpha\alpha$ and $\beta\beta$ to α and β, with transformation angle δ (Eq. 4.14). α and β satisfy Eqs. 4.5 and 4.6.

$$\alpha = \alpha\alpha \cdot \cos\delta - \beta\beta \cdot \sin\delta \tag{4.22}$$

$$\beta = \alpha\alpha \cdot \sin\delta + \beta\beta \cdot \cos\delta \tag{4.23}$$

- Wrap the normally distributed α and β around a circle of unit radius, obtaining α_0 and β_0 that satisfy **Eqs. 4.2** and **4.3**.

$$\alpha_0 = \alpha[\mathrm{mod}\, 2\pi] \tag{4.24}$$

$$\beta_0 = \beta[\mathrm{mod}\, 2\pi] \tag{4.25}$$

4.3.2.2 Orientation Angles of Multimodal Distributions 多峰分布的方位角

A similar procedure (forward transformation and backward generation) can be applied to realise dip and azimuth values that follow multimodal circular distribution.

Assume both dip and azimuth angles abide by bimodal wrapped normal distributions:

$$\alpha_0 = p_\alpha \cdot \mathrm{WN}(\mu_1, R_1) + (1 - p_\alpha) \cdot \mathrm{WN}(\mu_2, R_2) \tag{4.26}$$

$$\beta_0 = p_\beta \cdot \mathrm{WN}(\mu_3, R_3) + (1 - p_\beta) \cdot \mathrm{WN}(\mu_4, R_4) \tag{4.27}$$

Similar to the previous case, α_0 and β_0 can be simulated by α and β, which follow bimodal normal distributions. Each unimodal distribution is in turn represented by α_1, α_2, β_1 and β_2.

$$\alpha = p_\alpha \cdot \mathrm{N}(\mu_1, \sigma_1) + (1 - p_\alpha) \cdot \mathrm{N}(\mu_2, \sigma_2) \tag{4.28}$$

$$\alpha = p_\alpha \cdot \alpha_1 + (1 - p_\alpha) \cdot \alpha_2 \tag{4.29}$$

$$\beta = p_\beta \cdot \mathrm{N}(\mu_3, \sigma_3) + (1 - p_\beta) \cdot \mathrm{N}(\mu_4, \sigma_4) \tag{4.30}$$

$$\beta = p_\beta \cdot \beta_1 + (1 - p_\beta) \cdot \beta_2 \tag{4.31}$$

$$\alpha_1, \alpha_2, \beta_1, \beta_2 \Rightarrow (Cor_{12}, Cor_{13}, Cor_{14}, Cor_{23}, Cor_{24}, Cor_{34}) \tag{4.32}$$

As there are six correlation factors that associate α_1, α_2, β_1 and β_2, six transformations are required. Each transformation is taken as in **Eqs. 4.7** and **4.8**, with rotating angle (δ) computed as in **Eq. 4.14**. The aim is to transfer α_1, α_2, β_1 and β_2 to new set of variables that follow non-correlated unimodal normal distributions. As values of means, standard deviations, correlations and proportional factors have been calculated, it is possible then to stochastically generate the new variables. Similar to forward transformation, backward generation can also be directly adopted as in the previous section (**4.3.2.1**). Thus, a sample Gaussian field for stochastic simulation of fracture orientations has been generated.

4.3.3 Stochastic Simulation of Fracture Size 裂缝尺寸的随机模拟

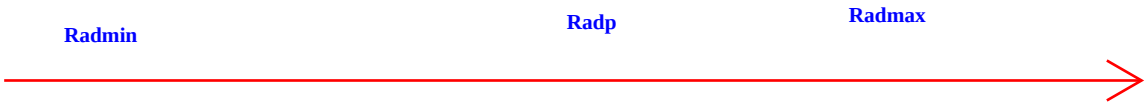
In the previous stochastic simulations, fracture size was mostly generated by lognormal (Sahimi, 1995; Jensen et al., 1998; Gurpinar et al., 1999) fractal or power law characteristics (Willis-Richards, 1996; Sahimi, 2000; Al Qassab et al., 2002; Tamagawa et al., 2002). In this work, discrete multifractal dimensions are used for the stochastic generation of fracture size (length, radius). As presented in **Chapter 3** (**3.2.2** and **3.4.4**), discrete multifractal could be used to examine variability of the fracture size. A combination of box-counting method and FNN produces the pixel-based fractal dimension map of the reservoir. The map represents spatial distribution of total number of fractures and their radii.

利用盒子法和模糊神经网络生成基于像素的油藏分数维图。

4.3.3.1 Radius Generation using Single Fractal Dimension
利用单一分数维产生半径

First, the stochastic generation based on single fractal dimension is assessed. Radii of randomly distributed fractures are stochastically simulated based on their fractal dimensions (Tran et al., 2002b). Assume there is a single fractal dimension (D), according to the fractal definition:

$$N_{Rad} = \frac{C}{Rad^{D}} \tag{4.33}$$



where N_{Rad} is the number of fractures whose radii are equal to or greater than *Rad*; and *C* is a constant. Let Rad_{min} and Rad_{max} be the minimum and maximum values of radii and $N_{Rad_{\min}}^{Rad_{\max}}$ be number of fractures having radii between the limits Rad_{min} and Rad_{max}. From **Eq. 4.33**:

$$N_{Rad_{\min}}^{Rad_{\max}} = C\left(Rad_{\min}^{-D} - Rad_{\max}^{-D}\right) \tag{4.34}$$

Now, consider *p* as fraction of total number of fractures counting from Rad_{min} upward. Let Rad_p be the largest radius in that fraction.

$$N_{Rad_{\min}}^{Rad_p} = p\,N_{Rad_{\min}}^{Rad_{\max}} = pC\left(Rad_{\min}^{-D} - Rad_{\max}^{-D}\right) \tag{4.35}$$

Also, **Eq. 4.34** can be rewritten as:

$$N_{Rad_{\min}}^{Rad_p} = C\left(Rad_{\min}^{-D} - Rad_{p}^{-D}\right) \tag{4.36}$$

Combine the two equations to eliminate *C*:

$$Rad_p = \left[(1-p)Rad_{\min}^{-D} + pRad_{\max}^{-D}\right]^{-1/D} \tag{4.37}$$

Thus, based on this equation, generation scheme for fracture radius can be developed. A random *p* of a uniform deviates (0,1) is firstly generated. Then, according to **Eq. 4.37**, values of fracture radii can be evaluated from the specified fractal dimension.

4.3.3.2 Radius Generation using Multifractal Dimension

Stochastic simulation of fracture radius based on the discrete multifractal dimensions can be performed in the same manner as the case of single fractal. First, fractal dimension value is taken from the map, according to the fracture location (stochastic mechanism for fracture centre will be discussed later). It is then directly applied to **Eq. 4.37** for realisation of fracture radius.

4.3.4 *Estimation of Fracture Aperture*

裂缝的开度和长度有很强的相关性。如何利用这种相关性呢？？

Throughout the history of fracture origination and propagation, rock faces undergo relative displacement. Longer fractures are likely to be displaced more. In other words, there is strong correlation between fracture radius and aperture. If there are abundant aperture data, the same characterisation and generation procedure as for fracture radius can be applied. However, in many cases, radius and aperture values can be simulated together.

裂缝的开度同长度有正比例关系。比例系数为p，关键问题是确定p。

Many investigators (Willis-Richards, 1996; Mazureck et al., 1998; Hossain, 2001; Tamagawa et al., 2002) have concluded that fracture aperture (a) is related to fracture radius (Rad) by a proportionality constant (p):

$$a = p \cdot Rad \tag{4.38}$$

$$p = \left(\frac{12 \cdot \overline{K} \cdot \sum_{i}^{N} Rad_i}{FracDen \cdot \sum_{i}^{N} \frac{Rad_i^{\,4}}{\left(1 + 9 \cdot \frac{\sigma_{eff\,i}}{\sigma_{nref}}\right)^3}} \right)^{\frac{1}{3}} \tag{4.39}$$

p的确定是很困难的。如果是常数，可以回归得到。

Where $\sigma_{eff\,i}$ is the effective normal stress acting normal to the i^{th} fracture. σ_{nref} is the effective normal stress applied to cause 90% reduction in the compliant aperture. $\overline{K}$ is mean virgin permeability of the fracture medium. All of these properties can be evaluated from laboratory tests on reservoir rock samples (Willis-Richards, 1996).

4.3.5 *Stochastic Simulation of Fracture Centre Points*

4.3.5.1 Stochastic Simulation based on Distribution Patterns

Similar to orientation and size, stochastic generation of fracture location should be a data-driven process. From spatial data analyses (**Chapter 3: 3.3.1**), distribution of fracture centre points can be concluded to be either complete spatial random (CSR), regular or clustered. For CSR, coordinates of the fracture centre points can be generated

using a homogeneous Poisson process. If regularity is detected, uniform distributions are used. The coordinates are constrained within the model boundary.

In case of clustering, generation process is more complex. To tackle various degrees of clustering, one could follow three directions. First, variograms of orientation and size are used (Deutsch and Journel, 1992). Such geostatistical tools is desirable, however, not applicable. This is because stochastic simulation could not utilise experimental variograms, while the conversion from experimental to model variograms might contain enormous errors. Besides, only one set of rules can be applied: either probability density function of the fracture properties or their model variograms. Second, probability density functions of coordinates are applied. This is only relevant when the density functions are representative. The third, and probably the most accurate way, is based on the fracture density distribution map, which has been obtained from FNN analysis (**Chapter 3: 3.2.2** and **3.4.4**). Although it is difficult to be realised, spatial distribution of fractures can be correctly portrayed.

4.3.5.2 Stochastic Simulation based on Fracture Density Map

根据裂缝密度图的随机模拟

Fracture density map is a pixel-based map, representing total fracture area over reservoir volume. It is one of the most indicative measurements for spatial distribution of fractures and could be obtained from the FNN analysis (**Chapter 3: 3.2.2** and **3.4.4**). Stochastic simulation is carried out such that the density map is preserved for the output DFN.

首先，根据裂缝密度图建立裂缝概率图。裂缝密度大的网格内，生成裂缝的概率大。

First, a probability map is constructed from the density map, which symbolises the probability of fractures to be generated. Blocks with high density correspond to higher chance of fracture appearance. For block i^{th}, probability (P_i) is calculated from local fracture density ($FracDen_i$):

$$P_i = \frac{FracDen_i}{\sum_i FracDen_i} \tag{4.40}$$

Then, based on the set probability, a grid-block is chosen, within which, coordinates of fracture centre are randomly generated. Orientation and size values are

然后，根据概率分布，选择一个网格，随机生成裂缝的中心坐标。然后生成其属性。

then realised according to schemes above (**Sections 4.3.2** and **4.3.3**). The generated fracture is checked to be inside the modelling boundary. This completes realisation of a fracture.

在这一步中，密度概率图需要即时更新。生成了裂缝的网格，概率会降低。更新后的密度概率图决定了生成下一条裂缝的位置。

At this stage, the density probability map needs to be updated for subsequent realisations. The probability is reduced, for those grids that contain the generated fracture. The restructured probability density map determines location of the next fracture realisation. The generation-update procedure is repeated until all probabilities of all blocks reduce to zero and total fracture density is met (i.e. no more fractures needed). Then, the generated network would have reproduced the fracture density distribution. Fracture spatial distribution has been modelled.

4.4 CONDITIONAL SIMULATION COMPONENT

条件模拟

Due to its random characteristics, a stochastic simulation process can output an infinite number of possibilities. The result of simulation is chosen among the possibilities based on the experimental data at actual data locations. In other words, the result is conditioned to the data. The conditioning gives robustness to the whole simulation, providing anchor points that directly tie simulated DFN to the real situation (Journel and Huijbregts, 1997).

All quantitative measurements can be incorporated as conditional data. In this work, the following information is applied:

1. Some big fractures, which are directly observed from seismic and outcrop.
2. Orientation values of fractures that intersect wellbores and are detected from sources such as dip-meter logs and wellbore images.
3. Local fracture densities, which are available at wellbores from core and images.

The conditional data are of different nature and available readily from the data characterisation. Stochastic simulation has the capacity to combine deterministic conditional data, where they are input and maintained without modifications. For

example, to satisfy the conditional data of type 2, when a random generation points to location of fixed fracture orientation, only fracture size is then generated. For data of type 3, local fracture density is controlled by adjusting the initial probability map for the fractures to be generated (see **Section 4.3.5.2**).

4.5 HIERARCHICAL SIMULATION COMPONENT

Multi-scaled characteristics and high degree of heterogeneity of the NFR could be further assessed by a nested geological modelling methodology (Cacas et al., 2001). According to this methodology, the above stochastic modelling is carried out in different steps, going from larger to smaller scales. In this manner, a structural frame is first built and details are added subsequently. The first step simulates major faults of the whole reservoir while the second one simulates smaller-scaled fractures.

In the first stage, the whole reservoir is treated as one block, in which only major faults are considered. Necessary fracture data could be computed from large-scaled data sources such as seismic and outcrop images. Some of the faults are deterministically observed. Others are stochastically generated. Then, geological and lithological such as bedding layers could be manually added. In the later stage, it is necessary to modify the fracture density map to ensure that previously generated fractures have been taken into consideration.

4.6 THE HYBRID STOCHASTIC SIMULATION REALISATION

In summary, combining all the discussed individual aspects of hybrid stochastic simulation, procedure for NFR characterisation and modelling is derived and presented in **Fig. 4.4**.

The fracture characterisation stage consists of various statistical, spatial and artificial neural analyses. Its results include boundary condition, conditional data and

statistical behaviours of individual fracture properties (i.e. location, orientation and size). Reservoir maps are also derivable for discrete multifractal dimension and fracture density.

Both the discrete and continuum information are then input to the hybrid stochastic simulation. First, conditional data such as observed fractures are fixed. Then, within the hierarchical framework, individual fractures are iteratively simulated, until total fracture density is satisfied. The stochastic generation for one fracture follows the steps:

- A reservoir grid-block is picked according to the probability map (which in turn is a result of the fracture density distribution map).
- Within the block, coordinates of the fracture centre are randomly generated.
- Dip and azimuth of the fracture are generated according to the characterised multimodal distributions (with consideration of correlations).
- Radius of the fracture is generated based on the discrete fractal dimension value that corresponds to the chosen grid-block.
- Aperture of the fracture is estimated from the radius and other parameters.
- Fracture object is a composite of all attributes. It is then confirmed with conditional data and boundary conditions.
- If the fracture conditions are satisfied, the next step is to update total density and probability map for subsequent generations.

Output of the hybrid stochastic simulation is a DFN that contains details of all fracture properties (e.g. total number of fractures, location, orientation and size) and honours representative fracture characteristics (both discrete and continuum). It is ready to be combined with conventional geological reservoir models as inputs for reservoir simulation and stimulation studies.

本页已使用福昕阅读器进行编辑。
福昕软件(C)2005-2007，版权所有，
仅供试用。

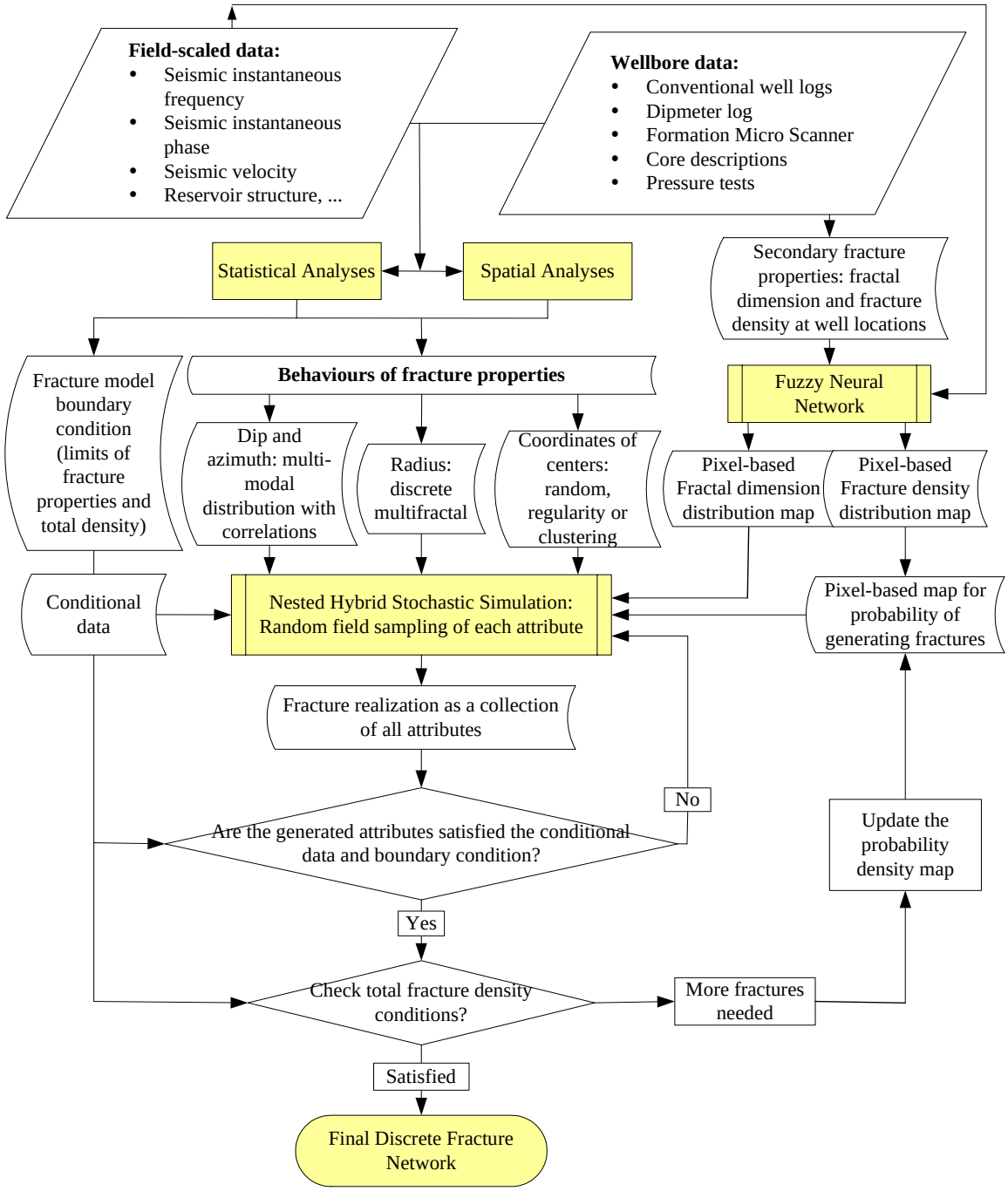


Fig. 4.4: Flowchart of the Hybrid Neuro Stochastic simulation: from fracture characterisation by statistical, spatial and artificial neural analyses, to hybrid stochastic realisation of DFN for NFR.

返回首页

4.7 APPLICATION

To illustrate the procedure of NFR characterisation and modelling (**Fig. 4.4**), a case study is carried out on the Palm Valley fractured gas field. The objective is to build DFN model for the reservoir from actual data available.

This figure has been removed due to copyright requirements

Fig. 4.5: Location map of the Palm Valley NFR: showing location of the field, wells and gas pipelines (with reference to Berry et al., 1996).

4.7.1 Palm Valley Fractured Gas Field

The Palm Valley field is located in the Amadeus Basin, Northern Territory, Australia. It is a naturally fractured tight gas reservoir, formed by a near-symmetrically East West trending anticline. Details of stratigraphy, sedimentary, tectonic history, geology and other petroleum aspects of the Palm Valley field are explained in Wells et al. (1970), Milne and Barr (1990), Do Rozario (1991) and Berry et al. (1996). Simplified location map and stratigraphy are presented in **Fig. 4.5** and **Fig. 4.6**.

This figure has been removed due to copyright requirements

Fig. 4.6: Stratigraphy of the Palm Valley NFR: the gas reservoirs are in Stairway, Horn Valley and Paccota horizons (Ordovician age) (with reference to Oaks et al., 1991).

The previous works have described that gas is contained in rock matrix of low porosity and low permeability. Reservoir permeability is largely accounted by a system

of interconnected fractures. The fracture system is extensive and hierarchical, varying from small wellbore-scaled to large reservoir-scaled. The large fractures contribute greatly to total permeability and high flow rate of up to 3.88 Mm^3/day (Berry et al., 1996).

A comprehensive fracture model is, thus, essential for development of the Palm Valley NFR. This application study covers all three gas-producing horizons of Stairway, Horn Valley and Paccota, especially the P1 unit (**Fig. 4.7**). The model encompasses a large extent of the reservoir, with size of 4000m (north south) by 20000m (east west) by 1000m (from 1000m to 2000m true vertical depth sub sea).

This figure has been removed due to copyright requirements

Fig. 4.7: Top P1 unit depth structure map, Palm Valley NFR: as interpreted from seismic data (2D presentation) (with reference to Roe, 1995).

4.7.2 Available Fracture Data

The majority of fracture information is acquired from wellbore sources. Among the 10 wells drilled, available data include cores (4 wells), FMS (2 wells) and borehole breakout data (5 wells). There are also full suites of logs in every well. Additionally, limited 2D seismic data are also available.

From intersections between fractures and wellbores, several important properties are readily measured, e.g. dip, azimuth, density and multifractal dimension. First, reports by Barr (1989a), Barr (1989b) and Berry (1991) have identified 310 fractures from various cores in the four wells A, B, C and D. Among the 311 fractures, 211 are oriented (i.e. both dip and azimuth values are obtainable). The core samples were not taken for all sections of the wells. Second, wellbore images were run continuously through sections of interest in two other wells E and F, which reveal 271 fractures (Rayner, 1995). FMS to core correlation analysis have shown that both core and FMS data are of very good quality (Berry, 1995).

Apart from core and FMS images, fracture properties cannot be directly interpreted from other data sources. Borehole breakouts with dipmeter processing data are present in five wells, from which certain information on fracture and bedding orientation can be inferred. At every well, there is a composite log suit, containing spontaneous potential SP, gamma ray GR, density RHOB, sonic DT, neutron NPHI, micro-spherically focused resistivity MSFL, shallow resistivity LLS, deep laterolog LLD, Calliper CAL, density correction DRHO, photoelectric factor PEF and true formation resistivity RT.

Several large-scaled fractures could be interpreted from seismic maps. In addition, the 2D seismic reveals attributes such as time, amplitude, instantaneous phase and instantaneous frequency for the P1 unit (horizon of interest). Velocity values are only available at wells.

4.7.3 Characterisation of Fracture Properties

裂缝属性描述

From intersections between these fractures and wellbores, several important properties are readily measured, e.g. dip, azimuth, density and multifractal dimension. The interpreted data are then analysed statistically and spatially, as per **Chapter 3**. Important information on geometrical properties of fractures is presented herein.

4.7.3.1 Fracture Orientation: Dip and Azimuth
裂缝方位

Statistical analyses on dip and azimuth values are carried out on the values obtained from cores and FMS. First, all the orientation data are converted to circular data, with range from zero to 360°. Basic circular statistics such as mean and standard deviation are listed in **Table 4.1**.

Statistics	Azimuth 1	Azimuth 2	Dip
Weight factor	0.75	0.25	1
Circular Mean	3.11	6.16	3.14
Circular StdDev	0.91	0.37	0.71
Circular Variance	0.31	0.07	0.22
Skewness	-0.038		0.000
Kurtosis	-0.336		4.025

Table 4.1: Summary of statistics for all fracture orientation (dip and azimuth) data observed in six wells (A to F), Palm Valley NFR.

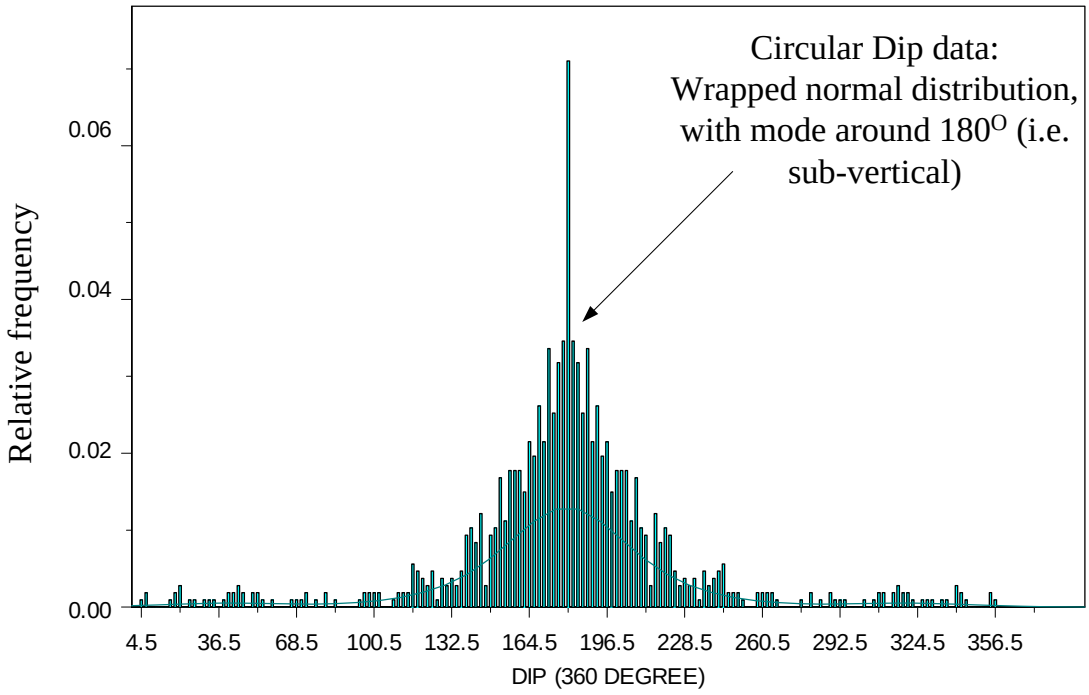


Fig. 4.8: Circular statistical analysis: histogram and probability density function plot for fracture dip (Dip_c) (unit degree, range 360°), Palm Valley NFR: showing one-modal wrapped normal distribution, whose mode is at 180° (equivalent to sub-vertical *Dip* value).

Most of the observed fractures are sub-vertical, with dip angles range predominantly between 75° and 90°. The circular dip data (Dip_c) could be fitted by a wrapped normal distribution (**Fig. 4.8**). Mathematical equation for the probability density distribution is presented as in **Eq. 4.41**:

$$P(Dip_c) = WN(3.14, 0.71) \tag{4.41}$$

$$P(Azimuth_c) = 0.75 \cdot WN(3.11, 0.91) + 0.25 \cdot WN(6.16, 0.37) \tag{4.42}$$

Fracture azimuth could be observed to have two distinct trends, perpendicular to one another. Statistical analysis on the circular azimuth data ($Azimuth_c$) reveals a bimodal wrapped normal distribution, with modes at approximately zero (or 360°) and 175° (**Fig. 4.9**). The observation is confirmed by the calculated circular statistics as in **Eq. 4.42** (with orientation unit of radian). Circular covariances and correlations of two azimuth data sets and a dip data set are calculated as in **Table 4.2**.

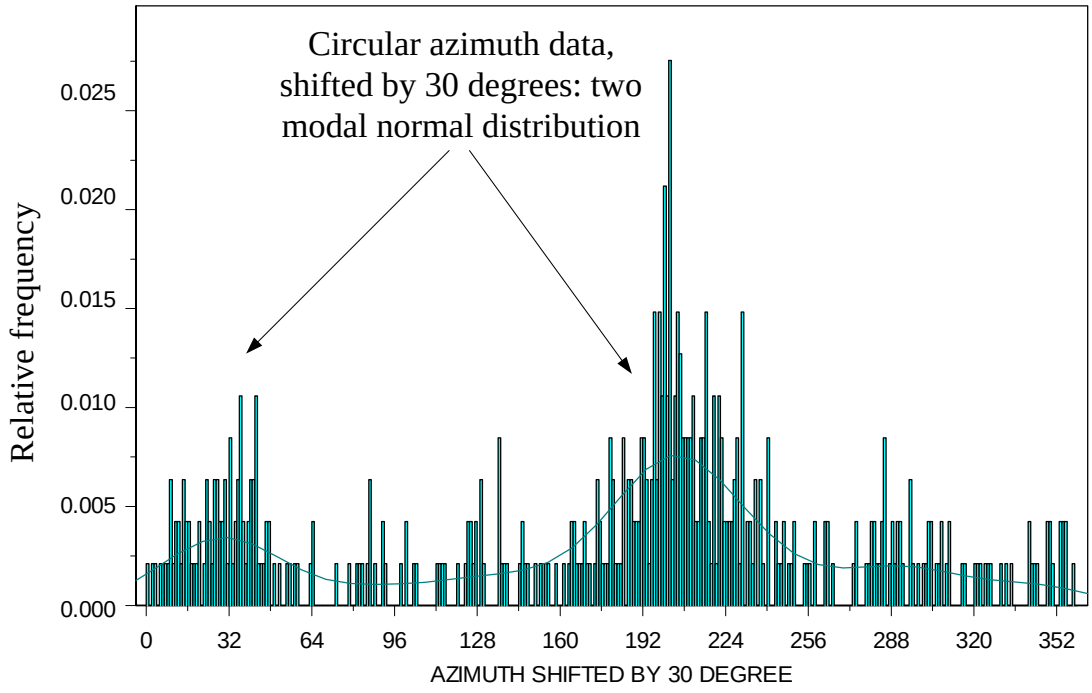


Fig. 4.9: Circular statistical analysis: histogram and probability density function plot for fracture azimuth ($Azimuth_c$) (unit degree, range 360°, data shifted to the right by 30°), Palm Valley NFR: showing bimodal wrapped normal distribution.

Correlations	Azimuth 1	Azimuth 2	Dip
Azimuth 1	1	-0.516	-0.163
Azimuth 2	-0.516	1	0.076
Dip	-0.163	0.076	1
Covariances	**Azimuth 1**	**Azimuth 2**	**Dip**
Azimuth 1	0.310	-0.174	-0.105
Azimuth 2	-0.174	0.070	0.020
Dip	-0.105	0.020	0.220

Table 4.2: Summary of correlations and covariances for all fracture dip and azimuth data observed in six wells (A to F), Palm Valley NFR.

The maximum in-situ stress was found from borehole breakout study (Fett and Williams, 1994; Hillis, 1994) and core analysis (Rough, 1974) to be principally in a north-south direction. In the reservoir, fractures are dominantly oriented around 85° (azimuth) and 180° (in smaller quantity). The orthogonal system is thus "remarkably consistent" with the field stress data (Berry et al., 1996).

4.7.3.2 Fracture Radius
裂缝半径

描述裂缝半径或者开度的分布是不现实的，因此，用到分形几何。

Because most of the data are from the wellbores, values of fracture size are limited. It is not practical for an attempt to delineate statistical distributions of neither radius nor aperture. Thus, fractal (or rather, multifractal) geometry is applied.

分数维可以沿井筒计算。裂缝同岩心的交线是圆周。利用盒子法计算分数维。对于某深度段裂缝迹线尺寸同裂缝条数为指数关系。通过关系图可以计算分数维。即是线的斜率。

Fractal dimension values can be calculated along the wellbores, where core or FMS data are available. Intersections between fractures and wellbores result in circumferential fracture traces. Then, for a depth section, simple box-counting method is applied (as in **Chapter 3: 3.2.2.1**). Graphical representation of the power-law relationship between size of fracture traces and number of fractures are illustrated in **Fig. 4.10** to **Fig. 4.13**. Fractal dimension values are readily obtained from the graphs, as (negative) slopes of the lines.

From the listed figures, fractal dimension values are found to vary from 0.7 to 1.9. However, for 2D traces, the theoretical range of fractal dimension is between 1.0 and 2.0. The error might come from graphical approximation, data gathering or possible

lack of fractures in the data sources. To comply with the theoretical range, those values lower than 1.0 are rounded up to 1.0.

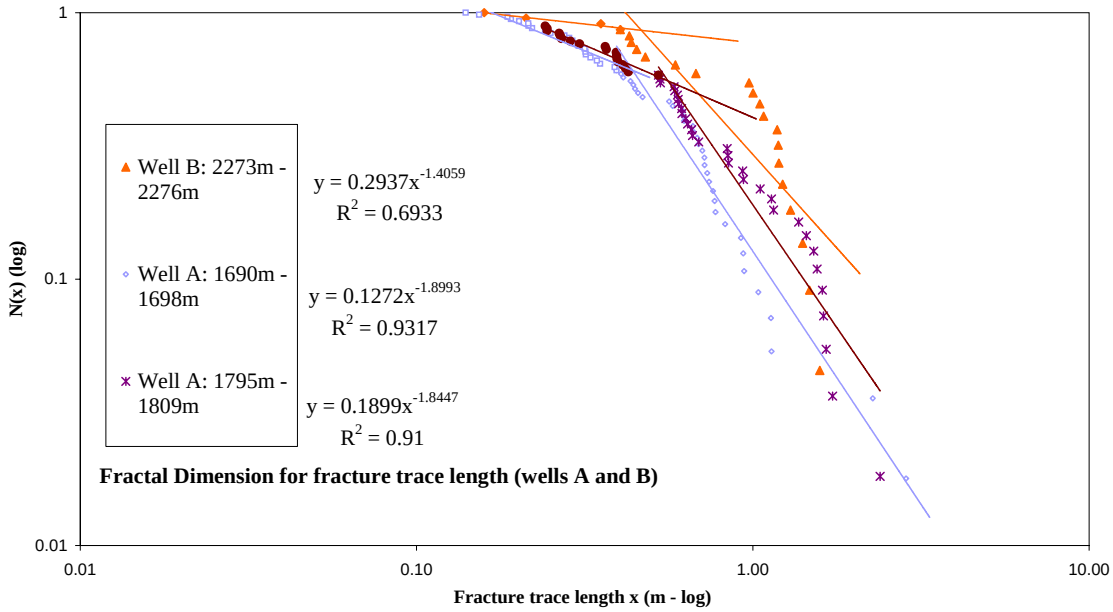


Fig. 4.10: Box-counting method for fractal dimension calculation: for sections of different depth in well A and B, Palm Valley NFR. Fractal dimension values are (negative) slopes of the straight lines.

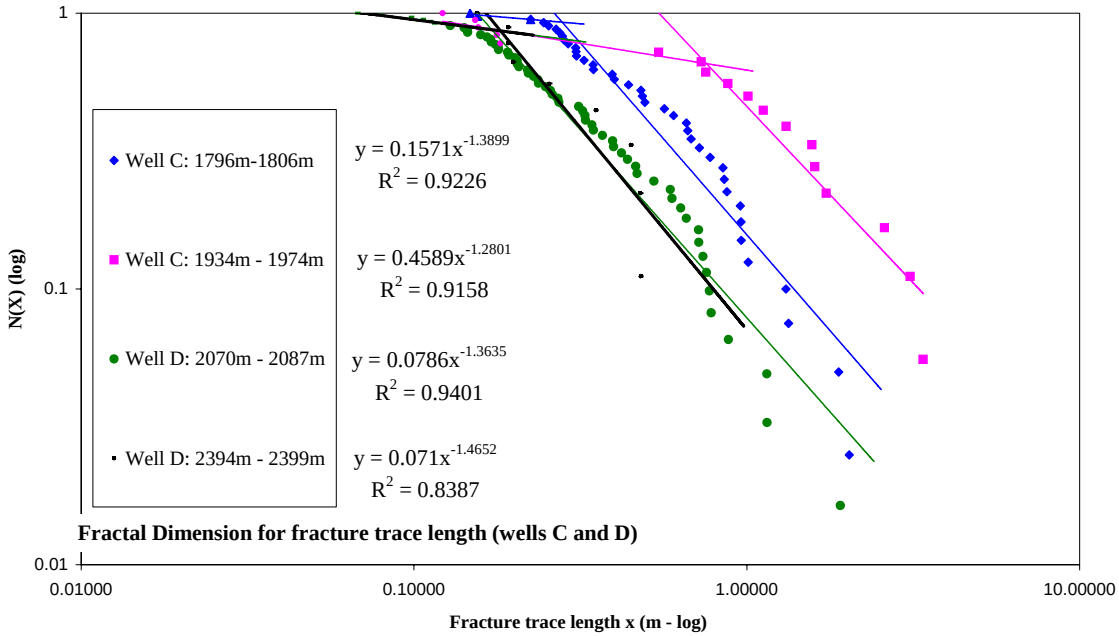


Fig. 4.11: Box-counting method for fractal dimension calculation for sections of different depth in well C and D, Palm Valley NFR. Fractal dimension values are (negative) slopes of the straight lines.

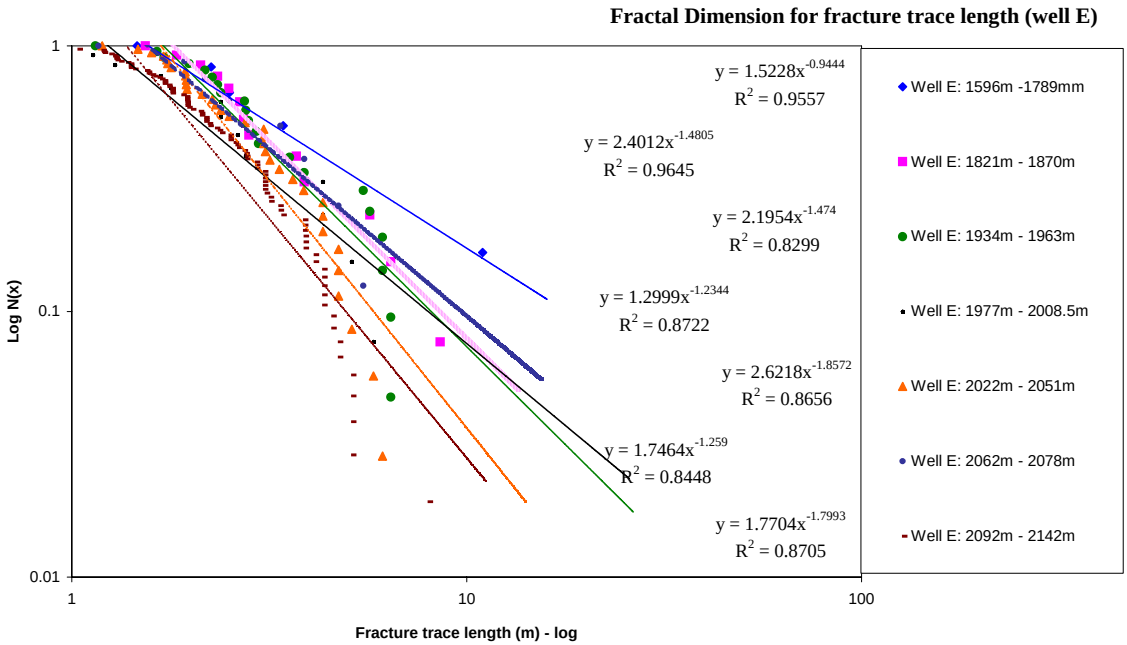


Fig. 4.12: Box-counting method for fractal dimension calculation: for sections of different depth in well E, Palm Valley NFR. Fractal dimension values are (negative) slopes of the straight lines.

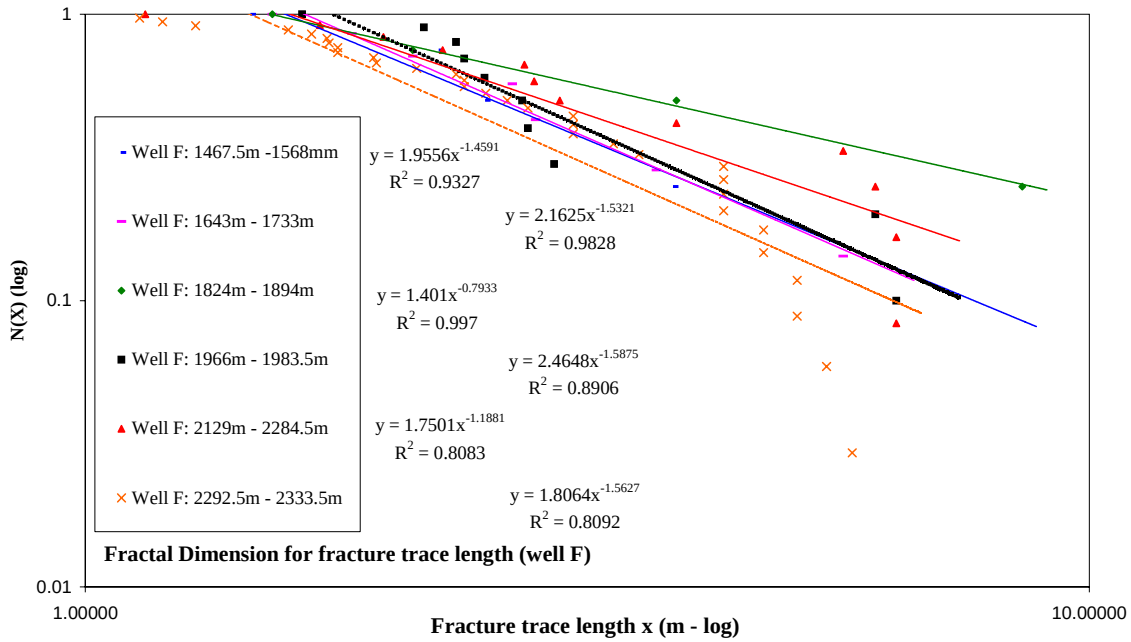


Fig. 4.13: Box-counting method for fractal dimension calculation: for sections of different depth in well F, Palm Valley NFR. Fractal dimension values are (negative) slopes of the straight lines.

4.7.3.3 Fracture Density
裂缝密度

通过岩心或者成像测井可以获得一部分井段的裂缝密度。对于其它部位，需要利用成像测井。

Similar to fractal dimension analysis, fracture density can be quickly quantified as total area of fracture intersection over unit borehole volume (**Chapters 2** and **3**). Results of density values along wellbores are presented in **Fig. 4.14**. It is also noted that the quantities are only attained for limited sections where core and FMS data are available. For all other sections, as well as for wells where core and FMS were not collected, a FNN regression is required.

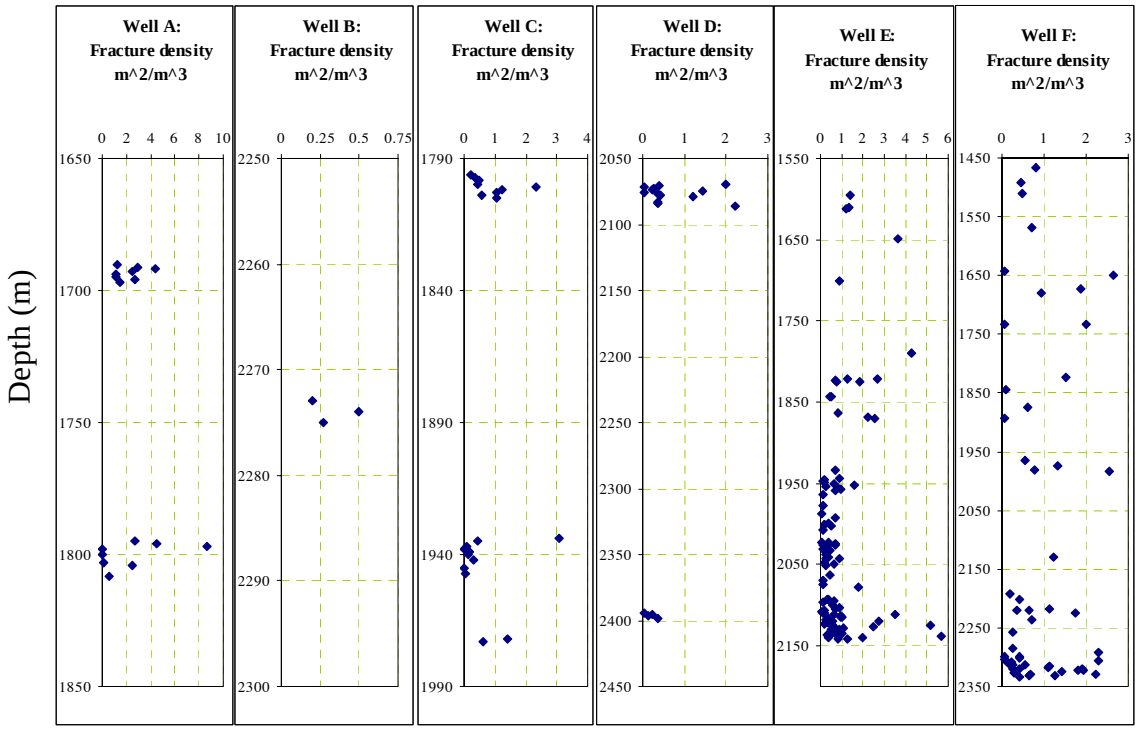


Fig. 4.14: Fracture density as calculated from FMS and core data in six wells (A to F), Palm Valley NFR (Note: depth sections vary with wells).

4.7.4 Application of Fuzzy Neural Network
模糊神经网络的应用

Total porosity (matrix and fracture), fracture density, intensity and multifractal dimensions have been calculated where core or wellbore images are available. The FNN (as described in **Chapter 3: 3.4**) is applied to approximate the quantities at locations where the hard data are not available. It is performed twice: along the wellbores and spatially over the whole reservoir.

4.7.4.1 Fuzzy Neural Network Analysis along the Wellbores
沿井筒的模糊神经网络

Along the wellbores, training data for the FNN are composed of calculated total porosity, fracture density, intensity, multifractal dimensions and all well log measurements (SP, GR, RHOB, DT, NPHI, MSFL, LLS, LLD, CAL, DRHO, PEF, RT) from four wells (A, B, C and D). Similar data in other two wells (E and F) are reserved for validation.

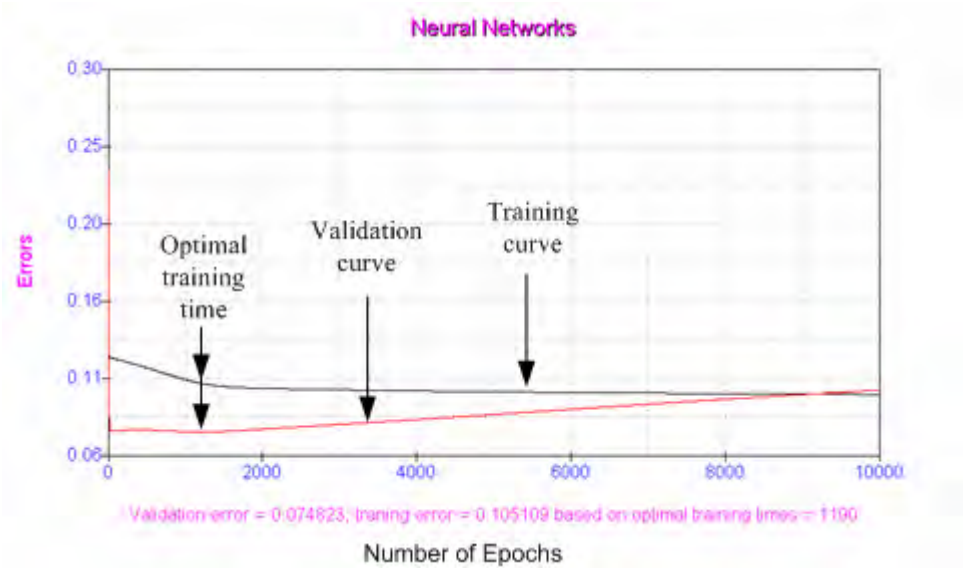


Fig. 4.15: Behaviours of the ANN in training and validation stages for fracture density along wellbores, Palm Valley NFR: showing reduction of error function with iterations and the optimal training time of 1190 epochs.

The three layer BPNN is designed to have 16 input nodes (including one node representing bias) and 4 output nodes. There are 12 nodes in the hidden layer (including one node representing bias). Both learning rate and momentum parameters are set at 0.01. Behaviours of the training and validation are illustrated in **Fig. 4.15**. The training curve shows reduction of error with iterations. The validation curve indicates optimal training time is 1190 epochs, after which overtraining is likely to occur (validation error increases).

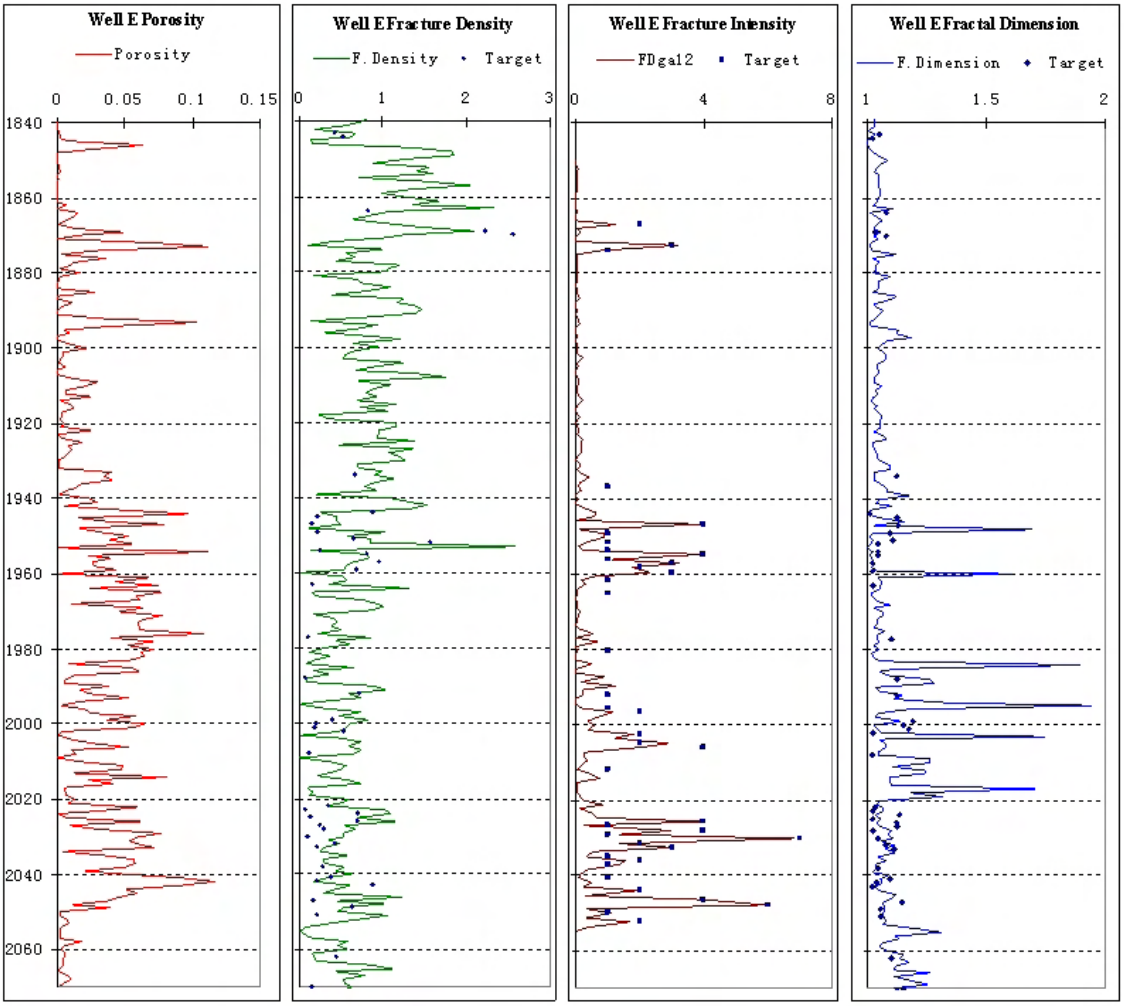


Fig. 4.16: Prediction result of FNN at validation well E, Palm Valley NFR: showing distributions along the wellbores (continuous lines) for total porosity, fracture density, intensity and multifractal dimension. Sampled data are presented where available for comparison (discrete points). Note: there is no validation data for porosity.

模糊神经网络建立了裂缝属性和测井曲线之间的复杂关系。

Through training (i.e. minimising error function), the FNN establishes complex relationships between the fracture properties and well log measurements. Using these relationships, it generates distributions of porosity, fracture density and multifractal dimensions along all wellbores in the reservoir. In **Fig. 4.16** and **Fig. 4.17**, examples of such distributions are illustrated for validating wells E and F. The computed values can be compared with measured values where available (Note that in the wells E and F, since there is no core samples, the comparisons could not be made for porosity).

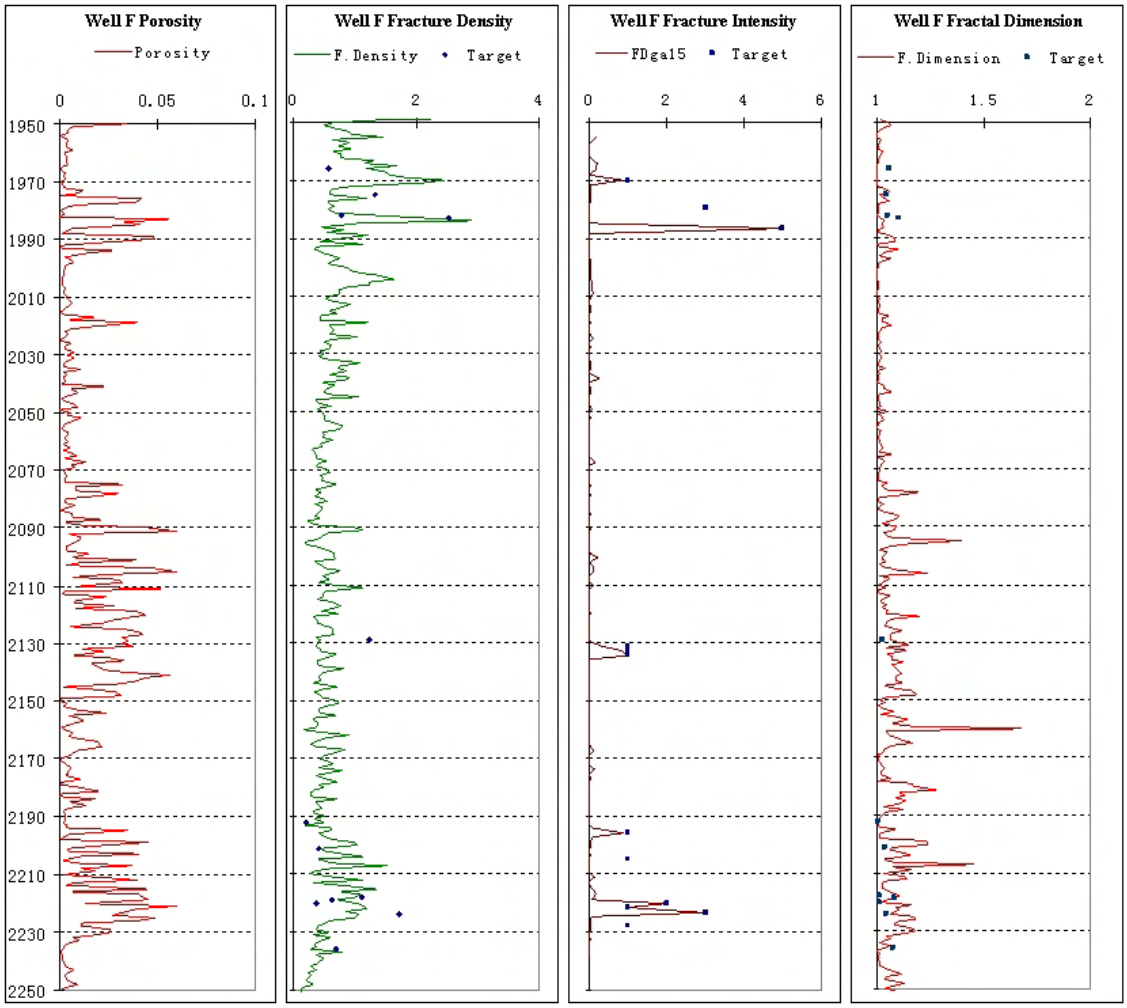


Fig. 4.17: Prediction result of FNN at validation well F, Palm Valley NFR: showing distributions along the wellbores (continuous lines) for total porosity, fracture density, intensity and multifractal dimension. Sampled data are presented where available for comparison (discrete points). Note: there is no validation data for porosity.

As seen in the two graphs, all computed distributions match sampled data values well. Accuracy of the BPNN is further assessed by cross-plotting the output and target values (**Fig. 4.18**). Good correlations are shown for all three quantities of total porosity, fracture density and multifractal dimension. Their correlation values are closed to one (0.9623, 0.8606 and 0.9395, respectively).

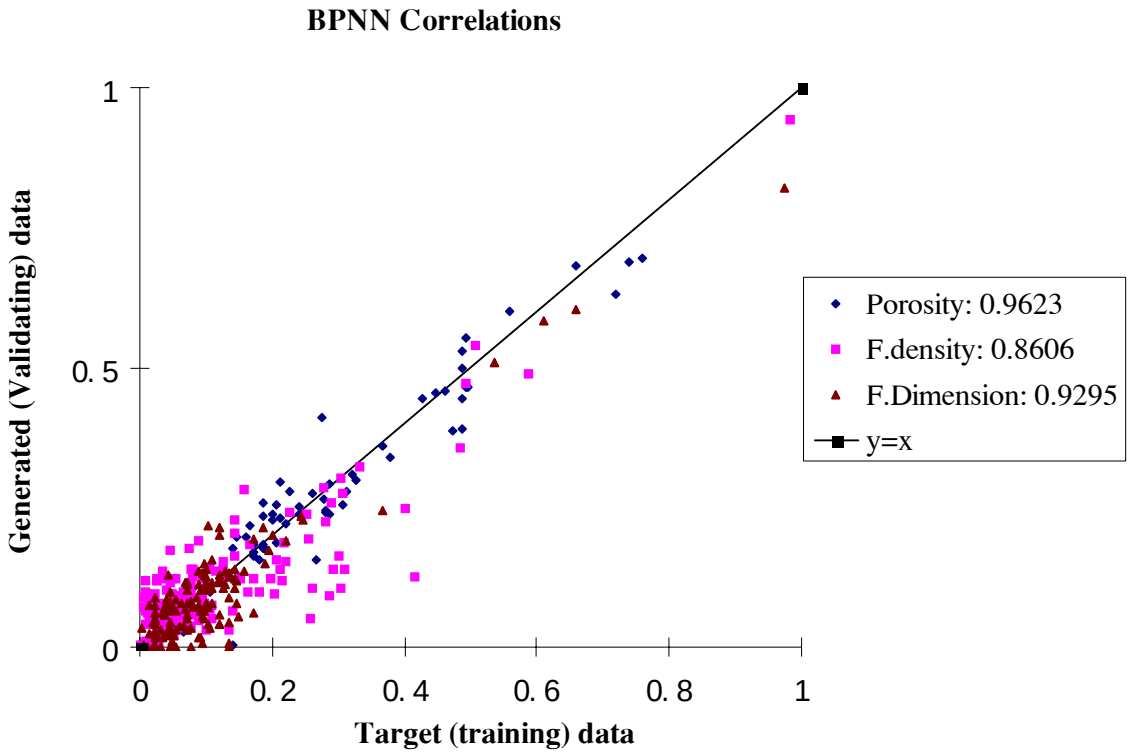


Fig. 4.18: BPNN validation result at wells E and F, Palm Valley NFR: Target and generated values for total porosity, fracture density and multifractal dimension are similar, with correlation values closed to one.

4.7.4.2 Fuzzy Neural Network Analysis Spatially Over The Field

井间应用模糊神经网络

FNN analysis is then performed over the whole reservoir in similar manners. Training data include the computed properties at well locations and field-scaled measurements. In this case study, the later contains 2D seismic for the P1 horizon, whose attributes are time (**Fig. 4.19**), instantaneous frequency (**Fig. 4.20**) and instantaneous phase (**Fig. 4.21**). Because availability of field-scaled data is limited, their ranking is not achievable.

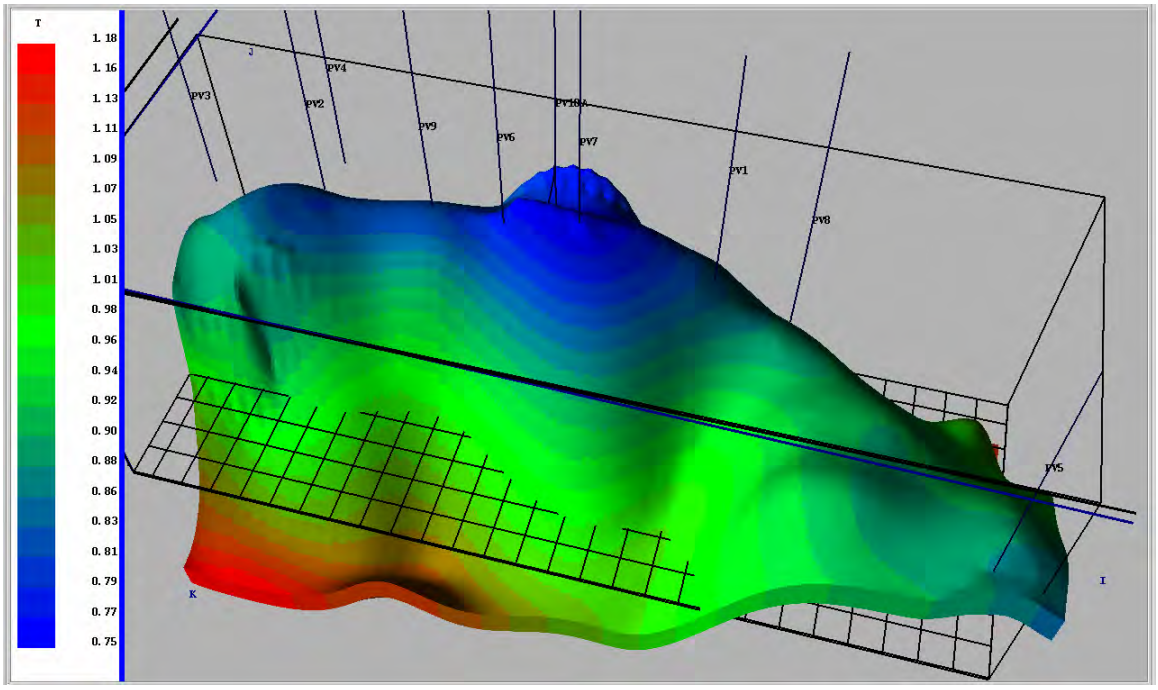


Fig. 4.19: 2D seismic time for the P1 unit, Palm Valley NFR

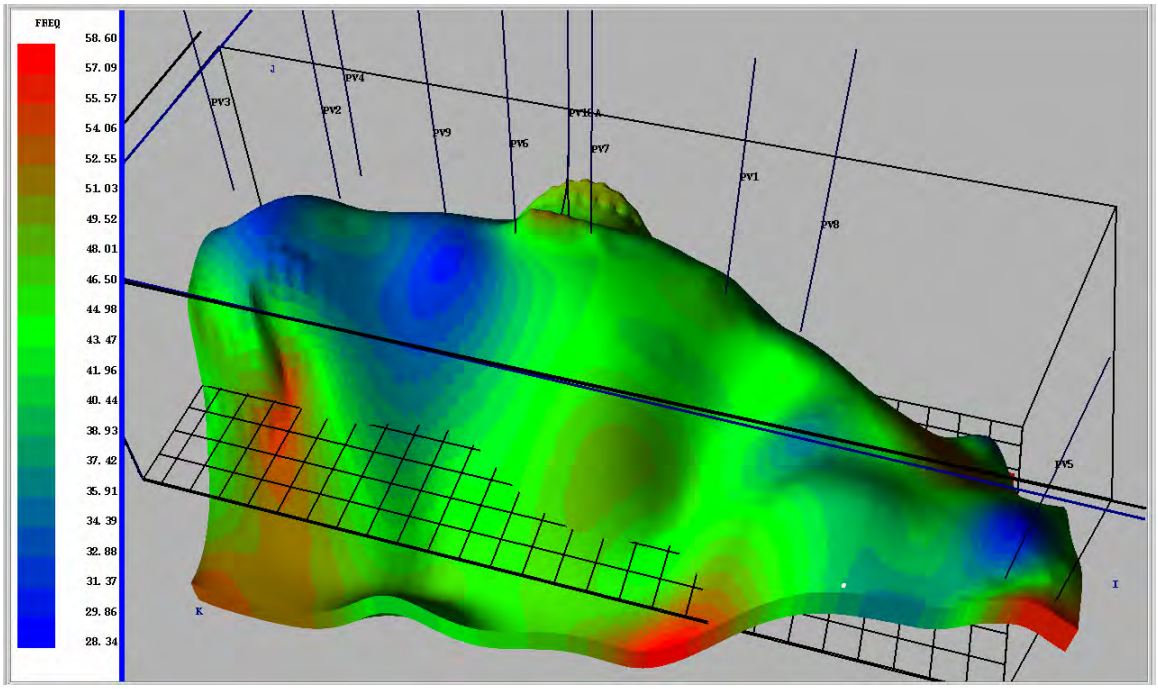


Fig. 4.20: 2D seismic instantaneous frequency for the P1 unit, Palm Valley NFR

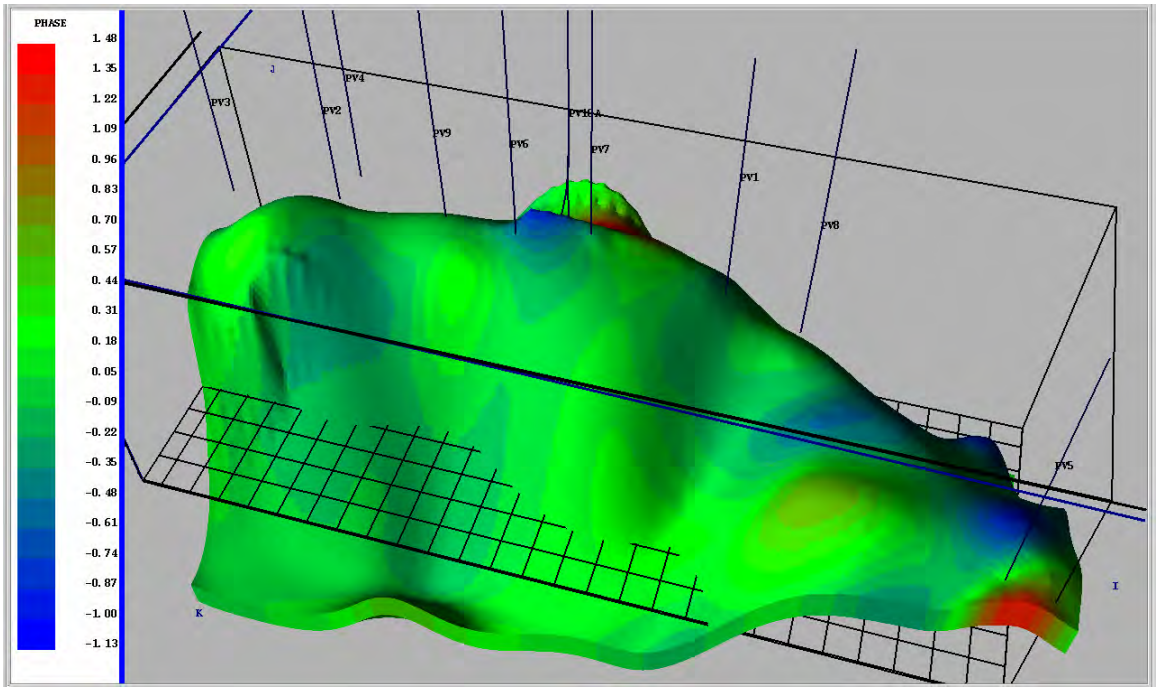


Fig. 4.21: 2D seismic instantaneous phase for the P1 unit, Palm Valley NFR

First, BPNN is used to evaluate top surface map of the P1 unit. The calculation is based on depth of the top surface recorded at wellbores. The BPNN is trained as in **Fig. 4.22**. The result, as shown in **Fig. 4.23** and **Fig. 4.24**, is compared to the depth structure map derived from seismic (**Fig. 4.7**, with reference to Roe (1995)). The aim of this step is to validate data quality. Even though there are several variances between the two maps, it can be observed that they display similar general topological trends. Both show anticline (folding) elongating roughly east to west. The eastern section of the map follows NW to SE direction. Given the limited availability of field-scaled seismic data, the result is encouraging.

After geological geometry has been set up, 3D distribution of properties such as total porosity, fracture density and multifractal dimension are computed. The resulting continuum maps are presented in **Fig. 4.25** to **Fig. 4.30**. These results are important inputs for the next stage of hybrid stochastic simulation.

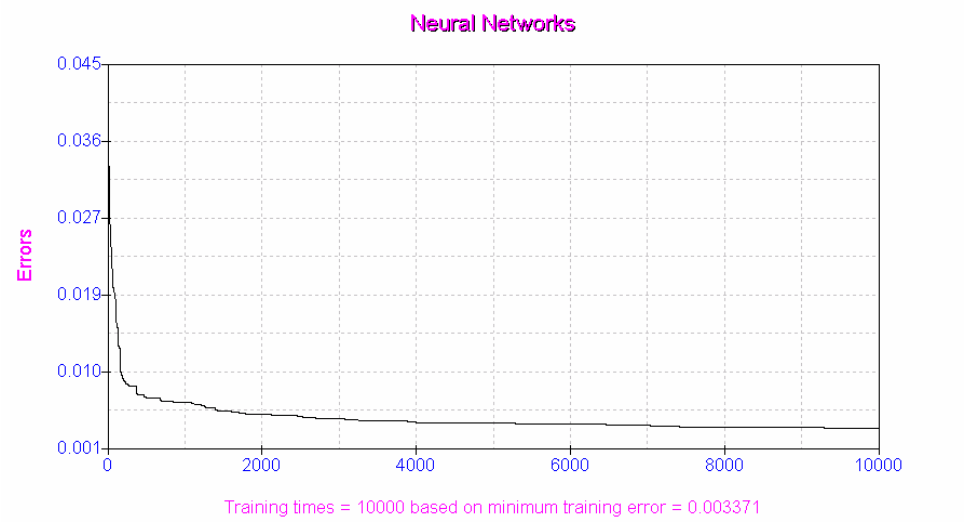


Fig. 4.22: BPNN training for depth of top structure for unit P1, Palm Valley NFR: showing pattern in which error function reduces with iterations

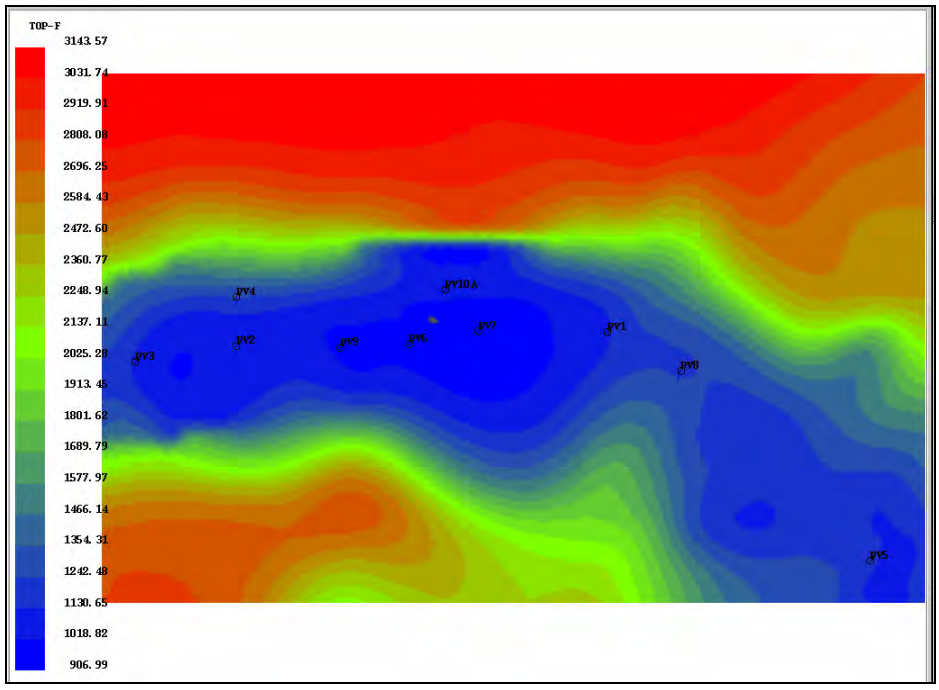


Fig. 4.23: Top P1 unit depth structure map, Palm Valley NFR: a result of artificial neural analysis (2D presentation).

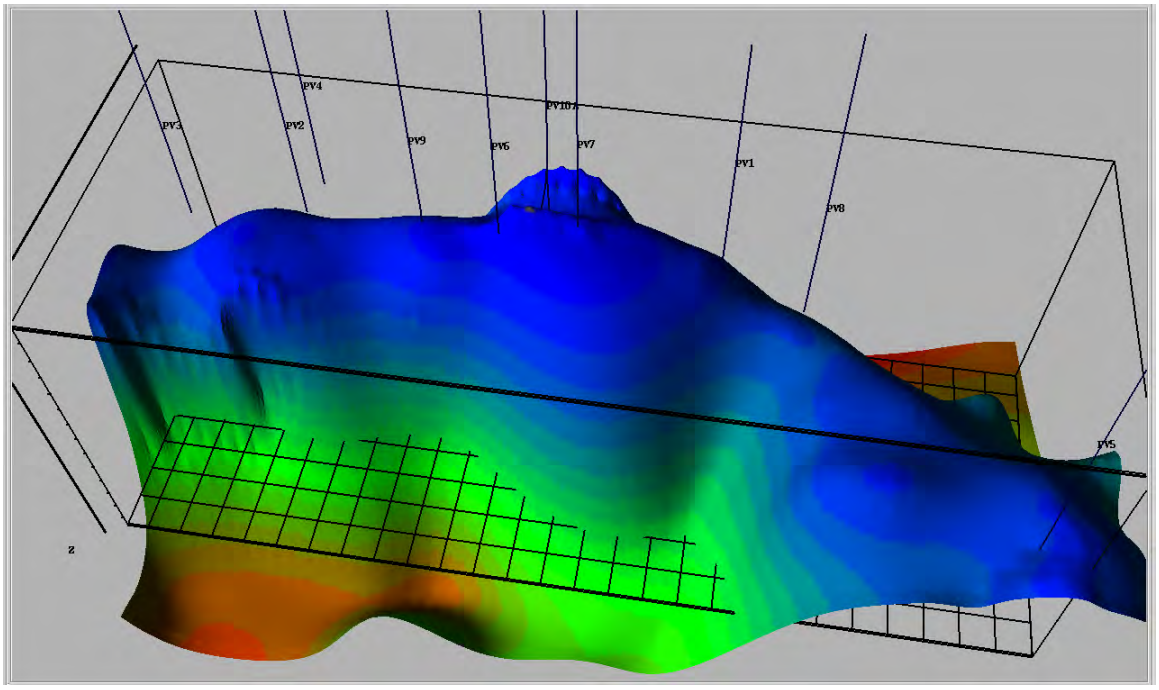


Fig. 4.24: Top P1 unit depth structure map, Palm Valley NFR: a result of artificial neural analysis (3D presentation).

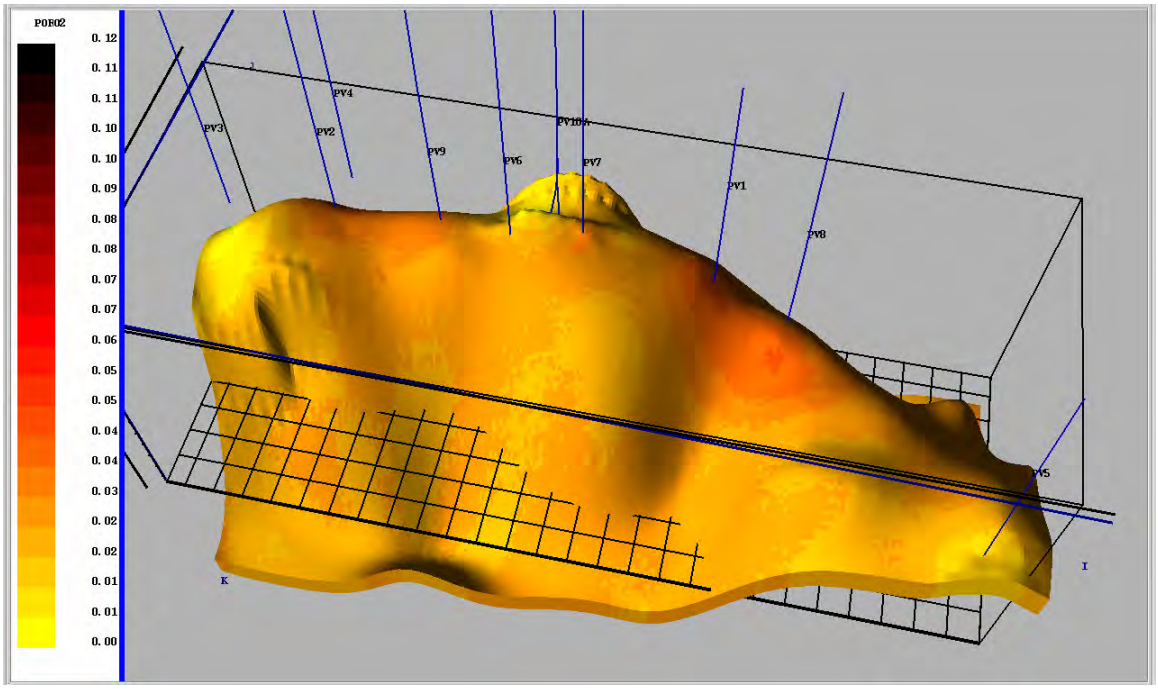


Fig. 4.25: 3D distribution map for total porosity for the P1 unit, Palm Valley NFR: a result of artificial neural analysis: view of top layer.

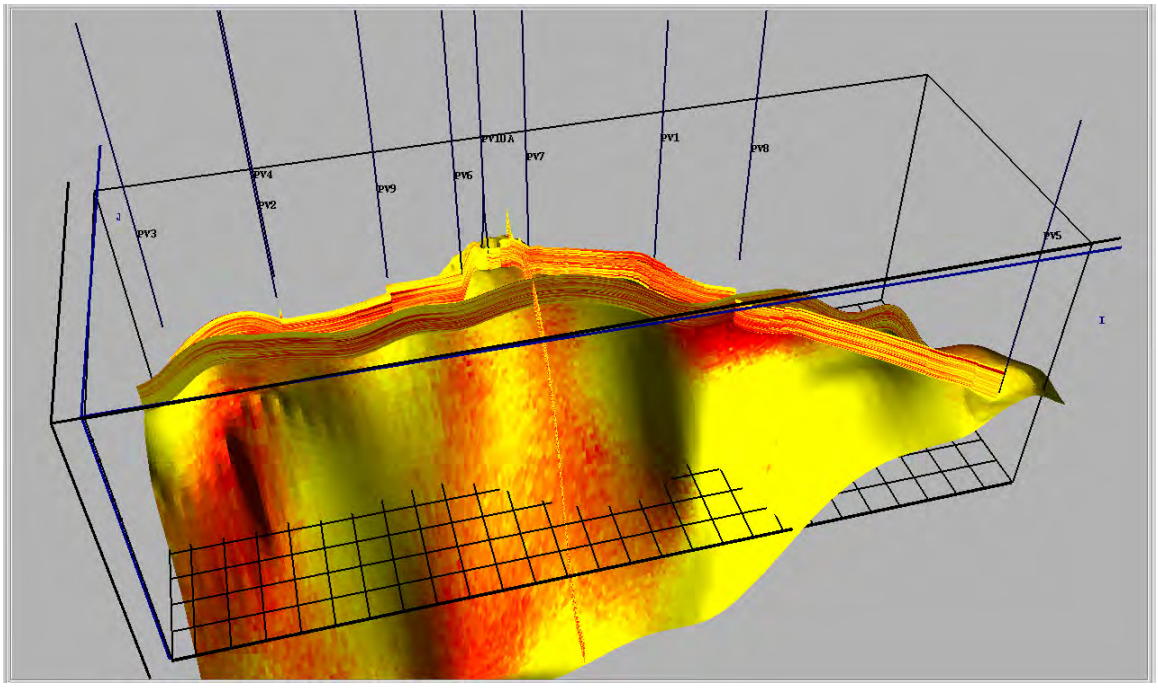


Fig. 4.26: 3D distribution map for total porosity for the P1 unit, Palm Valley NFR: a result of artificial neural analysis: view of bottom layer and cross-sections (Same value scales as in **Fig. 4.25**).

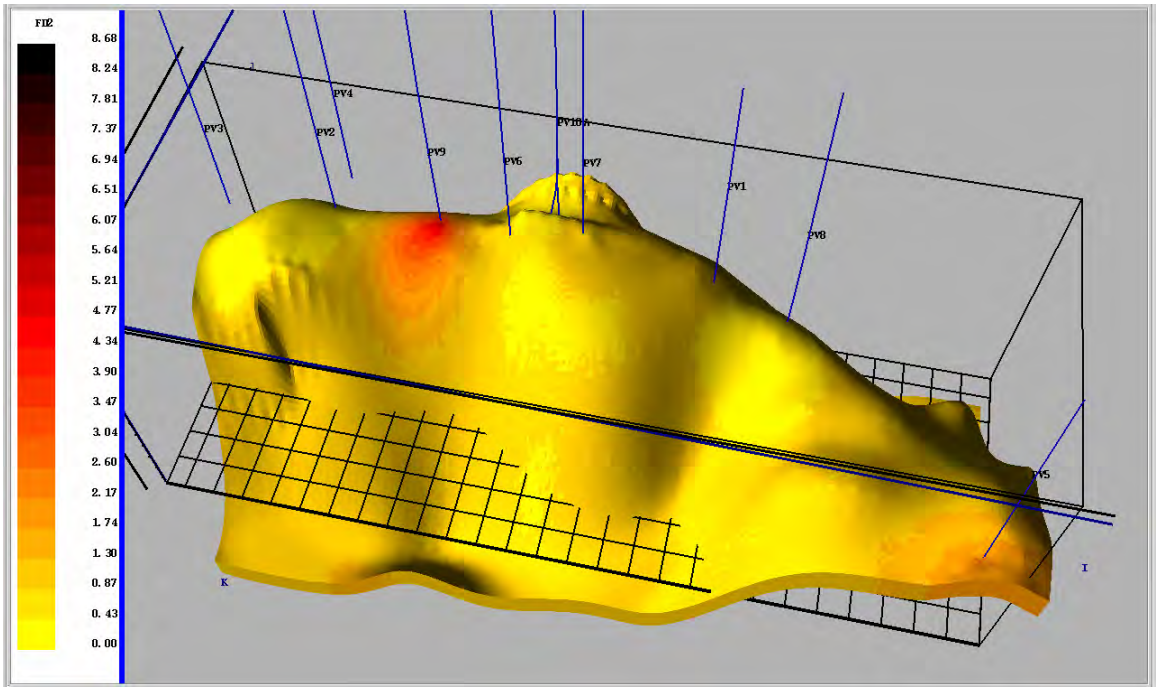


Fig. 4.27: 3D distribution map for fracture density for the P1 unit, Palm Valley NFR: a result of artificial neural analysis: view of top layer.

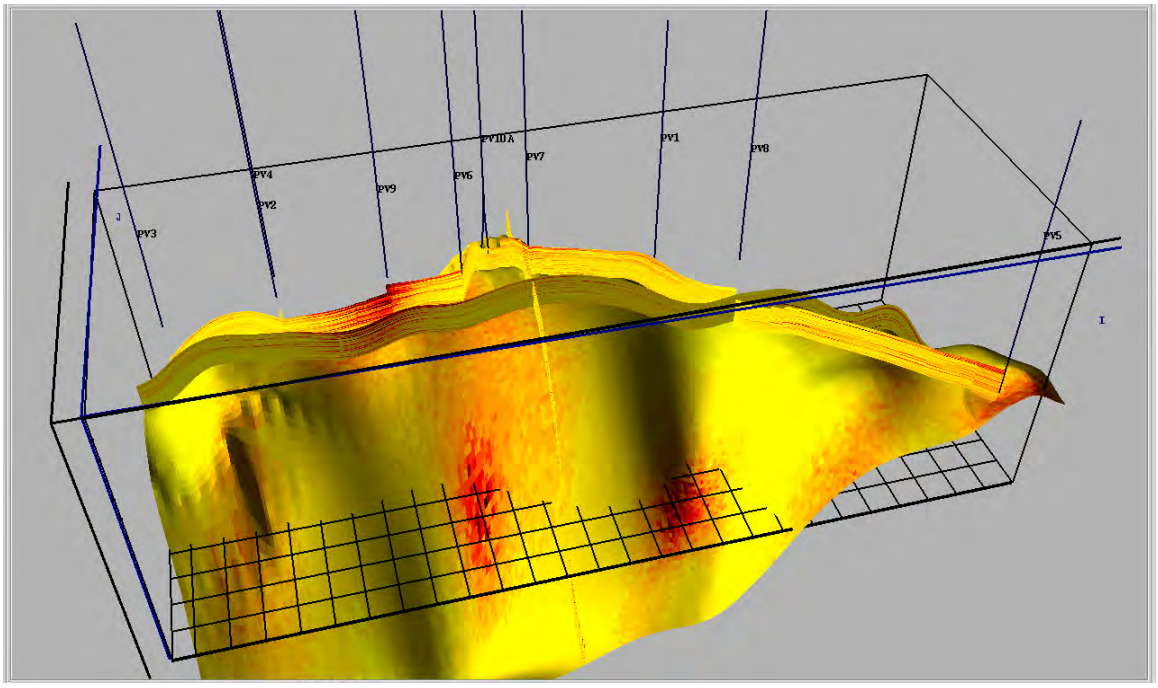


Fig. 4.28: 3D distribution map for fracture density for the P1 unit, Palm Valley NFR a result of artificial neural analysis: view of bottom layer and cross-sections (Same value scales as in **Fig. 4.27**).

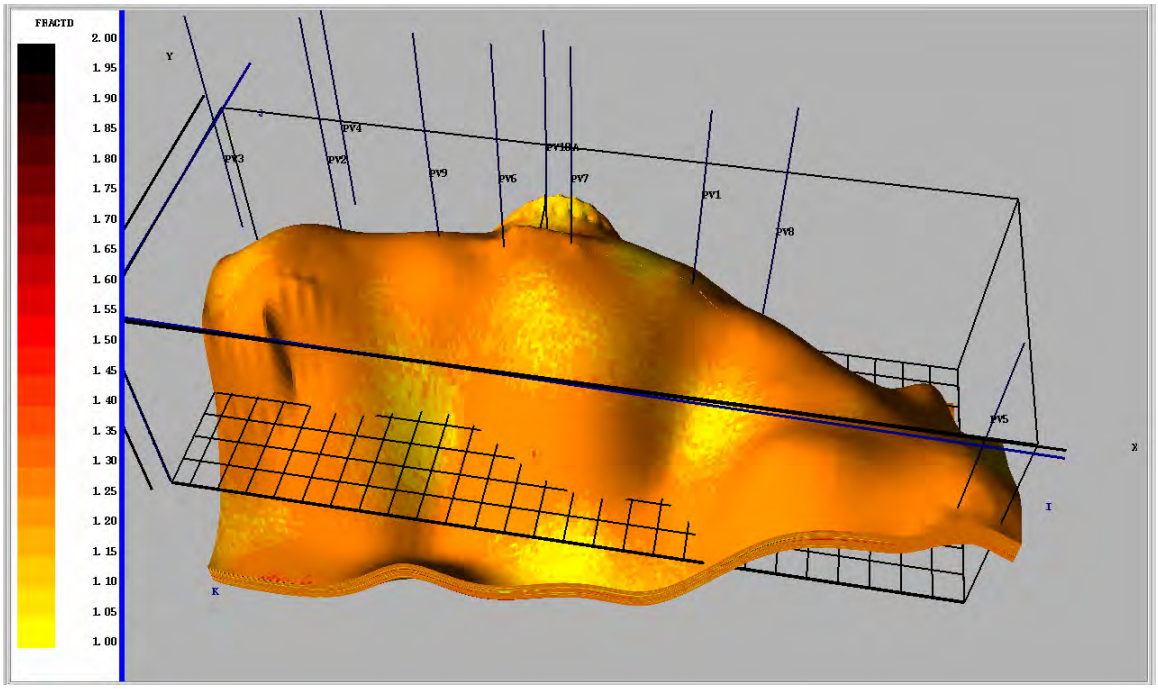


Fig. 4.29: 3D distribution map for multifractal dimension for the P1 unit, Palm Valley NFR: a result of artificial neural analysis: view of top layer.

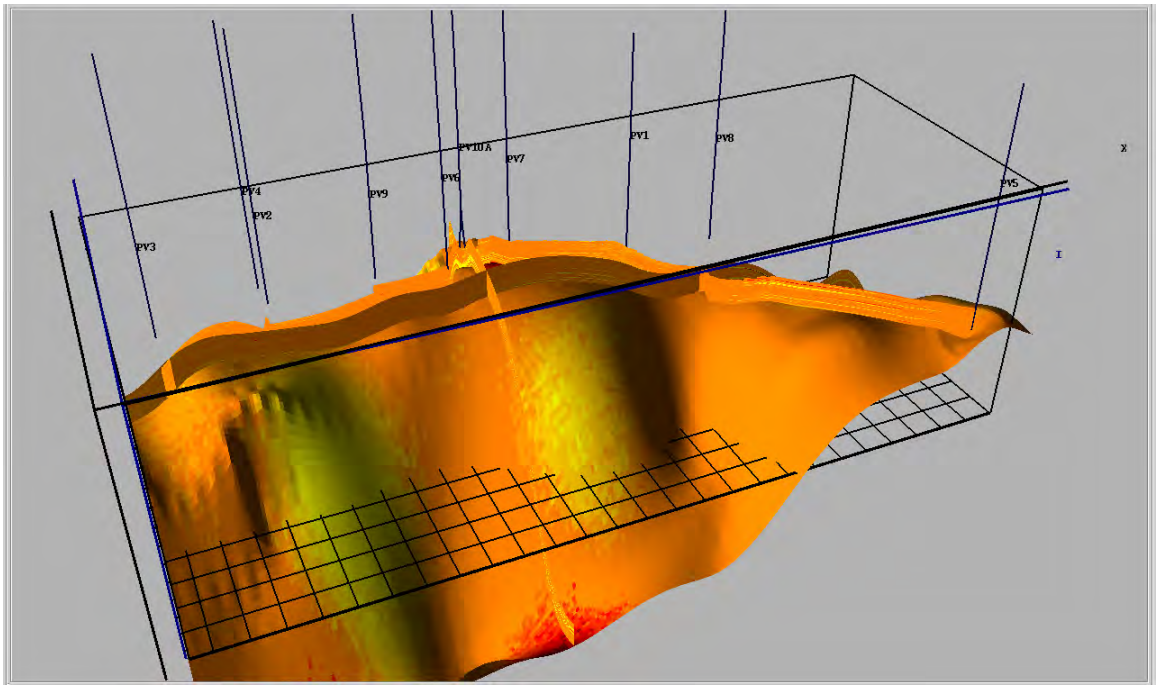


Fig. 4.30: 3D distribution map for multifractal dimension for the P1 unit, Palm Valley NFR: a result of artificial neural analysis: view of bottom layer and cross-sections (Same value scales as in **Fig. 4.29**).

4.7.5 Results of the Hybrid Stochastic Simulation

混合随机模拟结果

In this final stage, the hybrid stochastic simulation integrates all characterised fracture behaviours to hierarchically generate DFN of the reservoir. Modelling area for the stochastic simulation is set as a rectangular block that fully covers the geological P1 unit (**Fig. 4.31**). First, conditional fractures and major faults, whose radii bigger than 500m, are simulated in the entire reservoir (Run 1). Then, the reservoir is divided into five modelling regions, where smaller fractures are stochastically realised (Runs 2 to 6) (**Fig. 4.31**).

首先，在整个油藏上模拟大于500米的裂缝和断层。
其次，油藏分为5个建模区域，小裂缝在其中随机实现。

The output DFN, containing all fractures that intersect the modelling area, is displayed in **Fig. 4.32**. Fractures are represented by circular discs, where details of the disc centre coordinates, orientation and radius are known. For better visualisation, results from every hierarchical simulation (Runs 1 to 6) are individually demonstrated. Variances in fracture density between different regions can be clearly recognised. Major faults are shown in **Fig. 4.33**. Medium fractures generated in the five sub-regions are

shown in **Fig. 4.34** to **Fig. 4.38**. All the medium-scaled fractures in the reservoir are again summarised in **Fig. 4.39**.

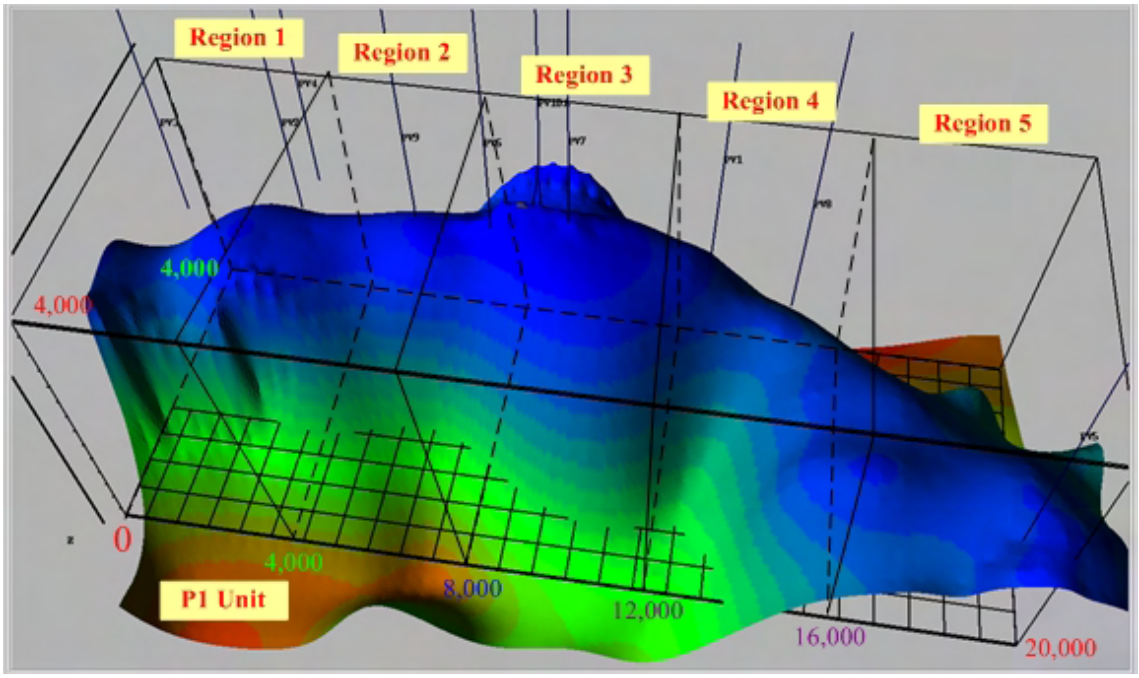


Fig. 4.31: Modelling area for hybrid stochastic simulation of Palm Valley NFR, including five sub-regions for nested simulation. The rectangular block covers the geological P1 unit.

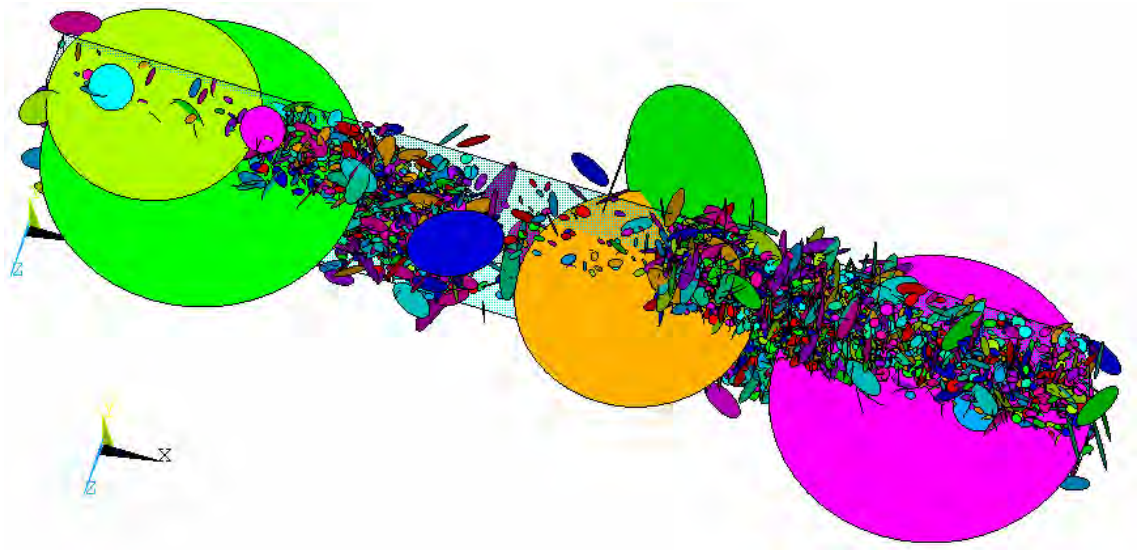


Fig. 4.32: Final fracture model, Palm Valley NFR: showing all fractures generated from the hybrid stochastic simulation (x 0 to 20000m east to west, y: 0 to 4000m south to north, z: 1000m to 2000m true vertical depth).

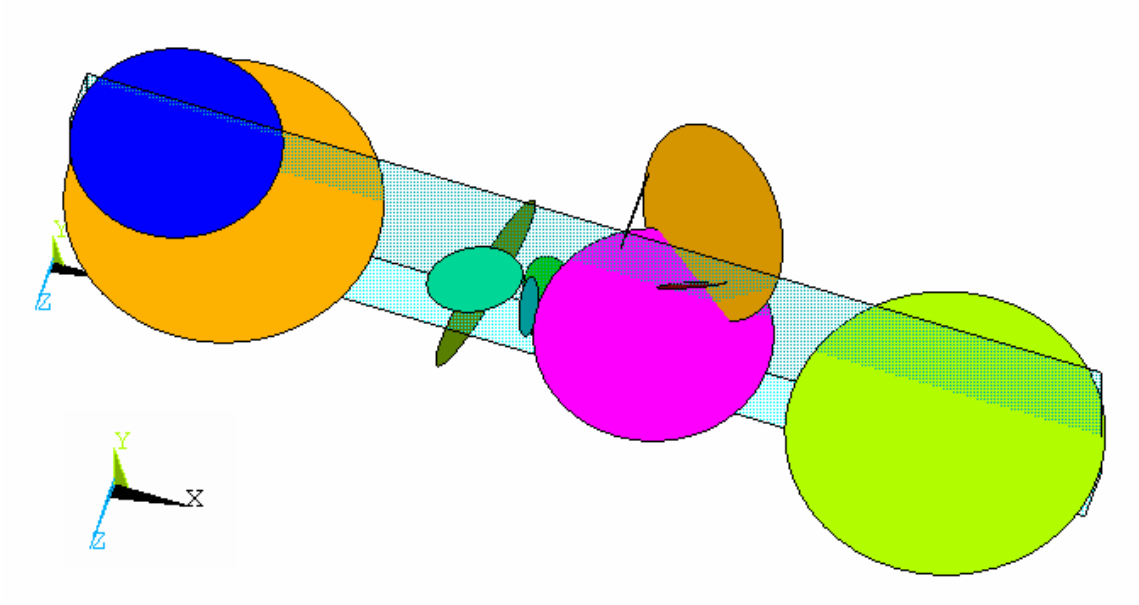


Fig. 4.33: Major faults in Palm Valley NFR: showing fractures generated from the first run of the hierarchical simulation (to simulate reservoir-scaled fractures in the whole reservoir) (x: 0 to 20000m east to west, y: 0 to 4000m south to north, z: 1000m to 2000m true vertical depth).

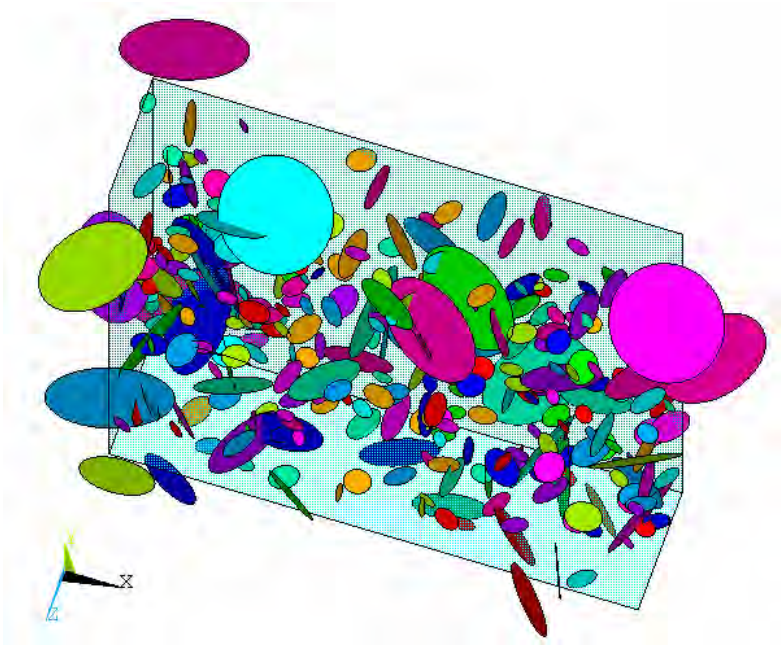


Fig. 4.34: Medium-scaled fractures in region 1, Palm Valley NFR: showing fractures generated from the second run of the hierarchical simulation on a portion of the reservoir (x: 0 to 4000m east to west, y: 0 to 4000m south to north, z: 1000m to 2000m true vertical depth).

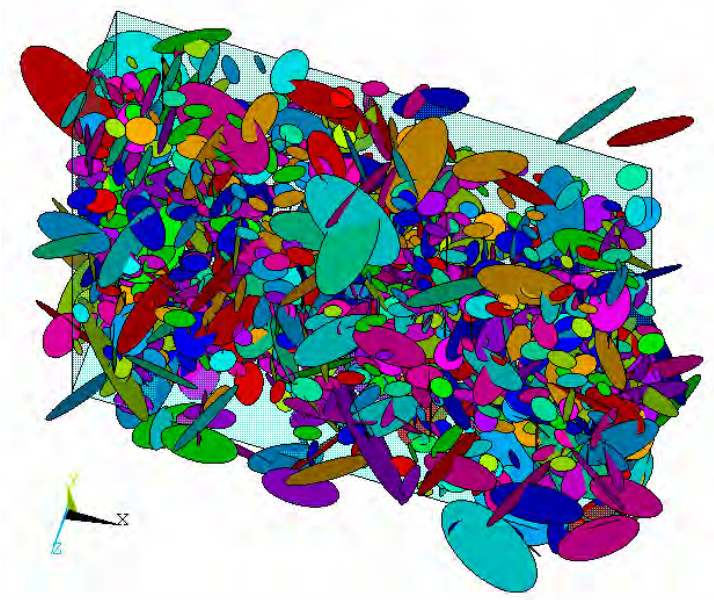


Fig. 4.35: Medium-scaled fractures in region 2, Palm Valley NFR: showing fractures generated from the third run of the hierarchical simulation on a portion of the reservoir (x: 4000m to 8,000m east to west, y: 0 to 4000m south to north, z: 1000m to 2000m true vertical depth).

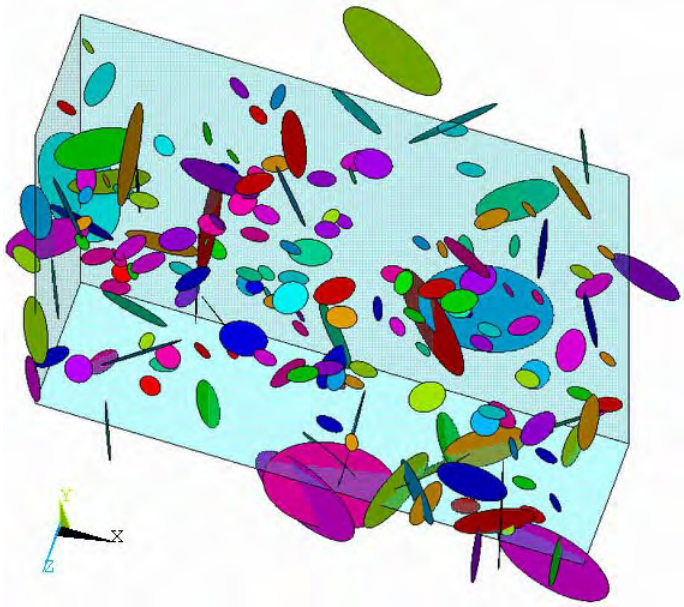


Fig. 4.36: Medium-scaled fractures in region 3, Palm Valley NFR: showing fractures generated from the fourth run of the hierarchical simulation on a portion of the reservoir (x: 8,000m to 12000m east to west, y: 0 to 4000m south to north, z: 1000m to 2000m true vertical depth).

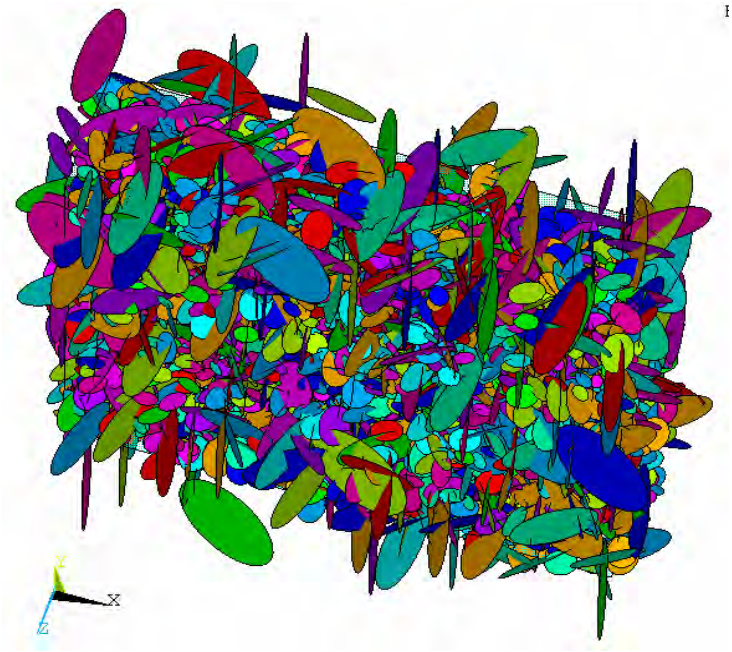


Fig. 4.37: Medium-scaled fractures in region 4, Palm Valley NFR: showing fractures generated from the fifth run of the hierarchical simulation on a portion of the reservoir (x: 12000m to 16000m east to west, y: 0 to 4000m south to north, z: 1000m to 2000m true vertical depth).

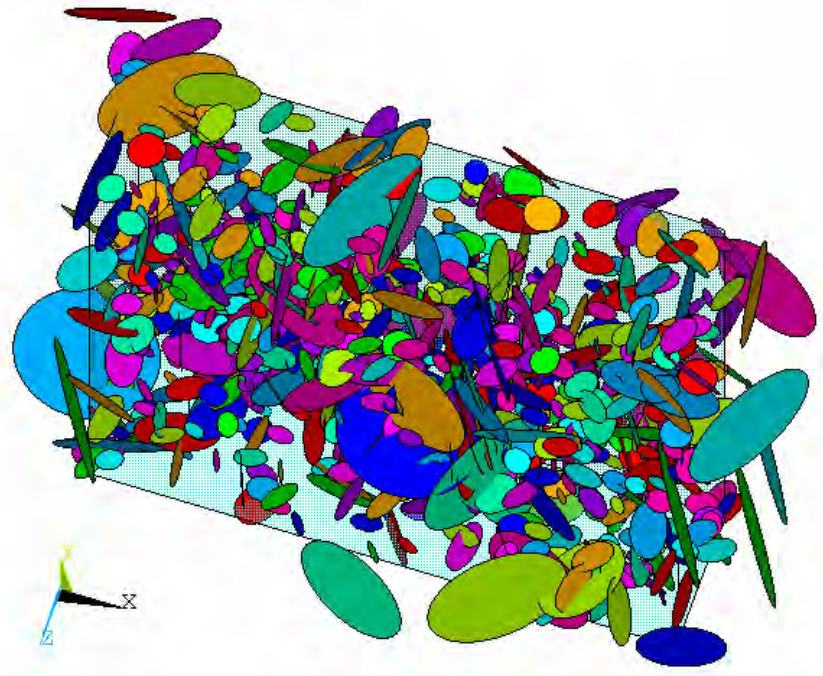


Fig. 4.38: Medium-scaled fractures in region 5, Palm Valley NFR: showing fractures generated from the sixth run of the hierarchical simulation on a portion of the reservoir (x: 16000m to 20000m east to west, y: 0 to 4000m south to north, z: 1000m to 2000m true vertical depth).

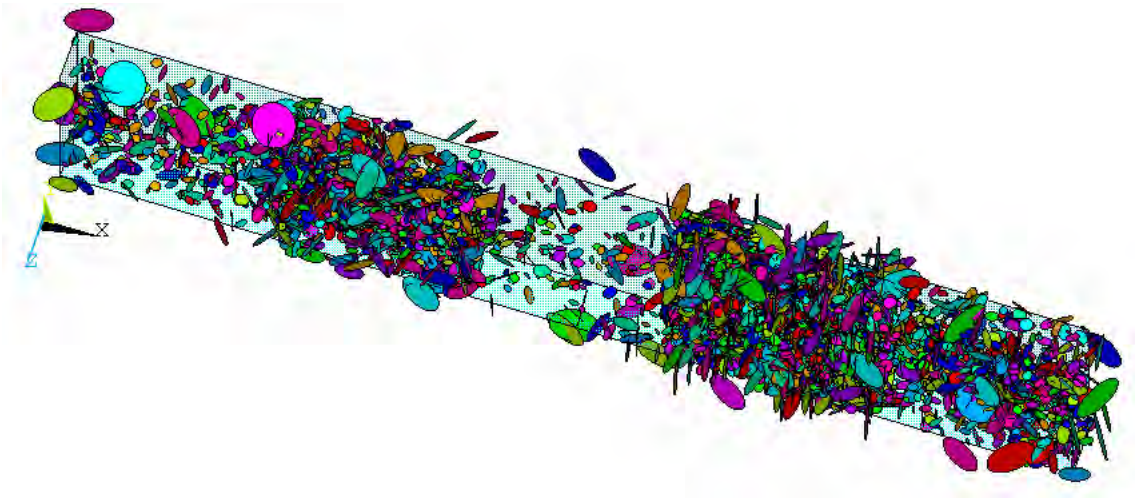


Fig. 4.39: Medium-scaled fractures in the whole model, Palm Valley NFR: showing all fractures generated from the second to sixth runs of the hierarchical stochastic simulation (x: 0 to 20000m east to west, y: 0 to 4000m south to north, z: 1000m to 2000m true vertical depth).

4.8 DISCUSSIONS
讨论

The case study has been used to demonstrate procedure and application of the hybrid neuro stochastic simulation for characterising and modelling NFR. It has been observed that the hybrid neuro stochastic simulation is an integrated approach. Various techniques have been systematically combined to produce a realistic fracture model for the reservoir. In addition, all available field data (e.g. seismic, well logs, cores and borehole images) have been essentially utilised. Additionally, from procedure and results of the case study, several observations have also been noted, as herein:

4.8.1 Fracture Characterisation

Throughout the characterisation part, data from different sources have been processed by statistical, spatial, fractal and FNN analyses. The data sources are of different scales and nature. The use of FNN minimises scale errors and assesses the spatial complexity of NFR (by producing comprehensive spatial fracture density distribution). The multi-scaled complexity of NFR is further assessed by discrete multifractal and hierarchical simulation. Accuracy of the fracture modelling is also

improved by characterisation of multimodal probability density functions and correlations for fracture dip and azimuth.

4.8.1.1 Discrete Multifractal

Discrete multifractal dimensions have been used to portray the complexity of fracture size. They are first computed directly from well imaging data by the box-counting method. The results vary dramatically from 1.0 to 1.9. There are possibly two implications for such variances. First, they are errors due to inaccuracy of the box-counting method. In the actual images, even though most lines are relatively straight, some of them are not. For such cases, the box-counting method could be simplistic and biased. This observation is proved by several fractal values that are less than the topological dimension (one). Second, such wide variance would further the argument for multifractal geometry, instead of single fractal dimension, in natural fracture characterisation. The result is similar to various investigations on fracture's multifractal, as described in **Chapter 3** (**3.2.2**) (Xie et al., 1999; Stach et al., 2001).

There have been a number of fracture models using single fractal dimension (e.g. Soares et al., 1996; Willis-Richards, 1996). Many other works recognised the importance of multifractal geometry in fracture modelling. For example, Cheng (1997) proposed several methods to study multifractal characteristics of a DFN. However, applications of NFR modelling using multifractal have not been previously presented. This is possibly because the conventional continuous multifractal spectrum is too difficult to be computed and utilised in a modelling procedure. In this work, in combination with FNN, discrete multifractal has been proved suitable to characterise multi-scaled NFR.

4.8.1.2 Fuzzy Neural Network

As demonstrated in the case study, FNN is shown as an intelligent and efficient method to interpolate and extrapolate well data along the wellbores and throughout the whole reservoir. It is especially suitable for NFR, which are extremely heterogeneous. As a result, spatial distributions of important fracture properties (fractal dimension and fracture density) could be derived from limited data available at the wellbores.

Success of a FNN relies on the amount of inter-dependent data sources. For example, for analysis along the wellbores, useful well logs are those providing physical indication on fracture presence. This is the reason why FNN was not applied for properties such as orientation. Apart from dipmeter log, few well logs can distinguish fractures of different dip and azimuth values. Therefore, the review of field data sources (as in **Chapter 2**) is pre-mandatory for a successful FNN application, where only suitable data are used.

As reviewed in **Chapter 1** (**1.4.3.2**), there exist previous models applying FNN analysis in NFR (e.g. Zellou et al., 1995; Zellou and Ouenes, 2001). In principle, the FNN scheme in this work is similar to the previous ones. However, there are differences, especially those concerning the output parameters. First, in this work, fracture density is analysed to assess the actual effect of fracture length and number of fractures (instead of fracture intensity that only covers number of fractures, regardless of sizes). Second, FNN is used to characterise discrete multifractal. The combination of FNN and multifractal geometry is novel in this work, proposing an effective mean to quantify complexity of NFR. Moreover, this work is also distinguishable from previous ones that it does not stop at FNN analysis. The output density map is furthered analysed, together with other characterised information, producing DFN that represent the NFR.

4.8.2 Fracture Modelling

In the modelling part, spatial complexity and heterogeneity of the NFR have been portrayed. Individual fractures are modelled as composite of location, orientation and size attributes. In previous works, each of the property is generated randomly based on simple probabilistic distributions (**Chapter 1: 1.4.2.2**, e.g. Willis-Richards, 1996; Tamagawa et al., 2002). In this work, upgrades of the generation scheme for all the properties have been demonstrated:

- Instead of the usual total random sampling (with or without clustering classification), generation of fracture location is based on the density distribution map. The ability to incorporate such continuum information into a discrete model is a significant improvement over other object-based and grid-based

一、裂缝的生成基于密度分布图。

models. The simulated fractures can now honour both spatial heterogeneity of the whole network (continuum) and behaviours of individual components (discrete).

二、裂缝方位和尺寸使用了多峰圆周分布和多元分数维。

- Generation of fracture orientation is based on multimodal wrapped distributions, which is a result of circular statistical analysis on the fracture data. Generation of fracture size is based on discrete multifractal. Both of these generation schemes are progressively advanced, compared to previously documented methods.

没有使用克里金插值和变差函数。而是使用了模糊神经网络。

Various geostatistical measurements such as kriging and model variograms could have been applied in a stochastic simulation for better spatial characterisation. However, they are avoided in this work due to several reasons. First, both kriging and model variograms contain biases and errors. They involve a great deal of assumptions, which are unrealistic in such complex systems as NFR. Second, there exist regression scheme by FNN that are much more comprehensive and reliable than kriging (as discussed in **Chapter 3: 3.4**). Besides, spatial distribution of fractures has been taken into consideration through fracture density and discrete multifractal dimension maps.

4.8.3 Modelling Limitations

建模的局限性

Several limitations of the method have also been recognised. First, the modelling procedure requires large amount of field data, at both wellbore scales and reservoir scales. It is understood that confidence levels in characterisation results are dependant on availability of representative data (e.g. in statistical analysis on fracture orientation). However, neural analysis is especially 'data demanding'. The consequence is that the whole process would be considered more suitable for well-developed fields.

Second, there are many inherent disadvantages of stochastic simulation, which have been discussed in **Chapter 1** (**1.4.2.2**). Examples include uncertain distributions away from the wellbores and assumptions of statistical distributions that might not agree with the actual data. In addition, stochastic simulation cannot make effective use of complex geostatistical measurements such as variograms. It can reflect model variograms of fracture orientation and size. However, only one set of rules can be

applied: either probability density function of the fracture properties or their model variograms.

4.8.4 Modelling Validation

模型验证

Stochastic models have been argued to be able to reproduce behaviours of the observed DFN (**Chapter 1: 1.4.2.2**, with reference to Long et al. (1991), Olsson et al. (1992) and National Research Council (1996)). In addition, the hybrid neuro stochastic simulation has been demonstrated to replicate many indicative measurements, such as local fracture density and statistical distributions. However, validation of the DFN from the stochastic simulation model remains an issue. This discussion concerns two most common methods for such validation: via direct comparison or via fluid-flow simulation.

First, it is almost impossible to directly compare the result with the target NFR, because the actual fracture system is not obtainable. It is also impractical to compare generated fractures with observable information such as major faults from seismic, fracture traces and local density at wellbores. One reason refers to randomness of the fracture generation that exact match is hard to be attained. Besides, the hybrid method has been formulated such that all experiential information, especially large-scaled features, could be included as conditional data.

The only viable validating option is, thus, to compare results of fluid flow simulation of the fracture model with measurable production and pressure data. Even though this method targets the important integral effect for any reservoirs (production), the validation is still indirect. It does not confirm actual details of fractures. Furthermore, the result is dependent on correct simulations of fluid flow, with many complexities to formulate. Examples include single-phase flow through matrix and fracture interfaces, flow through interconnected fractures, preferential flow of different phases in fractures and in matrix.

4.9 FINAL REMARKS

The hybrid neuro stochastic method for modelling DFN in NFR has been presented and discussed. It is an integrated and data-driven modelling method, which can combine continuum distributions (e.g. density and fractal) with statistical distributions and correlations of discrete fracture properties. This integration, which is supported by the comprehensive characterisation procedure (by FNN), accounts for perceptive and complete DFN model. The methodology represents a great improvement over other object-based stochastic simulation as well as all grid-based fracture models. The fracture simulation process can be repeated throughout the development of a field. The more data available, the more accurate the result is expected to be.

However, several inherent limitations remain; for example, there are lacks of ability to utilise sophisticated experimental spatial statistics, such as variogram, correlogram, rodogram and madogram. The issue of validation for stochastic simulation is also proved difficult to overcome.

CHAPTER 5 - MODELLING OF NATURALLY FRACTURED RESERVOIRS BY CONDITIONAL GLOBAL OPTIMISATION

利用全局优化技术建模

5.1 OVERVIEW

In **Chapter 4**, the first module of NFR modelling of hybrid stochastic simulation has been described. By integrating hybrid modelling and FNN to combine discrete and continuum information, it has been shown to be one of the most comprehensive NFR modelling methodology to date. Nevertheless, several disadvantages have been identified, most notably validation and the ability to utilise geostatistical variograms.

模型的验证、
地质统计变差函数的使用

In this chapter, an object-based conditional global optimisation is formulated to overcome the shortcomings of the stochastic simulation. The optimisation method is self-validated; offers great flexibility and hybrid integration ability; and utilises all fracture information as characterised in **Chapters 2** and **3**, including variograms and results of FNN analysis. It is designed to not only enhance results of the stochastic simulation but also outweigh other modelling methods presented in many engineering and geoscience disciplines.

The chapter begins with theoretical background of a general optimisation process and the global optimisation of simulated annealing. This is followed by formulation and procedure of the object-based conditional global optimisation for NFR modelling. This includes how and why individual components of the model (problem representation, objective function, initialisation, modification and stop criteria) are set up to satisfy the modelling objectives. Finally, applications of the object-based conditional global optimisation model in reproducing and predicting DFN are demonstrated via a case study.

5.2 THEORETICAL BACKGROUND OF GLOBAL OPTIMISATION
全局优化的理论背景

5.2.1 General Optimisation Process
一般优化过程

Optimisation is the process of finding minimum or maximum solutions for a mathematical function. It includes calculus of variations, control theory, convex optimisation, decision theory, game theory, linear programming, queuing systems, network analysis and Markov chains [http://mathworld.wolfram.com]. Stochastic optimisation refers to an optimisation process of a function in which randomness is present. Examples of various stochastic optimisation methods are greedy search, taboo search, stochastic approximation, stochastic programming, genetic algorithm and simulated annealing.

A general optimisation process involves a series of trials and errors. The function to be optimised is termed objective function. In a typical modelling task, where the aim is to produce a realisation that matches the target, their differences define the objective function to be minimised. Starting from an initial guess, a number of realisations are generated, each of which corresponds to a new objective function value. The generation is repeated until the minimum value of objective function is established. A general procedure of an optimisation program is illustrated in **Fig. 5.1**. The generation procedure is essential for an optimisation, as it determines if the objective function can be optimised and speed of the optimisation process.

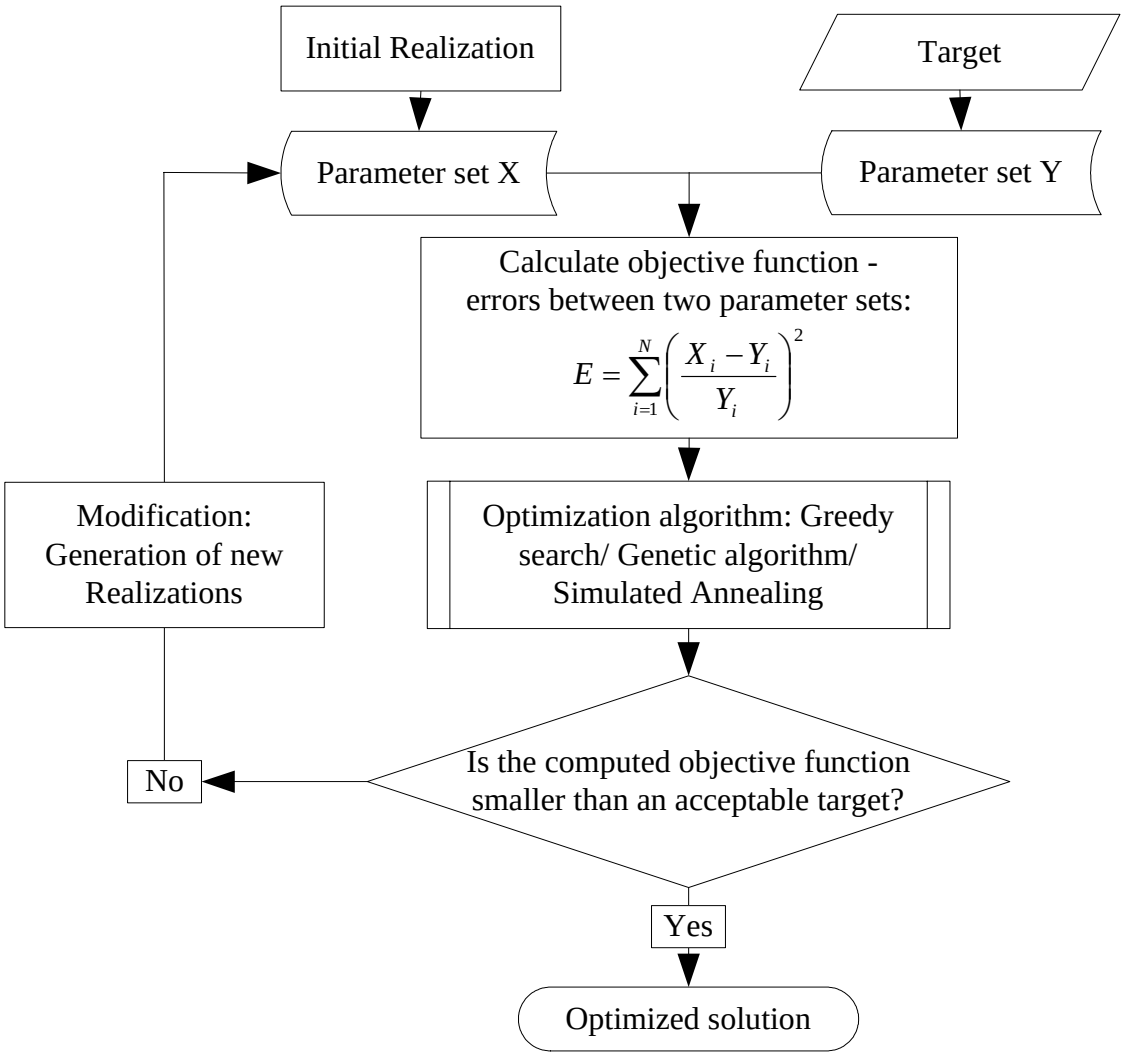


Fig. 5.1: Procedure for a general optimisation simulation. Different optimisation algorithms possess different schemes for modification and objective function minimisation.

返回首页

随机优化方法 贪婪搜索

One of the simplest forms of stochastic optimisation methods is greedy algorithm 穷举搜索 or exhaustive search. As the name suggested, iterations are carried out in a very random manner. For each iteration, a new realisation is computed from previous one (base). If there is a decrease in values of the objective functions, the new realisation becomes base for next iterations. The algorithm stops when the objective function does not change after a certain number of iterations (minimisation attained). It also stops if total number of iterations exceeds a limit (can not reach optimum value). For a complex problem, this method usually does not produce good results as it could be trapped into a local

optimum. Greedy algorithm cannot guide the transformation out of the local to the global optimum due to its total random characteristics.

5.2.2 Global Optimisation - Simulated Annealing

模拟退火的先进之处在于它接受所有的生成（以不同的概率）这样加速了收敛过程避免了陷入局部优化。

Unlike simple algorithm such as exhaustive search, advanced global optimisation algorithm of simulated annealing accepts all generations with a probability. This mechanism facilitates speed of convergence and avoids being trapped at local optima.

Kirkpatrick et al. (1983) introduced simulated annealing to complex problems in combinatorial optimisation. Since then, it has been used in a variety of problems that involve finding optimum values of a function of a very large number of independent variables. The basic concept of simulated annealing originates from physical process of metallurgical annealing. An annealing process occurs when a metal in a heat bath is initially at high temperature and is slowly cooled. At first, all particles are distributed randomly in a quasi-liquid state. As temperature drops, particles arrange themselves in a low energy ground state (i.e. at or very close to the global minimum of energy), forming crystal. If the cooling process is too rapid, equilibrium conditions are not always maintained, a crystal is not form and the total energy of the system is not at minimum (Metropolis et al., 1952; Sen and Stoffa, 1995).

Simulated annealing optimisation is formulated based on the above annealing algorithm. Model parameters of an optimisation problem play the role of particles in an idealised physical system. Objective function (E) is an analogue of the energy function, which is to be minimised. Starting from an initial state, the system is perturbed at random to a new state in its neighbourhood, from which change in value of the objective function (ΔE) can be quickly calculated. If this change represents a reduction in E, the transformation to new state is accepted. If it represents an increase in E, the transformation is accepted with a specified probability, *P(accept)*:

$$P(accept) = \begin{cases} \exp\left(\frac{-\Delta E}{T}\right) \leftarrow (\Delta E > 0) \\ 1 \leftarrow otherwise \end{cases} \tag{5.1}$$

where T is a control parameter, which corresponds to absolute temperature in the physical process of annealing.

According to Deutsch and Journel (1992), a transformation is better to be as random as possible. The modification is kept small so that new realisation is in the neighbourhood of previous ones. The acceptance probability determines whether the transformation is counted or not. If not, another new state is generated. This generation-acceptance process provides a mechanism that enables simulated annealing algorithm to avoid becoming trapped in local minima in its search for the global minimum (Goldstein and Waterman, 1988; Tovey, 1988; Aarts and Korst, 1989; Deutsch and Cockerham, 1994).

If the generation-acceptance progression is repeated a large number of times at a value of T, it can be shown that a steady state is attained after that value of T (Sen and Stoffa, 1995). When T is reduced slowly (cooling), new equilibria are achieved. Eventually, the system converges to an optimum equilibrium that corresponds to the minimum objective function. Theoretically, there exist cooling schedules that are slow enough to guarantee convergence to the global minimum (Geman and Geman, 1984; Collins et al., 1988). The following linear schedule is simple and yet effective, where α_1 is a reduction factor or learning rate parameter:

$$T_{new} = \alpha_1 . T_{old} \tag{5.2}$$

In general, a simulated annealing program contains a number of parameters that control the search and acceptance algorithm: rate of transition, maximum number of iterations required to reach steady state at a constant temperature, temperature reduction factor and objective function limit. To guarantee optimal solution, equilibrium conditions are maintained and annealing process is kept gradual. The maximum number of iterations under a constant temperature is set to be large and reduction factor close to one (1). However, all those requirements result in longer simulation time. Thus, an appropriate annealing schedule and effective method of system perturbing is problem-specific and requires experimentation (Laarhoven and Aarts, 1987).

5.2.3 Global Optimisation and Fracture Network Modelling

全局优化和裂缝网络建模

Global optimisation has effectively solved complex problems in combinatorial optimisation, acquiring optimum values of functions of large number of independent variables (Sen and Stoffa, 1995). It is especially suitable for such complicated problems as modelling DFN, where there are many parameters and statistics to optimise. The algorithm brings about a number of modelling advantages compared to previous methods, especially when combined with data characterisation by geostatistical and artificial neural analyses. First, it contains no mathematical assumptions on statistical distributions of fracture properties. Second, it offers great data integration scheme and improved simulation result. With correct choice of statistics and measurements as components for the objective function, result of a global optimisation algorithm is self-validated.

优点：
一、没有裂缝属性符合概率分布的假设。
二、全局优化算法是自我验证的。

The important feature of using global optimisation for DFN modelling is problem representation. When a typical procedure as in **Fig. 5.1** is considered, the actual DFN is represented as "target" of the optimisation program. The differences between the target and any generated realisation are formulated in "objective function". The optimisation algorithm continuously modifies DFN realisations, guiding the objective function to minimisation. The minimum value is equivalent to achieving the DFN, which is expected to be closed to the target.

There have been a limited number of works in literature applying simulated annealing to fracture modelling (Farmer, 1992; Sahimi, 1995; Day-Lewis et al., 2000; Guerreiro et al., 2000). However, as discussed in **Chapter 1** (**1.4.3.3**), previous models were too simplistic and insufficient for complex fractured system. Due to limitation in mathematical and computational capabilities, comprehensive models for actual complexity of NFR have not been developed to date.

5.3 OBJECT-BASED CONDITIONAL GLOBAL OPTIMISATION
基于目标的条件全局优化

Thanks to advantageous features as described in the previous **Section 5.2.3**, global optimisation is used for the NFR modelling task. The program consists of not only a global optimisation algorithm, but also the comprehensive fracture characterisation, FNN, object-based and conditional modelling. It is designed to improve upon the previous simulated annealing fracture models, as well as the previous hybrid stochastic simulation (**Chapter 4**).

5.3.1 Problem Representation and Optimisation Procedure
问题表述和优化过程

The object-based conditional global optimisation model is set up as in **Fig. 5.2**. As the first step of the object-based conditional global optimisation model, fracture characteristics that have been obtained from various geostatistical, spatial and artificial neural analyses (**Chapters 2** and **3**) are used to define the problem representation (conditional data, solution space and objective function) of the global optimisation. The object-based model or marked point process allows analysis and treatment of discrete fracture properties and individual fractures (**Chapter 4: 4.2**).

First, since the characterisation analyses are performed on the actual fractured network, its results portray the target for the optimisation. Conditional data relates simulated result with the actual network by maintaining the anchor points. Conditional data include observed fractures, measured fracture properties at specific locations (e.g. at wellbores) (as discussed in **Chapter 4: 4.4**). Solution space outlines boundaries for every fracture attribute, including reservoir model boundary, upper and lower limits for fracture location coordinates, orientation and size. Objective function combines all representative fracture statistics and behaviours. It defines the difference between simulated DFN realisation (guess) and the target (the actual NFR).

Next, the optimisation algorithm is performed to minimise the defined objective function. Starting from an initial DFN realisation, discrete fractures keep re-organising themselves, changing from one DFN realisation to another. Through out the

本页已使用福昕阅读器进行编辑。
福昕软件(C)2005-2007，版权所有，
仅供试用。

modifications, conditional data and solution space are preserved. When objective function is minimised, the final DFN realisation matches with the target (actual DFN).

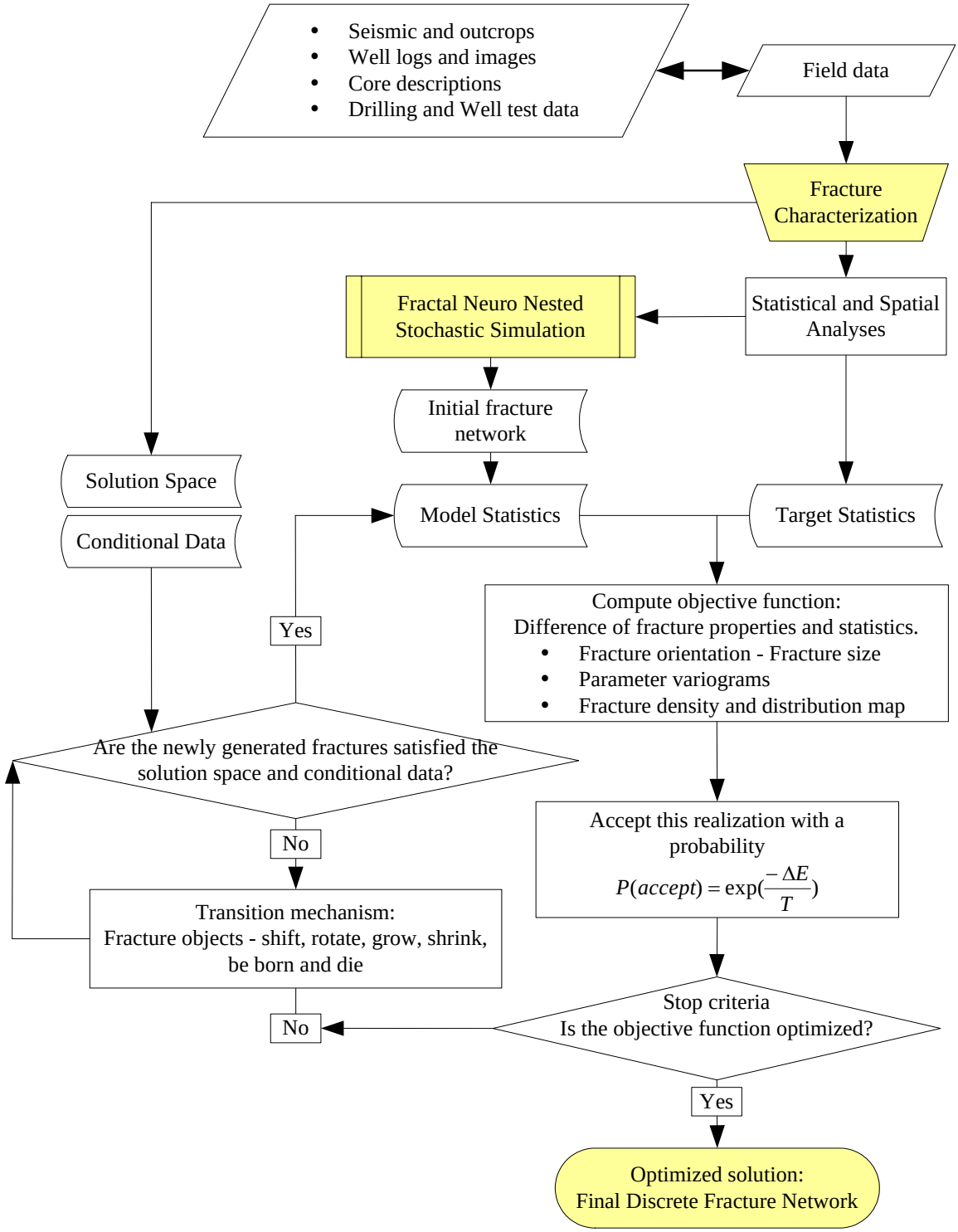


Fig. 5.2: Procedure for the object-based conditional global optimisation algorithm for a typical NFR modelling job.

返回首页

More details of objective function's formulation, initialisation, modification scheme and stop criteria are explained in subsequent sections.

5.3.1.1 Objective Function Formulation 目标函数的建立

The objective function represents statistical difference between generated DFN realisation and the target (*) (characterised fracture data from the field). It is composed of a weighted average of positive functions, as:

$$E = \sum_i w_i \cdot \left[\frac{z_i - z_i^*}{z_i^*} \right]^2 \tag{5.3}$$

where z_i denotes arbitrary components of the objective function. w_i is weighting factor of the component i ($\Sigma w_i = 1.0$). The weighting factors are chosen proportionally to importance of each statistics on convergence of the optimisation process.

Defining appropriate components of an objective function is the key to success of an optimisation model. It is desired that a large number of statistics and measurements to be included to fully portray the DFN. However, since too many components and inappropriate weighting factors might slow the optimisation down and prevent it from converging, only appropriate information should be used. In this work, objective function incorporates information of fracture density, statistics and spatial distributions of fracture location, orientation and size. Its components include total density, (local) density distribution map, semi-variogram, cross-variogram, modified multi histograms, mean, variance and correlation of orientation and size. Multimodal behaviour of fracture orientation as well as correlation between dip and azimuth angles are also considered. Non-parametric forms of distributions of orientation and size can also be used. Data of different nature are incorporated as independent components.

数学期望

While mean values signify mathematical expectations, they supply no information about the total size of individuals or the variations of properties among themselves and across the field. This is why histogram and variance are required. Semi-variogram is a popular second order moment that can effectively portray distribution of fracture

properties in space. Cross-variogram shows correlation between orientation and size. All of these measurements can be obtained from statistical and geostatistical analyses (as in **Chapter 3**). Fracture density points out not only average number of fractures but also relative size and spatial distribution of fractures. In a NFR, local density distribution map could be achieved by using FNN analysis (as in **Chapter 3**). General observations indicate that first order statistics (e.g. mean, modified multi-histogram mean and variogram distance) should correspond to small weight factors, compared to other second order moments and fracture densities.

The key feature of the object-based conditional global optimisation model is the above comprehensive objective function, which contains valuable information that defines the target system. All measurements could be obtained from available field data and the formulation is a data-driven process. This offers great flexibility, avoids many mathematical assumptions and facilitates the use of non-parametric density functions. With the use of ANN and improved statistical characterisation, target DFN is represented by more representative and more accurately acquired statistics and measurements. These are the most determinant factors that separate the object-based conditional global optimisation model to the previous optimisation and stochastic simulation methods.

For example, in contrast to most of previous continuum models, fracture intensity map has been already achieved by the use of comprehensive FNN (**Chapter 3**). Instead of being the final result, the intensity/ density distribution map now serves as one of many inputs for more accurate modelling job. In addition, unlike stochastic simulation methods, probability density functions of fracture properties are not required. The assumption for existence of the distribution is not needed, as there are other ways to identify characteristics of the fracture properties. Non-parametric distribution is one effective alternative, as it can be readily estimated from field data.

5.3.1.2 Initialisation 初始化

The stochastic simulation module is used to generate an initial DFN realisation. As discussed in **Chapter 4**, the simulation module is already capable of producing

consistent fracture models. The resulting DFN is further improved by not limiting to using probabilistic distributions and by introducing advanced spatial statistics such as semi-variogram and cross-variogram. It will be modified through the optimisation modification towards better representation of NFR target.

5.3.1.3 Modification - Transition Mechanism 修正—转化机理

The global optimisation algorithm systematically transfers DFN from current state to a new state, starting from the initial realisation and finishing when the objective function is minimised. A learning rate parameter dictates rigorousness of the modification, such that new and current states (two realisations) are distinguishable yet difference remains small (New state is in the neighbourhood of current state). This ensures smooth transition and helps achieving equilibria.

在转化的过程中，每一个离散裂缝对象有一种或多种行为：平移、旋转、增大、缩小、消失或者重新生成。

During the transition, each discrete fracture object exercises one or combination of the possible behaviours: shift, rotate, grow, shrink, die or be born while still stays within the solution space (**Chapter 4: 4.2**). The conditional data are kept unaltered. The algorithm continually observes overall fracture density to be within its pre-defined range. At any point where the density value is higher than the upper limit, fractures are forced to shrink or disappear. Similarly, if the fracture density falls below the lower limit, fracture size is enlarged. More fractures are inserted if it is required.

As in annealing process, some transition-controlling parameters govern speed of the generation-acceptance process (i.e. speed of the optimisation algorithm). They are maximum number of generation-acceptance iterations at a temperature (T) and temperature reduction factor (α_1). They are chosen such that there are enough transformations for equilibrium at each T, yet convergence is not too slow. Typically, the former ranges between 1000 and 10,000 while the later is closed to one. In the beginning, when objective function remains high and most modifications are accepted, rate of transition is high, fracture objects are varied dramatically. Later, when the objective function gets smaller, changes need to be minor to guarantee convergence.

For each modification, the new objective function is updated rather than re-computed. Value of the new objective function is calculated based on incremental variation and the old value. For example, when a fracture $z(x_i)$ is perturbed to $z'(x'_i)$ and total number of fractures is unchanged, semi-variogram is updated as:

$$\gamma_{new}(h) = \gamma_{old}(h) - \left\{ \begin{array}{l} \left[z(x_i + h) - z(x_i)\right]^2 - \left[z(x_i - h) - z(x_i)\right]^2 + \\ \left[z(x_i + h) - z'(x'_i)\right]^2 + \left[z(x_i - h) - z'(x'_i)\right]^2 \end{array} \right\} \quad (5.4)$$

If the total number of fractures is altered, an incremental variation caused by the change in number of fractures is added to the above equation (**Eq. 5.4**). The equation can be applied to other statistical quantities, such as mean, variance and cross-variogram. Moreover, continuum density values are only revised for those blocks that contain new and old fractures. First, the intersecting blocks are identified. Next, density values of every block are updated. When a region of large number of fractures is considered, this process drastically reduces computational time and resources.

5.3.1.4 Stop Criteria 停止界限

As the generation-acceptance process (transition mechanism) is repeated, value of the objective function reduces. The process stops when the objective function gets smaller than a pre-defined value, or when it does not significantly improved after several temperature changes. When maximum number of iterations at each temperature is exceeded and the process repeats for several temperature values, it can be reasonably assumed that the objective function has reached its global minimum (the annealing process has been "cooled" to the state of optimum energy).

If the minimised objective function is not smaller than the desired value, it is necessary to check if the chosen statistics and their relative weighting factors are representative for the target DFN. The simulation controlling parameters could also be adjusted. When the objective function is satisfactorily minimised, the final DFN realisation is recorded, which satisfies the overall modelling objectives.

5.3.2 Remarks

The object-based global optimisation model can incorporate both discrete data (e.g. distributions of fracture orientation and size) and grid-based data (e.g. fracture density map). The innovative hybrid integration adds both versatility and accuracy. On the one hand, it is important that discrete fractures and their individual properties are assessed and evaluated. On the other hand, continuum reservoir-scaled fracture and rock properties (e.g. lithology, fractal, density and permeability tensor) can also be included. This combination means longer and more complex modelling simulation. Its results, however, are more physically meaningful.

In general, the objective function contains components that are not only representative of the actual DFN, but also appropriately simple for good convergence. By minimising the objective function, the global optimisation has utilised data from different sources and scales to output a realistic model for reservoir fractures. The result will be further confirmed through a case study.

5.4 APPLICATION 应用

In the case study, fault map of Otsego County and the surrounding areas (New York, USA) is examined (**Fig. A.1** and **Fig. 5.3**) [http://www.nywaterfind.com]. Two different scenarios are designed to assess ability of the object-based conditional global optimisation model in reproducing and predicting fractured fields. In the first scenario, it is assumed that all necessary information on the fault map is obtainable, including a group of fractures as conditional data. The aim of the scenario is to reproduce the target fault map, illustrating and confirming the modelling procedure, especially the appropriate formulation of objective function. In the second scenario, it is assumed that data are limited to the previous group of conditional fractures. The purpose is, thus, to demonstrate the model's ability to produce prediction of DFN map from the limited available data.

5.4.1 Otsego Fault Map

This region has dimension of 100km (east west) by 70km (north south), which covers parts of four counties of Otsego, Chenango, Delaware and Schoharie in the New York State, USA. An overall observation indicates that faults in the region tend to be distributed in three different directions at approximately 30°, 80° and 135°. Fracture sizes are diverse. There are many segmented fractures propagating in lines, which could lead to speculation that there existed long faults before being fragmented. This explains the absent of noticeable correlations between orientation and present length. Evidences of fracture orientation and fragmentation suggest that the region have been through several tectonic regime changes. Fracture distribution is rather even, except in the northwest where it is visibly denser.

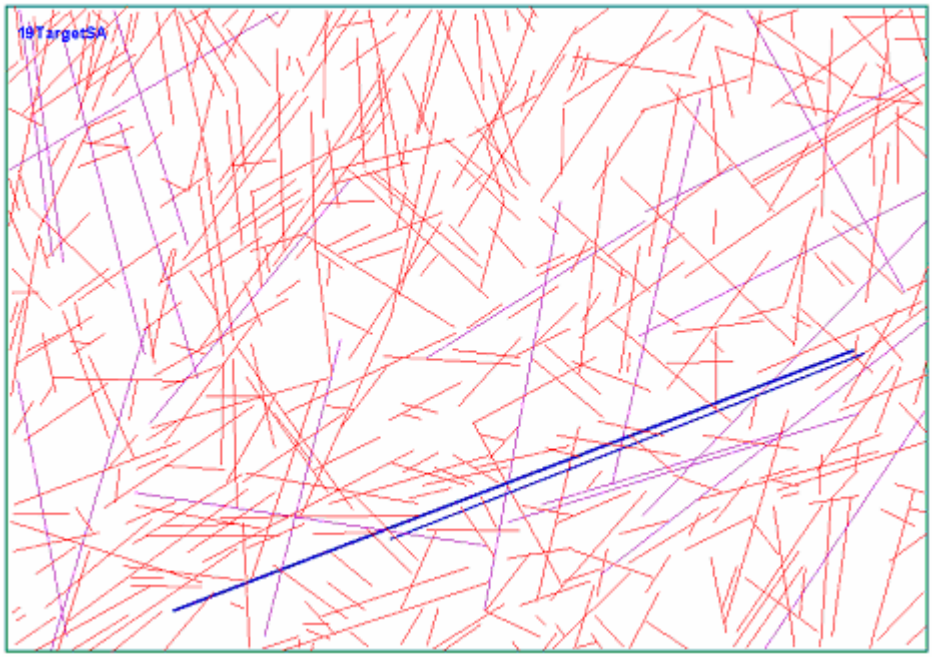


Fig. 5.3: Fault map of Otsego County and the surrounding areas (New York, USA) (digitisation of **Fig. A.1**), with assumptions of some large-scaled fractures.

There are 442 fractures in the target network. Each fracture line is portrayed by x-y coordinates of centre (x, y), orientation (θ) and fracture half-length (Rad). The object-based composite model for the 442 fractures is:

$$M = M_F \otimes 442\{X \otimes Y \otimes \theta \otimes Rad\} \tag{5.5}$$

Following the prescribed procedure (**Fig. 5.2**), the first step is surveying the fracture surface and computing target parameters and statistics. The aim is to identify behaviours of the target network and define a characteristic objective function. Formulation of the objective function is a data-driven process, adding versatility and accuracy to the general modelling module.

The hybrid stochastic simulation is then used to generate an initial DFN. The global optimisation algorithm continuously modifies the initial realisation to minimise the objective function. The final DFN will be compared with the target original.

5.4.2 Reproduction Scenario 重建方案

Through this reproduction scenario, procedure and considerations of the modelling method are illustrated. It is shown how fracture characteristics are studied from various data analyses and how such information is applied in the global optimisation model to produce a representative DFN. The resulting network is compared with the actual Otsego fault map. A comparison with the stochastic simulation model is also carried out.

5.4.2.1 Fracture Data Analysis

In the first step of fracture characterisation, geometric properties such as location, orientation and size are statistically analysed (according to methods described in **Chapter 3**). The aim is to examine the target DFN, identifying factors that define its characteristic behaviours and combine them as components of the objective function. In this scenario, with the large amount of data, it is possible to estimate probability distributions of all fracture properties. Then, their spatial distribution and inter-correlation are evaluated.

首先，是裂缝属性的概率分布；
然后，评价其空间分布和相关性。

Basic statistics

A number of uni-variate statistics for fracture geometric properties are presented in **Table 5.1**. The basic statistics illustrate each property's mean, standard deviation,

upper and lower bounds. Correlations and covariances for the same properties are shown in **Table 5.2**. For example, small values of correlations (~0.03) indicate that fracture radius is not directly interrelated with either x or y coordinates. Radius and orientation are better correlated (~0.12). In general, the statistics are simple and only serve as initial data assessments.

Statistics	X	Y	Orientation	Radius
Min	5.50E+00	4.50E+00	0	3.5
Mean	3.92E+02	3.00E+02	78.508	42.868
Median	3.70E+02	3.05E+02	73.464	30.433
Max	8.20E+02	5.75E+02	179.31	325.74
Variance	5.78E+04	3.01E+04	2337.3	1386.3
Standard Deviation	2.40E+02	1.74E+02	48.346	37.233
Skewness	1.45E-01	-4.60E-02	0.363	2.433
Kurtosis	-1.16E+00	-1.27E+00	-0.953	10.037

Table 5.1: Summary of statistics for fracture location x-y coordinates, orientation and radius (Otsego fault map - Reproduction scenario).

Correlations	X	Y	Orientation	Radius
X	1	-0.06487	0.077107	0.029286
Y	-0.06487	1	0.024042	-0.026524
Orientation	0.077107	0.024042	1	-0.121753
Radius	0.029286	-0.026524	-0.121753	1
Covariances	X	Y	Orientation	Radius
X	57818.9988	-2707.8507	896.3808	262.194
Y	-2707.8507	30136.1317	201.78	-171.439
Orientation	896.3808	201.78	2337.341	-219.167
Radius	262.1941	-171.4392	-219.1665	1386.322

Table 5.2: Correlations and covariances for fracture location x-y coordinates, orientation and radius (Otsego fault map - Reproduction scenario).

Statistical analysis of fracture size (Rad)

Fracture radius histogram indicates roughly a lognormal distribution, whose probability density function is plotted in **Fig. 5.4**. Further analysis is done by graphing

empirical distribution function against the theoretical distribution (i.e. correlation plot) and the approximate 95% and 99% Kolmogorov-Smirnov bounds. Parameters of the theoretical distribution are estimated using maximum likelihood (Silverman, 1998). The Kolmogorov-Smirnov statistic is the maximum absolute deviation between the above correlation plot and the line y = x. When there is a perfect fit, the plotted data should lie along line y = x, within the bounds [http://mathworld.wolfram.com]. **Fig. 5.5** confirms lognormal distribution for fracture radius.

Mathematical equations for the lognormal density distribution of radius are presented below (**Eqs. 5.6** and **5.9**), where M_L and S_L correspond to location and shape parameters, respectively. They can be solved from **Eqs. 5.7** and **5.8**, either by using maximum likelihood method or from mean (μ) and standard deviation (σ) of the data set.

$$P(Rad) = \frac{1}{S_L \cdot Rad \cdot \sqrt{2\pi}} \cdot \exp(-\frac{(\ln Rad - M_L)^2}{(2 \cdot S_L{}^2)}) \tag{5.6}$$

$$\mu = \exp(M_L + 0.5 S_L{}^2) \tag{5.7}$$

$$\sigma = \{\exp(S_L{}^2 + 2M_L) \cdot [\exp(S_L{}^2) - 1]\}^{0.5} \tag{5.8}$$

$$P(Rad) = \frac{1}{0.75 \cdot Rad \cdot \sqrt{2\pi}} \cdot \exp[-\frac{(\ln Rad - 3.477)^2}{(2 \cdot 0.75^2)}] \tag{5.9}$$

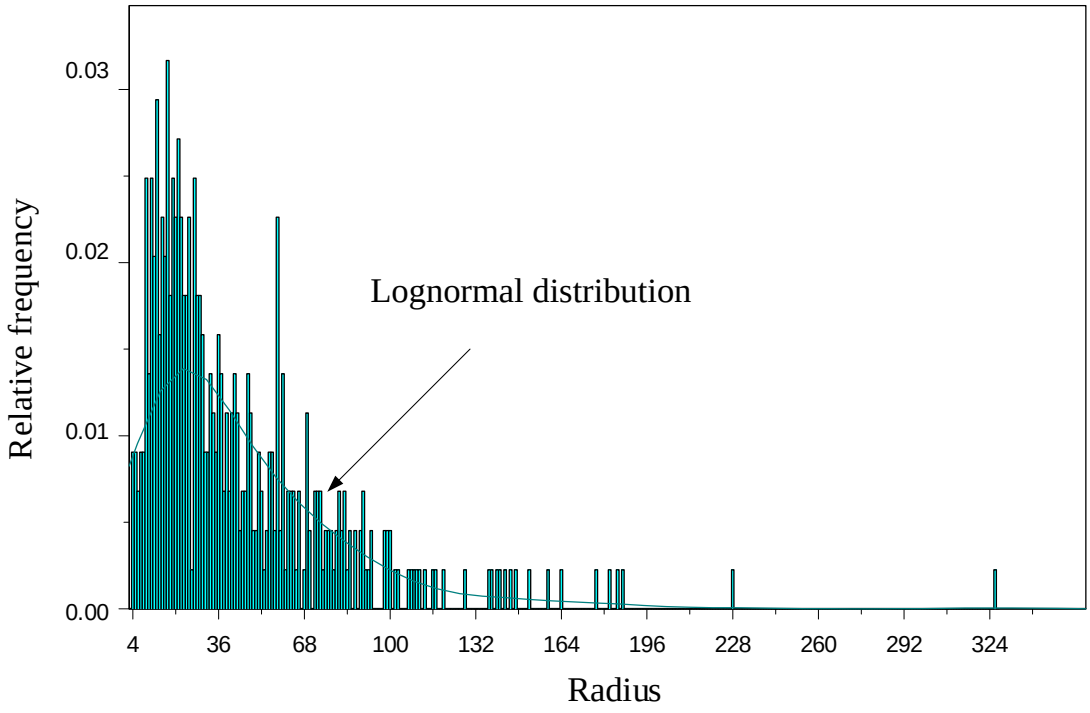


Fig. 5.4: Histogram and probability density function plot for fracture radius: showing lognormal distribution. One unit of the radius is equivalent to 120m (Otsego fault map - Reproduction scenario).

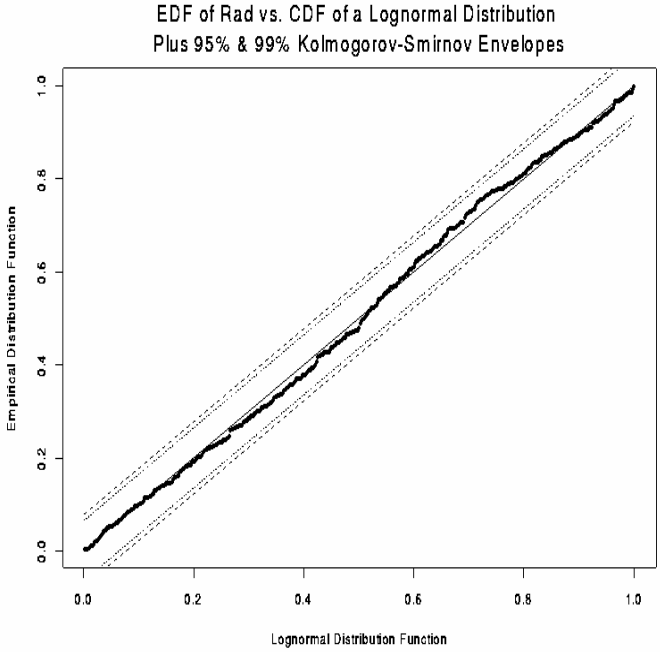


Fig. 5.5: Cross plot of Empirical Distribution Function (EDF) against theoretical lognormal distribution, with the approximate 95% and 99% Kolmogorov-Smirnov bounds: confirming lognormal fracture radius (Otsego fault map - Reproduction scenario).

Statistical analysis of fracture orientation (θ)

Histogram of fracture orientation distribution shows complex behaviour such that conclusion on probability density function is not straightforward (**Fig. 5.6**). A circular data analysis indicates at least three modes (at approximately 32°, 78° and 136°), which could be fit by a three modal wrapped normal distribution:

$$P(\theta) = p_1 \cdot WN(\mu_{c1}, \sigma_{c1}) + p_2 \cdot WN(\mu_{c2}, \sigma_{c2}) + p_3 \cdot WN(\mu_{c3}, \sigma_{c3}) \quad (5.10)$$

$$P(\theta) = 0.44 \cdot WN(1.14, 0.6) + 0.32 \cdot WN(2.99, 0.5) + 0.24 \cdot WN(5.06, 0.58) \quad (5.11)$$

where $WN(\mu_c, \sigma_c)$ stands for a uni-variate wrapped normal distribution with circular mean direction (μ_c) and circular standard deviation (σ_c) (units radian).

In addition, the 442 fractures could have been divided into three separate sets according to orientation, similar to the way the three normal distributions are constructed, to identify how fracture size behaves within an orientation range. Since size distribution is usually complicated, the division makes it easier to be formulated. In this case, however, dividing fractures into sets is not necessary. Fracture length distribution for the whole data set has been characterised with high degree of confidence.

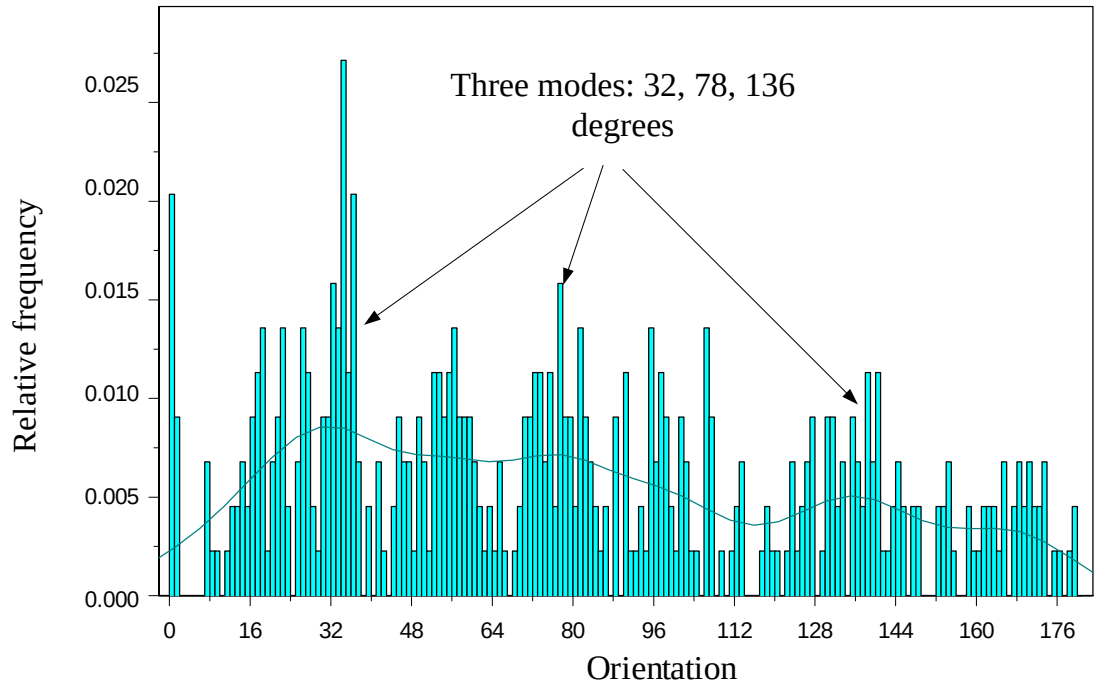


Fig. 5.6: Histogram and probability density function plot for fracture orientation (unit degree): showing three modes at approximately 32°, 78° and 136° (Otsego fault map - Reproduction scenario).

Distribution of marked point centres (fracture location)

Spatial point patterns are analysed in several ways, including histogram analysis for the coordinates, spatial point intensity distribution, examination for complete spatial randomness (CSR) and calculation of Ripley's K-functions. The data set is considered as marked points where fractures and their properties are represented at the fracture centre points. Location map is presented in **Fig. 5.7**.

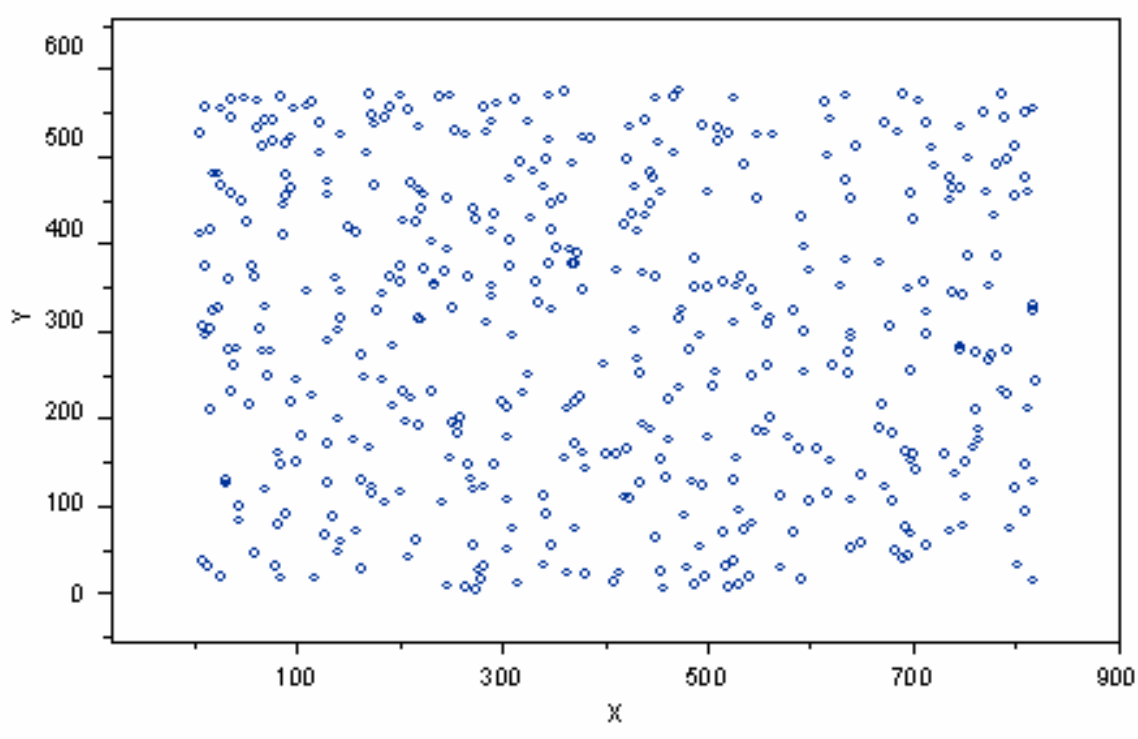


Fig. 5.7: Scatter plot for fracture centre location – x-y coordinates. One x-y unit is equivalent to 120m (Otsego fault map - Reproduction scenario).

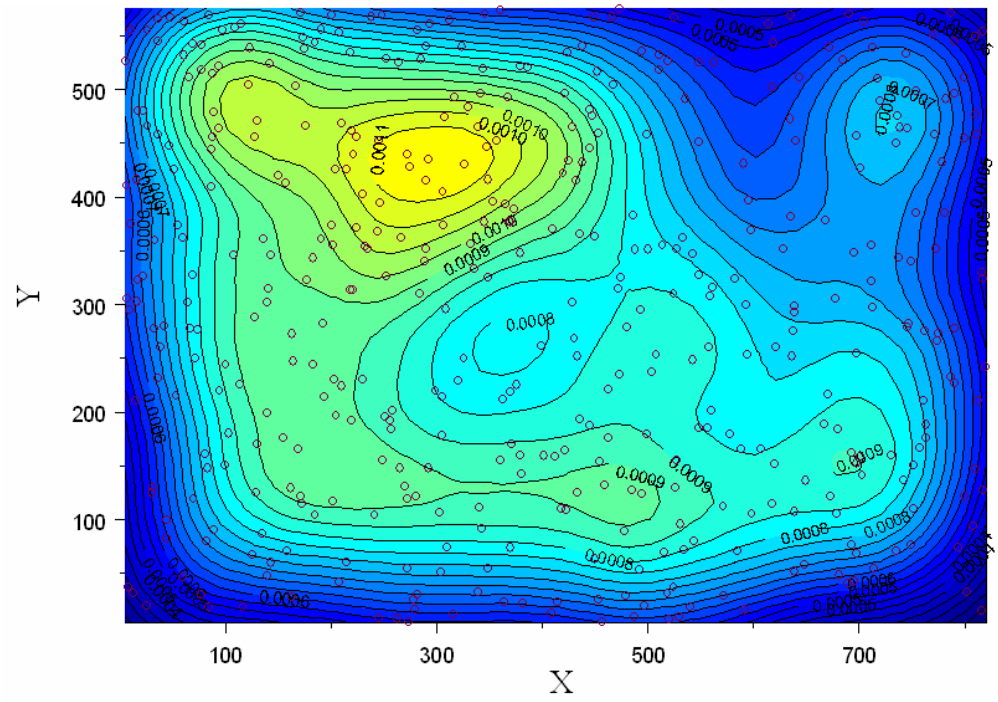


Fig. 5.8: Target fracture intensity (λ) map, including scatter plot of fracture centres. Intensity distribution is smoothed by kernel method. Lighter colours indicate denser intensity. Contour unit is number of points per area. One x-y unit is equivalent to 120m (Otsego fault map - Reproduction scenario).

Similar to earlier observations based on the original fault map, the points in **Fig. 5.7** seem to be distributed near uniformly. Their intensity is plotted in **Fig. 5.8**, using kernel approximation contour map (as described in **Appendix B**). The contour map reflects the scatter point distribution as fracture point intensity quantifies mean number of points per unit area. There are several zones of different intensity, most notably clusters in top left and right quarters. However, the difference is small. Histograms of coordinates of the fracture centres x-y also show the relative uniformity (**Fig. 5.9**).

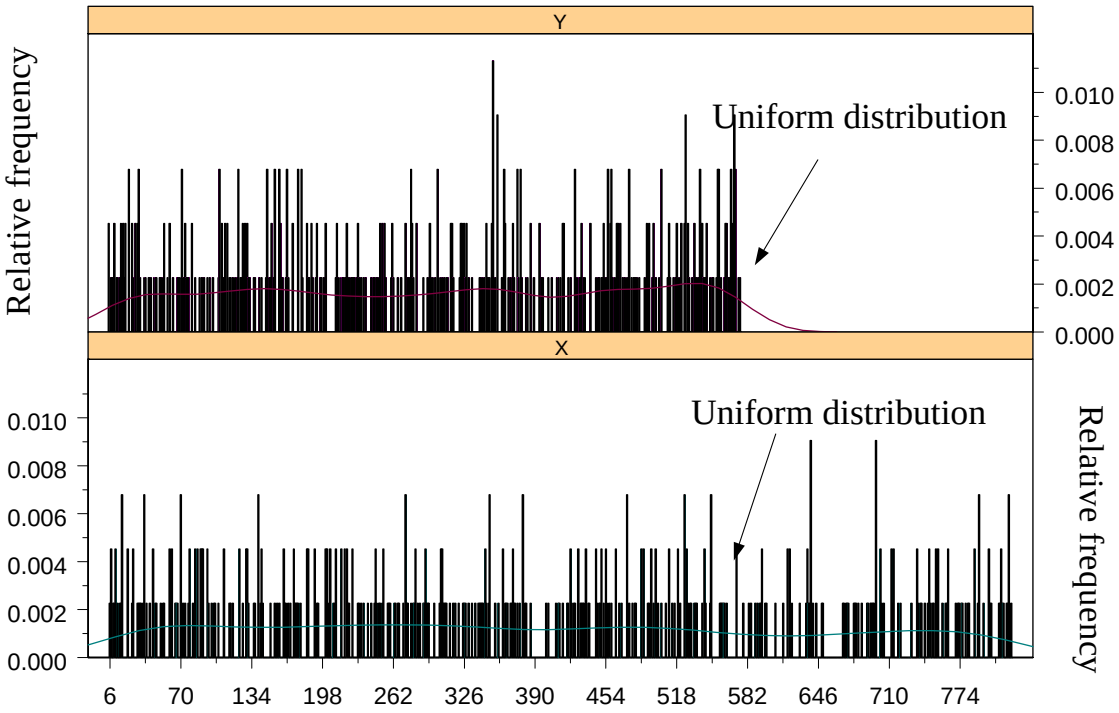


Fig. 5.9: Histogram and probability density function plot for fracture centre location – x-y coordinates: showing uniform distributions. One x-y unit is equivalent to 120m (Otsego fault map - Reproduction scenario).

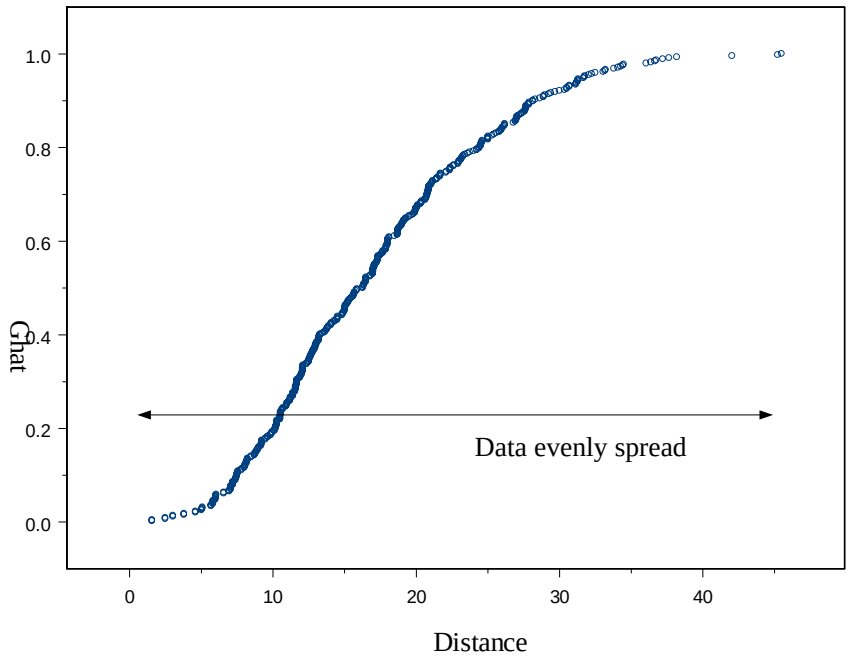


Fig. 5.10: Empirical density function of point-to-point nearest neighbour distances for fracture centres (G-function plot): showing data evenly spread, no signs of clustering or regularity (Otsego fault map - Reproduction scenario).

In addition, various measurements for CSR are performed. Point-to-point nearest neighbour statistic (G-function) plot could not indicate any clear sign of clustering or regularity (**Fig. 5.10**). There is no excess data over any distanced neighbourhood.

Analyses using K-function estimates and variance stabilising transformation (L-function) provide quantitative supports for CSR. Values of both K-function and L-function over distance are close to the values of a homogenous CSR process (parabolic $y=\pi.(distance)^2$ as in **Fig. 5.11** and straight line $y = x$ as in **Fig. 5.12**). In general, it can be concluded that the marked points are distributed completely random.

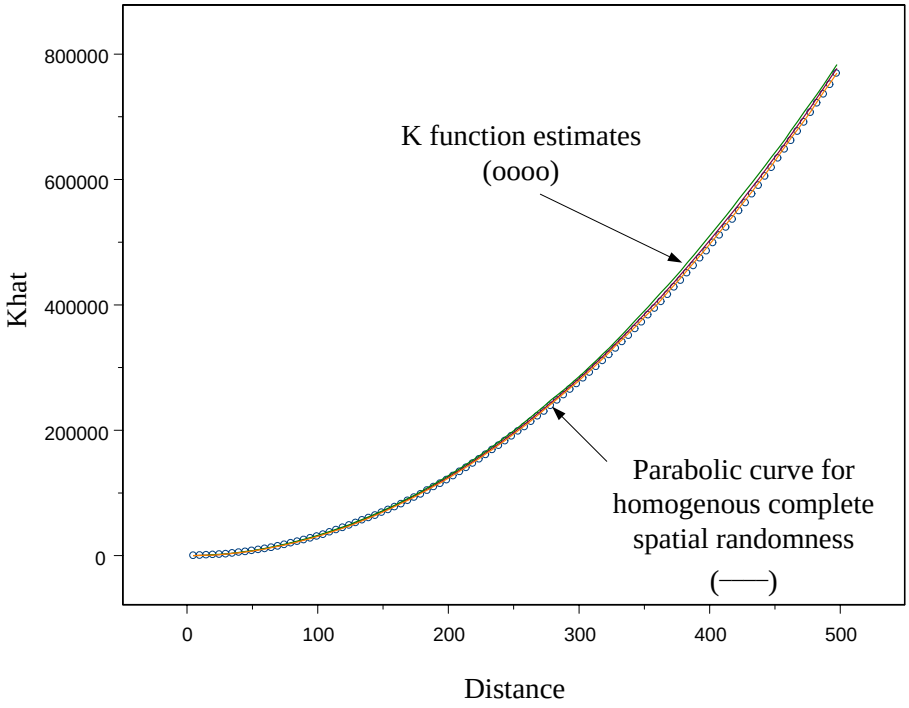


Fig. 5.11: K-function estimates for fracture centre locations (K-function plot): showing CSR (Otsego fault map - Reproduction scenario).

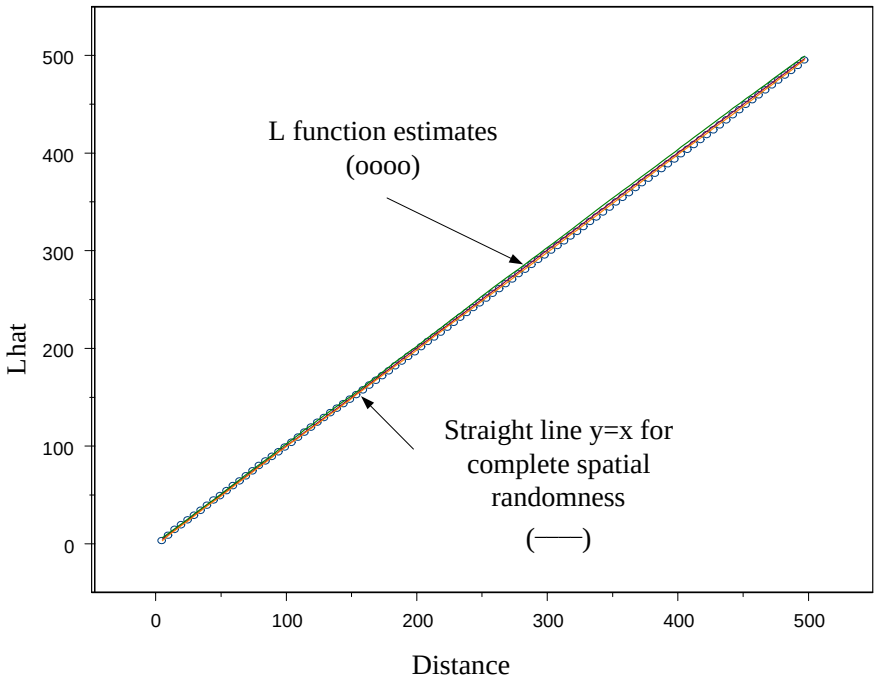


Fig. 5.12: Variance stabilising transformation for fracture centre locations (L-function plot): showing CSR (Otsego fault map - Reproduction scenario).

Spatial distribution of fracture orientation, size and density

Up to this point, individual fracture geometrical properties of location, orientation and size have been investigated. Their distributions have been modelled from corresponding data. Many other research works stopped their data analysis at this point. They moved on to the modelling part, where the statistical distributions were used in discrete stochastic simulations to generate DFN (Anraku et al., 2000; Swaby and Rawnley, 1996; Willis-Richards, 1996).

Nevertheless, the above statistics only portray basic behaviours of individual properties. Several questions remain: how different properties interact with one another and how each of them varies in space. As pointed out earlier, the global optimisation model can make use of fracture density distribution and numerous variogram measurements, which provide valuable quantitative information on spatial distribution and inter-correlation of fracture orientation and size. The ability to incorporate such complex data of different nature provides the current model with a leading edge over stochastic simulation methods.

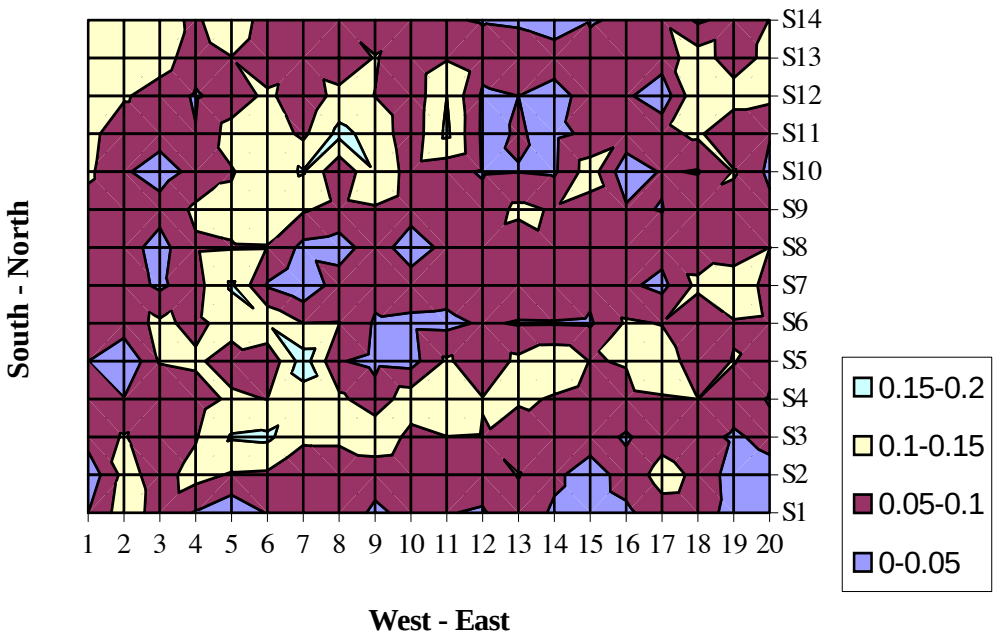


Fig. 5.13: Target grid-based fracture density distribution map (grid-based). Density unit is m/m^2. Lighter colours indicate denser fracture distribution (Otsego fault map - Reproduction scenario).

Density distribution map of target DFN is displayed in **Fig. 5.13**. Unlike the centre point intensity, fracture density actually incorporates mean number of fractures and their lengths. It is thus expected to monitor more closely the effects of fractures on fluid flow. It could be visually observed that the density distribution is also pretty even, with most values range from 0.05 to 0.1 m/m^2. There is a cluster of higher density (light colour region in **Fig. 5.13**), which is also recognisable in the fracture intensity map (**Fig. 5.8**).

Variograms measure spatial continuity and spatial variability of regionalised variables. In this model, experimental semi-variograms, modified multi-histogram means and variogram distance vectors are used to examine variation of fracture orientation and size in space. By using the experimental measurements, biased variogram models are avoided, maintaining accuracy and generalisation. In addition, covariance and a cross-variogram vector are used to measure correlations between orientation and size. While a semi-variogram relates the properties (orientation and size) to number of fractures and their locations, cross-variogram associates one property to another.

As discrete fractures are represented by marked point models, their properties (e.g. orientation and size) are assumed to be located at the line centres. As a result, all variogram vectors representing the Otsego fault map can be directly evaluated, which are presented in **Fig. 5.20** to **Fig. 5.23**.

5.4.2.2 Objective Function Formulation 目标函数公式

Data analyses have provided valuable information on behaviours of the target fault map. Fracture statistics and spatial distribution measurements have been computed. The objective function is then formulated as weighted sum of all statistical differences between simulated realisations and the target (as in **Eq. 5.3**). It contains two parts.

In the first part of the objective function, there are first order statistics that define probability distributions of geometric properties. The statistics contain a set of mean and standard deviation for the log-normally distributed fracture radius. They also enclose three sets of means and variances as well as their relative proportions for the three-modal fracture orientation. Fracture location data are omitted because of random distribution of the centre coordinates. The complete randomness can be preserved during the transition procedure. In addition, spatial distribution is partially controlled in the second part.

Values of various experimental variogram vectors and fracture density distribution constitute the second part of the objective function. Different experiment variograms are used, including semi-variogram, cross-variogram, modified multi-histogram mean and variogram distance for both fracture orientation and radius. Fracture density distribution refers to the continuum local fracture density map and total fracture density, which are input in non-parametric forms (local density values for all grid-blocks).

Weighting factors w_i are chosen according to the importance of each statistic on convergence of the optimisation process. The determination process involves trials and errors. As discussed earlier, first order statistics generally correspond to very small weight factors while the second order moments (e.g. various variograms) and fracture density embodies bigger values. Details of all statistics used in this case study and optimised ranges for corresponding weighting factors are tabulated in **Table 5.3**.

OBJECTIVE FUNCTION	Fracture properties	Statistics and measurements	Weighting Fractor Range
First order statistics	Size	Logmean	0.01-0.1
		Log Std Dev	
	Orientation	Mean	0.01-0.1
		Std Dev	
		Proportion	
	Size	multi-histogram mean vector	0.01-0.1
	Orientation	multi-histogram mean vector	
	Size	Variogram distance vector	0.01-0.1
	Orientation	Variogram distance vector	
	Size + Orientation	Covariance	0.01-0.05
Second order moments	Size	Semi-variogram vector	0.5-0.8
	Orientation	Semi-variogram vector	
	Size + Orientation	Cross-variogram vector	
	Density	Grided densities	0.1-0.3
	Density	Total density	

Table 5.3: Objective function components and their relative optimised ranges for weighting factors (Otsego fault map - Reproduction scenario).

5.4.2.3 Conditional Data 条件数据

Apart from the evaluated fracture properties, it is assumed that a group of fractures are available as conditional data (as in **Fig. 5.14**). Analogous to a typical NFR case, they are taken as ones that can be directly observed from various field data, e.g. outcrop and seismics. Conditional data are not modified during the transformation. In other words, they are maintained as anchor points for the statistical simulation.

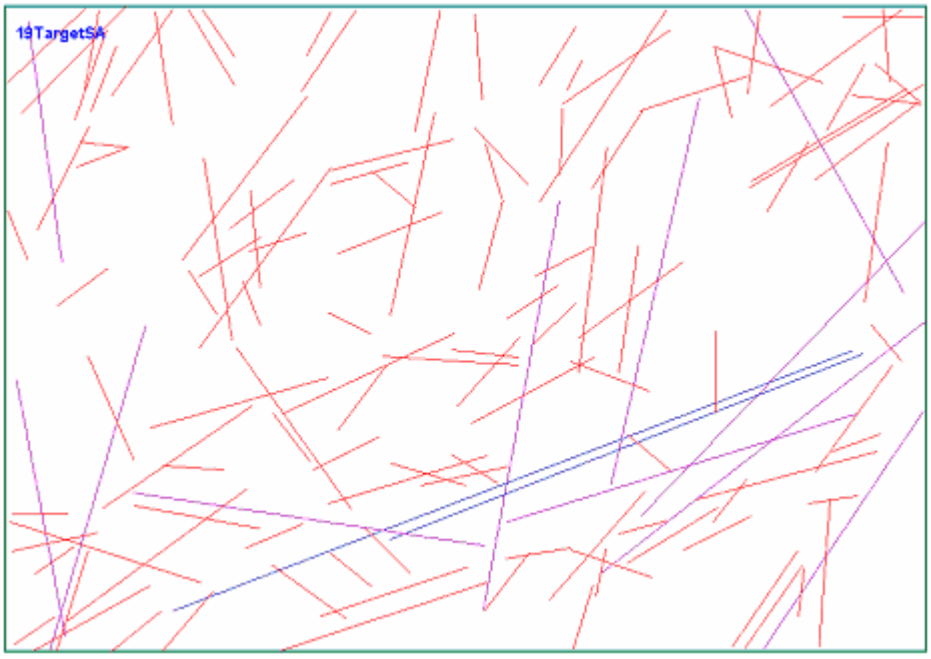


Fig. 5.14: Conditional fracture data: observed fractures are maintained throughout the simulation (Otsego fault map - Reproduction scenario). These fractures are also the available inputs for the later prediction scenario.

5.4.2.4 Initialisation 初始化

The hybrid stochastic simulation (as in **Chapter 4**) is used to generate an initial realisation of DFN (**Fig. 5.15**). First, a library of fractures is built from the statistical distributions of location, orientation and size. Second, random fractures are chosen from the library to form the network. As density distribution map is available, the fracture selection at each grid-block is based on a probability, which in turn depends on density value of the block. When a fracture has been generated, local fracture density values of all blocks that it crosses are updated. This results in a new set of probabilities. The process is carried out until the total fracture density for the reservoir equals to the target value. Density distribution map of the initial realisation is presented in **Fig. 5.16**.

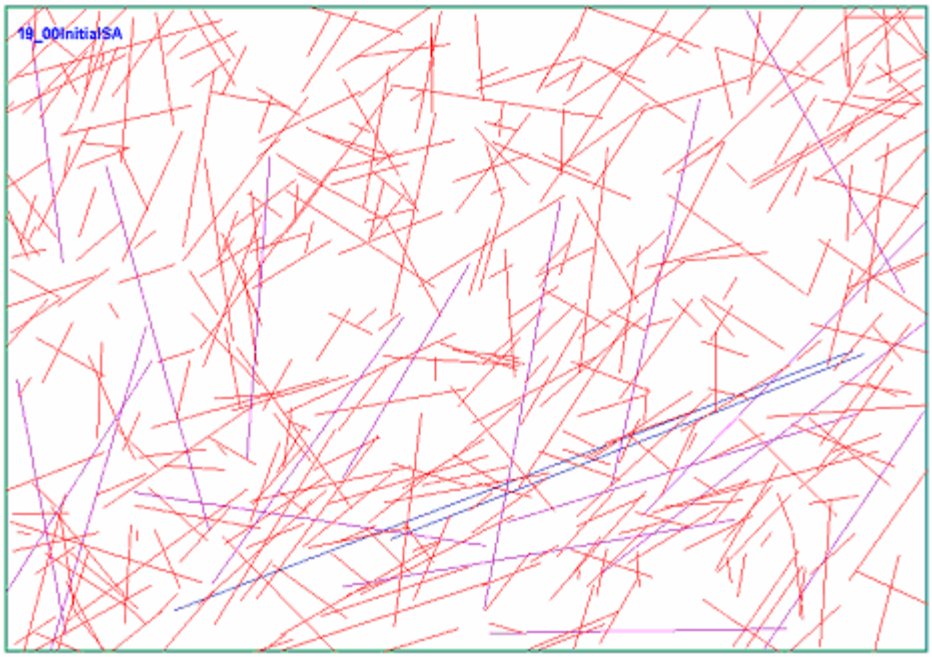


Fig. 5.15: Initial DFN realisation generated from the stochastic simulation module (Otsego fault map - Reproduction scenario).

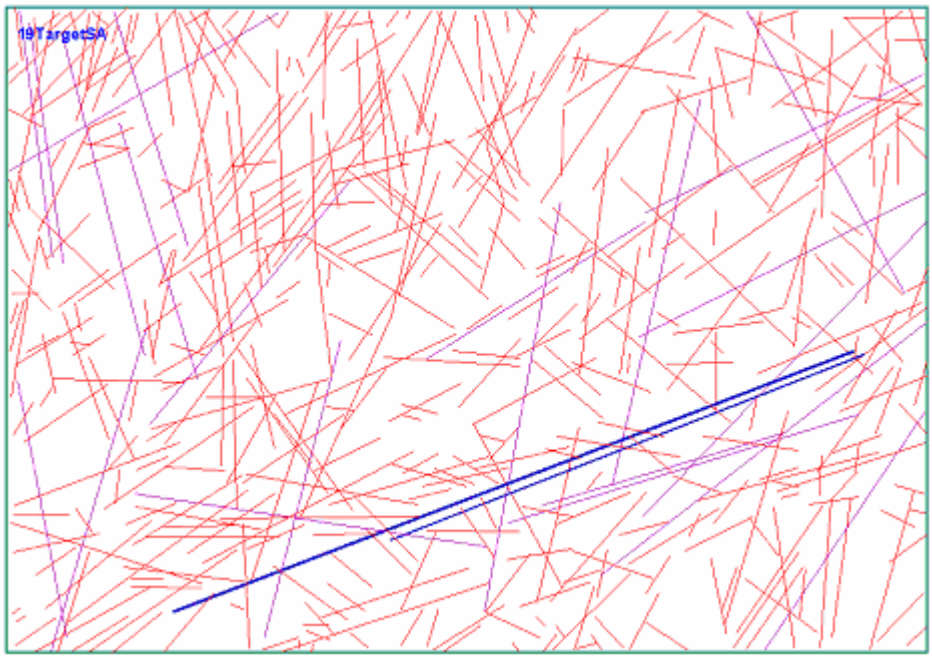


Fig. 5.3: Fault map of Otsego County and the surrounding areas (New York, USA) (digitisation of **Fig. A.1),** with assumptions of some large-scaled fractures.

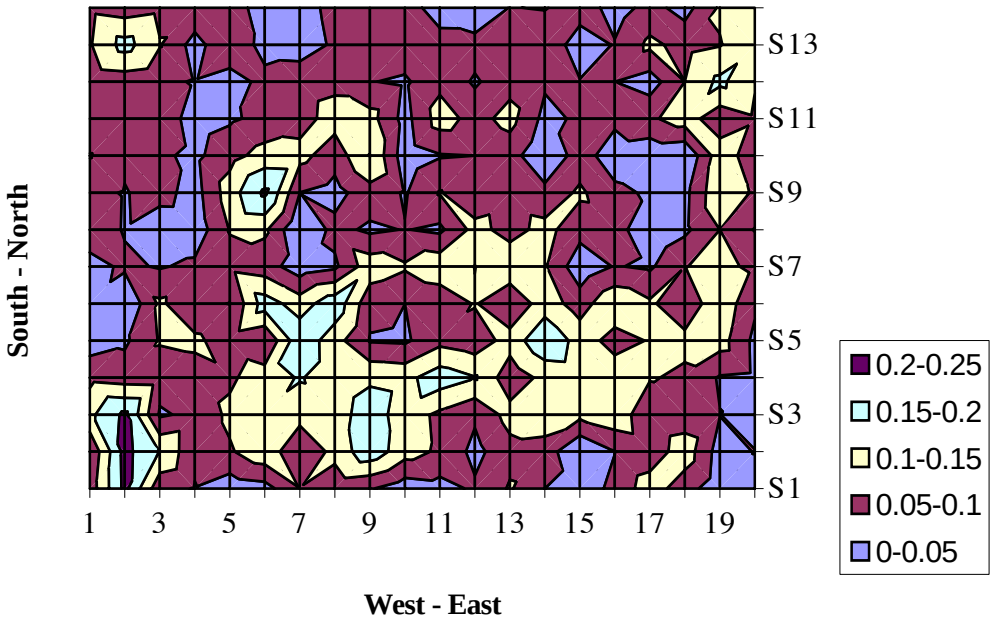


Fig. 5.16: Grid-based density distribution map generated from the hybrid stochastic simulation (initial realisation). Density unit is m/m^2. Lighter colours indicate denser fracture distribution (Otsego fault map - Reproduction scenario).

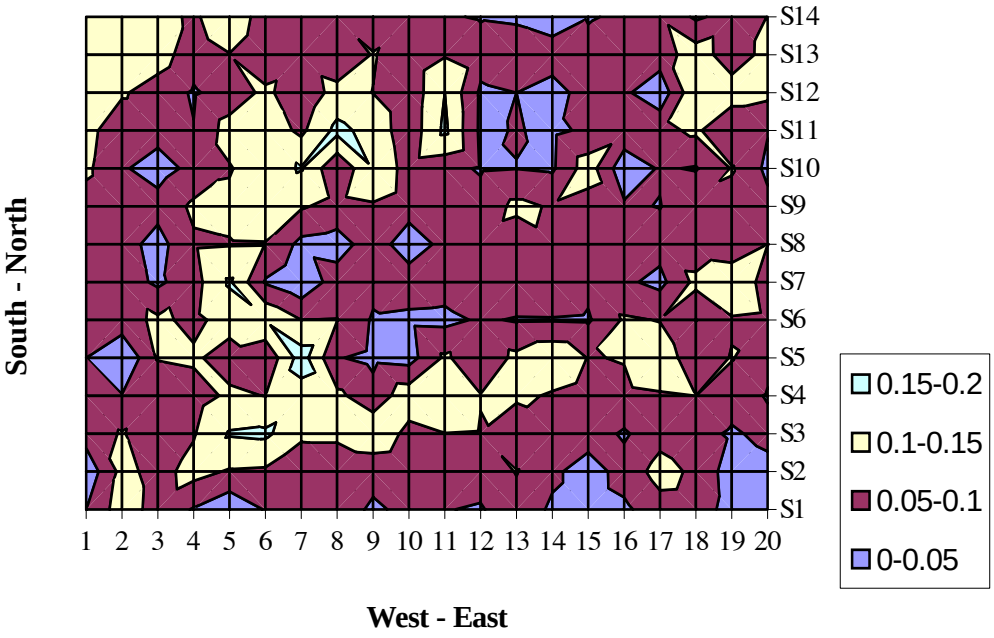


Fig. 5.13: Target grid-based fracture density distribution map (grid-based). Density unit is m/m2. Lighter colours indicate denser fracture distribution (Otsego fault map - Reproduction scenario).

5.4.2.5 Convergence of the Global Optimisation Algorithm
全局优化算法的收敛

The conditional global optimisation algorithm is performed to optimise the formulated objective function. Controlling parameters in **Table 5.4** are used. Fracture properties are individually varied (performing one of the behaviours of shift, rotate, grow, shrink, die or be born). At each temperature, equilibrium condition is considered attained after certain amount of accepts (2500). Stop criteria are achieved as the objective function falls below the target limit (1.0E-05). The whole simulation takes reasonably short time (around one hour) with a normal desktop PC (Pentium IV, 2.9 MHz and 256 MBRAM).

Variable	Value
Temperature reduction factor	0.693
Learning rate	0.9
Max number of accepts at each temperature	2500
Max number of temperature changes	20
Max number of temperature changes without success	3
Target for the objective function	0.00001
Max number of iterations at each temperature	2500000

Table 5.4: Controlling parameters for the global optimisation algorithm (Otsego fault map - Reproduction scenario).

The declination of the objective function is demonstrated in **Fig. 5.17**, showing approximately logarithmic declination. In the beginning, the objective function decreased faster, since it was easier to get away from local minima. Towards the end, it required a much greater number of iterations. For example between step 10th and 11th, it takes approximately 8.8e+05 iterations to satisfy the equilibrium condition. **Fig. 5.17** displays typical behaviour of a global optimisation process.

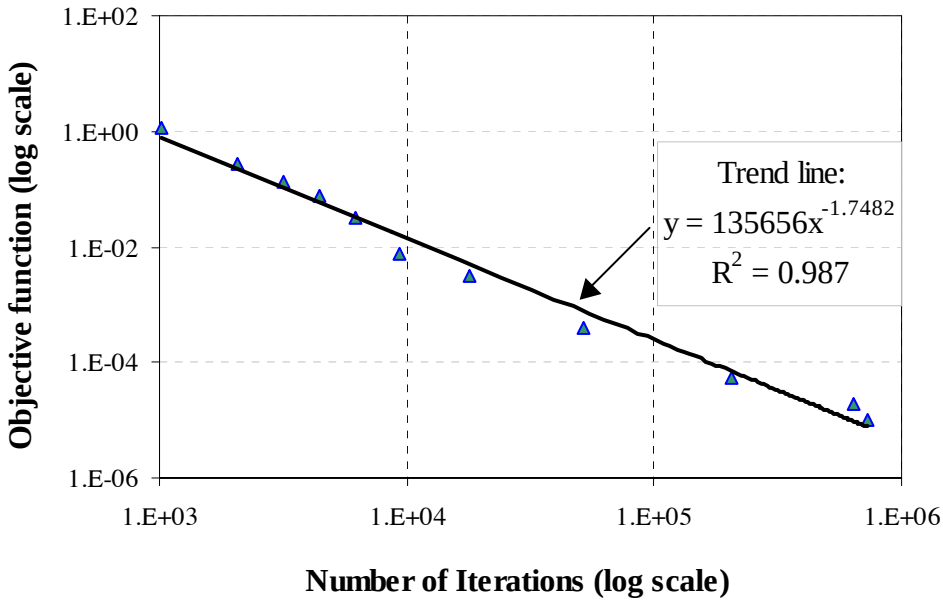


Fig. 5.17: Graph showing how objective function decreases logarithmically with iterations (Otsego fault map - Reproduction scenario).

5.4.2.6 Results of Reproduction Scenario

The objective function is minimised to final value of 1.0e-5. Small value of objective function means that all of its components have been coordinated and that the simulated data are well matched with the target's. The final network realisation for this scenario is shown in **Fig. 5.18**. Total fracture density and density distribution map of the final simulated DFN are displayed in **Table 5.5** and **Fig. 5.19**.



Fig. 5.18: Final DFN image, reproduction result of the object-based conditional global optimisation (Otsego fault map - Reproduction scenario).

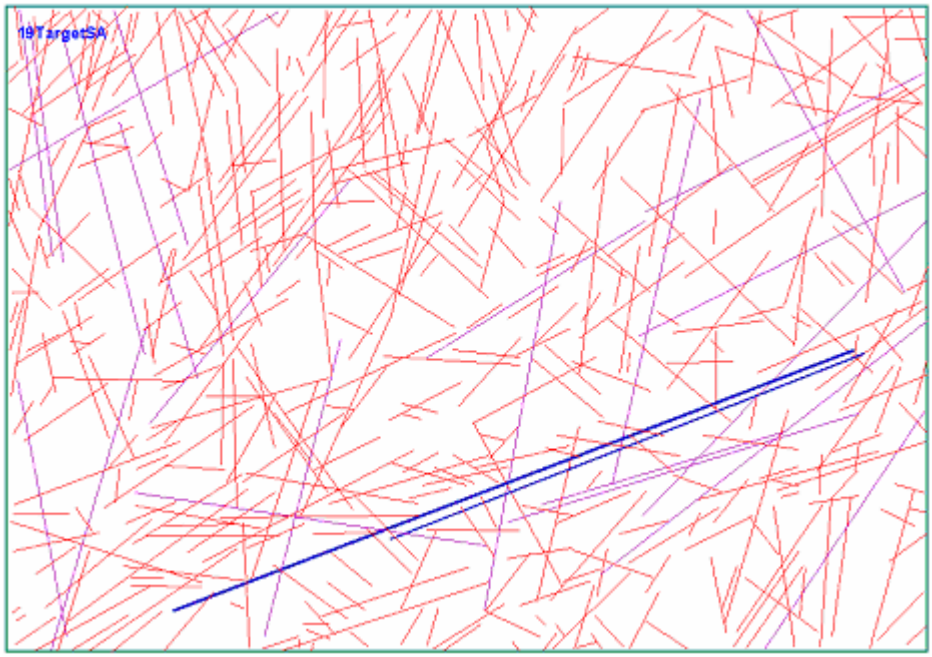


Fig. 5.3: Fault map of Otsego County and the surrounding areas (New York, USA) (digitisation of **Fig. A.1),** with assumptions of some large-scaled fractures.

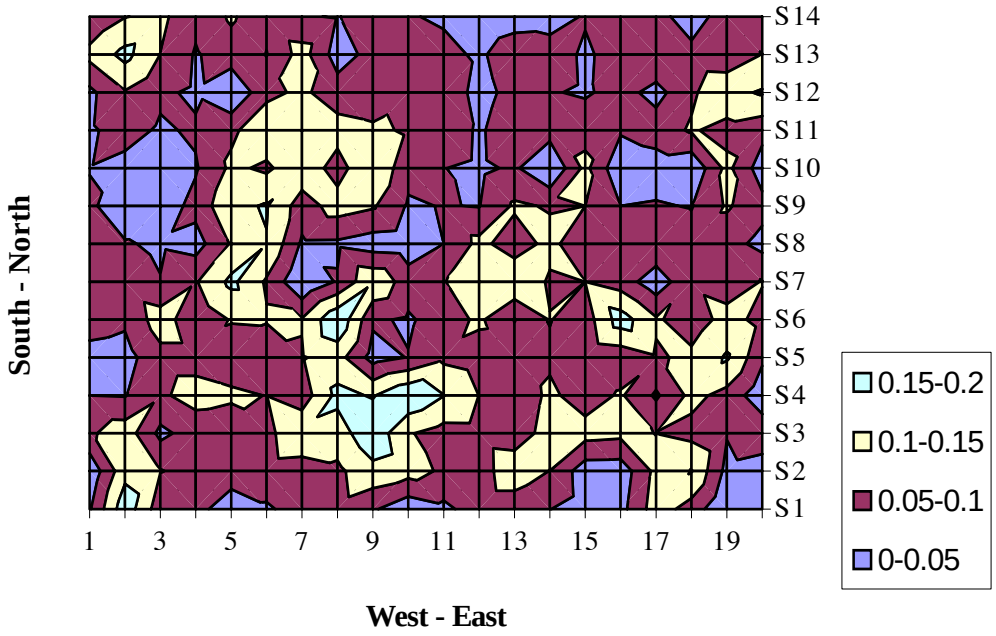


Fig. 5.19: Final simulated grid-based fracture density distribution map. Density unit is m/m^2. Lighter colours indicate denser fracture distribution (Otsego fault map - Reproduction scenario).

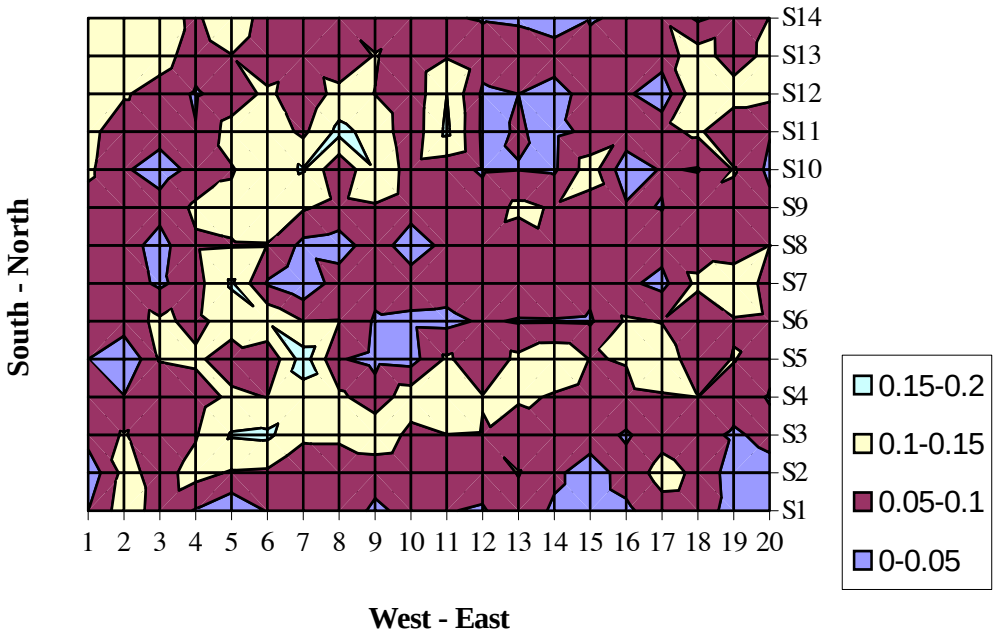


Fig. 5.13: Target grid-based fracture density distribution map (grid-based). Density unit is m/m2. Lighter colours indicate denser fracture distribution (Otsego fault map - Reproduction scenario).

Simple statistics comparison					
	Target (0)	**FraCGOM (2)**	**Percentage error (%)**	**Stochastic simulation (1)**	**Percentage error (%)**
Radius (m)					
Lognormal mean	**42.87**	41.55	3.085	40.42	5.719
Lognormal std deviation	**37.23**	35.76	3.948	31.92	14.281
Orientation (radian)					
Set 1: Mean	**1.140**	1.131	0.756	1.054	7.506
Std dev	**0.600**	0.600	0.000	0.435	27.434
Weight factor	**0.440**	0.439	0.287	0.428	2.726
Set 2: Mean	**2.990**	3.007	0.553	3.165	5.864
Std dev	**0.500**	0.510	1.953	0.727	45.313
Weight factor	**0.320**	0.322	0.660	0.340	6.271
Set 3: Mean	**5.060**	5.027	0.654	4.722	6.685
Std dev	**0.580**	0.586	0.977	0.369	36.373
Weight factor	**0.240**	0.239	0.474	0.229	4.498
Total fracture density (m/m*m)	**0.0792400**	0.0793000	0.076	0.0794400	0.252

Table 5.5: Comparison of objective function components: total fracture density and simple statistical measurements of fracture radius and orientation. For: Target DFN (0), Initial realisation by hybrid stochastic simulation (1), and Final realisation by conditional global optimisation (FraCGOM 2) (Otsego fault map - Reproduction scenario).

5.4.2.7 Comparison with the Target Otsego Fault Map

First, the generated fracture image map (**Fig. 5.18**) appears visually similar to the target Otsego fault map (**Fig. 5.3**).

This observation can be proved quantitatively. The matching of simple statistical measurements for radius and orientation is illustrated in **Table 5.5**. Even though these properties correspond to smaller weighting factors, percentage errors are very low, at most 4%. The matching of semi-variogram, modified multi-histogram mean, variogram distance and cross-variogram vectors of fracture radius and orientation are displayed from **Fig. 5.20** to **Fig. 5.23**. In most cases, graphs representing target and final simulated DFN overlap, where errors are less than 1%.

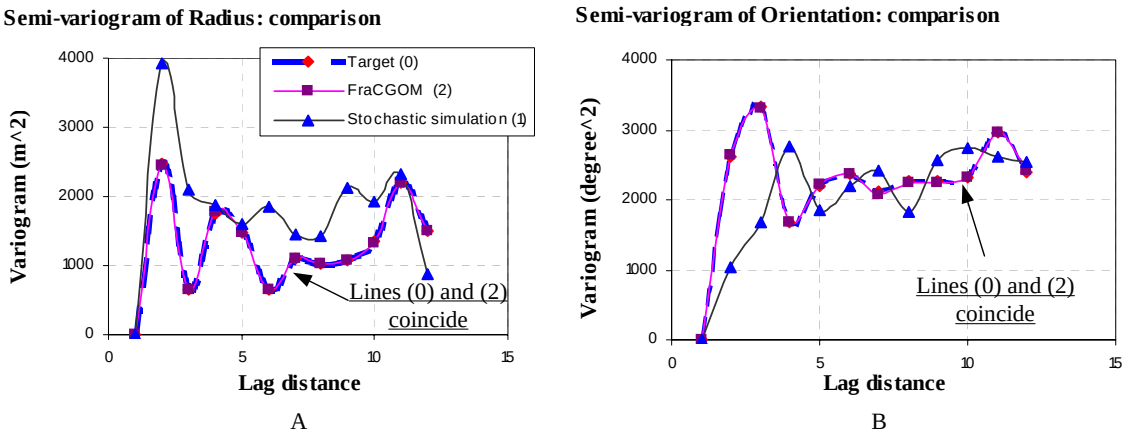


Fig. 5.20: Comparison of experiment semi-variogram vectors. For: Target DFN (0), Initial realisation by stochastic simulation (1), and Final realisation by conditional global optimisation (FraCGOM 2) (Otsego fault map - Reproduction scenario). A. fracture size – B. fracture orientation.

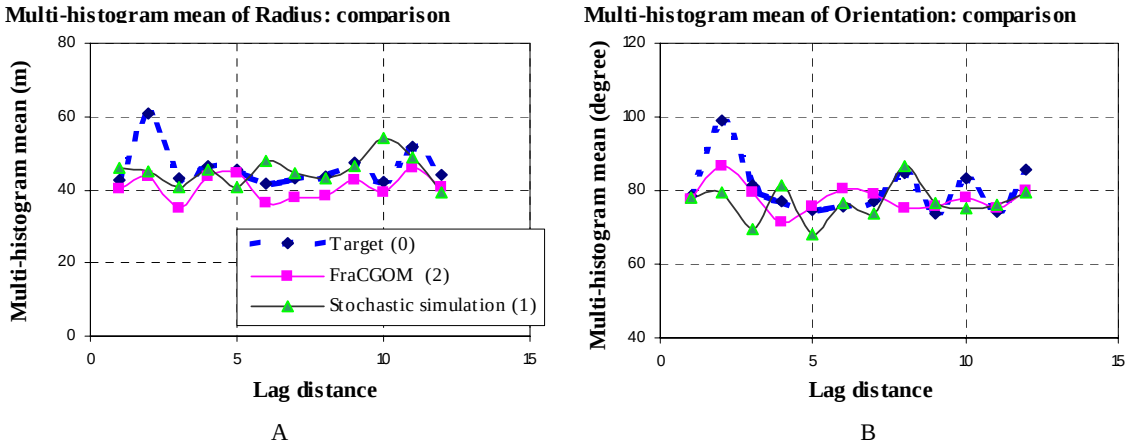


Fig. 5.21: Comparison of modified multi-histogram mean vectors. For: Target DFN (0), Initial realisation by stochastic simulation (1), and Final realisation by conditional global optimisation (FraCGOM 2) (Otsego fault map - Reproduction scenario). A. fracture size – B. fracture orientation.

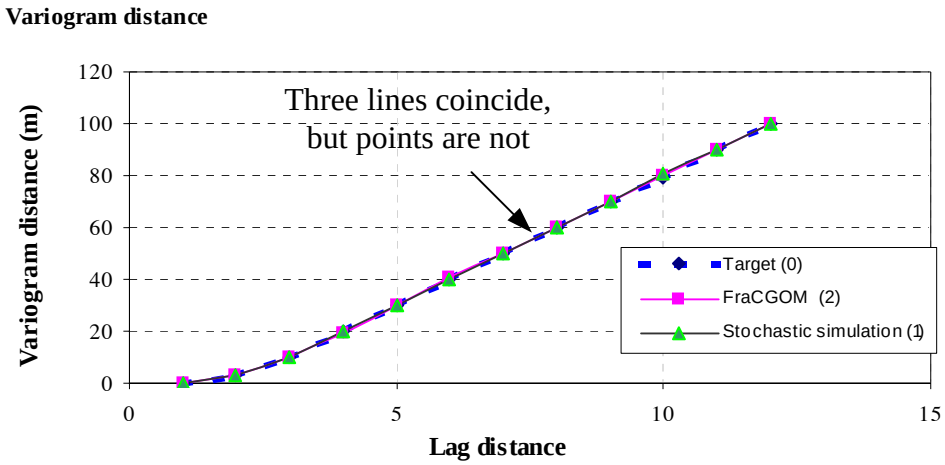


Fig. 5.22: Comparison of experiment variogram distance vectors. For: Target DFN (0), Initial realisation by stochastic simulation (1), and Final realisation by conditional global optimisation (FraCGOM 2) (Otsego fault map - Reproduction scenario).

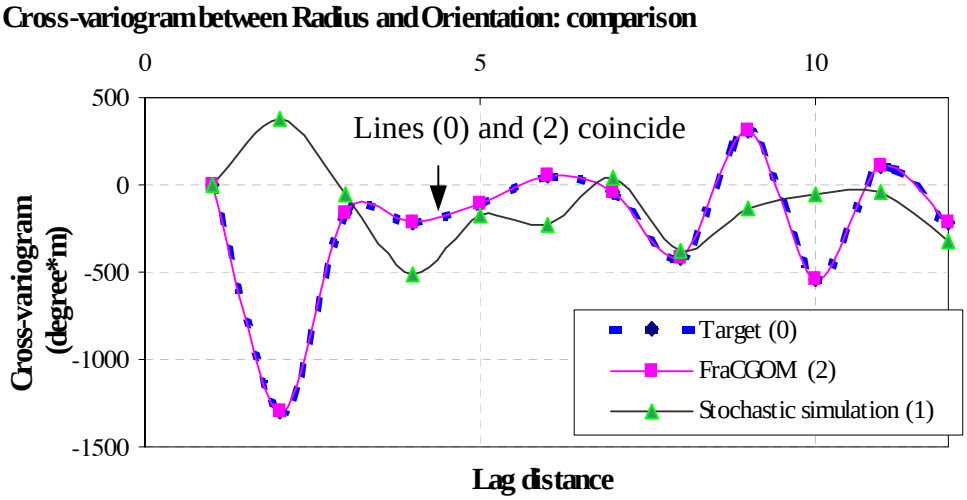


Fig. 5.23: Comparison of experiment cross-variogram of fracture radius and orientation. For: Target DFN (0), Initial realisation by stochastic simulation (1), and Final realisation by conditional global optimisation (FraCGOM 2) (Otsego fault map - Reproduction scenario).

Because total density has been controlled during transformation, an error of 7.6E-4 is due to mathematical inaccuracy. Characteristics of density distribution map are also quite similar to the target's. As shown in **Fig. 5.13** and **Fig. 5.19**, density values of all

grid-blocks have been matched. This demonstrates that the object-based model can successfully implement grid-based data.

5.4.2.8 Remarks

As the objective function represents the difference between characteristics of output realisation and the target fault map, its small value indicates their similarity. First, known conditional fractures have been replicated. Second, fracture density distribution, various statistical and geostatistical characteristics have been reproduced. As all characteristics and behaviours of the two fracture systems are similar, the method is self-validated. This result has confirmed procedure and reproduction ability of the object-based conditional global optimisation model.

5.4.3 Comparison with Stochastic Simulation

The DFN produced by the stochastic simulation (**Fig. 5.15**) can be compared with that of the global optimisation (**Fig. 5.18**).

First, by visual comparison, one could observe that both fracture maps are quite similar to the target network. **Fig. 5.18** might appear more closely matched with **Fig. 5.3** than **Fig. 5.15**, but it is not visually obvious. Similar observations can be made from the density distribution maps. Block by block, density values generated by the stochastic simulation (**Fig. 5.16**) are a little different to those of the target's (**Fig. 5.13**) and those generated by the global optimisation (**Fig. 5.19**). Nevertheless, overall patterns of high- and low-density clusters are relatively matched. The similarity is due to the mechanisms that control the local density distribution in both modules (as discussed earlier).

The resulting DFN might look similar, however, quantitative analysis indicates that the objective function has been improved by around 1000 fold, from 0.40 (in the case of stochastic simulation) to 1.0e-5 (in the case of global optimisation). In addition, different components of the objective function behave differently. Although the stochastic simulation module fits the first order statistics and total fracture density well (**Table 5.5**), they have failed to match the second order statistics. The differences can be

observed through all graphs comparing experimental semi-variogram, cross-variogram, modified multi-histogram mean and variogram distance vectors (**Fig. 5.20** to **Fig. 5.23**). As disputed earlier (**Chapter 4**), stochastic simulation could not utilise such sophisticated spatial statistics effectively.

Another advantage of the global optimisation model is that it does not require assumptions on statistical distributions of fracture properties. In fact, even in cases where fracture properties do not fit into any standard distributions, they can still be characterised and modelled. Non-parametric forms could be used, as shown in the case study for fracture density map. Furthermore, by using the experimental measurements, errors created from fitting process for variogram models have been avoided.

In general, it has been shown that result of the global optimisation model is greatly improved over stochastic simulation. The former is an effective tool to directly improve results of the later.

5.4.4 Prediction Scenario

In the prediction scenario, it is assumed that data are limited and do not cover all aspects of the target fault map. Available data are those fractures that have been observed, or equivalently, those that have been used as conditional data in the previous scenario (**Fig. 5.14**). This is closer to a typical petroleum engineering situation, where the model is required to predict the optimum fracture map. Because the model has been validated in the previous reproduction scenario, similar procedure and set up are applied. The result is again compared with the actual target Otsego map (**Fig. 5.3**).

5.4.4.1 Fracture Data Analysis

There are 153 fractures available for data characterisation (**Fig. 5.14**). Similar to the previous case, various analyses are conducted to study characteristics of available fracture data. The characteristics are then generalised for the whole network, forming target components for the objective function.

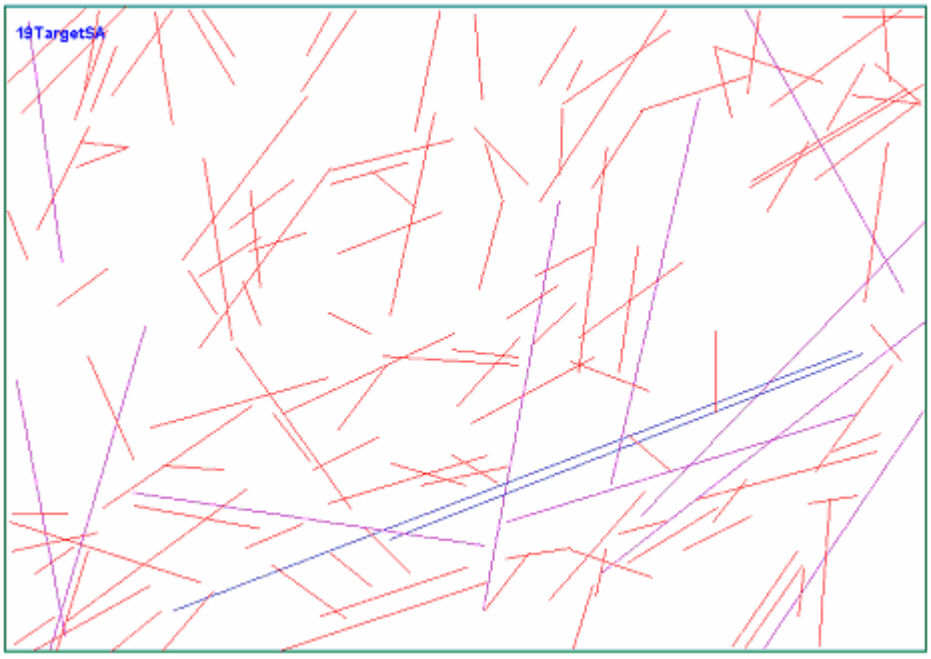


Fig. 5.14: Conditional fracture data: observed fractures are maintained throughout the simulation (Otsego fault map - Reproduction scenario). These fractures are also the available inputs for the later prediction scenario.

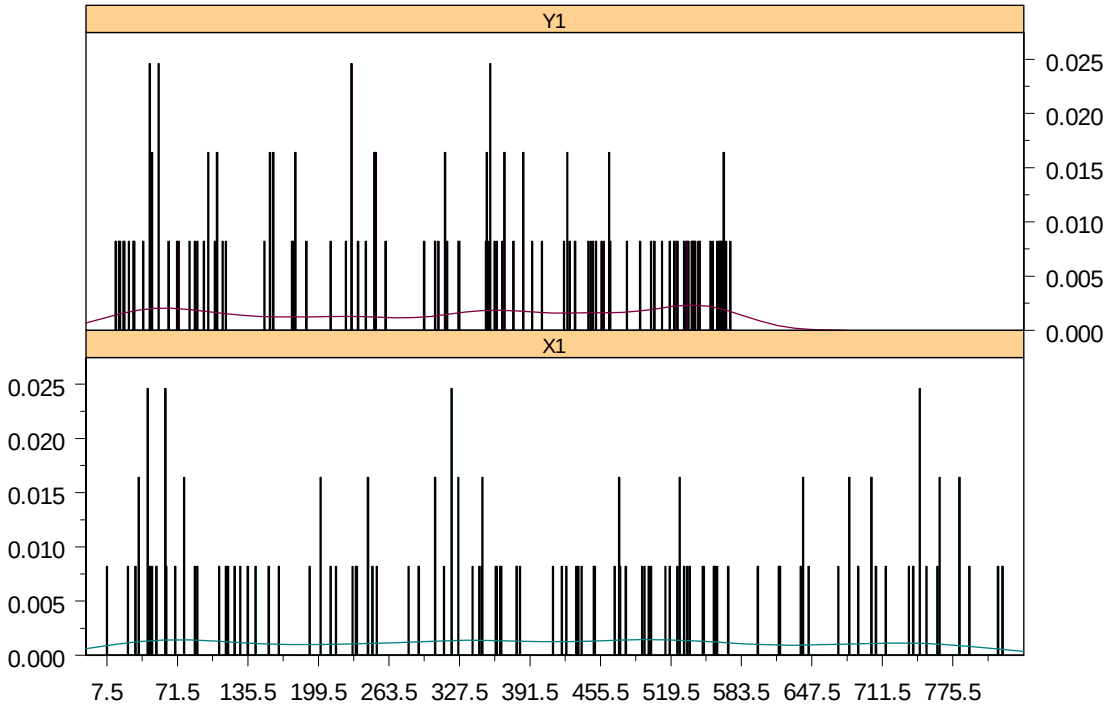


Fig. 5.24: Histogram and probability density function plot for fracture centre location – x-y coordinates: showing uniform distributions. One x-y unit is equivalent to 120m (Otsego fault map - Prediction scenario).

First, in statistical analyses, histograms of all geometric properties (**Fig. 5.24** to **Fig. 5.26**) generally show similar trends as those of the original target data (**Fig. 5.4** to **Fig. 5.9**). This indicates that the available data are, to a certain degree, statistically representative. Coordinates of the object centre are uniformly distributed (**Fig. 5.24**). Fracture radius follows a lognormal distribution (**Fig. 5.25**). Data samples are scarce and there are absents of small and medium sized fractures. Even though fracture orientation histogram shows three peaks (**Fig. 5.26**), it can be well fitted by a two modal normal distribution. The two mode values are at 35^{o} and 78^{o}, which are closed to two of the three modes in **Fig. 5.6**.

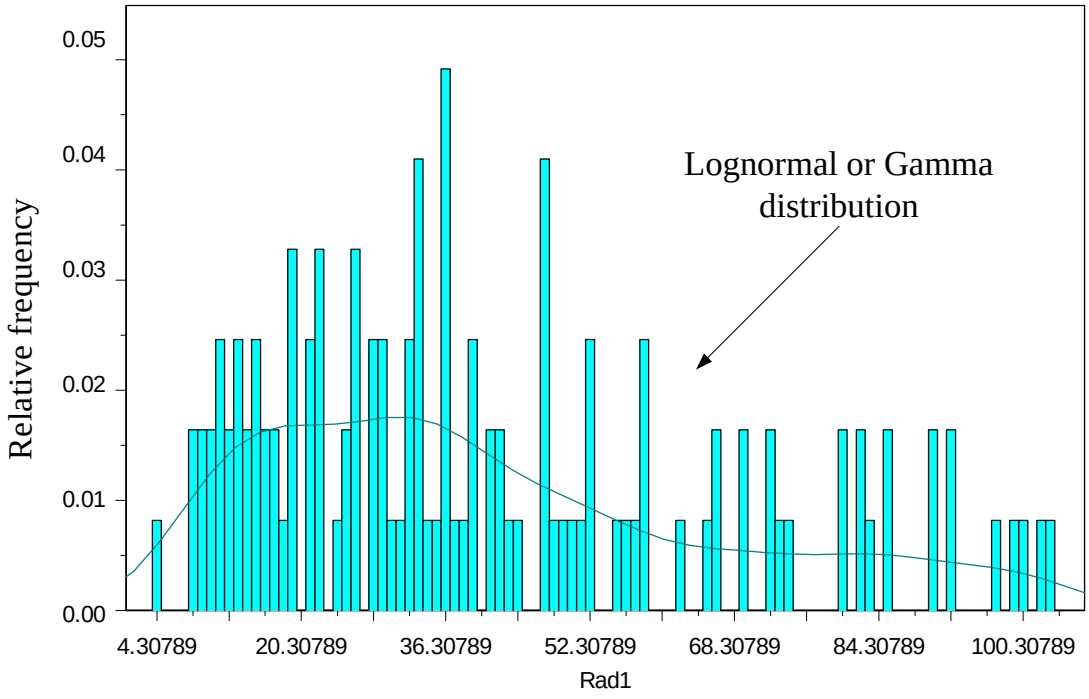


Fig. 5.25: Histogram and probability density function plot for fracture radius: showing either lognormal or gamma ray distribution. One unit of the radius is equivalent to 120m (Otsego fault map - Prediction scenario).

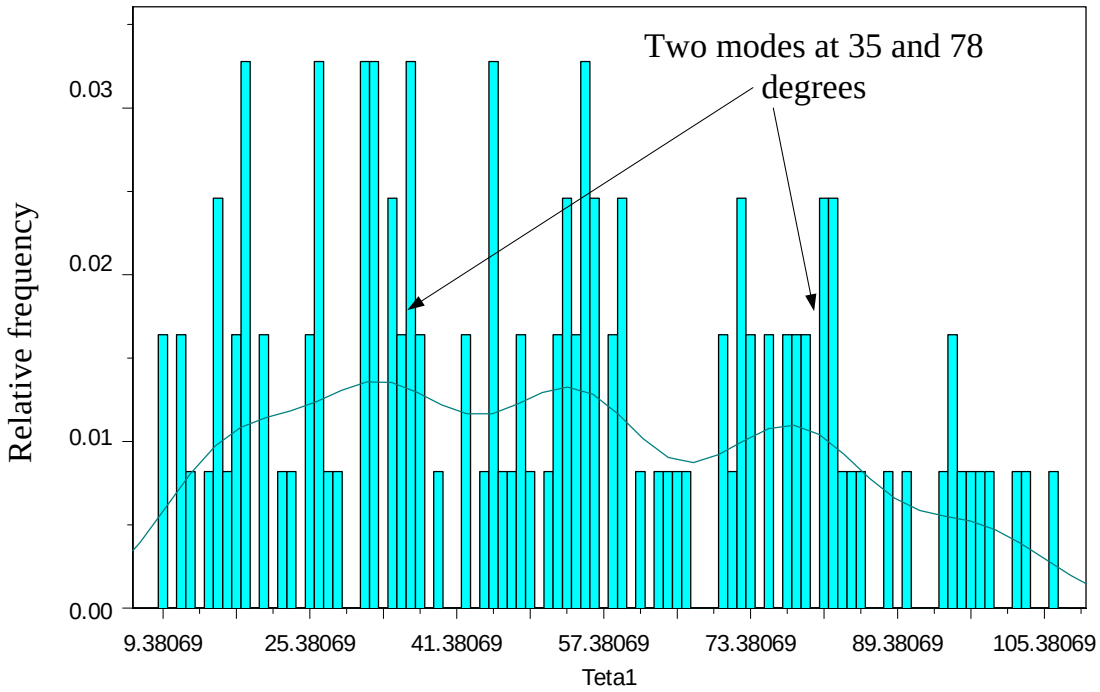


Fig. 5.26: Histogram and probability density function plot for fracture orientation (unit degree): showing roughly bimodal distribution with modes at 35°, and 78° (Otsego fault map - Prediction scenario).

From the fracture data available, semi-variogram, cross-variogram, modified multi-histogram mean and variogram distance vectors are computed for both fracture orientation and size (**Fig. 5.29** to **Fig. 5.32**). The geostatistical measurements generalise spatial distribution of the fracture properties regardless of the total sample size.

Similar application of fracture density and density distribution map is not possible in this case. This is because fracture density values obtained from the available fractures would be smaller than the actual target's. Thus, local density map is not used and a total density value of 0.8 m/m^2 is assumed. In a typical NFR, the assumption is, however, not necessary. Local fracture density can be calculated at the wellbores and up-scaled by FNN analysis for every grid-blocks of the whole reservoir (as in discussed **Chapters 2** and **3**). Total fracture density can be summarised from the local density map.

5.4.4.2 Optimisation Algorithm Formulation

Objective function is formulated in the same manner as the previous case. It includes simple statistics, more complex geostatistical variograms and total fracture density. Details of components and corresponding weighting factors are as listed in **Table 5.3**.

All available fractures are used as conditional data. This ensures that the generated DFN would not contradict known data. Thus, the conditional data are the same in both reproduction and prediction scenarios (**Fig. 5.14**).

The same procedure for global optimisation algorithm (as in **Fig. 5.2**) is carried out.

5.4.4.3 Results of Prediction Scenario

Conditional global optimisation converges. The objective function declines to 4.0E-5. The predicted DFN is shown in **Fig. 5.27**.

Small value of the objective function indicates that all of its components have been optimised. The matching of various statistical and spatial measurements are illustrated in **Fig. 5.29** to **Fig. 5.32**. This has again demonstrated the usefulness of the conditional global optimisation module in modelling fracture systems to match complex statistics.

The prediction results are also compared with the actual target fault map and shown in the same figures. One could notice several dissimilarities and errors. They are mainly originated from the shortage of available data.

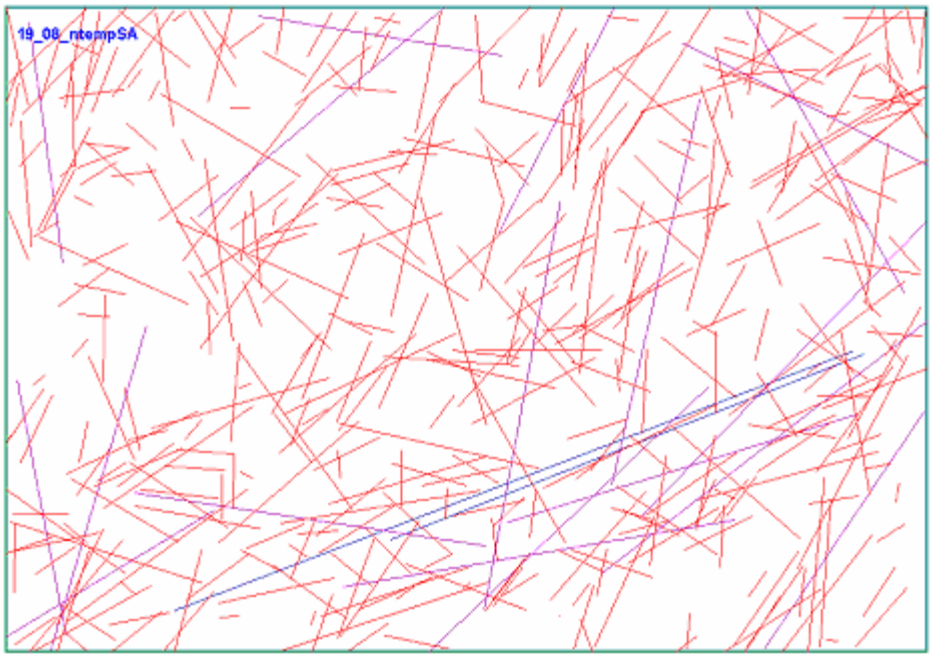


Fig. 5.27: Final predicted DFN image by object-based conditional global optimisation (Otsego fault map - Prediction scenario).

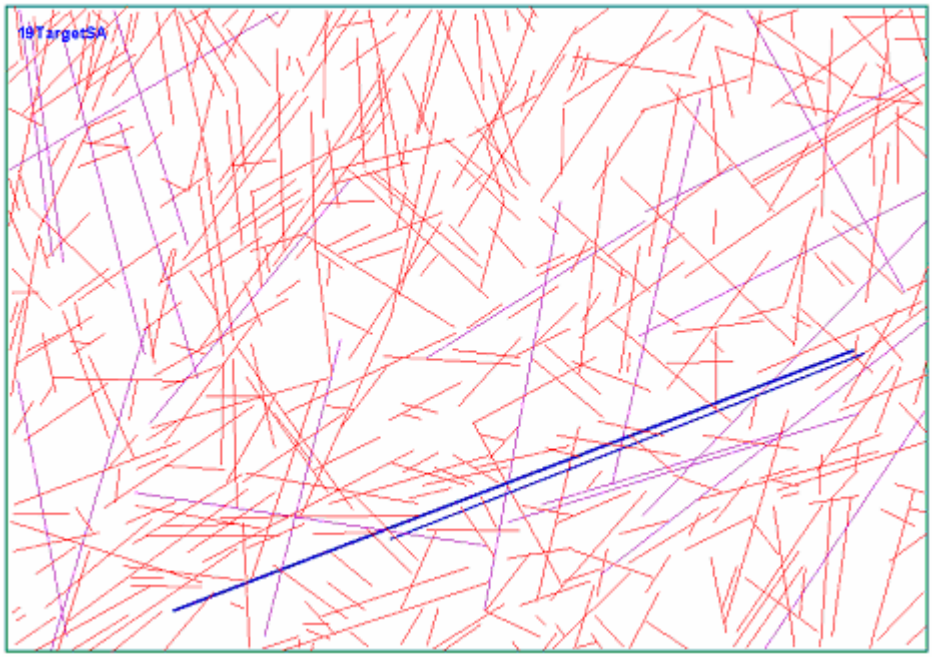


Fig. 5.3: Fault map of Otsego County and the surrounding areas (New York, USA) (digitisation of **Fig. A.1),** with assumptions of some large-scaled fractures.

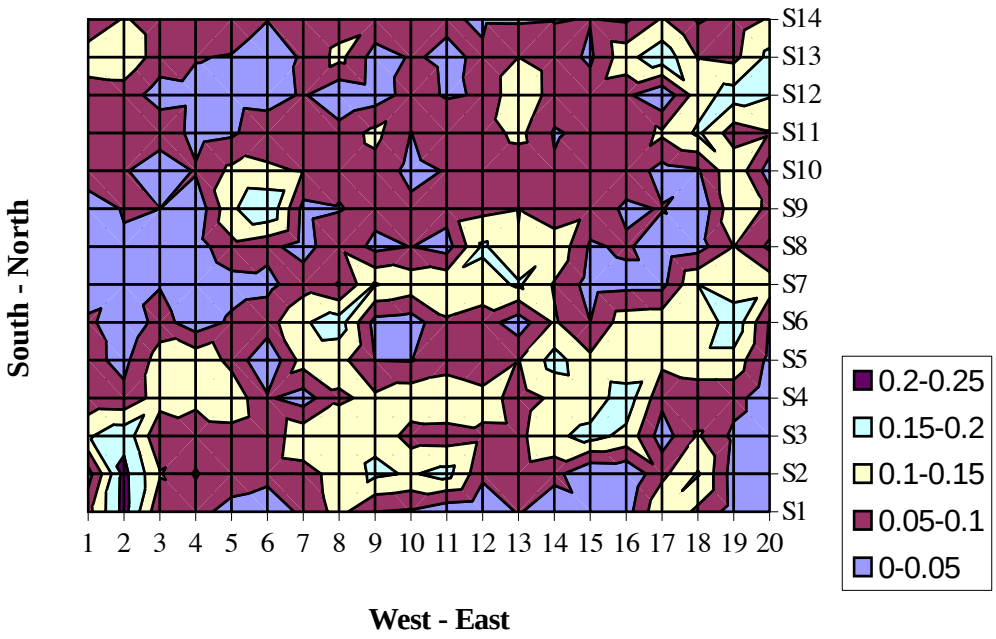


Fig. 5.28: Final predicted grid-based fracture density distribution map. Density unit is m/m^2. Lighter colours indicate denser fracture distribution (Otsego fault map - Prediction scenario).

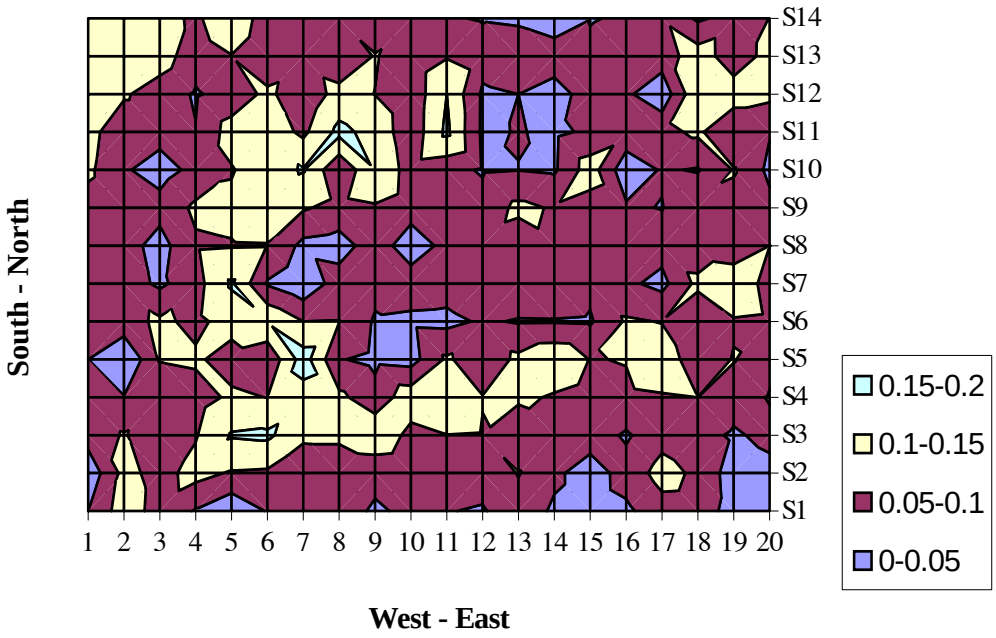
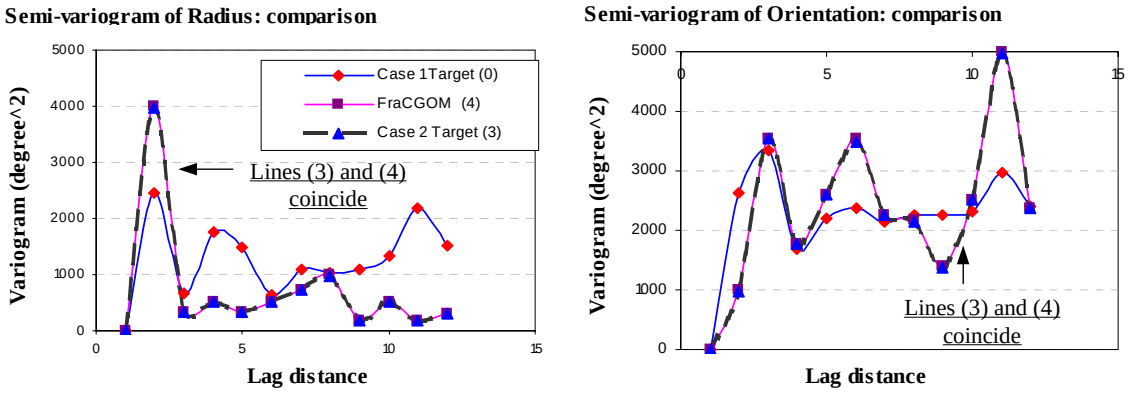
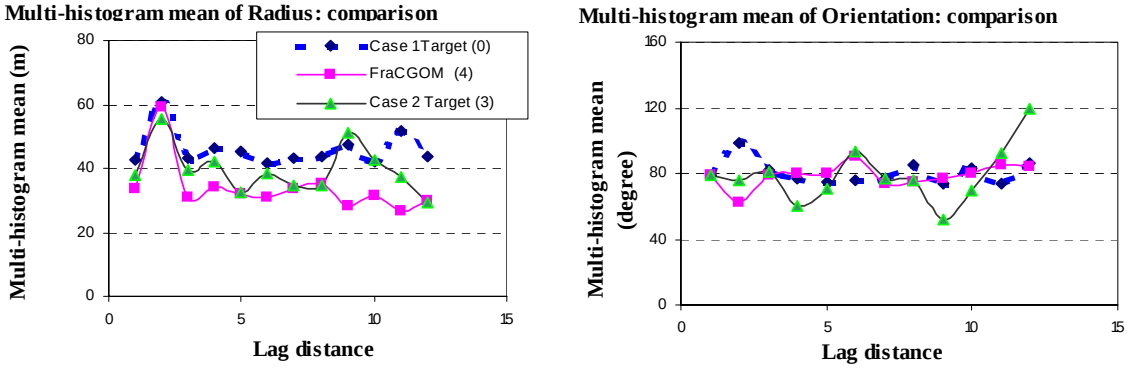


Fig. 5.13: Target grid-based fracture density distribution map (grid-based). Density unit is m/m2. Lighter colours indicate denser fracture distribution (Otsego fault map - Reproduction scenario).



A B

Fig. 5.29: Comparison of experiment semi-variogram vectors. For: Target DFN (0), Target data available in Prediction scenario (3) and Final prediction by conditional global optimisation (FraCGOM 4) (Otsego fault map - Prediction scenario). A. fracture size – B. fracture orientation.



A B

Fig. 5.30: Comparison of modified multi-histogram mean vectors. For: Target DFN (0), Target data available in Prediction scenario (3) and Final prediction by conditional global optimisation (FraCGOM 4) (Otsego fault map - Prediction scenario). A. fracture size – B. fracture orientation.

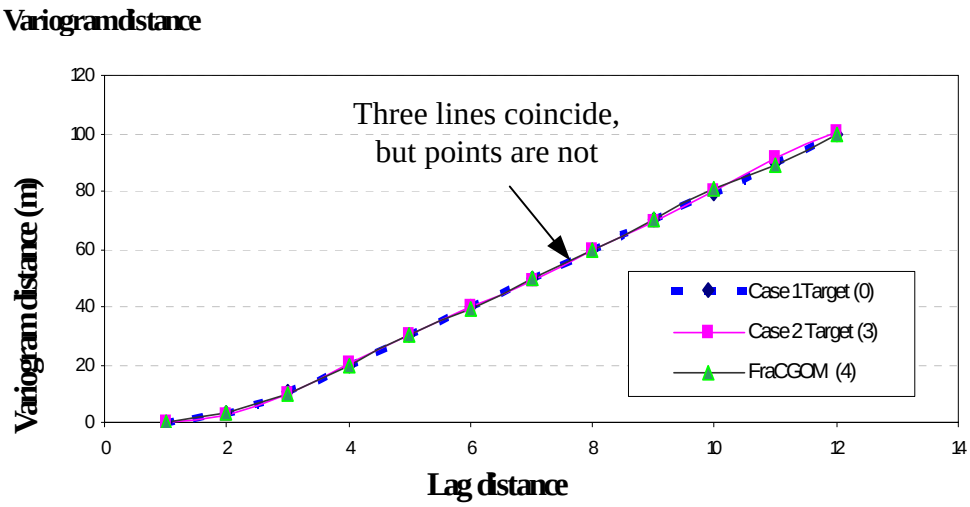


Fig. 5.31: Comparison of experiment variogram distance vectors. For: Target DFN (0), Target data available in Prediction scenario (3) and Final prediction by conditional global optimisation (FraCGOM 4) (Otsego fault map - Prediction scenario).

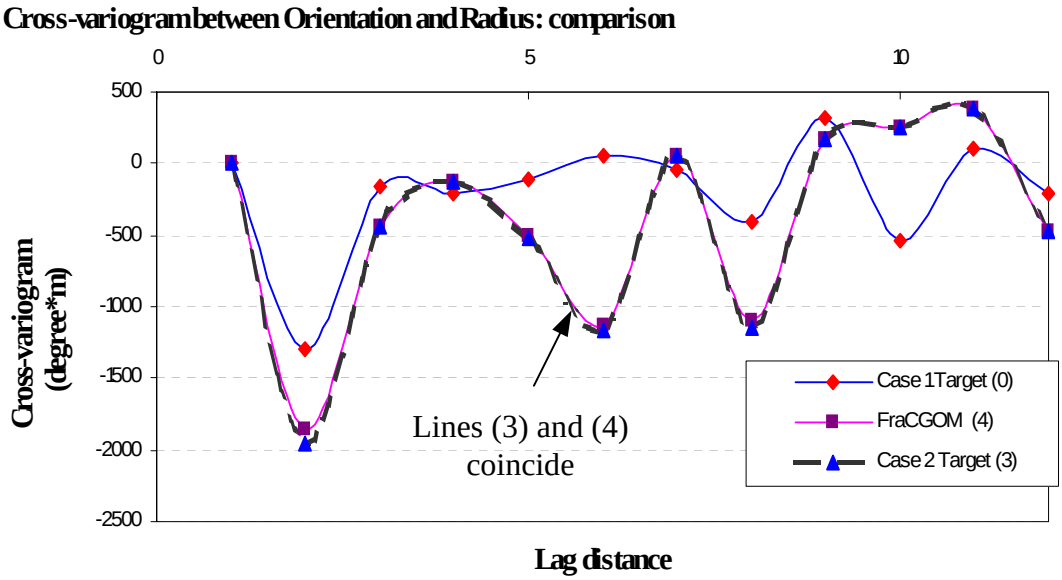


Fig. 5.32: Comparison of experiment cross-variogram of fracture radius and orientation. For: Target DFN (0), Target data available in Prediction scenario (3) and Final prediction by conditional global optimisation (FraCGOM 4) (Otsego fault map - Prediction scenario).

5.4.4.4 Remarks

From limited data available, with a well setup procedure, reasonable results have been produced. The prediction model could be considered statistically well matched with the target fault map. All conditional fractures are maintained. The modelling results can be improved with better data availability and characterisation. When there are more data available, fracture characteristics could be better understood. Then, the output DFN would become closer to the actual target. In cases of actual NFR, advantages of the object-based global optimisation could be better observed when FNN analysis is incorporated. In general, it can be said that the prediction results are satisfactory in the context of geostatistical modelling.

5.5 DISCUSSIONS

A case study on the Otsego fault map has illustrated and validated the procedure and applicability of the object-based conditional global optimisation model. In the reproduction scenario, as a wide range of data is available, the model has produced DFN that is similar to the target fault map. In the prediction scenario, from limited data, the model has generated satisfactory prediction of the target fault map. In both cases, the simulations have been relatively fast.

5.5.1 Modelling Advantages

The object-based conditional global optimisation model offers the following advantages:

一、作为基于目标的模型，对裂缝单独处理，结果更为精确。

Being object-based model, treatment on individual fracture and generation of DFN are ensured. First, from data characterisation and statistical analyses, important behaviours of fracture location, orientation and size as well as their spatial relationships are identified and modelled. Second, each of the fracture properties is modified separately in the transition mechanism. Although a marked point process is more

complex than a grid-based model, it has been used to attain more accurate and useful results.

二、优化方法的使用，不需要预设随机分布。可以利用实际的概率分布和变差函数。建模过程是自我验证的。

Moreover, the use of an optimisation method implies that there is no need for presumed knowledge of any statistical distributions. Fracture properties are not restricted to empirical functions. This enables the use of non-parametric probability distributions and experimental variograms, depending on actual data behaviours. This data-driven feature makes this model much superior over many others, especially stochastic simulation (e.g. Willis-Richards, 1996; Ouenes, 2000; Sahimi, 2000; Zellou and Ouenes, 2001). It is also noted that because the aim of optimisation is to match target characteristics, the program is self-validated.

三、模拟退火可以综合各种数据。

In addition, although simulated annealing requires some trials and errors to fine-tune the objective function and annealing schedule, it offers unique flexibility in integrating data, a feature not easily achieved with other algorithms. Integrated data can be of different nature, sources and scales of investigation. Integrated data can also be both discrete and continuum. For an object-based model, the ability to combine continuum data adds versatility and accuracy. While it is important to analyse individual fracture properties for thorough understanding, many useful rock and fluid properties can only be quantified by dividing modelling region into blocks. The quantities include lithology, fractal, density and permeability tensor. As a result, the hybrid integration helps to output more complete and more physically meaningful fracture model results.

四、目标函数的使用

Furthermore, in this global optimisation model, objective function formulation is a data oriented or data-driven process, which follows comprehensive statistical and spatial analyses. The use of FNN results in better fracture characterisation, which means better target for optimisation. This feature and the ability to incorporate discrete and continuum measurements distinguish the object-based conditional global optimisation from other optimisation fracture models (e.g. Farmer, 1992; Soares et al., 1996).

With the objective function consisting of probability density functions, variogram measurements (e.g. semi-variogram, cross-variogram, modified multi-histogram mean and variogram distance) of fracture properties (e.g. orientation and size) and fracture density distribution, the models could be considered efficient in both accuracy and

speed. The measurements chosen are both informative and obtainable. More components can be included into the objective function, however, convergence would become slower and harder to achieve. It has also been observed that the statistical second order moments and density functions attract higher weighting factors, compared to first order means and variances.

五、条件数据

Another remarkable aspect of this method is its ability to reproduce conditional experimental data. Conditional data could be in the forms of observed fractures, measured orientation values and calculated density values for fractures crossing the wellbores. Preservation of the conditional data ensures that the resulting network would not contradict with what have been positively known. Thus, as more data are available, the result certainly becomes closer to the actual target.

In general, the object-based conditional global optimisation possesses many modelling advantages, especially when the general modelling module is combined with the comprehensive data characterisation (i.e. statistical, geostatistical and FNN analyses: **Chapter 3**). The program is flexible and has many options to accommodate different types of DFN and fracture properties. It represents a great improvement over previous stochastic simulation as well as other optimisation techniques, which could only simulate limited aspects of a complete model.

5.5.2 Modelling Limitations

Nevertheless, from the results of this study, a number of issues have also been identified.

一、该程序需要不断的试错。

First, the program is computationally intensive and requires trials and errors to fine-tune components of the objective function and their respective weighting factors. These limitations are inherent for simulated annealing optimisation.

Second, the output network is not a perfect replica of the target fault map, although all statistics are matched. There are several reasons. Firstly, there are always some components of randomness and generalisation in geostatistical simulation, so that

perfect match is not a criterion. Secondly, the objective function can become very small but it can never reach zero. The final, and perhaps the most important, reason is the choice of components of the objective function.

Apart from the problems in choosing an appropriate and representative set of statistics, there are mathematical and computational obscurities. For example, when presenting the experiment variogram components, only a limited number of intervals could be used as an approximation for the continuous functions.

Furthermore, the use of variogram suggests an assumption of existence. By definition, variogram calculation depends on locations (x_i and $x_i + h$). On the average, this dependence is supposed to cancel out, leaving the separation vector (h) the only factor in the variogram equations that accounts for locations and distances. This is an assumption (intrinsic hypothesis). Geostatistics does not have a test to verify the compliance of this assumption. In addition, covariance requires not only intrinsic hypothesis, but also second order stationarity hypothesis (Cressie, 1991; Olea, 1994). Nevertheless, this assumption is still less rigorous than, for example, assumptions on probability density distributions. Besides, effect of such assumption on the result could be adjusted by using other representative measurements and by choosing appropriate weighting factors that correspond to variograms.

本证假设是很难满足的。虽然如此，比起概率密度函数的假设要宽松。

5.5.3 Final Remarks

Finally, it could be concluded that the object-based conditional global optimisation model has been able to satisfactorily simulate a DFN and its statistics. With the current high standard of computer processing capability, advantages of the model do overcome its limited disadvantages. This is especially true when the model is combined with FNN analysis and the hybrid stochastic simulation model. In addition, due to its versatility, this method can be improved further from researches on different possible objective function components (e.g. different statistical measurements with different combinations) and their respective weighting factors.

CHAPTER 6 - CONCLUSIONS AND RECOMMENDATIONS

6.1 CONCLUSIONS

In this dissertation, two innovative and integrated methodologies to characterise and model NFR have been presented. The final result is representative and reliable DFN models with details of all individual fracture properties such as location, orientation, size and density. "As it is impossible to estimate the reality correctly in sufficient detail, one simple idea is to simulate it on the basis of a model" (Journel and Huijbregts, 1997).

In the characterisation part, the heterogeneity of reservoir fractures, as well as the multi-scaled characteristics of conventional field data, have been examined. Because the field data are of different scales and relevancies, a combination of statistical, spatial, geostatistical and FNN analyses has been incorporated. As a result, important statistical behaviours and spatial distributions (along the wellbores and over the whole field) of the fracture properties are described. They are then used as inputs for the two modules of NFR modelling.

The first module of NFR modelling is the hybrid neuro stochastic simulation. Being an object-based model, discrete fracture attributes are analysed and simulated. Fracture properties are generated based on their characterised statistical distributions by selective random sampling schemes. Continuum maps of fracture density and multifractal dimensions are integrated in the discrete model, accounting for spatial complexity of the fracture distribution. In addition, different degrees of heterogeneity in the reservoir are catered for by the use of hierarchical simulation technique. The simulation is conditioned to the available geological, geophysical and engineering data. The result is expected to model closely with the physical distribution of the reservoir fractures and their properties.

The second module of NFR modelling is the object-based conditional global optimisation. It upgrades the first module by introducing more complex measurements that stochastic simulation and other methods could not make use of, e.g. experimental variograms, non-parametric statistical and spatial distributions. All important fracture characteristics are included in the objective function, which is optimised. In doing so, the global optimisation produces final DFN that match all the statistical and spatial behaviours of the reservoir fractures.

Based on the results of this study, the following conclusions can be drawn:

1. NFR are generally complex and highly heterogeneous. The conventional data sources are scarce and at a wide range of scales. Fracture characterisation is, thus, complicated and not straightforward. An integrated method is required to effectively overcome the multi-scaled problems and combine data from as many tools as possible.
2. Computation of fracture properties (location, orientation, size and density) should be determined by the actual data. It is important to quantify both correlations between the properties and their spatial distributions.
3. Density distribution map and measurements of CSR can be used to study distribution of fracture location. Analyses also indicate that multimodal circular statistics and multifractal geometry are generally suitable to quantify behaviours of fracture orientation and size, respectively.
4. FNN is an effective tool to classify importance of the data sources and to predict fracture properties along the wellbores (by processing wireline log signatures) and spatially over the whole reservoir (by processing seismic attributes). Especially, it allows fracture density distribution and discrete multifractal to be quantified. When combined with statistical and geostatistical analyses, FNN represents arguably the most comprehensive fracture characterisation scheme to date.
5. The hybrid neuro stochastic model is an integrated and data-driven modelling method. It introduces and utilises several novel stochastic simulations: of multimodal circular statistics and correlations for fracture dip and azimuth; of

non-parametric distributions of fracture density; of discrete multifractal. In addition, by integrating continuum distributions (e.g. density and fractal) with statistical distributions and correlations of discrete fracture properties, the model is shown more advanced compared to other object-based stochastic simulation as well as all grid-based fracture models.

6. The object-based conditional global optimisation is self-validated; offers great flexibility and hybrid integration ability. The model is object-based, which allows movements of individual fractures to reach the optimum setup. It can incorporate both discrete data (e.g. distributions of fracture orientation and size) and grid-based data (e.g. fracture density map). It is efficiently fast, able to honour more data and capable to produce more reliable DFN than conventional geo-statistical simulation techniques.
7. The determinant factor for success of the global optimisation model is the appropriate formulation of objective function, where advantages from the advanced fracture characterisation could be applied. The optimum set up has been found to incorporate information of fracture density, statistics and spatial distributions of fracture location, orientation and size. This offers great flexibility, avoids many mathematical assumptions, facilitates the use of non-parametric density functions and efficient at the current computational standard.
8. In general, individual components of the two modules such as circular statistics, fractal geometry, variograms, FNN and simulated annealing have been documented. However, the integration into a comprehensive method (as described throughout this thesis) is innovative. The models and their results have been proved better than others in literature. The modelling can be repeated throughout the development of a NFR. The result can then be combined with conventional geological reservoir models as inputs for further reservoir simulation and stimulation studies.

6.2 SCOPE FOR FUTURE RESEARCH

The following recommendations are suggested:

1. Introduce more flexibility to both models by accommodating various fracture shapes. In addition, the global optimisation module can benefit from further researches on different possible objective function components (e.g. different statistical measurements with different combinations) and their respective weighting factors.
2. Design better visualisation of the final DFN, which is able to show other geological features of the reservoirs.
3. Incorporate a simulation module that is able to calculate effective permeability tensor and fluid flow in the modelling NFR (e.g. Teimoori et al., 2004). As a result, production data could be used for the purpose of better validation.

BIBLIOGRAPHY

REFERENCES

Aarland, R.K. and Skjerven, J. (1998) Fault and Fracture Characteristics of A Major Fault Zone in the Northern North Sea: Analysis of 3D Seismic and Oriented Cores in the Brage Field (Block 31/4). *Geological Society Special Publication*, 127, pp.209-229.

Aarts, E. and Korst, J. (1989) *Simulated Annealing and Boltzmann Machine.* John Wiley & Sons, pp.13-111.

Adams, S.J. (2000) Fracture Porosity from Conventional Logs with Image Tool Calibration. *SPE64408, Society of Petroleum Engineers Asia Pacific Oil and Gas Conference and Exhibition, Brisbane, Australia, Oct.16-18.*

Aguilera, R. (2003) Geologic and Engineering Aspects of Naturally Fractured Reservoirs. *Canadian Society of Exploration Geophysicists Recorder* (February), pp.44-49.

Al Qassab, H.M., Al Khalifa, M.A., Al-Ali, Z., Ameen, M., Phillips, R. and Hartley, L. (2002) New Integrated 3D-Fracture Modelling and Flow Simulation Study: A Giant Saudi Arabian Carbonate Reservoir. *SPE78295, Society of Petroleum Engineers EUROPEC, Aberdeen, Scotland, Oct.29-31.*

Al-Kaabi, A.U. and Le, W.J. (1990) Using Artificial Neural Nets to Identify the Well Test Interpretation Model. *Society of Petroleum Engineers Formation Evaluation*, Sep., pp.233-240.

Anraku, T., Namikawa, T., Herring, T., Jenkins, I., Price, N. and Trythall, R. (2000) Stochastic Fracture Modelling of the Yufutsu Field. *SPE59400, Society of Petroleum Engineers Asia Pacific Conference on Integrated Modelling for Asset Management, Yokohama, Japan, Apr.25-26.*

Ass'ad, J.M., Kusky, T.M., McDonald, J.A. and Tatham, R.H. (1992) Implications of Scale-Model Seismology in the Detection of Natural Fractures and Micro-cracks. *Journal of Seismic Exploration*, 1(1), pp.61-76.

Atkinson, C. and Theircelin, M. (1995) The Interaction Between the Wellbore and Pre-Existing Fractures. *International Journal of Fractures*, 73, pp.183-200.

Babadagli, T. (2001) Fractal Analysis of 2D Fracture Networks of Geothermal Reservoirs in South-western Turkey. *Journal of Volcanology and Geothermal Research*, 112, pp.83-103.

Babcock, E.A. (1978) Measurement of Subsurface Fractures from Dipmeter Logs. *American Association of Petroleum Geologists Bulletin*, 62(7), pp.1111-1126.

Baecher, G.B., Lanney, N.A. and Einstein, H.H. (1978) Statistical Description of Rock Properties and Sampling. *18th US Symposium on Rock Mechanics, USA.*

Bailey, T.C. and Gatrell, A.C. (1995) *Interactive Spatial Data Analysis*. Longman Group Limited, New York, USA.

Baker, R.O. and Kuppe, F. (2000) Reservoir Characterisation for Naturally Fractured Reservoirs. *SPE63286, 2000 Society of Petroleum Engineers Annual Technical Conference and Exhibition, Dallas, USA, Oct.1-4.*

Baker, R.O., Contreras, R.A. and Sztukowski, D. (2000) Characterisation of the Dynamic Fracture Transport Properties in a Naturally Fractured Reservoir. *SPE59690, Society of Petroleum Engineers Permian Basin Oil and Gas Recovery Conference, Texas, USA, Mar.21-23.*

Baker, R.O., Schechter, D.S., McDonald, P., Knight, W.H., Leonard, P. and Rounding, C. (2001) Development of a Fracture Model for Spraberry Field, Texas USA. *SPE71635, Society of Petroleum Engineers Annual Technical Conference and Exhibition, Louisiana, Sep.30-Oct.3.*

Baraka-Lokmane, S. (2002) A New Resin Impregnation Technique for Characterising Fracture Geometry in Sandstone Cores. *International Journal of Rock Mechanics and Mining Sciences*, 39(6), pp.815-823.

Barker, J. (1988) A Generalised Radial-Flow Model for Pumping Tests in Fractured Rock. *Water Resources Research*, 24(10), pp.1796-1804.

Barman, I., Ouenes, A., and Wang, M. (2000) Fractured reservoir characterisation using streamline-based inverse modelling and artificial intelligence tools. *SPE63067, 2000 Society of Petroleum Engineers Annual Technical Conference and Exhibition, Dallas, USA, Oct.1-4.*

Barr, D.C. (1989a) *Core Fracture Study-wells: Palm Valley No.1, Palm Valley No.3, Palm Valley No.4*. Core Laboratories, for Magellan Petroleum Australia Limited (unpublished)

Barr, D.C. (1989b) *Core Structure Study-well: Palm Valley No.7.* Core Laboratories, for Magellan Petroleum Australia Limited (unpublished)

Barton, C.A. and Zoback, M.D. (1992) Self-Similar Distribution and Properties of Macroscopic Fractures at Depth in Crystalline Rock in the Cajon Pass Scientific Hole. *Journal of Geophysical Research,* 97(B4), pp.5181-5200.

Bates, C.R., Lynn, H.B. and Simon, M. (1999) Study of a Naturally Fractured Gas Reservoir Using Seismic Techniques. *American Association of Petroleum Geologists Bulletin,* 83(9), pp.1392-1407.

Bates, C.R., Phillips, D.R., Grimm, R. and Lynn, H. (2001) The Seismic Evaluation of a Naturally Fractured Tight Gas Sand Reservoir in the Wind River Basin, Wyoming. *Petroleum Geoscience,* 7, pp.35-44.

Bazant, Z.P. and Ohtsubo, H. (1978) Geothermal Heat Extraction by Water Circulation through A Large Crack in Dry Hot Rock Mass. *International Journal for Numerical and Analytical Methods in Geomechanics,* 2, pp.317-327.

Beckham, W.E. (1996) Seismic Anisotropy and Natural Fractures from VSP and Borehole Sonic Tools - A Field Study. *Geophysics,* 61(2), pp.456-466.

Belfield, W. (2000) Predicting Natural Fracture Distribution in Reservoirs from 3D Seismic Estimates of Structural Curvature. *SPE60298, Society of Petroleum Engineers Rocky Mountain Regional / Low Permeability Reservoirs Symposium, Colorado, USA, Mar.12-15.*

Belfield, W.C. (1998) Incorporating Spatial Distribution into Stochastic Modelling of Fractures: Multifractals and Levy-Stable Statistics. *Journal of Structural Geology,* 20(4), pp.473-486.

Bell J.S., Caillet G. and Adams J. (1992) Attempts to Detect Open Fractures and Non-sealing Faults with Dipmeter Logs. *In:* Hurst A. *et al*. (eds) *Geological Applications of Wireline Logs II.* Geological Society, London, England, 65, pp.211-220.

Berkowitz, B. and Hadad, A. (1997) Fractal and Multifractal Measures of Natural and Synthetic Fracture Networks. *Journal of Geophysical Research,* 102 (B6), pp.12205-12218.

Berry, M.D. (1991) *Palm Valley No.7, Core Analysis, Summary and Interpretation of Results.* Magellan Petroleum Australia Limited (unpublished)

Berry, M.D. (1995b) *FMS to Core Correlation, Palm Valley No.7.* Magellan Petroleum Australia Limited (unpublished)

Berry, M.D., Stearns, D.W and Friedman, M. (1996) The Development of a Fractured Reservoir Model for the Palm Valley Gas Field. *Journal of the Australian Petroleum Production and Exploration Association Ltd.*, pp.82-103.

Bloomfield, J. (1996) Characterisation of Hydro-geologically Significant Fracture Distributions in the Chalk: an Example from the Upper Chalk of Southern England. *Journal of Hydrology*, 184, pp.355-379.

Boadu, F.K. (1997a) Fractured Rock Mass Characterisation Parameters and Seismic Properties: Analytical Studies. *Journal of Applied Geophysics*, 36, pp.1-19.

Boadu, F.K. (1997b) Rock Properties and Seismic Attenuation: Neural Network Analysis. *Pure and Applied Geophysics*, 149, pp.507-524.

Boadu, F.K. (1998) Inversion of Fracture Density from Field Seismic Velocities using Artificial Neural Networks. *Geophysics*, 63(2), pp.534-545.

Boadu, F.K. and Long, L.T. (1994) Statistical Distribution of Natural Fractures and the Possible Physical Generating Mechanism. *Pure and Applied Geophysics*, 142(2), pp.273-293.

Bodvarsson, G.S. (1988) Reservoir Development Strategy for Hot Water Reservoirs with Emphasis on Reservoir Modelling. *Geothermal Resources Council Bulletin*, 7, pp.68-90.

Boerner, S., Gray, D., Zellou, A.M. and Schnerk, G. (2003) Employing Neural Networks to Integrate Seismic and Other Data for the Prediction of Fracture Intensity. *SPE84453, Society of Petroleum Engineers Annual Technical Conference and Exhibition, Colorado, USA, Oct.5-8.*

Bourbiaux, B.J., Cacas, M.C., Sarda, S. and Sabathier, J.C. (1997) A Fast and Efficient Methodology to Convert Fractured Reservoir Images Into a Dual-Porosity Model. *SPE38907, Society of Petroleum Engineers Annual Technical Conference and Exhibition, Texas, USA, Oct.5-8.*

Bourne, S.J., Rijkels, L., Stephenson, B.J. and Willense, E.J.M. (2001) Predictive Modelling of Naturally Fractured Reservoirs Using Geomechanics and Flow Simulation. *GeoArabia*, 6(1), pp.27-42.

Brown, A., Davies, M., Nicholson, H. and Gane, B.R. (1999) The Machar Field, Unlocking the Potential of a North Sea Chalk Field. *SPE56974, Society of*

Petroleum Engineers Offshore Europe Conference, Aberdeen, Scotland, Sep.7-9.

Brown, S.R. (1987) Fluid Flow through Rock Joints: The Effect of Surface Roughness. *Journal of Geophysical Research*, 94, pp.9429-9438.

Bunge, R.J. (2001) *Midale Reservoir Fracture Characterisation Using Integrated Well and Seismic Data, Weyburn Field, Saskatchewan.* Doctoral Thesis, Colorado School of Mines, USA.

Cacas, M.C., Daniel, J.M. and Letouzey, J. (2001) Nested Geological Modelling Of Naturally Fractured Reservoirs. *Petroleum Geoscience*, 7, pp.S43-S52.

Cacas, M.C., Ledoux, E., de Marsily, G. and Tillie, B. (1990) Modelling Fracture Flow With A Stochastic Discrete Fracture Network: Calibration And Validation. *Water Resources Research*, 26, pp.479-489.

Carrera, J., Heredia, J., Vomvoris, S. and Hufschmied, P. (1990) Modelling of Flow on A Small Fractured Monzonitic Gneiss Block. *In:* Neuman, S.P. and Neretnieks, I. (eds), *Hydrogeology of Low Permeability Environments*, 2. International Association of Hydro-geologists, Hanover, pp.115-167.

Castaing, C., Genter, A., Chiles, J.P., Bourgine, B. and Ouillon, G. (1997) Scale Effects in Natural Fracture Networks. *International Journal of Rock Mechanics and Mining Science & Geo-mechanics Abstracts*, 34(3-4),

Castrejon-Vacio, F. and Porres-Luna, A.A. (1994) Use of Seismic Attributes in Geological Description of Carbonate Rocks. *SPE28673, Society of Petroleum Engineers International Petroleum Conference and Exhibition of Mexico, Veracruz, Mexico, Oct.10-13.*

Cebastiant, A. (1997) Fracture Network Characterisation of Naturally Fractured Reservoir Using Dynamical System Concept and Artificial Neural Network. *Society of Petroleum Engineers Annual Technical Conference and Exhibition, Omega (2), Texas, USA, Oct.5-8.*

Chambers, K. T., DeBaun, D. R., Durlofsky, L. J., Taggart, I. J., Bernath, A., Shen, A.Y., Legarre, H. A. and Goggin, D. J. (1999) Geologic Modelling, Upscaling and Simulation of Faulted Reservoirs Using Faulted Stratigraphic Grids. *SPE51889, Society of Petroleum Engineers Reservoir Simulation Symposium, Texas, USA, Feb.14-17.*

Charkaluk, E., Bigerelle, M. and Iost, A. (1998) Fractals and Fracture. *Engineering Fracture Mechanics*, 61(2), pp.119-139.

Cheng, Q. (1997) Discrete Multifractals. *Mathematical Geology*, 29(2), pp.245-266.

Cheng, Q. and Agterberg, A.F. (1996) Comparison between Two types of Multifractal Modelling. *Mathematical Geology*, 28(8), pp.1,001-1,015.

Cherepanov, G.P., Balankin, A.S. and Ivanova, V.S. (1995) Fractal Fracture Mechanics. *Engineering Fracture Mechanics*, Elsevier, 51(6), pp.997-1033.

Chilingarian, G. and Fertl, W.H. (1987) Fracture Detection Using Circumferential Acoustic Logs. *Energy Sources*, 9(3), pp.149-160.

Cicerone, R.D. and Toksoz, M.N. (1995) Fracture Characterisation from Vertical Seismic Profiling Data. *Journal of Geophysical Research*, 100(B3), pp.4131-4148.

Clark, R.M, Cox, S.J.D. and Laslett, G.M. (1999) Generalisations of Power-law Distributions Applicable to Sampled Fault-trace Lengths: Model Choice, Parameter Estimation and Caveats. *Geophysics Journal International*, 136, pp.357-372.

Collins, N.E., Eglese, R.W. and Golden, B.L. (1988) Simulated Annealing – An Annotated Bibliography. *American Journal of Mathematical and Management Sciences*, 8(3&4), pp.209-307.

Cox, B.L. and Wang, J. S. Y. (1993) Fractal Surfaces: Measurement and Application in the Earth Sciences. *Fractals*, 1, Plenum Press, New York (ed. Feder, J.), pp.87-115.

Crampin, S., Lynn, H.B. and Booth, D.C. (1989) Shear-wave VSP's: A Powerful New Tool for Fracture and Reservoir Description. *Journal of Petroleum Technology*, 41(3), pp.283-288.

Cressie, N.A.C. (1991) *Statistics for Spatial Data*. John Willey & Sons Inc., New York, USA.

Davison, C.C. (1985) *URL Drawdown Experiment and Comparison with Models*. Atomic Energy of Canada Ltd., TR375, Pinawa, Manitoba.

Day-Lewis, F.D., Hiseh, P.A. and Gorelick, S.M. (2000) Identifying Fracture Zone Geometry Using Simulated Annealing and Hydraulic-Connection Data. *Water Resources Research*, 36(7), pp.1707-1721.

Deng, B., Lee, C. and Chang, J. (1995) Characterisation and Interpretation of Variability of Fracture Pattern in Jointed Andesites, Lan-Yu, Taiwan. *Journal of the Chinese Institute of Engineers*, 18(6), pp.787-799.

Dershowitz, W., Shuttle, D. and Parney, R. (2002) Improved Oil Sweep through Discrete Fracture Network Modelling of Gel Injections in the South Oregon Basin Field, Wyoming. *SPE75162, Society of Petroleum Engineers/ Department of Energy Thirteenth Improved Oil Recovery Symposium, Oklahoma, USA, Apr.13-17.*

Deshowitz, W.S. and Einstein, H.H. (1988) Characterising Rock Joint Geometry with Joint System Models. *Rock Mechanical Rock Engineering*, 21(1), pp.21-52.

Deutsch, C.V. and Cockerham, P.W. (1994) Practical Considerations in the Application of Simulated Annealing to Stochastic Simulation. *Mathematical Geology*, 26(1), pp.67-82.

Deutsch, C.V. and Journel, A.G. (1992) *GSLIB – Geo-statistical Software Library and User's Guide.* Oxford University Press, England, pp.39-60.

Deutsch, C.V. and Journel, A.G. (1994) The Application of Simulated Annealing to Stochastic Reservoir Modelling. *SPE23565, Society of Petroleum Engineers Advanced Technology Series*, 2(2).

Diggle, P. (1983) *Statistical Analysis of Spatial Point Patterns*. Academic Press, London, New York.

Do Rozario, R.F. (1991) The Palm Valley Gas Field, Amadeus Basin, Central Australia. *In:* Korsch, R.J. and Kennard, J.M. (eds.), Geological and Geophysical Studies in the Amadeus Basin, Central Australia. *BMR Bulletin* (236), pp.477-492.

Doughty, C. and Karasaki, K. (2000) *An Effective Continuum Model for Flow and Transport in Fractured Rock.* Berkeley Lap Annual Report, USA.

Duchane, D.V. (1995) Hot Dry Rock: A Versatile Alternative Energy Technology. *Society of Petroleum Engineers Annual Technical Conference and Exhibition, Dallas, USA, Oct.22-25.*

Dyke, C.G., Bailin, W. and Milton-Taylor, D. (1995) Advances in Characterising Natural-Fracture Permeability from Mud-log Data. *Society of Petroleum Engineers Formation Evaluation*, 10(3), pp.160-166.

Edwards, L.M., Chiligar, G.V., Rieke III, H.H. and Fertl, W.H. (eds) (1982) *Handbook of Geothermal Energy.* Gulf Publishing Co., Houston, Texas, USA, pp.44-176.

Einstein, H.H., Baecher, G.B. and Veneziano, D., et al. (1980) *Risk Analysis for Rock Slopes in Open Pit Mines*. Department of Civil Engineering, Massachusetts Institute of Technology, R80-17, Cambridge.

Elkewidy, T.I., and Tiab, D. (1998) Application of Conventional Well Logs to Characterise Naturally Fractured Reservoirs with their Hydraulic (Flow) Units; A Novel Approach. *SPE40038, Society of Petroleum Engineers Gas Technology Symposium, Calgary, Canada, Mar.15-18.*

Emmendorfer, A. (1989) Fracture Orientation: Use of the Dip-meter Type Fracture Log. *Mountain Geologist*, 26(2), pp.63-67.

Ericsson, L.O. and Ronge, B.S.H. (1989) Fracture Mapping on Outcrops in Crystalline Bedrock: a Case Study Within the Sub Cambrian Peneplain, Southern Sweden. *International Journal of Rock Mechanics and Mining Science & Geomechanics Abstracts*, 26(5), p.245.

Escuder Viruete, J., Carbonell, R., Marti, D. and Petrz-Estaun, A. (2003) 3-D Stochastic Modelling and Simulation of Fault Zones in the Albalá Granitic Pluton, SW Iberian Variscan Massif. *Journal of Structural Geology*, 25(9), pp.1487-1506.

Evertsz, C.J.G. and Mandelbrot, B.B. (1992) Multifractal Measures. In Peitgen, H.O., Jurgens, H. and Saupe, D., eds, *Chaos and Fractals*. Springer-Verlag, New York, USA, pp.922-953

Farmer, C.L. (1992) Numerical Rocks. *In:* King, P.R. (eds), *The Mathematics of Oil Recovery*. Clarendon Press, Oxford, England, p.437.

Fett, T. and Williams, A. (1994) *Palm Valley Borehole Breakout Study*. Schlumberger, for Magellan Petroleum Australia Limited (unpublished)

Fisher, N.I. (1993) *Statistical analysis of Circular Data.* Cambridge University Press, Cambridge.

Fitzgerald, E.M., Bean, C.J. and Reilly, R. (1999) Fracture-Frequency Prediction from Borehole Wireline Logs using Artificial Neural Networks. *Geophysical Prospecting*, 47, pp.1031-1044.

Gale, J.E., Schaefer, R.A., Carpenter, A.B. and Herbert, A. (1991) Collection, Analysis, and Integration of Discrete Fracture Data From the Monterey Formation for Fractured Reservoir Simulations. *SPE22741, Society of Petroleum Engineers 66th Annual Technical Conference and Exhibition, Texas, USA, Oct.6-9.*

Gallant, S.I. (1994) *Neural Network Learning and Expert Systems*. The MIT Press, Massachusetts, USA, Chapter 6, 11, 12.

Ganzer, L.J. (2002) Simulating Fractured Reservoirs Using Adaptive Dual Continuum. *SPE75233, Society of Petroleum Engineers/ Department of Energy Thirteenth Improved Oil Recovery Symposium, Oklahoma, USA, Apr.13-17.*

Gauthier, B.D.M., Garcia, M. and Daniel, J-M. (2002) Integrated Fractured Reservoir Characterisation: a Case Study in a North Africa Field. *Society of Petroleum Engineers Reservoir Evaluation & Engineering*, 5(4), pp.284-294.

Geman, S. and Geman, D. (1984) Stochastic Relaxation, Gibbs' Distribution and Bayesian Restoration of Images. *Electrical and Electronics Engineers Inc. Transactions* (PAMI-6), pp.721-741.

Geothermal Resource Council (1995) Solicitation for Cooperative Agreement - Hot Dry Rock Geothermal Energy Systems Development of a Plant to Produce and Market Electric Power or Thermal Energy. *Geothermal Resources Council Bulletin*, 24(1), pp.31-32.

Glowka, D.A., Schafer, D.M., Leoppke, G.E., Scott, D.D., Wernig, M.D. and Wright, E.K. (1992) Lost Circulation Technology Development Status. *CONF/920378 Proceedings of Department of Energy Geothermal Program Review X*, San Francisco, USA, pp.81-88.

Goldstein, L. and Waterman, M. (1988) Neighbourhood Size in the Simulated Annealing Algorithm. *American Journal of Mathematical and Management Sciences*, 8(3&4), pp.409-423.

Gray, F.D. and Head, K.J. (2000) Fracture Detection in the Manderson Field: A 3D AVAZ Case History. *The Leading Edge*, 19(11), pp.1214-1221.

Gray, F.D., Head, K.J., Chamberlain, C.K., Olson, G., Sinclair, J. and Besler, C. (1999) Strike Analysis: A Core Matter. *American Association of Petroleum Geologists Explorer*, 9.

Gray, F.D., Roberts, G. and head, K.J. (2002) Recent Advances in Determination of Fracture Strike and Crack Density from P-wave Seismic Data. *The Leading Edge*, 21(3), pp.280-285.

Gringarten, A.C., Withrspoon, P.A. and Ohnishi, Y. (1975) Theory of Heat Extraction from Fractured Hot Dry Rocks. *Journal of Geophysical Research*, 80, pp.1120-1124.

Gringarten, E. (1996) 3D Geometric Description of Fractured Reservoirs. *Mathematical Geology*, 28(7), pp.881-893.

Gross, M.R. and Engelder, T. (1995) Strain Accommodated by Brittle Failure in Adjacent Units of the Monterey Formation, USA: Scale Effects and Evidence for Uniform Displacement Boundary Conditions. *Journal of Structural Geology*, 17(9), pp.1303-1318.

Grove, G.P. and Whittaker, J.L. (1985) Continuous Fracture Probability Determination as Applied to the Monterey Formation. *SPE13652, Society of Petroleum Engineers California Regional Meeting, California, USA, Mar.27-29.*

Gudmundsson, A. (1987) Tectonics of the Thingvellir Fissure Swarm SW Iceland. *Journal of Structural Geology*, 9(1), pp.61-69.

Guerreiro, L., Silva, A.C., Alcobia, V. and Soares, A. (2000) Integrated Reservoir Characterisation of a Fractured Carbonate Reservoir. *SPE58995, Society of Petroleum Engineers International Petroleum Conference and Exhibition, Villahermosa, Mexico, Feb.1-3.*

Gurpinar, O., Kalbus, J. and List, D. (1999) Numerical Modelling of a Triple Porosity Reservoir. *SPE57277, Society of Petroleum Engineers Asia Pacific Improved Oil Recovery Conference, Kuala Lumpur, Malaysia, Oct.25-26.*

Haldorsen, H.H. and Damsleth, E. (1993) Challenges in Reservoir Characterisation. *AAPG Bulletin*, 77(4), pp.541-551.

Haller, D. and Porturas, F. (1998) How to Characterise Fractures in Reservoirs Using Borehole and Core Images: Case Studies. *Geological Society Special Publication*, 136, pp.249-259.

Harstad, H, Teufel, L.W. and Lorenz, J.C. (1995) Characterisation and Simulation of Naturally Fractured Tight Gas Sandstone Reservoirs. *SPE30573, Society of Petroleum Engineers Annual Technical Conference and Exhibition, Dallas, USA, Oct.22-25.*

Heffer, K.J. and Bevan, T.G. (1990) Scaling Relationships in Natural Fractures: Data, Theory, and Application. *SPE20981, Society of Petroleum Engineers EUROPEC 90, The Hague, Netherlands, Oct.22-24.*

Heffer, K.J., King, P.R. and Jones, A.D.W. (1999) Fracturing Modelling as Part of Integrated Reservoir Characterisation. *SPE53347, Society of Petroleum Engineers Middle East Oil Show, Bahrain, Feb.20-23.*

Hennings, P.H., Olson, J.E. and Thompson, L.B. (2000) Combining Outcrop Data and Three-Dimensional Structural Models to Characterise Fractured Reservoirs: An Example from Wyoming. *American Association of Petroleum Geologists Bulletin*, 84(6), pp.830-849.

Herrmann, H.J. (1995) Some New Results on Fracture. *Physica A*, Elsevier, 221, pp.125-133.

Hewett, T.A. (1994) Fractal Methods for Fracture Characterisation. *Stochastic Modelling and Geostatistics - Principles, Methods and Case Studies,* Yarus, J.M. and Chambers, R.L., The American Association of Petroleum Geologists, Tulsa, USA

Hews, P. (2000) *Structural Features that Can Be Identified from Drill Cuttings, Interpretations, Implications and Fracture Evaluation.* Hara Consulting Ltd. Course Manual.

Hillis, R. (1994) *Review of Palm Valley Borehole Breakout Study*. Schlumberger/ University of Adelaide, for Magellan Petroleum Australia Limited (unpublished)

Hirata, T. (1989) Fractal Dimension of Fault Systems in Japan: Fractal Structure in Rock Fracture Geometry at Various Scales, *Pure and Applied Geophysics*, 131(1/2), pp.158-170.

Hirsch, J.M., Cisar, M.T., Glass, S.W., and Romanowski, D.A. (1981) Recent Experience with Wireline Fracture Detection Logs. *SPE10333, Society of Petroleum Engineers 56th Annual Technical Conference and Exhibition, Texas, USA, Oct.5-7.*

Hirst, J. P. P., Davis, N., Palmer, A. F., Achache, D. and Riddiford, F. A. (2001) The 'Tight Gas' Challenge: Appraisal Results from the Devonian of Algeria. *Petroleum Geoscience*, pp.13-21.

Holbrook, P.W. (1989) A new Method for Predicting Fracture Propagation Pressure from MWD or Wireline Log Data. *SPE19566, Society of Petroleum Engineers 64th Annual Technical Conference and Exhibition, Texas, USA, Oct.8-11.*

Hooper, G. and Duchane, D. (1996) Hot Dry Rock: An Untapped Resource. *The Sustainable Energy Industry Journal*, 1(2), European Media Marketing Ltd., London, England, pp.58-61.

Hossain, M.M. (2001) *Reservoir Stimulation by Hydraulic Fracturing: Complexities and Remedies with reference to Initiation and Propagation of Induced and Natural Fractures.* PhD dissertation, School of Petroleum Engineering, The University of New South Wales, Sydney, Australia, Chapter 6.

Hossain, M.M., Rahman, M.K. and Rahman, S.S. (2000) Volumetric Growth and Hydraulic Conductivity of Naturally Fractured Reservoirs During Hydraulic Fracturing: A Case Study Using Australian Conditions. *Society of Petroleum Engineers Reservoir Engineering*, pp.545-560.

Hsieh, P.A. and Neuman, S.P. (1985) Field Determination of the Three-Dimensional Hydraulic Conductivity Tensor of Anisotropic Media. *Water Resources Research*, 21, pp.1655-1666.

Huang, Y., Wong, P. and Gedeon, T.D. (1999) An AI Integrated Method for Permeability Prediction in Petroleum Reservoir. *International Workshop on Soft Computing in Industry 1999, Hokkaido, June 16-18*, pp.299-304.

Hurst, A., Griffiths, C.M. and Worthington, P.F. (1992) *Geological Applications of Wireline Logs II.* Geological Society, London, England, 65.

Iverson, W.P. (1992) Fracture Identification From Well Logs. *SPE24351, Society of Petroleum Engineers Rocky Mountain Regional Meeting, Wyoming, USA, May 18-21.*

Jamison, R.W. (1997) Quantitative Evaluation of Fractures on Monkshood Anticline, a Detachment Fold in the Foothills of Western Canada. *American Association of Petroleum Geologists Bulletin*, 81(7), pp.1110-1132.

Jang, J.S.R, Sun, C.T. and Mizutani, E. (1997) *Neural - Fuzzy and Soft Computing - A Computational Approach to Learning and Machine Intelligence.* Prentice-Hall International Inc., New Jersey, USA.

Jensen, C.L., Lee, S.H., Milliken, W.J., Kamath, J., Narr, W., Wu, H. and Davies, J.P. (1998) Field Simulation of Naturally Fractured Reservoirs Using Effective Permeabilities Derived From Realistic Fracture Characterisation. *SPE48999, Society of Petroleum Engineers Annual Technical Conference and Exhibition, Louisiana, USA, Sep.27-30.*

Jensen, O.K., Bresling, S., Christensen, O.W., Rasmussen, F.O., Foged, N. and Petersen, K. (1989) Natural Fracture Distribution in Reservoirs Modelled by Back-stripping and Finite Element Stress Analysis. *SPE18429, Society of*

Petroleum Engineers Symposium on Reservoir Simulation, Texas, USA, Feb.6-8.

Jin, Y. and Zhang, X. (2002) Research on Log Fracture Parameter Estimation and Reservoir Fracture Evaluation Method. *Tianranqi Gongye/Natural Gas Industry*, 22(SUPPL), pp.64-67 +6.

Journel, A.G. and Huijbregts, C.J. (1997) *Mining Geostatistics*. Academic Press, London, Great Britain.

Kacewicz, M. (1994) Model-free Estimation of Fracture Aperture with Neural Networks. *Mathematical Geology*, 26(8), pp.985-994.

Karimi-Fard, M. and Firoozabadi, A. (2003) Numerical Simulation of Water Injection in Fractured Media Using the Discrete Fracture Model and the Galerkin Method. *SPE83633, Society of Petroleum Engineers Reservoir Evaluation & Engineering* (April).

Kazemi, H., and Gilman, J.R. (1993) Multiphase Flow in Fractured Petroleum Reservoirs. *In:* Bear, J., Tsang, C.F. and De Marsily, G. (eds), *Flow and Contaminant Transport in Fractured Rocks.* Academic Press, New York, USA, pp.267-323.

Kirkpatrick, S., Gelatt, C.D., Jr., and Vecchi, M.P. (1983) Optimisation by Simulated Annealing. *Science*, 220, pp.671-680.

Klinkenberg, B. (1994) A Review of Methods Used to Determine the Fractal Dimension of Linear Features. *Mathematical Geology*, 26(1), pp.23-46.

Koike, K. and Kaneko, K. (1999) Characterisation and Modelling of Fracture Distribution in Rock Mass Using Fractal Theory. *Geothermal Science and Technology*, 6(1), pp.43-62.

Kosko, B. (1992) *Neural Networks and Fuzzy Systems: A Dynamical Systems Approach to Machine Intelligence*. Prentice Hall, New Jersey, USA, Chapter 1, 5.

Kubik, W. and Lowry, P. (1993) Fracture Identification and Characterisation using Cores, FMS, CAST, and Borehole Camera: Devonian Shale, Pike County, Kentucky. *SPE25897, Society of Petroleum Engineers Rocky Mountain Regional/ Low Permeability Reservoirs Symposium, Denver, USA, Apr.12-14.*

Kumar, V., Burns, D., Dutta, D. and Hoffmann, C. (1999) A Frame Work for Object Modelling. *Computer-Aided Design*, 31, pp.541-556.

Kuwahara, Y., Ito, H. and Kiguchi, T. (1991) Comparison between natural Fractures and Fracture Parameters from VSP. *Geophysical Journal International*, 107, pp.475-483.

Kuwahara, Y., Ito, H., Ohminato, T., Nakao, S. and Kiguchi, T. (1995) Size Characterisation of In Situ Fractures by High Frequency S-wave Vertical Seismic Profiling (VSP) and Borehole Logging. *Geothermal Science and Technology*, 5(1-2), pp.71-78.

Laarhoven, P.J.M. and Aarts, E.H.L. (1987) *Simulated annealing: theory and applications.* Kluwer Academic Publishers, Boston, USA, pp.23-46.

Lanyon, G.W., Batchelor, A.S. and Ledingham, P. (1993) Results from A Discrete Fracture Network Model of A Hot Dry Rock System. *Proceedings of 18th Workshop on Geothermal Reservoir Engineering Stanford University*, Stanford, California, USA, Jan.26-28.

LaPointe, P., Wallmann, P. and Dershowitz, W. (1993) Flow Compartmentalisation of Effective Permeability in 3D Fractal Fracture Networks. *International Journal of Rock Mechanics and Mining Sciences*, 34(3/4), p.390.

Laubach, S., Marrett, R. and Olson, J. (2000) New Directions in Fracture Characterisation. *The Leading Edge*, pp.704-711.

Laubach, S.E., Monson, E.R., Hunt, E., Meador, K.J. and Baumgardner Jr., R.W. (1988) Fracture Detection in Low-Permeability Reservoir Sandstone: A Comparison of BHTV and FMS Logs to Core. *SPE18119, Society of Petroleum Engineers 63rd Annual Technical Conference and Exhibition, Texas, Oct.2-5.*

Lee, D.S., Walden, A.F. and Wachi, N. (1994) Fracture Characterisation of the Monterey Formation Using VSP. *Journal of Seismic Exploration*, 3(4), pp.335-350.

Lee, S. H., Jensen, C.L. and Lough, M. F. (1999) An Efficient Finite Difference Model For Flow In a Reservoir With Multiple Length-Scale Fractures. *SPE56752, Society of Petroleum Engineers Annual Technical Conference and Exhibition, Texas, Oct.3-6.*

Lefeuvre, F., Turpening, R., Caravana, C., Born, A. and Nicoletis, L. (1993) Vertical Open Fractures and Shear-wave Velocities Derived From VSPs, Full Waveform Acoustic Logs, and Televiewer Data. *Geophysics*, 58(6), pp.818-834

Lei, W. and Chen, B. (1995) Fractal Characterisation of Some Fracture Phenomena. *Engineering Fracture Mechanics*, 50(2), pp.149-155.

Li, D., Liu, J., Sanchez-Barajas, J., Seader, R. and Lanz-Torres, C.L. (1997) A New Practical Approach to Building a 3D Naturally Fractured Reservoir Model. *SPE38012, Society of Petroleum Engineers Reservoir Simulation Symposium, Texas, USA, Jun.8-11*.

Li, X.Y. (1997) Fractured Reservoir Delineation using Multi-component Seismic Data. *Geophysical Prospecting*, 45, pp.39-64.

Lisle, J.L. (1994) Detection of Zones of Abnormal Strains in Structures using Gaussian Curvature Analysis. *American Association of Petroleum Geologists Bulletin*, 78(12), pp.1811-1819.

Locke, C.D., Salamy, S.P. and Overbey Jr., W.K. (1989) Correlations of Interference/ Pulse - Test Results with Tilt meter Studies of Fractures Induced in the Chattanooga Shale. *SPE19314, Society of Petroleum Engineers Eastern Regional Meeting, West Virginia, USA, Oct.24-27.*

Long, J.C.S and Billaux, D.M. (1987) From Field Data to Fracture Network Modelling: an Example Incorporating Spatial Structure. *Water Resources Research*, 23(7), pp.1201-1216.

Long, J.C.S., Doughty, C., Hestir, K. and Martel, S. (1992) Modelling Heterogeneous And Fractured Reservoirs With Inverse Methods Based On Iterated Function System. *In:* Linville, B. (eds.), *Reservoir Characterisation III*. Penwell Books, Tulsa, USA.

Long, J.C.S., Karasaki, K., Davey, A., Peterson, J., Landsfeld, M., Kemeny, J. and Martel, S. (1991) Inverse Approach to the Construction of Fracture Hydrology Models Conditioned by Geophysical Data. An Example from the Validation Exercises at the Stripa Mine. *International Journal of Rock Mechanics and Mining Sciences & Geomechanics Abstracts*, 28(2-3), pp.121-142.

Lorenz, J.C. and Hill, R.E. (1994) Subsurface Fracture Spacing: Comparison of Inferences From Slant/ Horizontal and Vertical Cores. *International Journal of Rock Mechanics and Mining Science & Geomechanics Abstracts*, 31(4), p.197.

Lynn, H.B., Bates, R., Layman, M. and Jones, M. (1995) Natural Fracture Characterisation Using P-Wave Reflection Seismic Data, VSP, Borehole Imaging Logs, and the In-Situ Stress Field Determination. *SPE29595, Society*

of Petroleum Engineers Rocky Mountain Regional / Low Permeability Reservoirs Symposium, Colorado, USA, Mar.20-22.

Lynn, H.B., Simon, K.M. and Bates, C.R. (1996) Correlation Between P-wave AVOA and S-wave Travel-time Anisotropy in a Naturally Fractured Gas Reservoir. *The Leading Edge*, 15(8), pp.931-935.

Main, I.G., Peacock, S. and Meredith, P.G. (1990) Scattering Attenuation and the Fractal Geometry of Fracture Systems. *Pure and Applied Geophysics*, 133(2), pp.283-304.

Mandelbrot, B. B. (1983) *The Fractal Geometry of Nature*. W. H. Freeman and Company, New York, USA.

Mardia, K.V. (1986) *Statistics of Directional Data.* Academic Press, Inc., London.

Marrett, R. and Peacock, D. (1997) Strain and Stress. *Journal of Structural Geology* (Aug.24), pp.2-16.

Mauldon A.D. *et al*. (1993) An Inverse Technique for Developing Models for Fluid Flow in Fracture Systems Using Simulated Annealing. *Water Resources Research*, 29(11), pp.3775-3789.

Mazurek, M., Lanyon, G.W., Vomvoris, S. and Gautschi, A. (1998) Derivation and Application of a Geologic Dataset for Flow Modelling by Discrete Fracture Networks in Low-permeability Argillaceous Rocks. *Journal of Contaminant Hydrology*, 35(1-3), pp.1-17.

McCoy, R.L., Kumar, R.M. and Pease, R. (1980) Identifying Fractures With Conventional Well Logs. *World Oil*, 191(7), pp.91-94 +96 +98.

McDonald, P, Lorenz, J.C, Sizemore, C., Schechter, D.S., and Sheffield, T. (1997) Fracture Characterisation Based on Oriented Horizontal Core from the Spraberry Trend Reservoir: a Case Study. *SPE38664, Society of Petroleum Engineers Annual Technical Conference and Exhibition, San Antonio, Texas, USA, Oct.5-8.*

Meadows, M.A. and Winterstein, D.F. (1994) Seismic Detection of a Hydraulic Fracture from Shear-Wave VSP Data at Lost Hills Field, California. *Geophysics*, 59(1), pp.11-26.

Metropolis, N., Rosenbluth, A., Rosenbluth, M., Teller, A. and Teller, E. (1952) Equation of State Calculations by Fast Computing Machines. *Journal of Chemical Physics*, 21, pp.1087-1092.

Miler, N. (1993) Predicting Flow Characteristics of a Lixiviant in a Fractured Crystalline Rock Mass. *Report of Investigations 9457,* Bureau of Mines, 24.

Milne, N.A. and Barr, D.C. (1990) Subsurface Fracture Analysis, Palm Valley Gas Field. *Journal of the Australian Petroleum Production and Exploration Association Ltd.*, 30(1), pp.321-341.

Nakagome, O., Uchida, T. and Horikoshi, T. (1998) Seismic Reflection and VSP in the Kakkonda Geothermal Field, Japan: Fractured Reservoir Characterisation. *Geothermics*, 27(5/6), pp.535-552.

Nakao, S., Najita1, J. and Karasaki1, K. (2000) Hydraulic Well Testing Inversion for Modelling Fluid Flow in Fractured Rocks Using Simulated Annealing: A Case Study at Raymond Field Site, California. *Journal of Applied Geophysics*, 45(3), pp.203-223.

Nanjo, K., Nagahama, H. and Satomura, M. (1998) Rates of Aftershock Decay and the Fractal Structure of Active Fault Systems. *Tectonophysics*, 287, pp.173-186.

Narayan, S.P., Naseby, D., Yang, Z. and Rahman, S.S. (1998) Petroleum and Hot Dry Rock: two types of energy sharing commonalities. *Journal of The Australian Petroleum Production And Exploration Association Ltd.*, pp.830-848.

National Research Council (1992) *Groundwater at Yucca Mountain: How High Can It Rise?*. National Academy Press, Washington, D.C., USA.

National Research Council (1996) *Rock Fractures and Fluid Flow - Contemporary Understanding and Applications.* National Academy Press, Washington, D.C., USA.

Nelson, R.A. (1982) An Approach to Evaluating Fractured Reservoirs. *SPE10331, Society of Petroleum Engineers Journal of Petroleum Technology* (September).

Nelson, R.A. (2001) *Geologic Analysis of Naturally Fractured Reservoirs*. Second Edition. Gulf Professional Publishing, Boston, USA.

Neuman, S.P. and Depner, J.S. (1988) Use of Variable Scale Pressure Test Data to Estimate the Log Hydraulic Conductivity Covariance and Dispersivities of Fractured Granites near Oracle, Arizona. *Journal of Hydrology*, 102(1-4), pp.475-501.

Neves, F.A., Al-Marzoug, A., Kim, J.J. and Nebrija, E.L. (2003) Fracture Characterisation of Deep Tight Gas Sands Using Azimuthal Velocity and AVO Seismic Data in Saudi Arabia. *The Leading Edge*, Tulsa, 22(5), pp.469-475.

Nikov, A. and Stoeva, S. (2001) Quick Fuzzy Back-propagation Algorithm. *Neural Networks*, 14, pp.231-244

Noblett, B.R. and Fertl, W.H. (1987) Circumferential Acoustic Log Finds Vertical Fractures. *World Oil*, 205(5), pp.37-38.

Oda, M., Hatsuyama, Y. and Ohnishi, Y. (1987) Numerical Experiments On Permeability Tensor And Its Application To Jointed Granite At Stripa Mine, Sweden. *Journal of Geophysical Research*, 92, pp.8037-8048.

Odling, N.E. (1997) Scaling and Connectivity of Joint Systems in Sandstones from Western Norway. *Journal of Structural Geology*, 19(10), pp.1257-1271.

Ohminato, T., Ito, H., Kuwahara, Y., Nakao, S. and Kiguchi, T. (1996) Vertical Seismic Profile (VSP) Measurement of Seismic Attenuation Due To Fractures. *International Journal of Rock Mechanics and Mining Science & Geomechanics Abstracts*, 33(7), p.307A.

Olea, R.A. (1994) Fundamentals of Semi-variogram – Estimation, Modelling and Usage. *In: Stochastic Modelling and Geostatistics – Principles, Methods, and Case Studies.* American Association of Petroleum Geologists Computer Applications in Geology, (3), Tulsa, USA, pp.27-35.

Olson, J.E., Hennings, P.H. and Laubach, S.E. (1996) Integrating Wellbore Data and Geo-mechanical Modelling for Effective Characterisation of Naturally Fractured Reservoirs. *SPE47352, Society of Petroleum Engineers /ISRM Eurock '96, Trondheim, Norway, July 8-10.*

Olson, J.E., Qiu, Y., Holder, J. and Rjken, P. (2001) Constraining the Spatial Distribution of Fracture Networks in Naturally Fractured Reservoirs Using Fracture Mechanics and Core Measurements. *SPE71342, Society of Petroleum Engineers Annual Technical Conference and Exhibition, Louisiana, USA, Sep.30 - Oct.3.*

Olsson, O. (eds) (1992) *Site Characterisation and Validation. Final Report, Stripa Project, 92-22.* Conterra AB, Uppsala, Sweden.

Ouenes, A. (2000) Practical Application of Fuzzy Logic and Neural Networks to Fractured Reservoir Characterisation. *Computers & Geosciences*, 26, pp.953-962.

Ouenes, A. and Hartley, L.J. (2000) Integrated Fractured Reservoir Modelling Using Both Discrete and Continuum Approaches. *SPE62939, 2000 Society of*

Petroleum Engineers Annual Technical Conference and Exhibition, Dallas, USA, Oct.1-4.

Overbey Jr., W.K., Yost, L.E. and Yost II, A.B. (1988) Analysis of Natural Fractures Observed by Borehole Video Camera in a Horizontal Well. *SPE17760, Society of Petroleum Engineers Gas Technology Symposium, Texas, USA, June 13-15.*

Ozgen, C., Firincioglu, T. and Albertoni, A. (2003) Fracture Characterisation for Integrated Studies: A new approach and its applications. *SPE84413, Society of Petroleum Engineers Annual Technical Conference and Exhibition, Colorado, USA, Oct.5-8.*

Ozkaya, S.I. and Mattner, J. (2003) Fracture Connectivity From Fracture Intersections in Borehole Image Logs. *Computers & Geosciences*, 29(2), pp.143-153

Padgett, M.J. and Nester, D.C. (1991) Fracture Evaluation of Block P-0315, Point Arguello Field, Offshore California, Using Core, Outcrop, Seismic Data and Curved Space Analysis. *In:* Sneider R.M. *et al*. (eds), *The Integration of Geology, Geophysics, Petrophysics and Petroleum Engineering in Reservoir Delineation, Description and Management.* American Association of Petroleum Geologists, pp.242-268.

Paillet, F.L. and Goldberg, D. (1991) Acoustic Televiewer Log Images of Natural Fractures and Bedding Planes in the Toa Baja Borehole, Puerto Rico. *Geophysical Research Letters*, 18(3), pp.501-504.

Palmer, I.D. and Sparks, D.P. (1991) Measurement of Induced Fractures by Down-hole TV Camera in Black Warrior Baskin Coal-beds. *SPE20660, Journal of Petroleum Technology*, pp.270-275 +326-328 +457-458.

Panek, L.A. (1985) Estimating Fracture Trace Length from Censored measurements on Multiple Scanlines. *Proceedings of the International Symposium on Fundamentals of Rock Joints, Bjorkliden, Sweden, Sep.15-20.*

Parney, R., Cladouhos , T., La Pointe, P., Dershowitz, W. and Curran, B. (2000) Fracture and Production Data Integration Using Discrete Fracture Network Models for Carbonate Reservoir Management, South Oregon Basin Field, Wyoming. *SPE60306, Society of Petroleum Engineers Rocky Mountain Regional/Low Permeability Reservoirs Symposium and Exhibition, Colorado, USA, Mar.12-15.*

Pistre, S., Bangoy, L.M. and Rives, T. (1995) A New Approach for the Prediction of Unexposed Fractured Reservoirs: A Case Study in Millas Granite (French Pyrenees). *Hydrological Sciences Journal*, 40(3), pp.351-365.

Pruess, K. and Narasimhan, T.N. (1988) Numerical Modelling of Multiphase and Non-isothermal Flows in Fractured Media. *Symposium Conference on Fluid Flow in Fractured Rocks, Georgia State University, May 15-18.*

Pyrak-Nolte, L.J. (1996) The Seismic Response of Fractures and the Interrelations among Fracture Properties. *International Journal of Rock Mechanics and Mining Sciences & Geomechanics Abstracts*, 33(8), pp.785-802.

Quintero, E.J., Martinez, L.P. and Gupta, A. (2001) Characterisation of Naturally Fractured Reservoirs Using Artificial Intelligence. *SPE67286, Society of Petroleum Engineers Production and Operations Symposium, Oklahoma, USA, Mar.24-27.*

Rahim, Z. and Al-Qahtani, M.Y. (2001a) Sensitivity Study On Geo-mechanical Properties To Determine Their Impact On Fracture Dimensions And Gas Production In The Khuff And Pre-Khuff Formations Using A Layered Reservoir System Approach, Ghawar Reservoir, Saudi Arabia. *SPE72142, Society of Petroleum Engineers Asia Pacific Improved Oil Recovery Conference, Kuala Lumpur, Malaysia, Oct.8-9.*

Rahim, Z. and Al-Qahtani, M.Y. (2001b) Using Radioactive Tracer Log, Production Tests, Fracture Pressure Match, and Pressure Transient Analysis to Accurately Predict Fracture Geometry in Jauf Reservoir, Saudi Arabia. *SPE71650, Society of Petroleum Engineers Annual Technical Conference and Exhibition, Louisiana, USA, Sep.30- Oct.3.*

Rahman, M.M., Rahman, M.K. and Rahman, S.S. (2000) The Recognition and Alleviation of Complexity with Hydraulic Fracturing Onshore Australia. *Journal of the Australian Petroleum Production and Exploration Association Ltd.*, pp.469-480.

Rahman, M.M., Rahman, M.K. and Rahman, S.S. (2001) An Integrated Model for Multi-objective Design Optimisation of Hydraulic Fracturing. *Journal of Petroleum Science and Engineering*, 31(1), pp.41-62.

Rawnsley, K. and Wei, L. (2001) Evaluation of a New Method to Build Geological Models of Fractured Reservoirs Calibrated to Production Data. *Petroleum Geoscience*, 7, pp.23-33.

Rayner, B.L. (1995) *Palm Valley 10 and 10A FMS Interpretation Report.* Schlumberger, for Magellan Petroleum Australia Limited, pp.762-774 (unpublished)

Reeves, M., Freeze, G.A., Kellel, V.A., Pickens, J.F., Upton, D.T. and Davis, P.B. (1991) *Regional Double Porosity Solute Transport in the Culebra Dolomite under Brine-Reservoir-Breach Release Conditions: an Analysis of Parameter Sensitivity and Importance*. Sandia National Laboratories, SAND89-7069, Albuquerque, N.M.

Renfang, P., Yuhua, Z, and Songqun, S. (2002) Study on the AVO Forward Modelling of Sandstone HE-8, Permian, Shuligemiao Gas Field. *Tianranqi Gongye/Natural Gas Industry*, 22(5), pp.7-10 +1-2.

Rives, T., Razack, M., Petit, J.P. and Rawnsley, K.D. (1992) Joint Spacing: Analogue and Numerical Simulations. *Journal of Structural Geology*, 14(8/9), pp.925-937.

Rodgerson, R.L. (2000) Impact of Natural Fractures in Hydraulic Fracturing of Tight Gas Sands. *SPE59540, Society of Petroleum Engineers Permian Basin Oil and Gas Recovery Conference, Texas, USA, Mar.21-23.*

Roe, L.E. (1995) *1994 Palm Valley Seismic Survey, Interpretation Report*. Magellan Petroleum Australia Limited (unpublished)

Rogers, S.F. (2000) Prediction of Fracture Frequency from Wireline Data with Aid of Artificial Neural Networks. *Transactions of the Institution of Mining and Metallurgy, Section B: Applied Earth Science*, 109(SEP-DEC), pp.190-195.

Rough, R.L. (1974) *Stress Measurements at Palm Valley, Gosses Bluff and Ooraminna Structures - Amadeus Basin, Northern Territory, Australia*. Magellan Petroleum Australia Limited (unpublished)

Rouleau, A. and Gale, J.E. (1985) Statistical Characterisation of the Fracture System in the Stripa Granite, Sweden. *International Journal of Rock Mechanics and Mining Science & Geo-mechanics Abstracts*, 22(6), pp.353-367.

Ruger, A. and Tsvankin, I. (1997) Using AVO for Fracture Detection: Analytic Basis and Practical Solutions. *The Leading Edge*, Tulsa, USA, 16(10), pp.1429-1430 +1432-1434.

Sahimi, M. (1995) New Models for Natural and Hydraulic Fracturing of Heterogeneous Rock. *SPE29648, Society of Petroleum Engineers Western Regional Meeting, California, USA, Mar.8-10.*

Sahimi, M. (2000) Fractal-Wavelet Neural-Network Approach To Characterisation And Up-scaling Of Fractured Reservoirs. *Computers & Geosciences*, 26, pp.877-905.

Saito, H. and Hayashi, K. (1999) Detection of a Reservoir Fracture by the Use of Sonic Log Data in EE-4, Higashi-Hachimantai. *Transactions - Geothermal Resources Council*, 23, pp.433-437.

Sanchez, D.M.A., Vasquez, A.R, Van Alstine, D., Butterworth, J., Carmona, R., Poquioma, W. and Ramones, M. (1999) Applications of Geo-mechanics in the Development of the Naturally Fractured Carbonates of the Mara Oeste Field, Venezuela. *SPE54008, Society of Petroleum Engineers Latin American and Caribbean Petroleum Engineering Conference, Caracas, Venezuela, Apr.21-13.*

Sarda, S., Jeannin, L., Basquet, R. and Bourbiaux, B. (2002) Hydraulic Characterisation of Fractured Reservoirs: Simulation on Discrete Fracture Models. *SPE77300, Society of Petroleum Engineers Reservoir Evaluation & Engineering*, (April).

Sayers, C.M. and Ebrom, D.A. (1997) Seismic Travel-time Analysis for Azimuthally Anisotropic Media: Theory and Experiment. *Geophysics*, 62(5), pp.1570-1582.

Sayers, C.M. and Rickett, J.E. (1997) Azimuthal Variation in AVO Response for Fractured Gas Sands. *Geophysical Prospecting*, 45, pp.165-182.

Schlumberger (1996) *Log Interpretation Principles/ Applications*. Fourth Printing. Texas, USA

Scholz, C. H. and Aviles, C. A. (1986). The Fractal Geometry of Faults and Faulting. *Earthquake Source Mechanics* (editors, Das, S., Boatwright, J. and Scholz, S. H.) Geophysical Monograph Series, Washington, D.C., American Geophysical Union, 37, pp.145-155.

Sen, M. and Stoffa, P.L. (1995) *Global Optimisation Methods in Geophysical Inversion.* Elsevier, Amsterdam, Holland, pp.79-123.

Serra, O. (1986) *Fundamentals of Well-Log Interpretation, 2. The Interpretation of Logging Data.* Developments in Petroleum Science, Elsevier, 15B.

Shen, F. and Ouenes, A. (2003) Seismically Driven Integrated Fracture Modelling. *SPE84460, Society of Petroleum Engineers Annual Technical Conference and Exhibition, Colorado, USA, Oct.5-8.*

Shen, F., Zhu, X. and Toksöz, M.N. (2002) Effects of Fractures on NMO Velocities and P-wave Azimuthal AVO Response. *Geophysics*, 67(3), pp.711-726.

Shibuya, Y., Sekine, H., Takahashi, Y. and Abe, H. (1985) Multiple Artificial Geothermal Cracks in A Hot Dry Rock Mass for Extraction of Heat. *Journal of Energy Resources Technology*, 107, pp.274-279.

Silverman, B.W. (1998) *Density Estimation for Statistics and Data Analysis*. Chapman & Hall/ CRC, Boca Raton, USA, pp.95-117.

Smith, M. (1993) *Neural Networks For Statistical Modelling*. Van Nostrand Reinhold, New York, USA.

Smith, R. and McGarrity, J.P. (2001) Cracking the Fractures-Seismic Anisotropy in An Offshore Reservoir. *The Leading Edge*, 20, 1, pp.18-27.

Snow, D.T. (1970) The Frequency and Apertures of Fractures in Rock. *International Journal of Rock Mechanics and Mining Science & Geo-mechanics Abstracts*, 7, pp.23-40.

Soares, A., Brusco, A. and Guimaraes, C. (1996) Simulation of Naturally Fractured Fields. *In:* Baafi, E.Y. and Schofield, N.A. (eds), *Geostatistics Wollongong*. Australia, pp.1433-1441.

Song, X., Zhu, Y., Liu, Q., Chen, J., Ren, D., Li, Y., Wang, B. and Liao, M. (1998) Identification and Distribution of Natural Fractures. *SPE50877, Society of Petroleum Engineers International Conference and Exhibition, Beijing, China, Nov.2-6.*

Stach, S., Cybo, J. and Chmiela, J. (2001) Fracture Surface - Fractal or Multifractal. *Materials Characterisation*, 26, pp.163-167.

Stach, S., Cybo, J. and Chmiela, J. (2001) Fracture Surface – Fractal or Multifractal. *Materials Characterisation*, 26, pp.163-167.

Stearns, W. and Fieldman, M. (1972) Reservoirs in Fractured Rocks. *In: Stratigraphic Oil and Gas Fields; Classification, Exploration Methods and Case Histories*. American Association of Petroleum Geologists, Memorandum (16), pp.82-106.

Suau, J. and Gartner, J. (1980) Fracture Detection From Well Logs. *Log Analyst*, 21(2), pp.3-13.

Swaby, P.A. and Rawnsley, K.D. (1996) An Interactive 3D Fracture Modelling Environment. *SPE36004, Society of Petroleum Engineers Petroleum Computer Conference, Texas, USA, June 2-5.*

Takayasu, H. (1990) *Fractals in the Physical Sciences*. Manchester University Press, Manchester, UK, pp.141-162.

Tamagawa, T., Matsuura, T., Anraku, T., Tezuka, K. and Namikawa, T. (2002) Construction of Fracture Network Model Using Static and Dynamic Data. *SPE77741, Society of Petroleum Engineers Annual Technical Conference and Exhibition, Texas, USA, Sept.29 - Oct.2.*

Tamanya, S., Fujiwara, S., Ishikawa, J. and Jingu, H. (1998) Fracture System Related to Geothermal Reservoir Based on Core Samples of Slim Holes. Example From the Uenotai Geothermal Field, Northern Honshu, Japan. *Geothermics*, 27(2), pp.143-166.

Tamhane, D., Wong, P.M. and Aminzadeh, F. (2002) Integrating Linguistics Descriptions and Digital Signals in Petroleum Reservoirs. *International Journal of Fuzzy Systems*, 4(1), pp.586-591.

Teimoori, A., Tran, N.H., Chen, Z. and Rahman, S.S., (2004) Simulation of Fluid Flow in Naturally Fractured Reservoirs with the Use of Effective Permeability Tensor. *Annual proceeding of Geothermal Resources Council (GRC) 2004*. Australia.

Terzaghi, R.D. (1965) Sources of Error in Joint Surveys. *Geotechnique*, 15, pp.287-304.

Tovey, C.A. (1988) Simulated Simulated Annealing. *American Journal of Mathematical and Management Sciences*, 8(3&4), pp.389-407.

Tran, N.H., Chen, Z. and Rahman, S.S (2003a) Characterising and Modelling of Naturally Fractured Reservoirs with the Use of Object-based Global Optimisation. *Canada International Petroleum Conference, Calgary, Alberta, Canada, June 10 - 12, PAPER 2003-179.*

Tran, N.H., Chen, Z. and Rahman, S.S (2003b) Object-Based Global Optimisation in Modelling Discrete-Fracture Network Map: A Case Study. *SPE Annual Technical Conference and Exhibition, Colorado, U.S.A., Oct.5–8.*

Tran, N.H., Rahman, M.K. and Rahman, S.S. (2002a) Developing a Hot Dry Rock Reservoir in Australia by Hydraulic Stimulation: a Shear-Dilation Model for Design and Evaluation. *Geothermal Resources Council Transactions*, 26.

Tran, N.H., Rahman, M.K. and Rahman, S.S. (2002b) A Nested Neuro-Fractal-Stochastic Technique for Modelling Naturally Fractured Reservoirs. *SPE77877, Society of Petroleum Engineers Asia Pacific Oil and Gas Conference and Exhibition, Melbourne, Australia, Oct.8-10.*

Trice R. (1999) Application of Borehole Image Logs in Constructing 3D Static Models of Productive Fracture Networks in the Apulian Platform, Southern Apennines. *Geological Society Special Publication*, 159, pp.155-176.

Twiss, R.J. and Moores, E.M. (1992) *Structural Geology*. W H Freeman & Co Ltd.

Walsh, J. J. and Watterson, J. (1993) Fractal Analysis of Fracture Patterns Using the Standard Box-Counting Technique: Valid and Invalid Methodologies. *Journal of Structural Geology*, 15, pp.1509-1512.

Wang, L., Wong, P.M., Kanevski, M. and Gedeon, T.D. (1999) Combining Neural Networks with Kriging for Stochastic Reservoir Modelling. *In Situ*, 23(2), pp.151-169

Warpinski, N.R. (1991) Hydraulic Fracturing In Tight, Fissured Media. *Journal of Petroleum Technology*, pp.146-209.

Watanabe, K. and Takahashi, H. (1995) Fractal Geometry Characterisation of Geothermal Reservoir Fracture Networks. *Journal of Geophysical Research*, 100(B1), pp.521-528.

Wealthall, G.P., Kueper, B.H. and Lerner, D.N. (2001) Fractured Rock-mass Characterisation for Predicting the Fate of DNAPLS. *Conference Proceedings of Fractured Rock 2001, Toronto, Ontario, Canada.*

Wells, A.T., Forman, D.J., Ranford, L.C. and Cook, P.J. (1970) Geology of the Amadeus Basin, Central Australia. *BMR Bulletin* (100).

Wen, R. and Sinding-Larsen, R. (1996) Stochastic Modelling and Simulation of Small Faults by Marked Point Processes and Kriging. *In:* Baafi, E.Y. and Schofield, N.A. (eds), *Geostatistics Wollongong.* Australia, pp.398-414.

Willis-Richards, J. (1996) Progress toward a Stochastic Rock Mechanics Model of Engineered Geothermal Systems. *Journal of Geophysical Research*, 101(B8), pp.17481-17496.

Wilson, T.H. (2001) Scale Transitions in Fracture and Active Fault Networks. *Mathematical Geology*, 33(5), pp.591-613.

Wong, P.M. (1999) Prediction of Permeability and Its Reliability from Well Logs using a Windowing Technique. *Journal of Petroleum Geology*, 22(2), pp.215-226.

Wong, P.M. and Shibli, S.A.R. (1998) Use of Interpolation Neural networks for Permeability Estimation from Well Logs. *Log Analyst*, 39(6), pp.18-26.

Wong, P.M., Henderson, D.J. and Brooks, L.J. (1998) Permeability Determination using Neural Networks in the Ravva Field, Offshore India. *Society of Petroleum Engineers Formation Evaluation*, Apr. 1(2), pp.99-104

Xie, H., Wang, J.A. and Kwasniewski, M.A. (1999) Multifractal Characterisation of Rock Fracture Surfaces. *International Journal of Rock Mechanics and Mining Science & Geo-mechanics Abstracts*, 36, p.19-27.

Yearsley, E.N. and Crowder, R.E. (1992) Acoustic Spectrum Analysis of Borehole Sonic Logs for Engineering Properties and Fracture Characterisation: a Case History. *International Journal of Rock Mechanics and Mining Science & Geomechanics Abstracts*, 29(1), p.A31.

Zadeh, L.A. (1965) Fuzzy Sets. *Information and Control*, 8, pp.338-353

Zellou, A., Ouenes, A. and Banik, A. (1995) Improved naturally fractured reservoir characterisation using neural networks, geo-mechanics and 3-D seismic. *SPE30722, Society of Petroleum Engineers Annual Technical Conference and Exhibition, Dallas, USA, Oct. 22-25.*

Zellou, M. and Ouenes, A. (2001) Integrated Fractured Reservoir Characterisation using Neural Networks and Fuzzy Logic: Three Case Studies. *Journal of Petroleum Geology*, 24(4).

Zemanek, J., Caldwell, R.L., Glenn Jr., E.E., Holcomb, S.V., Norton, L.J. and Straus, A.J.D. (1969) The Borehole Televiewer – A New Logging Concept for Fracture Location and Other Types of Borehole Inspection. *SPE2402, Journal of Petroleum Technology*, pp.762-774.

INTERNET REFERENCES

Eric Weisstein's World of Mathematics: http://mathworld.wolfram.com

Greek Astro: http://www.astro.gr/general/earth/icons/fault.jpg

Institut des Sciences de la Terre, de l'Environnement et de l'Espace de Montpellier: http://www.dstu.univ-montp2.fr

NASA: http://rst.gsfc.nasa.gov/Sect2/Sect2_7.html

New York Water Find maps: http://www.nywaterfind.com/fractureotsego.jpg

University of California at Santa Barbara - Institute for Crustal Studies: http://www.crustal.ucsb.edu/projects/mapcat/images/scal6.jpeg

University of South Dakota - Physics: http://www.usd.edu/phys/courses/astronomy/images/Venus/Fault.jpg

Warsaw University - Geology: http://www.geo.uw.edu.pl/ZASOBY/GEOIMAGE/FAULT/konon02.htm

APPENDIX A - SAMPLE FRACTURE MAPS

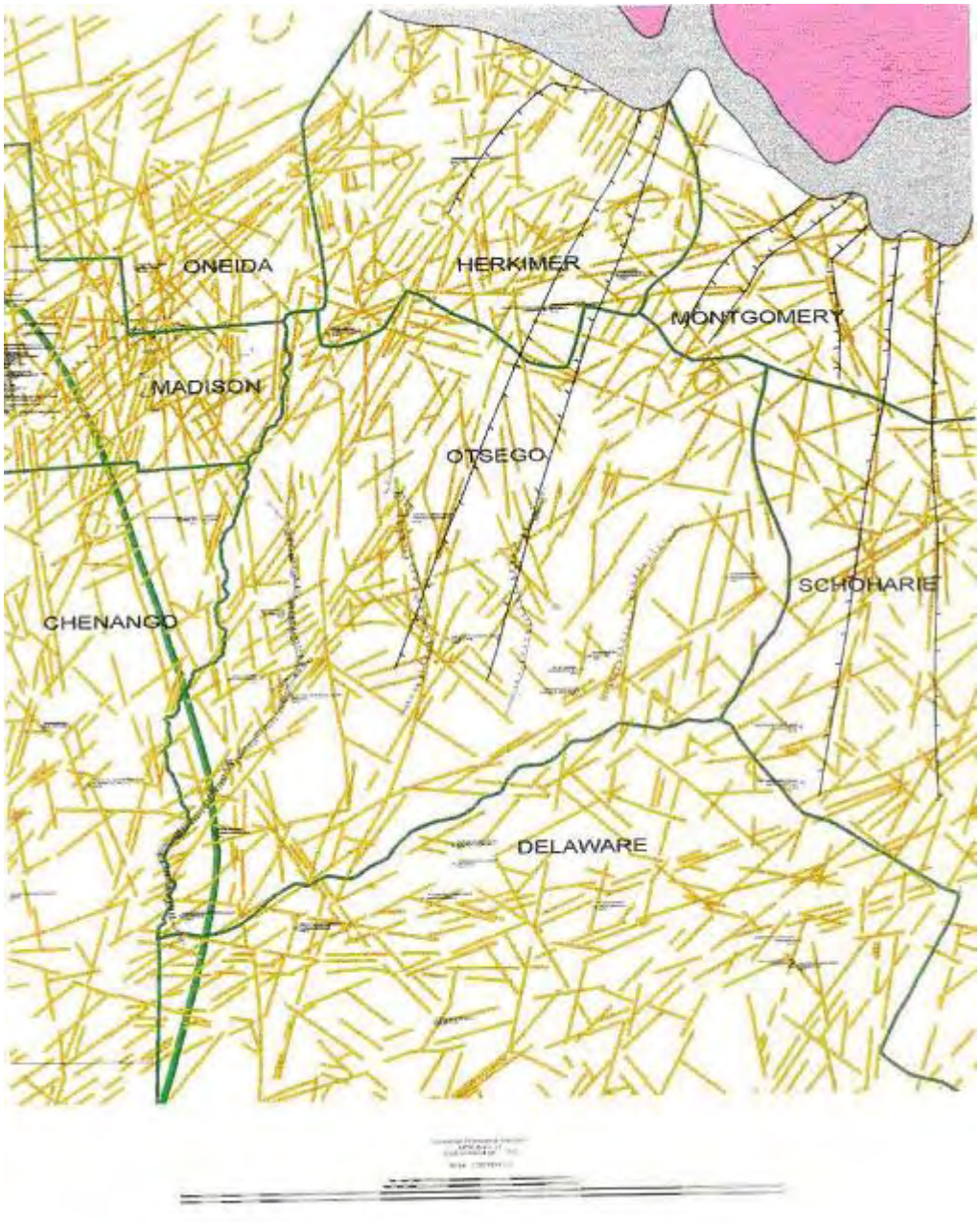


Fig. A.1: Fault map of Otsego county and surrounding area (New York, USA) [http://www.nywaterfind.com/fractureotsego.JPG]



Fig. A.2: Fault system of North East Mediterranean region (Greece) [http://www.astro.gr/general/earth/icons/fault.jpg]



Fig. A.3: Joint system cutting basalt flow in Zambia over which flows the Zambezi River (Victoria Falls): Joints are long, continuous, widely spaced and enlarged by erosion [http://rst.gsfc.nasa.gov/Sect2/Sect2_7.html]



Fig. A.4: Fault map of Southern California region (USA). Faults tend the same directions: towards NW and NWW, along the mountain range [http://www.crustal.ucsb.edu/projects/mapcat/images/scal6.jpeg]

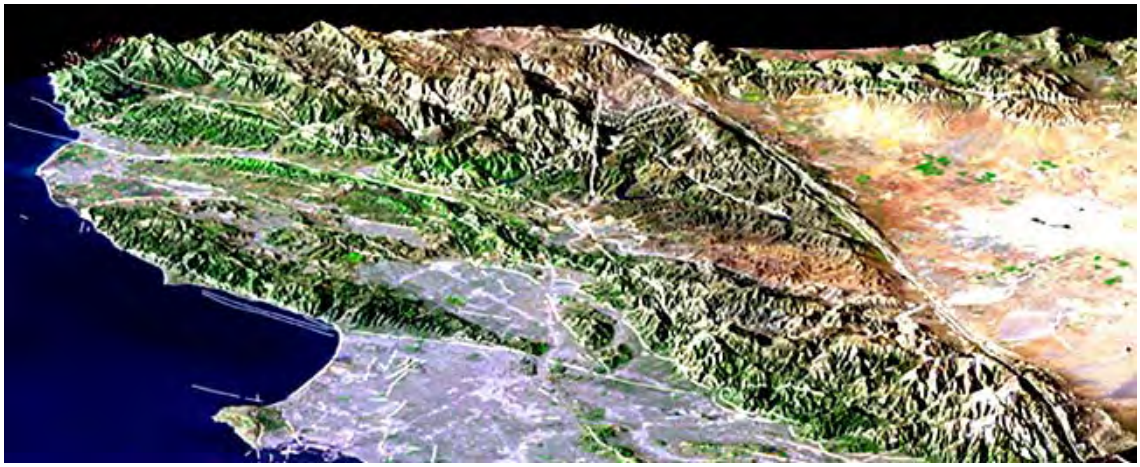


Fig. A.5: Perspective view of the Transverse Ranges (California, USA) made by combining Landsat imagery with topographic data acquired by JPL's SRTM mission (radar altimetry). Fault lines (in white) have been drawn on the resulting image, which also depicts the Los Angeles Basin (bottom centre) and the Mojave Desert (right) [http://rst.gsfc.nasa.gov/Sect2/Sect2_7.html]



Fig. A.6: Example of fault surfaces at very small scales
[http://geo.uw.edu.pl/ZASOBY/GEOIMAGE/FAULT/konon02.htm]

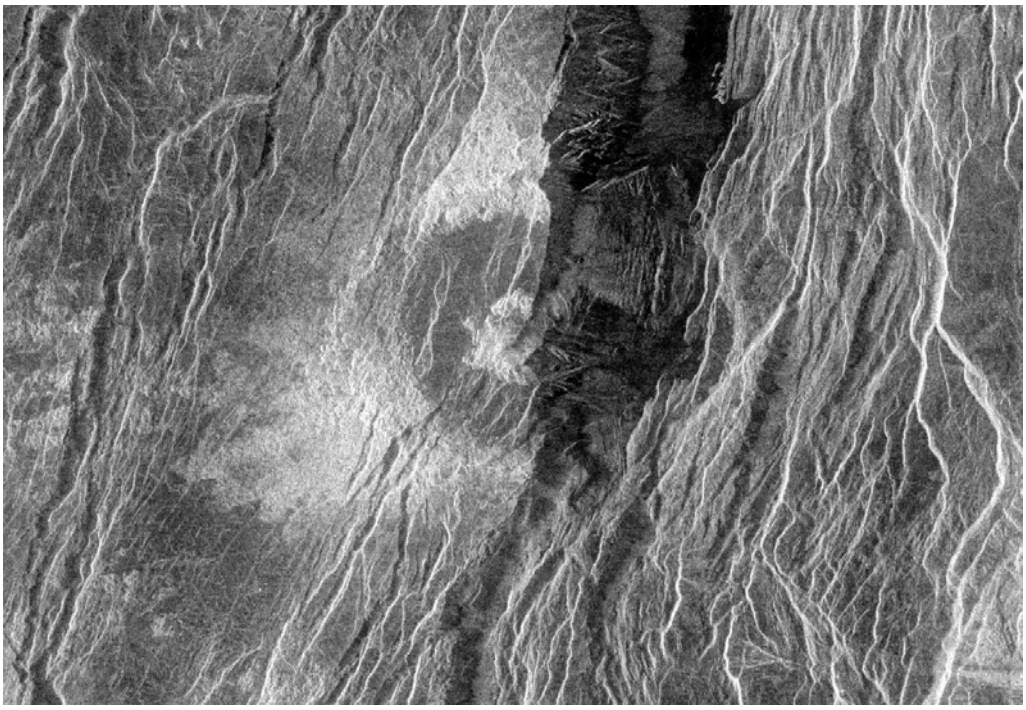


Fig. A.7: Fault system developed from volcanic activities in Venus
[http://www.usd.edu/phys/courses/astronomy/images/Venus/Fault.jpg]

APPENDIX B

SPATIAL GEOSTATISTICS – DISTRIBUTION OF FRACTURE LOCATION

Coordinates of Fracture Location

As mentioned in **Chapter 2** (**2.2**), individual fractures are presented as marked points, which are located at centres of fractures and include parameters such as orientation and size. The marked point data (or the regionalised variables) include fractures and part of fractures that could be observed from seismic interpretations, outcrops and wellbore images.

From marked point data, x, y and z coordinates of fracture location can be mapped. Their histograms can be plotted and probability density functions can be derived. In addition, map of fracture intensity (λ) can also be derived. Intensity is the first order property describing how the mean number of points per bounded region varies through space. The map is smoothed either by least of error squared or kernel algorithms. Kernel method estimates intensity at each point using a weighted function of the surrounding points (e.g. **Fig. 5.9**).

The plots provide initial notion of fracture distribution in the study region. It can identify obvious patterns of centre points, e.g. region of high and low fracture activities (clusters). Generally, these observations are neither conclusive nor quantitative.

Measurements of Complete Spatial Randomness

Nearest Neighbour Methods

Nearest neighbour methods include point-to-point and origin-to-point nearest neighbour statistics. The point-to-point ($\hat{G}(h)$) defines a nearest neighbour distance (l_i) from the i^{th} point to the nearest other point in the region. It is first order and comparable

to variogram correlatable distance (as discussed in **Section 3.3.2.1**). The statistic is the fraction of points (over total *n* points) that are within a distance (*h*) from one another.

$$\hat{G}(h) = \frac{1}{n} \cdot \sum_{l_i \le h} 1 \tag{B.1}$$

Origin-to-point nearest neighbour statistic ($\hat{F}(h)$) is an equivalent analysis, where distance (l_i) from *m* random origins to the nearest neighbours are compared:

$$\hat{F}(h) = \frac{1}{m} \cdot \sum_{l_i \le h} 1 \tag{B.2}$$

These two empirical functions can be used for comparison to a CSR process. If there is clustering in the data, in G-function plot, an excess of short distance neighbours is expected. In other words, the function ascends steeply in its early section. If there is regularity in the data, there will be an excess of long distance neighbours. The interpretation of F-function plot is opposite that of the G-function plot. An excess of high distance values is now interpreted as clustering. For CSR, the two functions are expected to be similar such that their cross-plot results in a straight line (e.g. **Fig. 5.11**).

The K-function

K-function is a second order property, which describes how the spatial interaction between points varies through space. K-function is defined as the product of fracture intensity (λ) and expected number of points (N_h) within a distance (h) of an arbitrary point.

$$\hat{K}(h) = \frac{1}{\lambda} \cdot E[N_h] \tag{B.3}$$

For a homogeneous process with no spatial dependence (i.e. CSR), K-function plot is the parabolic ($\pi \cdot h^2$). K-function is greater than $\pi \cdot h^2$ in case of clustering. It is lower than $\pi \cdot h^2$ for regularly spaced patterns (e.g. **Fig. 5.12**).

Variance Stabilising Transformation

Variance stabilising transformation L-function is defined to directly compare K-function with $\pi \cdot h^2$. It is a straight line for a homogeneous Poisson random process (e.g. **Fig. 5.13**).

$$\hat{L}(h) = \sqrt{\frac{\hat{K}(h)}{\pi}} \tag{B.4}$$

Practical Considerations

The edge or censoring bias should be noted when applying the above methods. For example, G-function is overestimated near the boundary where points are denied the possibility of neighbours that are located outside. Correction methods for such bias are listed in Bailey and Gatrell (1995), e.g. using guard area, toroidal edge correction or modified functions. A Monte Carlo simulation can also be used to assess bias effect and hypothesis of CSR (Cressie, 1991).

In addition, as each of the tests can only cover certain aspects of the spatial distribution, it is important that several tests are executed together. For each functions plot, adding error boundaries can assess the significance of clustering. It is noted that the above tests are only qualitative, which indicate a systematic pattern that fracture centre points might follow.